Nanodiamond Single Photon Sources for Quantum Information Processing

Laia Ginés Bartolomé

Submitted in partial fulfilment of the requirements for the degree of
Doctor of Philosophy

School of Physics and Astronomy
Cardiff University
2018

Acknowledgements

First, I would like to thank my Supervisor, Prof. Oliver Williams, Ollie, for the opportunity he gave me almost four years ago to start a PhD on diamond, a practically unknown material for me (not anymore!) Thanks for all the scientific discussions, your help in the lab, for reading and correcting abstracts, papers, the thesis (which I always sent too close to deadlines) and in general for pushing me in the right direction towards the completion of my PhD. I've never seen such an enthusiastic scientist/person, and I hope one day I can be half as enthusiastic as you are. I'm also really grateful for all the opportunities I've had over these years, being involved in many projects, that although sometimes stressful, have been so much fun. Outside the lab, thanks also for all the beers and for showing me what has become my favourite bar: the tiny rebel!

All the work done during this thesis would not have been possible without the help and company of all the Diamond people, especially Soumen and Evan, the lab bosses. Thanks both for your assistance in the reactor design, and in general for making sure everything work, I can't imagine a lab without the both of you! Soumen, thank you for your selfless help, and for being there whenever I needed, I've learnt a lot from you. Evan, you were the first member (with Ollie) of the Diamond group and his first PhD student, and dammit, you set the bar too high! Thanks for being an awesome diamond mate but also for becoming a good friend, always willing to help me, and cheering me up with you presents and sweets (thanks for the werewolf and Ramón Ramírez). I would also like to thanks Georgina, George, for her dedication and the implementation of the reactor control. The reactor would not be working without your help! Of course I would also like to thanks Jess...oh Jess...you beautiful amazing human being. You know how important you have been during the last three years and a half, my PhD sister. This thesis process would not have been the same without you. Thanks for sharing good and not that good moments both at University and outside. And thanks for the thousands of shelfies and pictures! I would also like to thanks the rest of the diamond people, Majdi, Henry, and the new

additions. I hope you enjoy Cardiff and the diamond group as much as I've done.

Special thanks for all our collaborators. Thanks Ashek-I-Ahmed and Prof. Chia-Liang Cheng, Charlie, for the FTIR measurements performed at National Dong Hwa University, in Taiwan, the really helpful scientific discussions and for the amazing stay we had in Taiwan. I wish to also say thanks to Phil Dolan and Prof. Jason Smith, at Oxford university for the PL measurements. Finally to Prof. Christoph Becher, Sarah Lidner and Alexander Bommer, at Saarland University, Germany, also for the PL measurements. Thanks to Prof. Gavin Morley and Angelo Frangeskou, from Warwick University. Thanks to Ryan and Prof. Paola Borri for their help during the XPS measurements.

Within the department, I wish to say thanks to Dr. Emmanuel Brousseau, for the assistance with the AFM. Thanks also to the technical staff, in particular to Hugh Lang, David Walker, Scott Cook, Dave Melhuish and Andrew Harrison.

Apart from my diamond group, I would also like to thank the people I've met at University. Lorenzo, my late-hours office mate, with whom I've shared so many complaints about how tough a thesis is, but always with a smile on his face. And Sara, for the conversations during lunch time and for organising trips around Wales. I would also like to thanks my French friend, Maabur. I had really good time working with you and you also made me laugh with your Spanish style...que pasa grapadora! I still owe you a visit to Oxford!. Y por supuesto no podía faltar agradecer al bando español, Dani Margineda, Kennet y mi amigo "the small Dani". Dani, tu llegada a Cardiff me dio la vida. Porque conectamos enseguida y porque contagiaste a todos con tu alegría. Gracias por todas nuestras conversaciones (por fin alguien con quien criticar), y por todos los cafés, tes, cervezas y tus increíbles tortillas...¡sólo nos faltan unos torreznos en Soria! Porque sé que tengo (y tienes) un amigo para siempre, y sé que nos seguiremos viendo. Y a ver si algún año conseguimos estar en el mismo pais...nuestro 10 de abril.

Outside University, I would also like to thank all the amazing people I've met during the last four years. Thanks to my friend Niek, best housemate ever! Thanks for the all the interesting conversations, and even scientific discussions during dinner. Also thanks for teaching me some Dutch words (THAT WORD will always be in my head, haha). Because at the end, what not a bad idea to put a Chemist and a Physicist in the same house. I would like to thank my friends David and Sue. David, thanks for the Saturday coffees and for your enthusiasm in learning Spanish. Thanks also for the wines and dinner invitations. You are more than welcome to visit me in Spain! Gracias también a mis chicas de Cardiff,

Marta, Eva y especialmente a Su. Su, gracias porque fuiste un gran apoyo cuando más lo necesité y por todos los buenos momentos que pasamos. No puedo creer que hace ya más de dos años que te fuiste de Cardiff, pero espero poder volver a vernos este verano y brindar con unas sidras.

Del mismo modo quiero agradecer a toda la gente que, aunque no han estado en Cardiff permanentemente, han supuesto un gran apoyo para mí. Gracias a mis amigos Maru y Alex. Gracias por la visita y ¡la excursión a Brecon Beacons! Al final me ha faltado tiempo para ir a veros a Londres. Gracias también a una de mis mejores amigas, Andrea, ¡a ver si te hago una visita en Barcelona pronto! También quiero dar las gracias a mi amiga María, una de las personas que mas aprecio. Es un placer compartir tiempo contigo, contagias alegría y ganas de vivir. Por supuesto no podían faltar mir amigas sorianas en los agradecimientos. Por Nosotras. Ya que aquí no pudo ser, a ver si lo celebramos en una semanita en Soria con unas limonadas en la herradores o donde sea, ¡aunque os habeis perdido un pais guay! Quiero agradecer a mis amigos Carmen e Ivanín, por siempre estar ahí. A ver si ahora que no tengo que leer papercillos nos ponemos las pilas y organizamos una quedada...que ya es hora cagüen dios! En estos agradecimientos no podía faltar una persona muy importante para mí, Eugenio. Porque no sólo fuiste el mejor compañero de trabajo que alguien podría tener, sino también un gran apoyo y amigo a lo largo de estos años. Gracias por estar siente pendiente y por preocuparte por mí. También quiero dar las gracias a otro excompanero, Javi. Tenemos que hablar de negocios, ¡aunque por supuesto con un par de cañas!

Quiero dar las gracias a Mari Carmen, por interesarte y preocuparte por mí. Quiero dar las gracias a una de las personas más importantes de mi vida, mi abuela Fermina. Un modelo a seguir. Mujer luchadora, perseverante y con muchas ganas de vivir. Y a mi hermano Al, Alberto, ¡que no conseguí que vinieras a Cardiff ni aun jugando el Madrid la final de la Champions League!. Si hay dos personas a las que siempre estaré agradecida por esto y por todo, son mis padres. Sin vosotros no podría ser quien soy ni estar donde estoy. Os debo todo. Por todas las oportunidades que me habéis dado y por todos vuestos sacrificios. Esta tesis va por vosotros. Gracias por apoyarme desde el principio y por entender mis ganas de crecer, aun suponiendo eso el tenerme lejos, comenzando de cero. Gracias por vuestra alegría, porque aunque haya tenido un mal dia, conseguís sacarme una sonrisa con sólo cogerme el teléfono. Os quiero Toñitos.

Junto con mis padres, a la persona a la que quiero dedicar esta tesis es a mi mejor amigo, mi companero y el hombre de mi vida, Isma. Gracias porque hace cuatro años me animaste a

venir a Cardiff, aunque supusiera el vivir lejos durante estos años. ¡Qué rápido han pasado! Gracias por las infinitas visitas y viajes por Gales, descubriendo juntos castillos increíbles y sitios maravillosos. Pero sobretodo, gracias por estos ultimos 6 meses en Suecia. Gracias por ayudarme en mi trabajo, y lo que es más importante, por enseñarme a relativizar y a tomarme todo con más calma, y por animarme en los momentos de frustración. Espero poder seguir discutiendo y riendo contigo muchos años más, y espero que este sea el comienzo de un nuevo capítulo, esta vez juntos.

Abstract

This thesis is focused on the production and characterization of diamond films and diamond nanoparticles containing custom colour centres. These defects intentionally created into the diamond lattice are promising candidates for single photon sources, and are becoming more important for quantum information technologies as photons can carry quantum information over long distances. With outstanding properties such as up to 80% of the photons emitted into the zero phonon line (ZPL), single photon count rates up to several Mcps under continuous excitation and a narrow ZPL at room temperature, the SiV centre has recently attracted more attention. Although different approaches for the creation of colour centres have been reported, this thesis details the creation of SiV centres by chemical vapour deposition. Colour centres are created through the incorporation of impurities during diamond growth. While Si doping can easily be achieved due to plasma etching of Si substrates or the incorporation of a Si solid source inside the reactor vacuum chamber, controlling the exact amount of Si present in the gas phase or effectively incorporated is still a handicap. Chapters five and six show comprehensive studies performed towards the creation of diamond nanoparticles with single emitters. Control over the Si content within the gas phase is achieved using silane as gas source. The subsequent milling of the diamond films hosting the SiV centres and their inclusion into a stable solution, will facilitate SiV coupling and incorporation into cavities or emission-enhancer devices.

A mis padres...

Publications

1. A.-I.- Ahmed, S. Mandal, L. Ginés, O.A. Williams, and C.-L. Cheng. Low temperature catalytic reactivity of nanodiamond in molecular hydrogen. *Carbon*, 110:438–442, 2016.

2. S. Mandal, E.L.H. Thomas, C. Middelton, L. Ginés, J.T. Griffiths, M. J. Kappers, R.A. Oliver, D.J. Wallis, L.E. Goff, S.A. Lynch, M. Kuball, O.A. Williams. Surface Zeta Potential and Diamond Seeding on Gallium Nitride Films. *ACS Omega*, 2(10):7275-7280, 2017.

3. L. Ginés, S. Mandal, A.-I.- Ahmed, C.-L. Cheng, M. Sow and O.A. Williams, Positive zeta potential of nanodiamonds. *Nanoscale*, 9(34):12549-12555, 2017.

4. S. Mandal, E.L.H. Thomas, L. Ginés, D. Morgan, J. Green, E.B. Brousseau, O.A. Williams. Redox agent enhanced chemical mechanical polishing of thin film diamond. *Carbon*, 130:25-30, 2018.

5. V. Nesvizhevsky, U. Köster, M. Dubois, N. Batisse, L. Frezet, A. Bosak, L. Ginés, O.A.Williams. Fluorinated nanodiamonds as unique neutron reflector. *Carbon*, 130:799-805, 2018.

6. A. Frangeskou, A. Rahman, L. Ginés, S. Mandal, O.A.Williams, P. Barker, G. W. Morley. Pure nanodiamonds for levitated optomechanics in vacuum. *New Journal of Physics*, 20: 043016, 2018.

7. E.L.H. Thomas, L. Ginés, S. Mandal, G.M. Klemencic, O.A. Williams. A simple, space constrained NIRIM type reactor for chemical vapour deposition of diamond. *AIP advances*, 8: 035325, 2018.

8. S. Lindner, A. Bommer, A. Muzha, A. Krueger, L. Ginés, S. Mandal, O.A. Williams, E. Londero, A. Gali, C. Becher. Strongly inhomogeneous distribution of spectral properties of silicon-vacancy color centers in nanodiamonds. *New Journal of Physics*, 20: 115002, 2018.

9. L. Ginés, S. Mandal, D. J. Morgan, R. Lewis, P.R. Davies, P. Borri, G. W. Morley, O. A. Williams. Production of Metal-Free Diamond Nanoparticles. *ACS Omega*, *In press*, 2018.

Contents

List of Figures

List of Tables

Chapter 1

Introduction

With the aim of exploiting the outstanding and unique properties of diamond, its synthesis has been developed over the last 70 years, and diamond has played an important role in many applications and technologies since then. Although difficult to summarise, some interesting applications rely on diamond as biomaterial, including optical bio-imaging [1] or drug delivery among the most used applications. [2] The parallel development of chemical vapour deposition (CVD) (which reduced diamond synthesis cost whilst allowing high quality diamond growth) and technology, have led to the emergence of more demanding applications in the field of quantum communication, quantum computation and quantum cryptography. Diamond has been highlighted as a promising material for all of them. [3]

The field of quantum computing has attracted a special interest over the last decade. The amount of data that researchers have to handle and the intricated operations and simulations of complex systems, make necessary the use of a powerful system/computer to deal with all the information as well as addressing machine learning and in general demanding quantum problems. The first idea of a quantum computer is thought to had been proposed by Richard Feynmann, in 1981, during a lecture titled: 'Simulating Physics with Computers'. [4] Although this talk was not about quantum computers, he however stated the following: *... 'Nature isn't classical, dammit, and if you want to make a simulation of nature, you'd better make it quantum mechanical, and by golly, it's a wonderful problem, because it doesn't look so easy'.* This idea set the precedents towards the search of a quantum computer.

Although the idea/concept of a quantum computer is easy to summarize, its practical development is arduous, hence a fully operative quantum computer is still not operative. Quantum computers use an information unit known as qubit, which can be in a quantum superposition of binary states, 0 and 1. Many physical systems have been explored to

implement qubits, including atoms, superconductors, ions, photons or electrons. [5] All them have to meet some requirements. First, it has to be possible to isolate the system and this system has to be able to keep its quantum properties during a reasonable time, and second, it is necessary to be able to manipulate and observe the system. Nowadays, the two more used physical systems as quantum computers are trapped ions and superconductors. For example, quantum computers created by IBM are based on superconducting Josephson junctions and consists of up to 50-qubit system. However, the use of quantum computers in day devices such a mobile phones is not possible as these systems require cryogenic cooling.

In the last decade, solid-state qubits (semiconductors qubits) based on defects on diamond, known as colour centres have been implemented. [6] Both Nitrogen-Vacancy (NV) and Silicon-Vacancy (SiV) electronic spins present promising qubit candidate and hence are among the most promising building blocks for quantum computers. [7] With the main drawback being the difficulty of processing and engineering diamond devices [8], scalable quantum computers are still far from being a reality, as a system/device to integrate the colour centre is needed. Nevertheless, *Schröder et al.* recently achieved the creation of controlled SiV centres embedded in diamond nanostructures. [9] The narrow SiV centres linewidths and the narrow inhomogeneous distribution they obtained (51 GHz), are promising for a range of quantum technologies, including quantum networks and quantum computing.

The era of the second quantum revolution has just started, and diamond will attract great attention, attracting a lot of funding within the next years. For instance, a new €1 billion European Commission flagship initiative in Quantum Technology, preparing for a start in 2018, specifically proposes NV colour centres as solid-state quantum sensors. [10]

The work performed in this thesis pursues the creation and improvement of the optical properties of SiV centres, as well as different approaches to create diamond nanoparticles with SiV centres ready to spin cast, thus making its integration into a cavity easier.

This thesis is structured in 7 chapters. After this brief introductory chapter, diamond structure, its synthesis by Chemical Vapour Deposition (CVD) and an overview of its more interesting properties are explained in chapter 2. Chapter 3 then details the experimental methods used within this thesis. Chapter 4 discusses the work done on diamond nanoparticles, in both commercial detonation diamond particles (5 nm) and larger ones (50 nm). The control over surface functional groups already present on these particles surfaces

and/or created by annealing procedures, will determine their surface charges, responsible for particle aggregation. Surface functional groups have been studied by the FTIR technique and surface zeta potential measurements have determined the particle behaviour and stability within a colloid. These studies have led to evidence for an explanation of the uncommon positive zeta potential on nanodiamonds.

Chapter 5 is then focused on the study and production of diamond nanoparticles from both commercial single crystal (SC) bulk diamond and CVD grown diamond films after milling processes. Post-milling acid cleaning processes as well as centrifuge processes have been used to improve the diamond nanoparticles quality and to control their size. Si doping during the CVD growth process (with subsequent milling) results on the creation of SiV colour centres, with unknown amounts of Si incorporated due to the use of a solid dopant source (either from the etching of the substrate or from the etching of Si pieces introduced inside the reactor chamber). This leads in general to the creation of SiV ensembles instead of single SiV emitters. Controlling the dopant source is possible introducing it in the gas phase during CVD growth. Chapters 6 discusses the Si gas-phase doping through the incorporation of silane. The construction of a new reactor consisting of a quartz tube that acts as deposition chamber is detailed. This reactor also allows easily interchangeability of the quartz tube, ensuring no cross-contamination if different dopants are used.

Finally, chapter 7 summarises the main findings of this thesis.

Chapter 2

Diamond: structure, synthesis and properties

Abstract

Diamond is one of the most stable carbon allotropes and due to its crystal structure (strong covalent bonding between its atoms), possesses outstanding and unique properties. Although it was first mined in India, the real diamond era began with the discovery of a huge diamond in the Kimberley mine, in 1871 in South Africa and the subsequent exploitation of this mine and diamond mines predominantly located in South Africa but also in Russia and now in Australia. Natural diamond is formed as a result of very high pressures and temperatures at depths of 140 to 190 kilometres in the Earth's mantle, with diamond growth occurring over periods from 1 billion to 3.3 billion years, making diamond relatively rare. However, natural diamonds lack practicability for many applications, so attempts for synthetic diamond growth were successfully performed in the early 1950s, relying on diamond being metastable with kinetics limiting the thermodynamically favoured transition to graphite. While some of the most commonly used industrial methods for synthetic diamond (such as detonation synthesis or High-Pressure High-Temperature (HPHT) techniques) will be detailed in chapter two, this chapter is focused on the most widely used technique for diamond growth, Chemical Vapour Deposition (CVD). Furthermore, the diamond structure and the most significant diamond properties will also be discussed.

2.1 Structure of Diamond

As previously introduced, diamond is one of the most common carbon allotropes and exhibits vastly contrasting physical properties compared to graphite, due to its different atomic structure. Carbon atom has six electrons with a $1s^2 2s^2 2p^2$ electronic configuration. Electrons within the carbon atom are situated within the K and L shells. As stated in the Pauli's exclusion principle, two identical fermions can not occupy the same quantum state within the same system. That is, e^- in an atom can not have the same quantum numbers so the 1s orbital in the K shell and the 2s orbital in the L shell will be occupied by two electrons with opposite spin. The L shell contains two remaining e^- with parallel spin, half-filling the 2p orbitals and hence providing the lowest energy possible. [11]

Nevertheless, this electronic configuration changes when the carbon atoms bond to form diamond. Although the K shell is not involved in bonding, the electrons in the L shell are re-arranged forming hybrid orbitals. One of the 2s electrons can be promoted to the empty p orbital, forming four sp^3 hybrid orbitals (figure 2.1 a)). With a 230 kJ/mol^{-1} energy expense upon the formation of the sp^3 hybrid orbitals, it is however substantially compensated by the energy decrease while bonds are formed. [12] The sp^3 electrons are covalent bonded (σ bonds) to another four sp^3 orbitals resulting in a tetrahedral carbon lattice, known as diamond, shown in figure 2.1 c). This lattice is formed by two face centred cubic structures (FCC) shifted by the vector (1/4, 1/4, 1/4).

A second alternative hybridisation is the one characteristic of graphite (figure 2.1 d), in which the 2s electrons are hybridised with only two of the 2p orbitals. This combination results in three sp^2 orbitals (forming hexagonal structures) and an un-hybridised de-localized p_z orbital, perpendicular to the plane formed by the sp^2 orbitals, shown in figure 2.1 b). The hexagonal structures are held together by this un-hybridised p_z orbital and weak Van Der Waals forces. The sp^2 orbitals form strong σ bonds whereas the perpendicular orbital forms weaker π bonds. As a result of this structure, the de-localized electrons can move parallel to the hexagonal planes conferring graphite electrical conductor properties. [11]

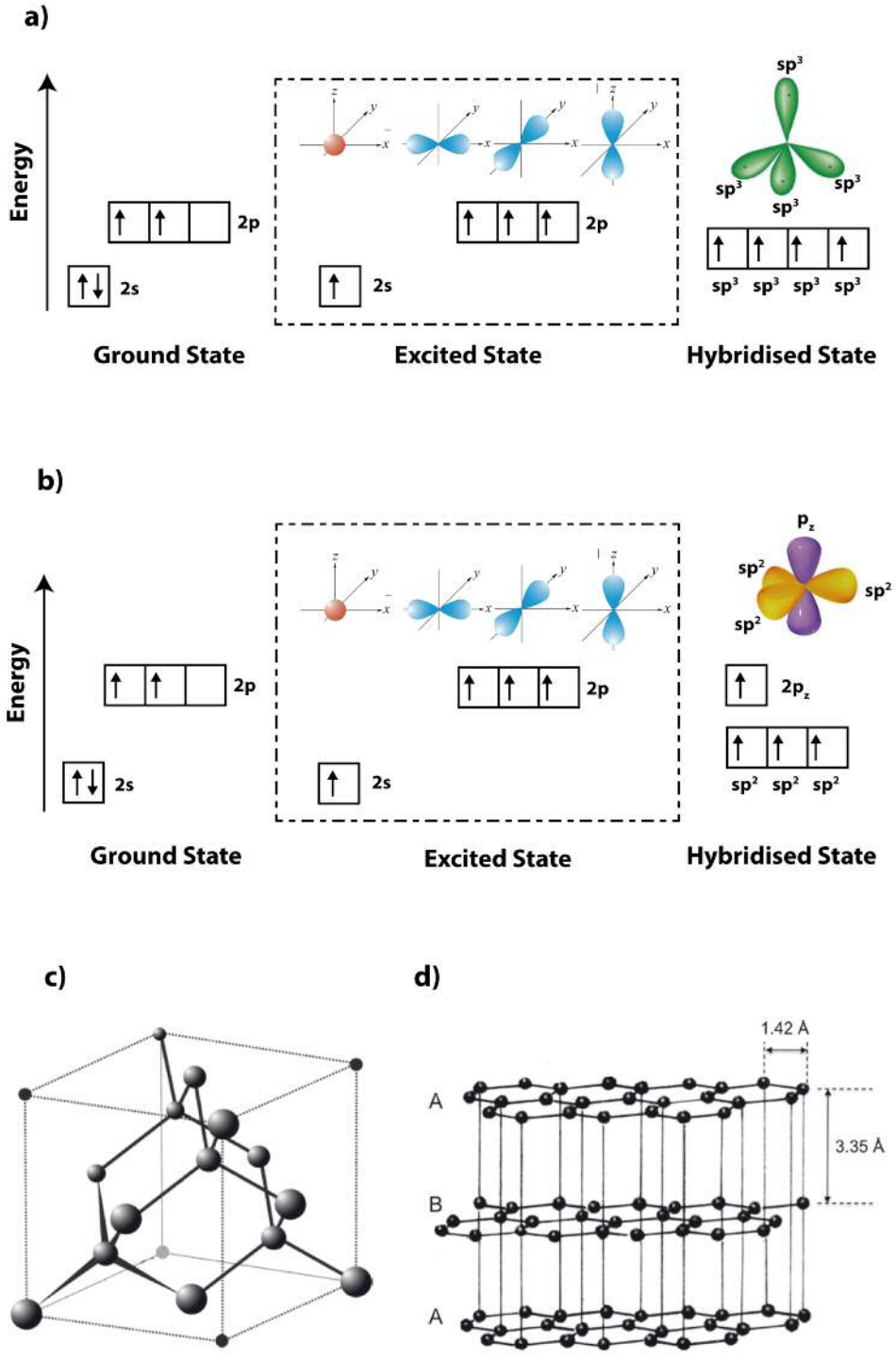

Figure 2.1: Electronic configuration for the carbon atom within the diamond and graphite structures. a) Electronic structure of diamond in the ground and in the excited states, with an electron promoted from the 2s to the 2p sub-shell and the formation of the four sp^3 valence electrons. b) Electronic structure and hybridisation of graphite. c) Diamond lattice. d) Graphite Lattice. Panels c) and d) reprinted from [11], ©2011 by John Wiley & Sons, Inc. all rights reserved, with permission by John Wiley & Sons, Inc.

2.2 Diamond synthesis by Chemical Vapour Deposition

The Chemical Vapour Deposition technique was developed in parallel with the HPHT technique in the late 1950s and it is based on gas phase chemical reactions that lead to diamond growth. [13] A more detailed description of the technique development and reactors used for CVD growth can be found in chapter six, whereas this section is focused on the chemistry behind the CVD diamond growth.

In a typical CVD growth process, carbon precursors such as methane, are diluted in an excess of hydrogen, with a typical flow ratio of $CH_4/H_2 = 1\%$. [14] The gases are fed into the reactor, while keeping pressures between 20 and 300 Torr and substrate temperatures typically above 700 °C. [13,14] An activation source is needed (either a hot filament [13] or a microwave discharge [15]) to break apart the molecules into the reactive species. These reactive species are then transported to the surface where they can be adsorbed, desorbed or diffused until reaching a nucleation site.

Hydrogen is the most critical component for diamond growth. Hydrogen stabilizes the surface during the growth, keeping and preventing surface graphitization or reconstruction, as it etches away graphitic carbon (sp^2) faster than diamond. [16] Furthermore, hydrogen reacts with methane fracturing it and creating the CH_3 reactive radical. When atomic hydrogen reaches a nucleation site, it removes a hydrogen atom from the surface (forming H_2), and leaves behind an unbounded carbon radical and hence an active site. While this active site will likely react with a H atom, a CH_3 radical will sometimes react at this place adding a carbon atom to the lattice. This process is repeated in adjacent sites until carbon atoms are locked into the diamond lattice, resulting in atom by atom diamond growth. A more detailed explanation of the chemistry behind the CVD growth process can be found in [13]. This process is schematized in figure 2.2.

Two different Microwave Plasma Enhanced Chemical Vapour Deposition Systems (MW-PECVD) have been used to growth both diamond films and particles within this thesis: a Seki reactor (formerly ASTEX) and a NIRIM reactor.

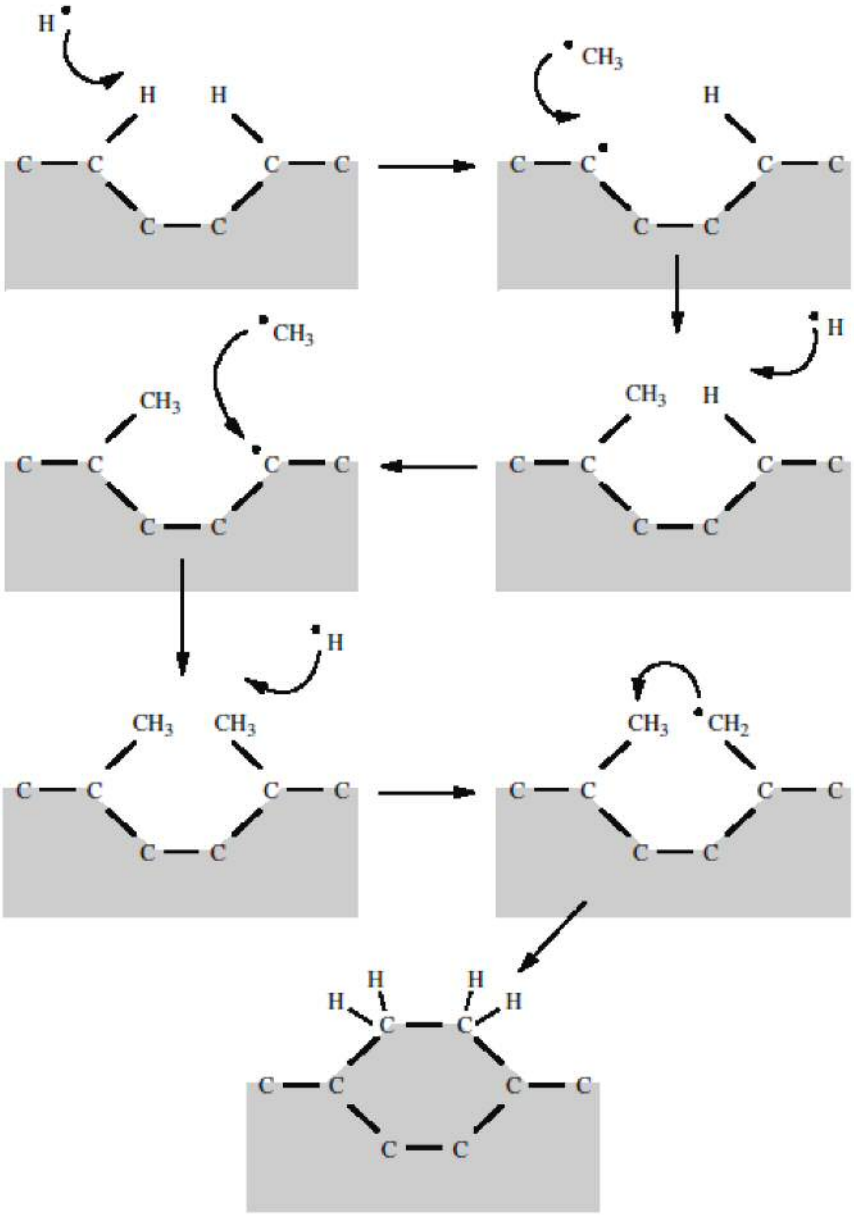

Figure 2.2: Schematic model of the different reactions behind the chemical vapour deposition diamond growth. In the step-by-step process, an atomic hydrogen atom removes hydrogen atoms bonded to the diamond surface, forming diatomic H_2 and leaving an active site. This active site can react with a methyl radical CH_3, adding a carbon atom to the lattice. The reiteration of this process leads to diamond growth. Reprinted from P. W. May, "Diamond thin films: a 21^{st} century material", Philosophical Transactions of the Royal Society of London A: Mathematical, Physical and Engineering Sciences, (2000), **358**, 473–495, by permission of the Royal Society.

2.2.1 The ASTEX reactor

The ASTEX reactor was first developed by *Bachmann et al.* in the late 1980s and then commercialised by *Applied Science and Technology, Inc.* as an improvement over the NIRIM reactor in terms of larger deposition areas and higher growth rates. [17] Larger deposition areas were obtained converting the TE_{10} fundamental mode of the NIRIM reactor into the TM_{01} mode, with the use of a cylindrical cavity. Several improvements were introduced in the next generation of the ASTEX reactor in 1993. [18] The aims of the new design pursued the creation of larger, symmetric, more stable and uniform plasmas within the reactor chamber, while maintaining the dielectric window far from the plasma. Furthermore, the new design meant an easier way to cool the substrate and to control its temperature. All these advances were feasible thanks to the design by *Besen et al.*, changing the concept of the microwave coupling design of the previous reactors. [19]

The reactor components are detailed in figure 2.3 a). The reactor chamber consists of a water-cooled lid, sitting on top of a plate, and sealed with a dielectric window (in between the plate and a water-cooled cooper electrode), and with a spring mechanically coupled to an electrode. The dielectric window is located in a low electric field region, preventing plasma breakdowns occurring near to the window and hence its heating, etching or coating. The electrode is connected to a coaxial conductor. Microwaves produced from a 2.45 GHz magnetron, enter the microwave guide and are coupled to the chamber through the coaxial conductor. The electric field then enters the chamber, and on the underside of the electrode, its strength decreases radially outwards from the centre, before travelling to the upper side of the electrode, in which the electric field strength increases converging at the centre, resulting in an efficient plasma generation just above the sample. The sample sits on top of a molybdenum holder placed at the centre of the copper electrode. The sample temperature is controlled through a plenum chamber, situated below the cooper electrode.

The design of this reactor leads to a multimode cavity, with the TM_{011} (blue dashes) as the main mode excited, and second radial lobes related to the TM_{021} mode (red dashes), as shown in figure 2.3 b). [15]

The reactor used in this thesis is one of our four reactors at Cardiff Diamond Foundry, a *Seki*, formerly ASTEX, *AX6500 series* reactor. Reactor control is fully automated with safety systems that allows unsupervised long growth duration processes. The reactor is equipped with a *Williamson dual wavelength pyrometer* with a measurable temperature

range between 475–1475 °C, allowing *in-situ* growth monitoring. Further diamond films thickness monitoring can be performed with a 445 nm laser and a photodetector at an angle of incidence of 28°. Both the pyrometer and the laser and photodetector are mounted on top of the reactor chamber.

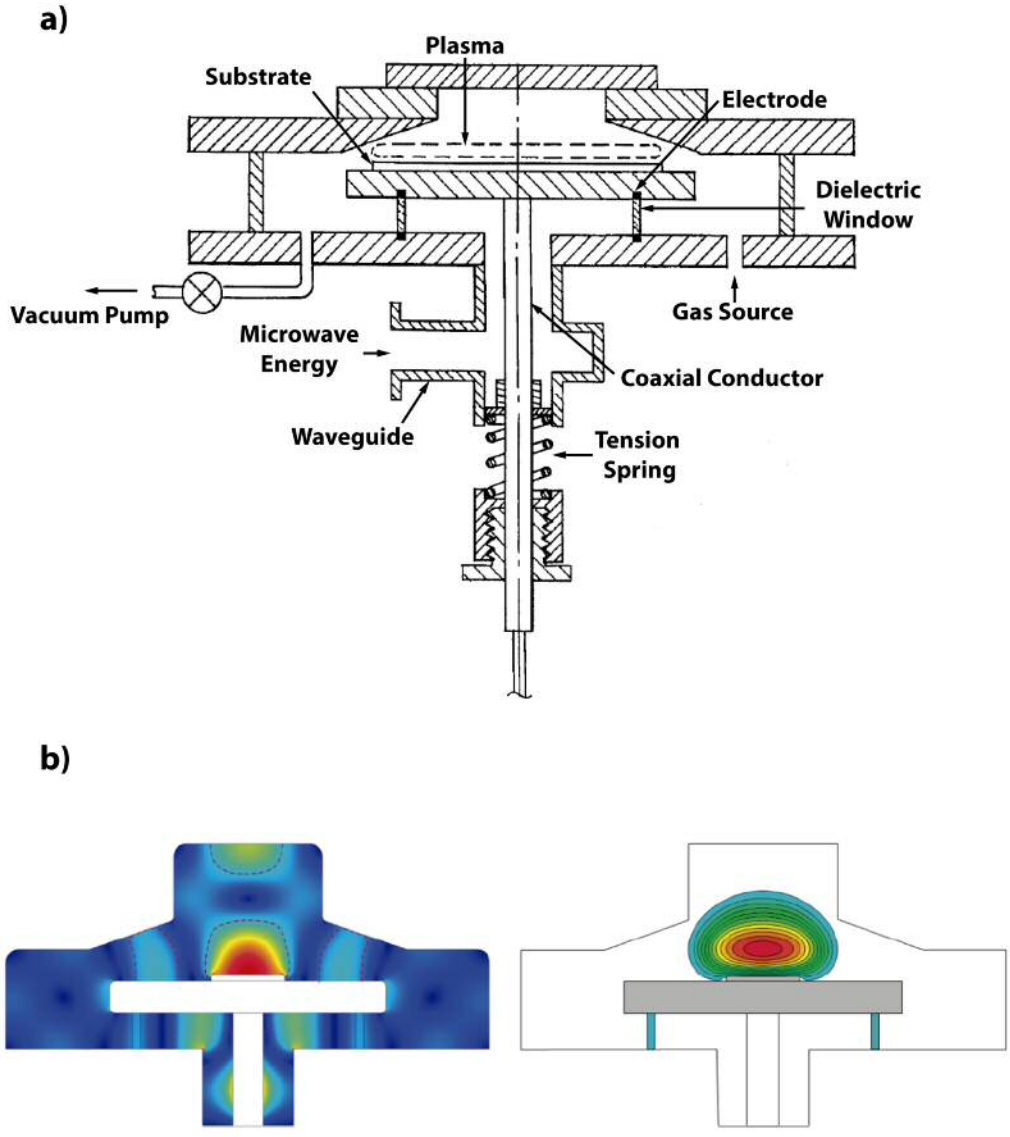

Figure 2.3: Seki AX6500 MWPECVD Reactor. a) Schematic cross sectional view of the reactor. Reprinted from [18]. b) Electric field distribution and a 200 mbar H_2 plasma modelling in the non-cylindrical resonant reactor cavity. Reprinted from [15],

2.3 Diamond properties

Although pure diamond is probably most well known for its extreme mechanical properties such as hardness (as a result of its dense packing structure), it also exhibits numerous more, hence resulting an interesting material for a wide range of applications. Some of these properties are summarised in table 2.1 and 2.2.

With a Vickers hardness (indentation resistance) of 100 GPa [20] and 10 on the Mohs scale (scratch resistance), diamond is an ideal choice as cutting tool and for polishing applications. [21] Furthermore, a Young's modulus of up to 1200 GPa [22] makes diamond an ideal material for making NEMS/MEMS devices. [23, 24] Another superior diamond quality is its thermal conductivity, as high as 150 W/cmK for high quality natural type IIa diamond (at 70 K) and 24 W/cmK at 300 K. [25] These high values surpass the ones for some metals such as copper (3.8 W/cmK), silver (4.2 W/cmK) or aluminium (2.4 W/cmK). This means that diamond can dissipate heat more efficiently than other materials hence being a promising material in thermal management applications. [26] Diamond is also chemically inert and stable and can be used in biological applications. [27] Additionally, with an optical transparency ranging from the UV to the far infrared, diamond is also advantageous for realizing optical windows. [28, 29] Diamond also has superior electronic properties (table 2.2), interesting for electronic devices. [30] Diamond has a particular interesting property: its wide bandgap (5.5 eV), which leads to high breakdown field of 10 MV/cm. If higher electric fields can be tolerated, smaller devices can be designed. [30] Furthermore, diamond has high carriers mobilities (for both electrons and holes). Electron and hole mobilities of about 4500 $cm^{-2}V^{-1}s^{-1}$ and 3800 $cm^{-2}V^{-1}s^{-1}$ respectively have been measured for high quality CVD-grown single crystal diamond. However, these mobilities are negatively affected by doping, imperative to provide carriers in a controlled manner. N-type doping (using phosphorus) and P-type doping (with Boron) has successfully been performed, essential to develop high frequency devices. [30] Nevertheless, high doping levels, exceeding $10^{20}cm^{-3}$, are needed to enable sufficient activation of carriers at room temperature to see a substantial change in conduction properties. [31]

It is precisely the possibility of doping or introducing non carbon atoms into the diamond lattice what has made diamond such an interesting material for the development of this thesis. Defects intentionally introduced in diamond show fascinating quantum properties. Therefore, this thesis will be focused on the production of these defects, on both diamond films and diamond nanoparticles, and improvements on their properties.

Property	**Diamond**	**Silicon**	**SiC**
Cohesive energy (eV)	7.36	4.64	6.64
Young's modulus (GPa)	1200	130	450
Shear modulus (GPa)	577	80	149
Knoop's Hardness (Kg/mm^2)	10000	1000	3500

Table 2.1: Mechanical properties of Diamond, Silicon and Silicon carbide (SiC). From reference [20].

Property	**CVD Diamond**	**Silicon**	**SiC**	**GaN**
Bandgap (eV)	5.47	1.12	3.2	3.44
Breakdown field (MVcm^{-1})	10	0.3	3	5
Electron saturation velocity ($x10^7 cm^{-1}$)	2	0.86	3	2.5
Hole saturation velocity ($x10^7 cm^{-1}$)	0.8	n/a	n/a	n/a
Electron mobility ($cm^2V^{-1}s^{-1}$)	4500	1450	900	440
Hole mobility ($cm^2V^{-1}s^{-1}$)	3800	480	120	200
Thermal conductivity (W $cm^{-1}K^{-1}$)	24	1.5	5	1.3

Table 2.2: Electronics properties of Diamond, Silicon, Silicon carbide (SiC) and Gallium Nitride (GaN). From reference [30].

Chapter 3

Experimental Methods

Abstract

In this chapter, the experimental techniques used in this thesis are explained. The chemical vapour deposition method (CVD) along with the different reactors used for the sample growth will be discussed in chapter five. This chapter is focused in the *ex-situ* sample characterization. However, some ex-situ sample characterization methods such as the measurement of the zeta potential and the different techniques used to determine it will be discussed in both chapter three and five.

The characterization of the grown samples has been performed in our laboratory in Cardiff University, at the Cardiff Catalysis Insitute, at the University of Warwick, at Saarland University (Germany), at the National Dong Hwa University (Taiwan) and at the Laboratorio de Microscopias Avanzadas-Insituto de Nanociencia de Aragon (LMA-INA), (Spain).

3.1 Microscopy techniques

Microscopy techniques are among the most extensively used techniques for sample characterization. These techniques allow sample surface visualization and magnification and microscopy techniques based on electron-sample interactions allow the study of sample composition and the study of crystallography. Electron microscopy techniques, such as scanning electron microscopy (SEM) or transmission electron microscopy (TEM) were first developed in 1937 and in 1936 respectively, to overcome the limitations on resolution set by the light wavelength. [32] However, it was soon realized the possibilities that these techniques offered. On the other hand, scanning probe microscopy, such as atomic force microscopy (AFM), was developed in 1982 allowing 3D atomic resolution on sample imaging and the possibility of measuring any kind of sample due to the existence of different operational modes. SEM, TEM and AFM techniques are explained throughout this section.

3.1.1 Scanning Electron Microscopy

Scanning Electron Microscopy (SEM) is a technique that operates under vacuum and is used to image and analyse the surface of a wide range of bulk samples. The working principle consists on an electron probe formed from a focused beam of electrons which is scanned on the surface following a raster scan pattern. When the electron probe enters the sample, most of the beam's electrons interact with the sample's atoms producing elastic or inelastic scattering. The electrons leaving the sample are then collected in the appropiate detector and are used to produce an image. The depth at which electrons can penetrate (usually from 1nm to 5 mm with incident beam perpendicular to sample) and the interaction volume in the sample depend on the incidence of the beam, the electrons' energy, the average atomic number (Z) and the density of the atoms of the sample. [33]

It is important to understand the interactions taking place in a microscope, in order to analyse the image, the diffraction pattern or any useful information we get from the electron-atom interactions. All the interactions can be defined with two terms, the cross-section or more commonly, the mean free path (λ), which defines the distance a electron travels before suffering any scattering event.

Electrons elastically scattered have high energy, typically varying from >50 eV to nearly the energy of the incident beam (keV order), large scattering angle (electrons trajectory

changes when entering the sample) and are produced by the interaction of the primary electrons with the nucleus. These electrons are commonly known as Backscattered Electrons (BSE), and the fraction thereof obtained is strongly dependant on the atomic number (Z). BSE electrons will be heavily scattered by elements with high atomic number in contrast to elements with low atomic number. Hereby, areas with high Z appear brighter than areas with low Z so BSE electrons can provide contrast useful to detect areas with different chemical composition. [34]

Electrons inelastically scattered escape from the sample with energy below 50 eV (by definition). These electrons, known as Secondary Electrons (SE), result from the excitation of loosely-bonded electrons produced by the primary electron beam that move toward a surface while undergoing inelastic or elastic collisions. These electrons can only escape from the sample if their energy exceeds the material's work function. Furthermore, the SE typical mean free path is around 1nm, so only electrons that are generated few nm deeper from the surface can escape from the specimen as the ones generated deeper are absorbed in the sample. For this reason, the resolution obtained by SE is better than the resolution obtained with BSE. The amount of SE emitted depends also in the incident angle of the primary electron beam, being larger with bigger tilted angle, making them very sensitive to topographical changes. [35] As SE electrons are characterized by having low energies, the potential in the sample surface that arises due to electrostatic charges produce an anomalous contrast or a reduction in the image resolution. This problem is more pronounced in insulating samples, so usually, a thin conductive layer (gold, carbon or palladium) is evaporated on top of these samples. When it is not possible to deposit a thin layer on top of the sample or when the sample is beam-sensitive other methods such operating at low currents, using compensatory voltages or operating at low vacuum, are employed. [36, 37]

A simple SEM schematic diagram is shown in figure 3.1. The system consists of an electron optical system, a sample stage, different detectors and a display unit. The electron optical system is formed by an electron source, a series of lenses and apertures and scanning coils. Electrons are emitted by the electron gun as a result of thermionic emission (using tungsten or LaB_6 filaments) or more commonly through field emission (FE) or Schottky-emission guns (SE). The latter have superior brightness, longer lifetime and higher energy spread resulting in better resolution. The electrons are accelerated to an energy of 0.5-30 keV and the electron beam goes through condenser lenses (CL) which excitation enables the electron beam's diameter adjustment and the probe current adjustment. Then the

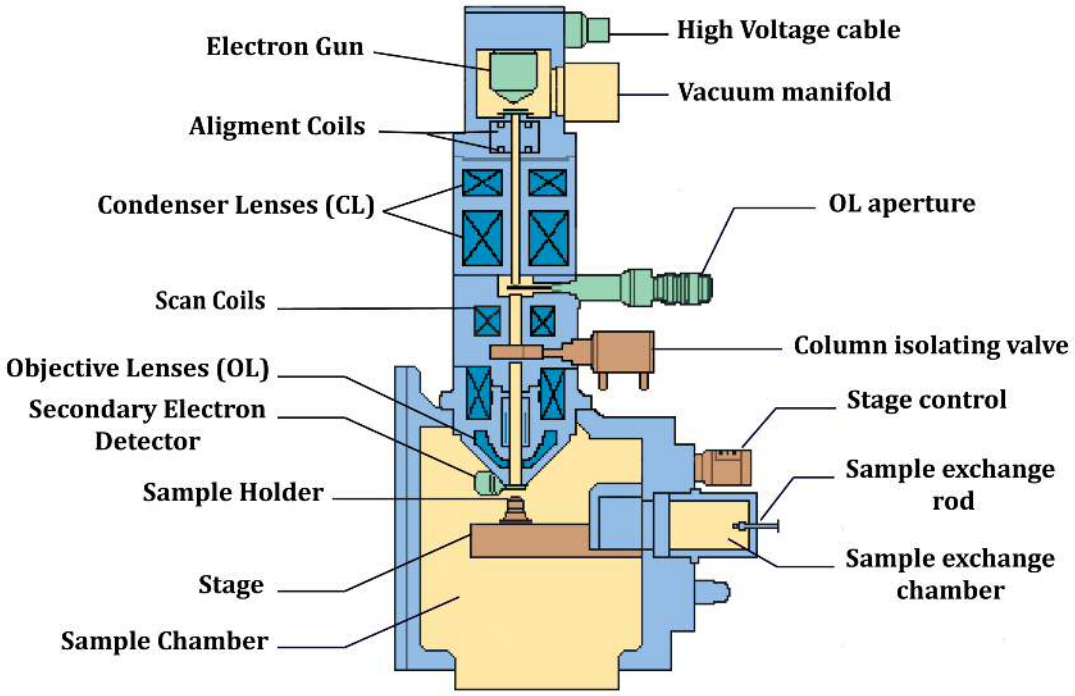

Figure 3.1: Schematic diagram of a scanning electron microscope detailing the different components, from the electron source to the optical system and the detectors and sample chamber.

beam goes through a thin-metal aperture that allows the electron beam to reach the objective lens after being rastered by the scan coils. The presence of this aperture is determinant for having a fine electron probe, due to this aperture lens aberration is avoided (allowing the electron beam to go through the centre of the objective lens). The role of the objective lenses (OL) is to focus the electron probe on the sample, reaching an electron probe diameter of about 1nm. Finally, different types of detectors are used to collect the electron-atom interactions produced in the sample. An Everhart and Thornley scintillator detector is commonly used for detecting SE although it is inefficient for detecting BSE. BSE are usually detected with scintillator or semiconductor ones.

During this thesis a *Raith eLine SEM* equipped with a field emission tip and placed in a class 1000 cleanroom was used for sample imaging. The SEM resolution is determined by the diameter of the electron probe and by high-performance objective lenses.

3.1.2 Transmission Electron Microscopy

Another microscopy technique that was used in this thesis was the Transmission Electron Microscopy (TEM). In this case, the electron beam goes through the thin sample (less than 100 nm for a conventional TEM) and the interactions between the electrons and the sample are used to produce either a projected image or its correspondent diffraction diagram in reciprocal space. TEM is more versatile than SEM due to the ability to obtain both morphological and structural information about the sample, depending on the microscope configuration mode. TEM also allows higher magnifications (down to atomic resolution) as a result of the higher acceleration voltages (between 60kV and 300kV). TEM can also be used as a combination of a SEM in transmitted mode through a complex electromagnetic lenses system, known as STEM mode. In this mode the electron beam is very finely focused and then is scanned across the sample in a raster pattern. [38]

TEM main drawbacks are related to the sample size. As small samples are required (less than 100nm thick and 3mm diameter), the sample preparation is arduous and the area under observation is tiny (a high resolution TEM image (HRTEM) will cover an area of 100 nm^2). For a standard TEM image formation, the main transmitted electron beam is used, cancelling out the deflected electrons with one of the apertures located just after the objective lens. The contrast in the image is due to different thickness (thinner areas appear brighter, more electrons are transmitted), or differences in composition (different atomic number). This operational mode or the images obtained with the transmitted electrons are referred to as Bright Field images. When working in STEM mode, low dispersion angles (LAADF) or high dispersion angles can be distinguished (HAADF). In this mode the central beam is cancelled and deflected electrons are used to form the image. In this case, areas with higher atomic number elements will appear brighter.

A schematic diagram of a TEM is shown in figure 3.2. For simplicity, not all the components are shown. As in the SEM ,the system consists of a column in vacuum with an electron gun, an optical system with a series of lenses and apertures a sample holder, detectors and a viewing screen. Electrons emitted by the electron gun (thermionic LaB6 crystal or Field emission) are accelerated between the cathode and the anode. The electron beam travels to a set of condenser lenses which demagnify the beam and control the spot size (between 1 nm and 100 nm) that hits the sample. This sample is introduced in the TEM column in a rod-like holder through an airlock system. This holder allows slight movement in x,y and z, and allows tilt along the holder axis (around 60 degrees) and the

perpendicular axis. Then, the objective lens is responsible for image generation focusing the image, and with the objective aperture below, bright field image or dark field image modes can be selected allowing or blocking the electrons from the transmitted beam. The set of intermediate lenses and projector lenses are responsible for the image magnification. The later projects the final image onto a fluorescent screen that emits light when the electrons hit it. [33, 34, 39]

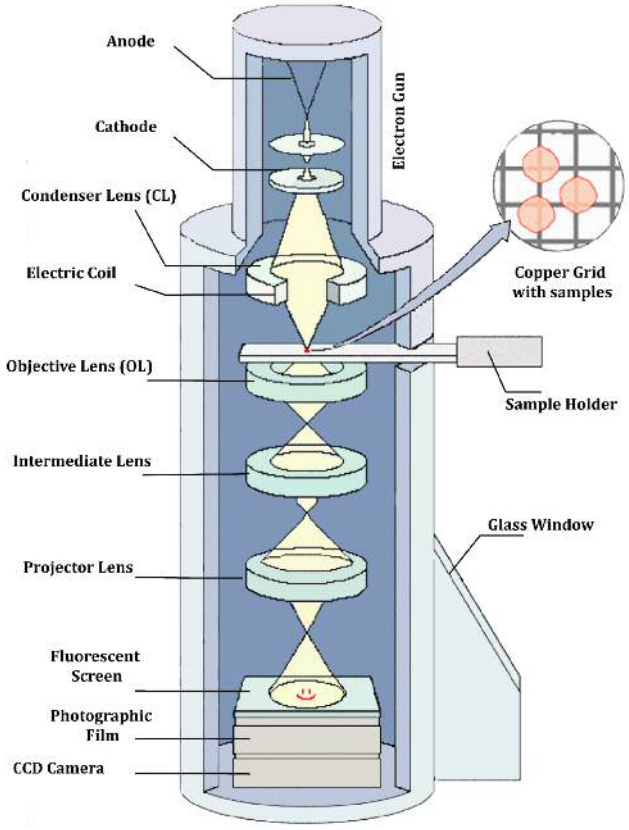

Figure 3.2: Schematic diagram of a transmission electron microscope, showing the electron-optical system within the TEM column and the viewing screen.

The TEM images shown in chapter four were conducted in the facilities of the Laboratorio de Microscopias Avanzadas, at the Instituto de Nanociencia de Aragon (LMA-INA), with the help of Dr. Cesar Magen. All the images were taken in a *Titan 3* equipped with a spherical aberration corrector, using an acceleration voltage of 80kV.

3.1.3 Atomic Force Microscopy

The last microscopy technique used in this thesis is the atomic force microscopy (AFM) also known as scanning force microscopy (SFM) or scanning probe microscopy (SPM) (which also includes the scanning tunneling microscope). This technique allows to measure

the superficial characteristics of all types of samples (conducting materials, insulators, semiconductors, or biological samples), producing three dimensional topographical images with atomic resolution. Topographical images of the surface are produced through the interaction of the existing forces between the sample's surface and the AFM tip. The origin of the interaction forces is strongly dependent on the sample' surface characteristics and dependent on the conditions the measurements are taken under (ambient conditions, high-vacuum or the sample inside a liquid). [40] The AFM nanometric tip, usually made of Si, SiO_2 or Si_3N_4, is used to raster the surface and it is mounted at the end of a cantilever, whose mechanical behaviour can be approximated to that of an elastic spring, governed by the Hooke's law:

$$F = -kx \tag{3.1}$$

where F is the spring restoring force, equivalent to the tip-sample interaction force; k is the spring recovery constant, which is equivalent to the elastic constant of the cantilever and x is the spring deformation, which is equivalent to the vertical deflection that the cantilever undergoes due to the interaction forces.

The cantilever acts as a force sensor, allowing the indirect measurement of the tip-sample interaction forces through the cantilever deflection with an optical detection system. The optical detection system consists of a laser which is directed towards the end of the cantilever, and the reflected laser beam falls upon a quadrant photodiode detector. The difference in intensity between the upper and lower segments measures the vertical deflection, proportional to the normal force, while the difference in intensity between the lateral segments measures the torsion, and is proportional to the lateral force. In this thesis, only topographical measurements have been performed, so that only the channel measuring the normal force, i.e. the vertical deflection, has been taken into account.

To scan the sample's surface a piezoelectric device is used, which by means of an applied voltage presents a deformation which allows to control with nanometric precision the sample's scanning. As the cantilever tip approaches the sample (few $\mathring{A}$ from the sample), the tip feels the interaction with the substrate and the cantilever is deflected. This signal is then collected in the photodiode, and a feedback system is involved in order to keep the tip-sample interaction force constant throughout the scanning process (when working in contact mode), as shown in figure 3.3.

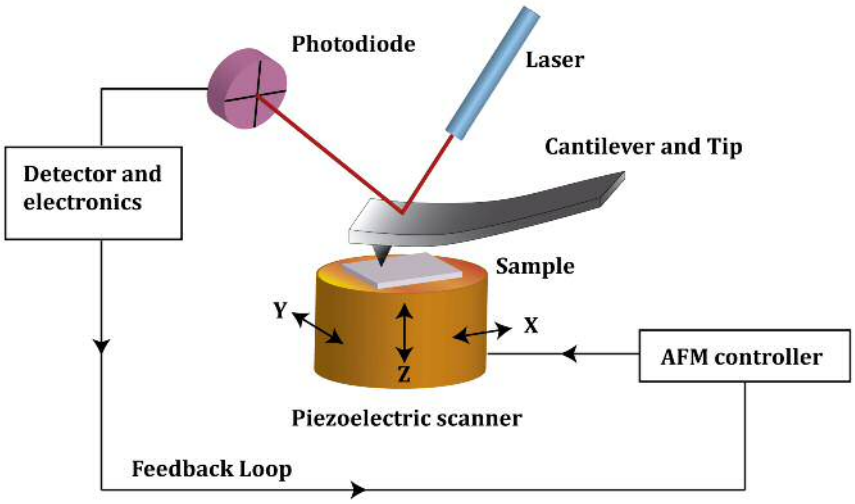

Figure 3.3: Schematic representation of the basic AFM equipment showing its different components, including the laser, the photodiode, the sample placed on top of the stage and on the piezoelectric scanner and the AFM controllers.

The large number of interactions between the tip and the sample make possible the use of different operational modes which depend on the predominant forces. The interaction forces between the tip and the sample derive from a Lennard-Jones potential, so both attractive (long distance) and repulsive forces (short distance) exist. If short-range repulsive forces predominate (i.e. contact forces or chemical interactions), static mode (or contact mode, previously described) is predominant, whereas if long-range forces predominate (i.e. Van der Waals forces, Coulomb forces or capilarity forces) dynamic mode (tapping or non-contact mode) will be selected. [41] All the measurements taken in this thesis have been performed in dynamic mode, to avoid (as far as possible) tip deterioration or tip contamination.

In dynamic mode, a small piezoelectric element mounted on the cantilever holder, allows to excite the cantilever to its free resonant frequency. This motion can be described by a forced harmonic oscillator in which two important parameters appear: amplitude and frequency. Amplitudes from 10 to 100 nm are achieved. Both amplitude and frequency are related to the force gradients, so that when the tip-sample distance decreases (the tip approaches the surface) these gradients cause a decrease in amplitude and a shift of the natural resonant frequency peak. Depending on the parameter chosen as the feedback signal we will have two modes either keeping the difference between the natural frequency of the cantilever and the interaction frequency constant or the amplitude set in a fixed value. [42, 43] The feedback signals will then be reflected in the piezoelectric movement,

registering changes in the topography.

AFM is a powerful technique that allows atomic resolution, however, artefacts commonly ocurring in an AFM such as tip convolution can cause changes in the images' features, usually overcome using AFM sharp tips. [44]

The AFM equipment used in this thesis was a *Park Systems Park XE-100* operating in non-contact mode, equipped with a TESPA silicon AFM tips (320 kHz resonant frequency, 42 N/m spring constant, and 8–12 nm tip radius).

3.2 Light Scattering Techniques

When incident light impinges a medium, i.e. a medium containing particles, light interacts with this medium and hence is scattered. The information obtained from this interaction provides facts about the dynamics of such sample and the structure of the material. The different types of scattering governing the process will be dependent on the dimensions of the particles (in this case) scattered compared to the light wavelength. Two techniques based in light scattered by particles in a colloid have been used in this thesis. Dynamic light scattering (DLS) and nanoparticle tracking analysis (NTA). In both techniques, the light scattered is Doppler shifted due to light being scattered by particles in motion.

3.2.1 Dynamic Light Scattering

Dynamic Light Scattering (DLS) is a technique that analyses a volume of particles in a liquid medium (a colloid) generating a particle size distribution. The technique is based on the assumption that particles undergo Brownian motion due to collisions between these particles and the molecules in the medium. [45, 46] The velocity of the Brownian motion is defined by the translational diffusion coefficient (D) which in turn is related to the hydrodynamic diameter d(H) (and hence to the particles' size) through the Stokes-Einstein equation:

$$D = \frac{kT}{3\pi\eta d(H)} \tag{3.2}$$

where k is the Boltzman factor, T the temperature and η the viscosity.

Figure 3.4 a) shows a schematic diagram of the commercial *Malver Zetasizer Nano ZS*

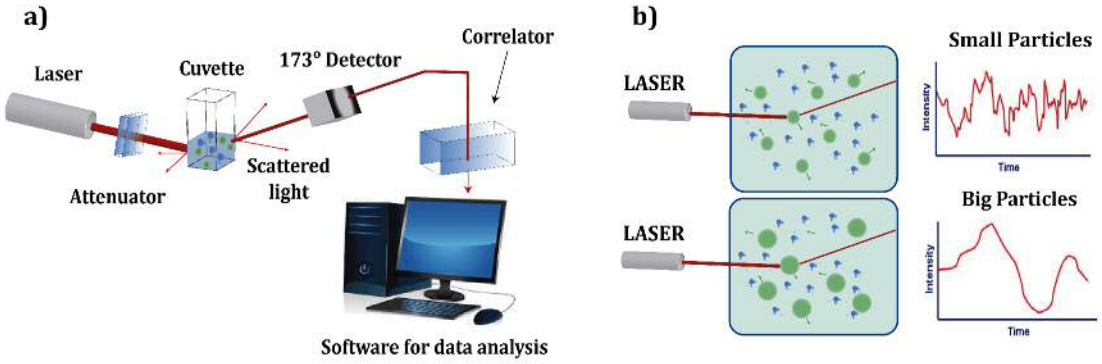

Figure 3.4: Illustration of the DLS technique. a) Schematic representation of the typical DLS equipment, showing its different components. b) Simplified representation of the intensity fluctuations caused by light scattered by the particles undergoing Brownian motion. Fluctuations vary over time with a rate dependant on particles' size.

Instrument in which this thesis measurements were performed. The equipment consists of a coherent monochromatic light source (633 nm laser) that hits the sample contained in a cuvette. The particles dispersed in the liquid medium scatter the incident light in all directions and due to the Brownian motion, the scattered intensity from the different moving particles produce constructive or destructive interferences resulting in a fluctuating scattered intensity. The intensity fluctuations will vary over time depending on the particles' size. Bigger particles will produce slower fluctuations compared to the ones produced by smaller particles, as shown in figure 3.4 b). The scattered light is then collected in a detector fixed at 173°. An attenuator controls the intensity of the scattered light, increasing or reducing the light coming from the laser source, preventing the detector from saturating. The signal collected in the detector is analysed in a correlator which measures the intensity fluctuations as a function of time. The correlator compares the intensity at a certain time (t), and the same signal is compared at a tiny amount of time later $(t + \tau)$, generating a correlation function. The two intensities will be strongly correlated at the beginning, but this correlation will be reduced with time, depending on how fast the particles move. The normalized intensity autocorrelation function is given by:

$$g^{(2)}(\tau) = \frac{\langle I(t)\rangle\langle I(t+\tau)\rangle}{\langle I(t)\rangle^2} \tag{3.3}$$

By means of the Siegert relation, the previous equation is related to the first-order auto-

correlation function:

$$g^{(2)}(\tau) = B + \beta[g^{(1)}(\tau)]^{(2)} \tag{3.4}$$

where B is the baseline, and should be equal to one (although in practice it differs) and β is the intercept of the correlation function. This autocorrelation function can be fitted to a single exponential decay function, assuming a monodispersed sample as:

$$g^{(1)}(\tau) = exp(-\Gamma\tau) \tag{3.5}$$

being Γ the decay rate, which is related to the diffusion coefficient D described in equation 3.2:

$$\Gamma = Dq^2 \tag{3.6}$$

Combining the equations described above with equation (3.2), the hydrodynamic diameter (the particles' size), can be obtained. However, equation (3.5) is only valid if single scatter size is considered. If the sample is polydisperse, the equation below must be defined as an integral over different decay rates, so it is not trivial to fit the data with the appropriate decay rate. However, the cumulant method [47] and the CONTIN method [48] have been postulated as the preferred methods for data analysis.

The intensity of the scattered light can be defined as a Rayleigh approximation when the particles in the colloid are smaller than the wavelength (Mie scattering when the particles' size is comparable to the light wavelength). As this intensity is proportional to d^6 (where d is the particles' diameter), large particles, aggregates or dust present in the solution can mask the measurements over smaller particles. For colloids prepared with commercial diamond particles, it is not a major problem as these particles usually produce a monodisperse size' distribution. Nevertheless, for colloids prepared out of diamond particles produced following milling techniques in which a broad distribution of particles can be obtained, it is necessary the use of a different technique or a combination of techniques to measure the particles' size. Such a method is described in the following section. [49]

3.2.2 Nanoparticle Tracking Analysis

Along with dynamic light scattering, Nanoparticle Tracking Analysis (NTA) is a technique used to measure the particles' size distribution and particles' concentration in a colloid.

NTA is a more accurate method to determine particles' size as it is based on the direct visualization and tracking of individual particles. [50] NTA is based on the particles' Brownian motion and the particles' size is determined evaluating the displacement of individual particles within in a 2D-frame, obtained in the recording, in a CCD camera, of the particles' movement. [51] . NTA measurements described in this thesis were carried

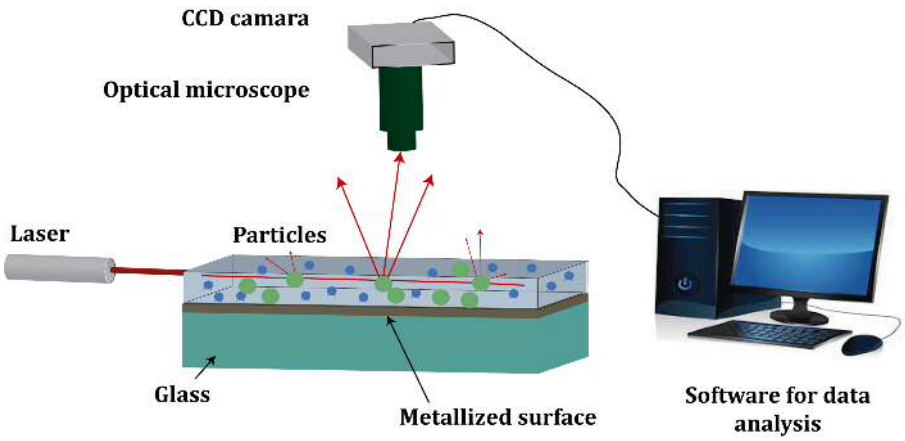

Figure 3.5: Schematic illustration of the NTA equipment

out in a *Malvern Nanosight LM10 equipment*, which was first commercialized in 2004. The equipment, schematized in figure 3.5, consists of a laser beam (638nm) that is deflected by a prism to fall within the sample chamber. The particles inside that sample chamber that are in the laser beam path, scatter the laser light. This scattered light is measured in a x20 magnification microscope objective, located perpendicular to the sample container, and a coupled CCD camera records a video of the particles moving under Brownian motion. The analysis software evaluates the different frames, tracking individual particles and locating the particles' centre and the displacement of these particles in the x and y plane. This speed of motion, or diffusion coefficient (D), is related to the hydrodynamic diameter (d(H)) as seen in equation (3.2). The software analyses all the particles in the frame simultaneously, and converts the distances moved by each particle in a size distribution through the Stokes-Einstein equation:

$$\frac{\overline{(x,y)^2}}{4} = D = \frac{kT}{3\pi\eta d(H)} \tag{3.7}$$

NTA is a method that provides more exact values for particle size distribution than DLS. Due to individual particle tracking, with NTA polydisperse samples can be measured although NTA also present some drawbacks. The first and most important is that particles with sizes below 30 nm can not be detected and the second one is that the Brownian motion of the particles detected is confined in the x-y plane. The third problem arisen is related

to the colloid' concentration. The scattering produced from high concentrated colloids make necessary the sample's dilution, being time-consuming and could produce particles' agglomeration.

3.3 Vibrational Spectroscopies

The study of the composition and molecular bonding within a sample can be carried out with the use of two non-destructive spectroscopy techniques, Raman Scattering and Fourier Transform Infrared Spectroscopy, commonly known as vibrational spectroscopies. These techniques provide a good analytical method to determine molecular bond structures due to each sample having a unique characteristic spectrum.

3.3.1 Raman Scattering

When a monochromatic light hits a sample, an interaction between the electric field and the electron cloud of the sample can result in a change of polarizability of the electric dipole moment of the molecules which will excite them to a virtual energy state. The energy stored in the electron cloud that forms the chemical bonds is then irradiated in all directions when the field is reversed. Most of the resulting photons are scattered off at the same frequency of the incident exciting beam through elastic scattering known as Rayleigh Scattering. Nevertheless, some photons (1 in 10^6-10^8 photons) are re-emitted shifted in frequency and hence in energy, resulting in either red-shifted Raman lines through Stokes Scattering, or blue-shifted lines [52] due to the relaxation from a thermally activated excited state to the ground state, through anti-Stokes scattering. Both processes are shown in figure 3.6.

The energy difference observed between the incident photons and the scattered photons, corresponds to the energy of a vibrational state or vibrational mode of the molecule. As anti-stokes scattering is temperature dependent, the anti-stokes Raman intensities are lower than the stokes scattering ones and are barely measured, necessitating the use of a different specific technique, coherent anti-stokes Raman spectroscopy (CARS). [53] Molecules have a different number of vibrational modes, which can be IR or Raman active. For symmetric diatomic molecules, only a single vibrational mode is observed, whereas complex normal vibrational modes i.e. bending and stretching vibrations are observed in complex molecules. For non-linear and linear molecules the number of vibrational modes

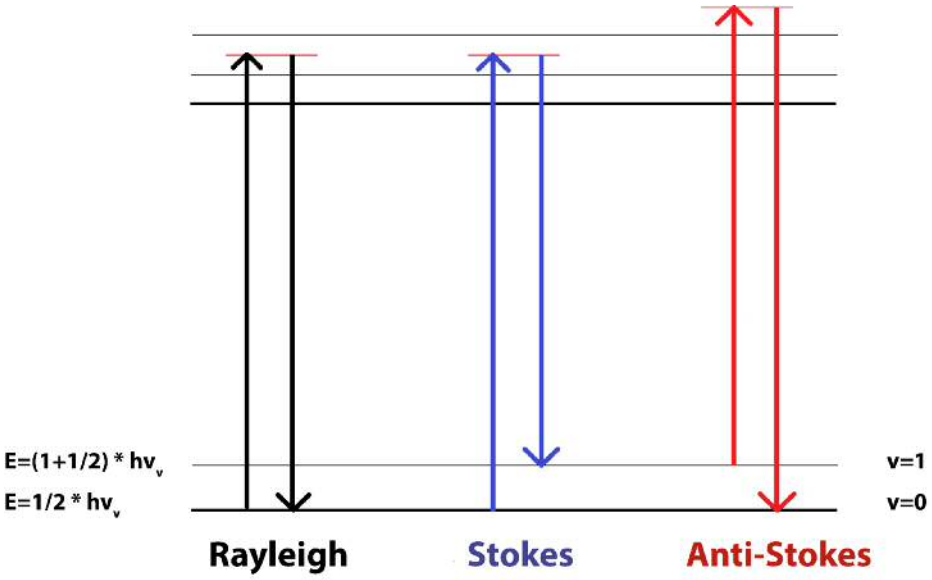

Figure 3.6: Schematic diagram of Raman Scattering Spectroscopy, detailing the Rayleigh, the Stokes and the Anti-stokes Raman Scattering

are $3n-6$ and $3n-5$ respectively, where n indicates the number of atoms in the molecule or in the primitive cell. Vibration frequencies depend on the mass of the atoms that constitute the molecules and the strength of the molecular bonds. In general terms, the weaker the bonds are the lower is the Raman shift and conversely.

Within this thesis both nanodiamond particles and nanocrystalline diamond films have been studied, with diamond showing a Raman vibrational mode at 1332 cm^{-1} (F_{2g} symmetry). [54] Raman spectroscopy is a fantastic technique to confirm the quality of diamond films. As it is well-known, diamond is a carbon allotrope in which carbon atoms present a sp^3 hybridization and in pure graphite, the carbon atoms show a sp^2 hybridization, exhibiting Raman peaks at 1580 cm^{-1} and 1350 cm^{-1}, known as G and D peaks respectively. Therefore, it is expected that the presence of amorphous or non-sp^3 carbon in diamond films with different content cause appreciable changes in the Raman spectrum, shifting the aforementioned peaks.

Despite being an excellent and simple technique to determine the composition and chemical bond structure of our material, there is a factor limiting the Raman technique which is the weak intensity of the scattered radiation compared to that of the exciting line ($I_{Raman} \approx 10^{-4}\ I_{Rayleigh} \approx 10^{-8}\ I_{Source}$) thus requiring monochromatic sources, usually continuous gas laser such as Ar or He-Ne in the visible or He-Cd in the UV, sensitive detectors and filter suppression of the Rayleigh line. [55]

The equipment used in this thesis is an *inVia Renishaw confocal* Raman microscope equipped with a 532 nm laser placed in Cardiff University Catalysis Institute.

3.3.2 Fourier Transform Infrared Spectroscopy

In combination with Raman spectroscopy, Fourier Transform Infrared Spectroscopy (FTIR) is a widely used technique to study and to identify the chemical bonds within molecules. A change in the electric dipole moment of the molecules has to occur to get infrared absorption whereas Raman spectroscopy is based on changes in the polarizability of the molecules, as was described previously. For this reason it is understandable that less 'infrared-active' vibrations will be present in symmetric molecules than in asymmetric molecules, with vibrations being weaker in the former ones due to small changes in the dipole moment. [56]

The purpose of the FTIR spectroscopy technique is to determine the intensity ratio between an incident light I_0 and the light after it has interacted with the sample I_t as a function of the light frequency ν. The plot of this ratio versus frequencies is known as the FTIR spectrum, which it is usually represented as the transmittance:

$$T_\nu = \left(\frac{I_t}{I_0}\right)_\nu \tag{3.8}$$

However, it is more convenient to represent the absorbance, which is related to the transmittance (T_ν) by the *Beer-Lambert Law*:

$$A_\nu = -logT_\nu = (\epsilon_\nu)(bc) \tag{3.9}$$

where ϵ_ν is absorptivity (frequency dependent), b is the sample thickness and c is the concentration of chemical bonds.

The incident light (I_0) comes from an infrared (IR) source, that is, the light beam contains many frequencies just opposite of monochromatic sources used in Raman. Some of the incident IR radiation will be absorbed by the sample at a certain energy or frequency which corresponds to a vibrational mode of the bonds in the molecule. Vibrations include both symmetric and asymmetric streching, or bending modes. The second ones also include more complex vibrations such as in-plane or out-of-plane bending vibrations or deformation, rocking, wagging and twisting modes. As each functional group presents an

intensity peak at a particular wavelength, FTIR is an appropriate method to determine the chemical bonds/ surface functional groups of almost any kind of sample. [34]

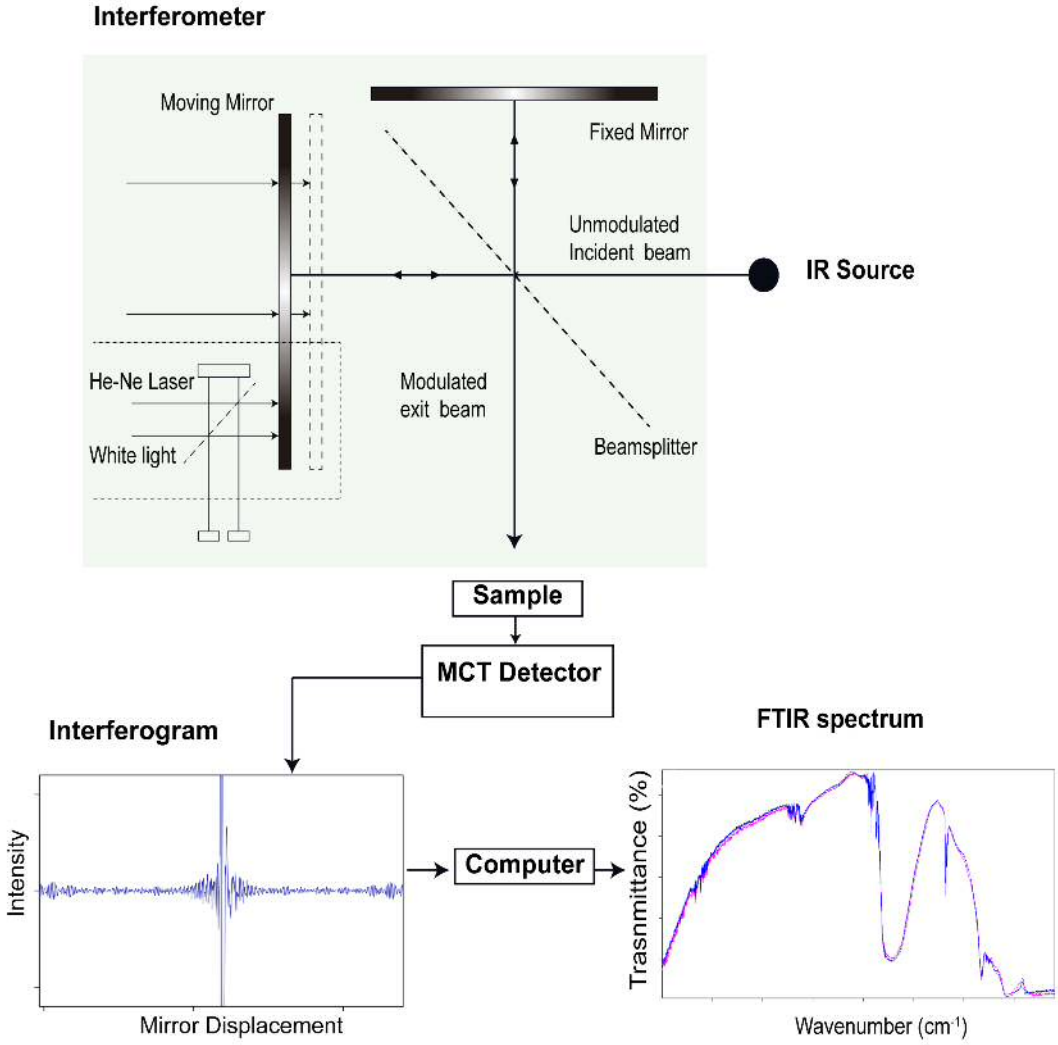

Figure 3.7: Schematic FTIR equipment, showing in detail the different components including the infrared source, the Michelson Interferometer, the interferogram obtained form the MCT detector and the final FTIR spectrum after software analysis.

A basic FTIR equipment is shown in figure 3.7 and comprises an infrared (IR) light source, a dispersive element and detectors.

The generally used IR source for FTIR measurements in the mid-Infrared (light from 4000 to 400 cm^{-1}) is a resistively heated silicon carbide rod of 5 to 10 mm width and 20 to 50 mm length, commercialized as *Globar*. The typical operation temperature of Globar is 1300K. The radiation produced from the IR source then enters a Fourier-transform spectrometer, commonly used nowadays as the dispersive element of the FTIR equipment.

Although infrared spectrometers have been commercially available since the mid 40s, the introduction of Fourier-transform spectrometers in 1970s (based on Michelson interferometers) replacing the old prism and diffraction gratings entailed a considerable advance. The beamsplitter of the Michelson interferometer divides the incoming radiation beam into two paths and the two beams are recombined after the introduction of a path difference. [57] The use of Michelson interferometers brought in considerable improvements such as a higher signal-to-noise ratio signal, a better resolution and shorter acquisition time (all frequencies are measured simultaneously). After entering the spectrometer, some of the light from the IR source will be absorbed by the sample and transmitted to the detector and part of the IR radiation will return to the source. The variation of intensity of the beam emerging from the interferometer is measured as a function of path difference by the detector, producing an interferogram. The most commonly used detector is a quantum detector type, the mercury cadmium telluride (MCT), which combines II-VI semimetals. As the photons to be detected have low energy, any thermal agitation can excite them, producing output noises. To avoid this noise and any other sources of noise, MCT detectors are usually cooled down to 77K with liquid nitrogen. The figure of merit for determining MCT detectors' sensitivity is given by the specific detectivity D^*. Detectors' sensitivity increases with wavelength. [58] Finally, computer software converts the data (intensity signal as a function of the difference in pathlength) to a signal in the frequency domain (intensity variation as a function of wavenumber) by applying Fourier transforms. [57]

The FTIR measurements of this thesis were performed at the National Dong Hwa university in Taiwan by Ashek-I-Ahmed and Prof. Chia-Liang Cheng in a *Bomem MB154 FTIR equipment* with a MCT-liquid nitrogen cooled detector and with a resolution set to be 4 cm^{-1}.

3.4 UV-Visible Spectroscopy

Ultraviolet-visible spectroscopy (UV-VIS) is a technique that uses UV light to study the different structural groups present in molecules. It is based in the same absorption principles than FTIR, but in this case high energy radiation is utilised to excite molecular electrons in an occupied orbital (HOMO) to higher energy unoccupied orbitals (LUMO), as represented in figure 3.8 a). Figure 3.8 b) represents the molecules' possible electronics transitions, which involves s, p and n electrons. The $\sigma \rightarrow \sigma^*$ transitions is the less probable transition as it is the one with largest energy requirement. These transitions can be

initiated with light of $< 150nm$. The second transition energetically more favourable is the $n \rightarrow \sigma^*$ which needs light below 250 nm. However, most absorption processes involve $\pi \rightarrow \pi^*$ and $n \rightarrow \pi^*$ transitions because they fall in the spectrum range from 200 to 700 nm. The absorption for different wavelengths is recorded in a spectrometer as a well as the amount of absorption, from 0 (no absorption) to 2 (99%), and is proportional to the absorptivity (ϵ), the sample concentration (c) and the sample pathlength (l) as given by formula (3.9).

The UV-VIS spectrometer used within this thesis is a *GENESYS^{TM} 10S UV-Vis Spectrophotometer* with scanning wavelengths from 190nm to 1100nm, allowing the measurement of small absorption changes. UV-Vis equipment comprises a high-intensity light source (Xenon lamp), a diffraction element, a beamsplitter, a sample compartment (integrated 6-cell changer) for the sample to analyse and for the reference sample and dual-beam silicon photodiode detectors. [59] The light coming from the Xenon lamp after passing the diffraction element is split into two beams, one that goes through the sample (1ml volume) and the other one through the reference, both placed in 10mm (pathlength) cuvettes. Finally the data is acquired in the detectors and the signal is processed.

The choice of the cuvette (disposable plastic, glass or quartz) will depend on the range of wavelengths of interest. The wide band gap of diamond make it optically transparent. However, diamond absorption is increased with increasing doping and diamond nanoparticles containing significant sp^2 content are highly absorbant at wavelengths below 250 nm. [60] This is because π- bonded carbon atoms cause the formation of a pseudogap, hence dominating the optical absorption [61] as will be explained in the next chapter. For the reason explained above, quartz cuvettes (which allow to measure wavelengths from 190 nm) have been used in this thesis and the use of disposable plastic cuvettes was discarded. The absorption measurements presented in chapter 4, were performed with the aim of getting quantitative information about changes in the sp^2 content. For defect absorption studies (with part per million or lower range levels), more sensitive techniques are required [61].

3.5 Photoluminescence

When a system is optically stimulated, it gains energy from the absorbed photons, and electrons are promoted to higher electronics states. When the system relaxes (electrons return to lower electronic states), photons are emitted producing a characteristic emission

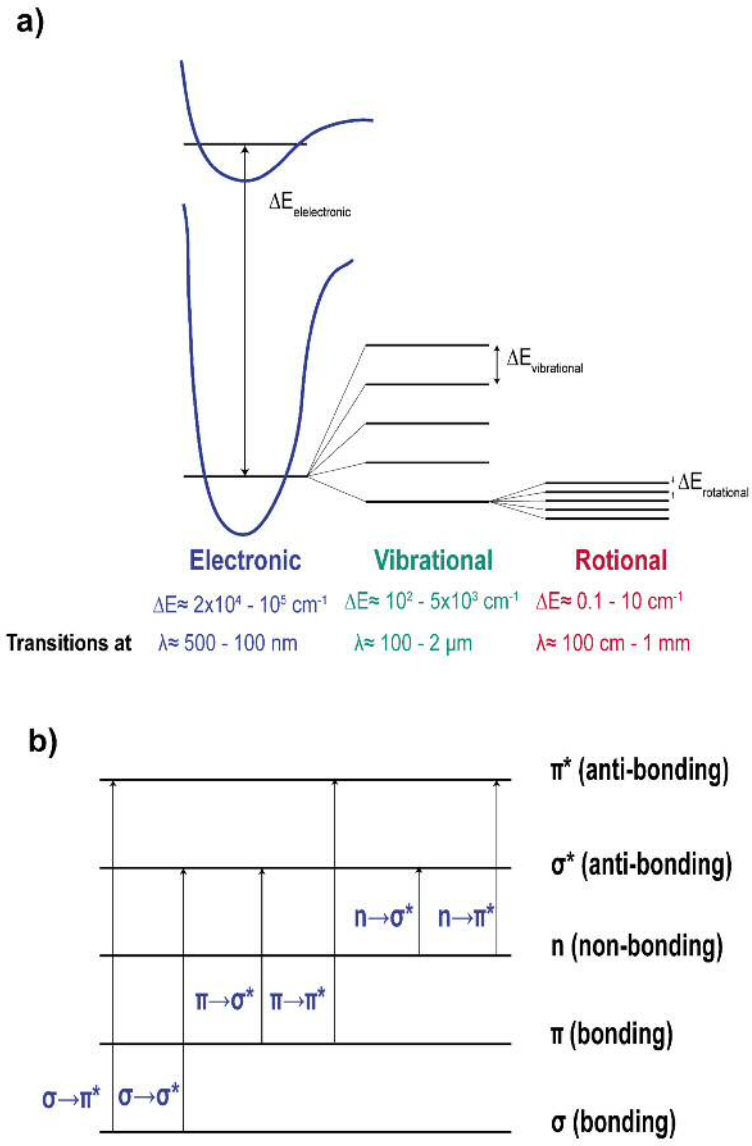

Figure 3.8: Molecular transitions. a) Schematic representation of the different possible transitions within a molecule and the energies and wavelength necessaries for each transition. b) electronics transitions involving s, p and n electrons for UV light.

spectrum. This process is known as photoluminescence (PL) and allows the identification of different electronic states and the transitions between them. In this thesis, PL measurements have been performed to study the structure of colour centres in diamond (more specifically the ones introduced in the first chapter, the NV and SiV) and to study how the electronic environment and stress affect their emission. [62] The sensitivity of this technique allows the analysis of samples even with a low concentration of these colour

centres.

Basic PL equipment comprises an excitation source (a laser light), optical filters, a confocal microscope with high-numerical-aperture objective lens and single photon detectors. The choice of the laser wavelength will be determined by the colour centre under study, and will be selected to fall upon the absorption band of the defect. Excitation wavelengths shorter than the defect fluorescence must be used to distinguish the fluorescence from the excitation laser light [63] Lasers with wavelengths of 514.5 nm and 690 nm are commonly used to study the NV and SiV centres respectively. Optical filters are generally used to separate the light coming from the laser from the single photon emission, and the use of the confocal microscope is indispensable to obtain a good signal-to-noise ratio from the emitter (colour centre).

The most important transition that results from the optical excitation is a purely electronic transition known as the zero-phonon line (ZPL). This transition is unique for each defect and is usually very sharp as phonons are not involved is the process and the transition's width can provide information about excited state's lifetime and strains induced in the crystal. [64] Other processes arisen following the optical stimulation can involve phonons excited within a vibrational mode, which give rise to the absorption and emission bands, both represented in figure 3.9 b). The absorption band occurs at higher energies (lower wavelengths) whereas the emission signal will be detected at lower energies.

3.6 X-Ray Photoelectron Spectroscopy

X-Ray Photoelectron Spectroscopy (XPS) is a non-destructive technique that is included in the electron emission spectroscopies as the energy distribution of electrons ejected from a material is measured. Although X-rays used in XPS technique can penetrate deeply in the bulk sample, only those electrons produced near the surface can escape from the sample without loosing energy and hence contributing to the XPS spectrum (not just as background scattered electrons). The distance electrons can ineslastically travel in a sample is defined by the inelastic mean free path (λ), which depends on the kinetic energy (KE) of the electron and the sample's material. Thus, in a typical XPS measurement the peak signals corresponding to different binding energies on the spectrum are generated within a depth of 25 Åto 60 Å(from 2 to 20 monolayers) for kinetic energies of 200 eV and 1400 eV respectively. [65] Thereby XPS is a surface sensitive technique which provides quantitative information about the samples' composition and samples' chemical

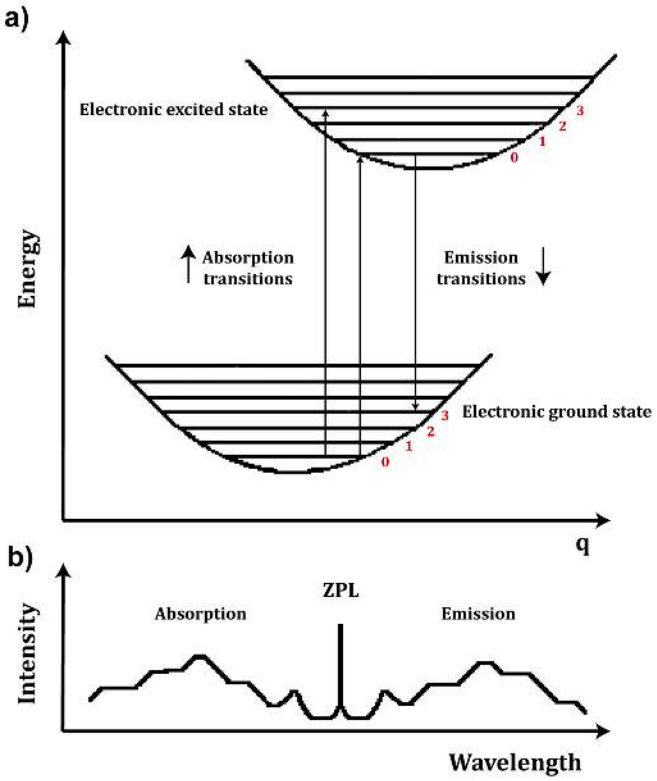

Figure 3.9: Illustration of the photoluminescence process in colour centres in diamond. a) Schematic representation of the absorption and emission transitions between the excited states and the ground state. b) Schematic representation of the absorption and emission bands.

state. XPS allows the identification of different elements (apart from hydrogen or helium), relating them with their binding energy (BE) which is dependent on the atomic number of each element. Knowing the photon energy ($h\upsilon$) and measuring its kinetic energy (KE), the binding energy can be determined applying the Einstein photoelectric law:

$$KE = h\upsilon - BE \tag{3.10}$$

Electrons are positioned in discrete orbitals and are electrostatically bounded around the nucleus. The energy of each orbital (occupied as maximum with two electrons of opposite spin) will be different depending on the atomic configuration as is the electrostatic attraction. Thus, the energy required to eject an electron, BE, provides information about the energy of the orbital (in a first approximation, ignoring final state effects), being specific for each atom and hence identifying that atom/element. The binding energy value will depend on whether the electrons are tightly bound to the nucleus (core electrons)

or weakly bound (valence electrons) with core electrons requiring higher energies to be ejected as shown in figure 3.10 b).

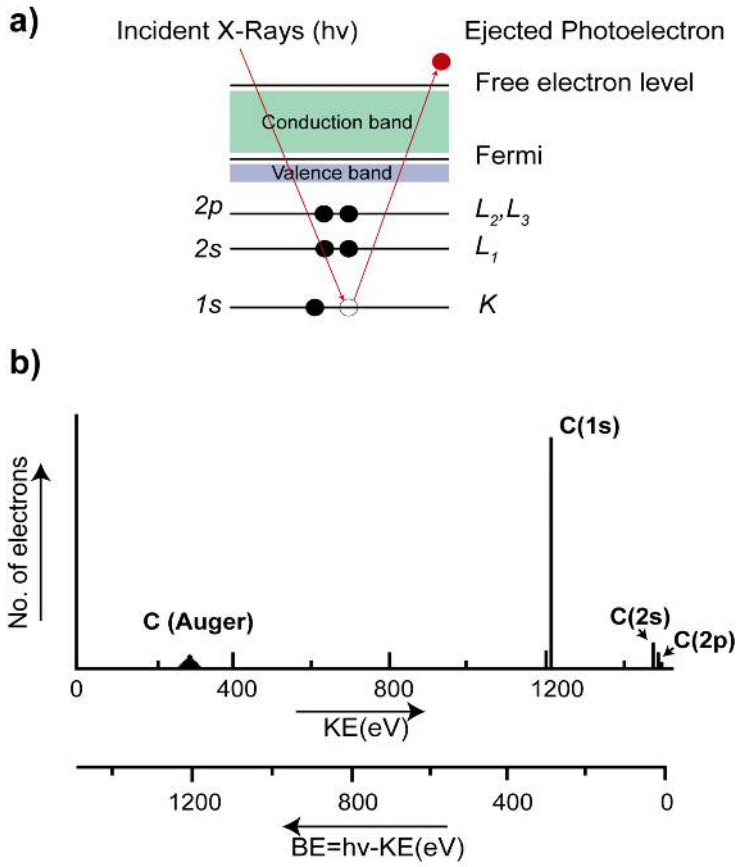

Figure 3.10: a)Schematic representation of the XPS principle and electronic configuration of a carbon atom b) schematic representation of a survey XPS spectrum for the C atom, with core electrons (1s) at higher binding energies.

In a classical XPS equipment soft X-rays generated bombarding a metal anode (usually Al or Mg anodes kept between 10-15kV), produce Kα radiation lines at energies of 1486 eV (1256 eV for the Mg anode) and are used to eject electrons (photoelectrons) from a sample. [66] The 100μm diameter x-ray beam is focused onto the sample and the photoelectrons produced are slowed down at the pass energy (PE) before entering a concentrical hemispherical analyzer (CHA). This CHA consists of two concentrical hemispherical electrodes to which voltages are applied.

X-ray photoelectron spectroscopy (XPS) data, mostly presented within chapter four, were taken using a *Thermo Scientic*^{TM} *K-Alpha*$^{+}$ *spectrometer*. Spectra were acquired using a monochromatic Al source operating at 72 W (6 mA x 12 kV) and at pass energy was achieved using the K-Alpha charge neutralization system, which employs a combination

of both electrons and low energy argon ions. Diamond powder samples as well as non-diamond films were analysed.

3.7 Secondary Ion Mass Spectroscopy

Secondary Ion Mass spectroscopy (SIMS) is a destructive technique used to measure the composition of a wide range of samples, from bulk materials to thin films. The basic operational principle consists of sputtering the sample's surface with a focused ion beam, and analysing the outcoming secondary ions in the appropriate detector, after passing through a mass spectrometer. In order to avoid undesired collisions between the secondary ions and the background gases, the SIMS setup also demands high vacuum pressures (10^{-6} mbar). [67]

The heavy ions that form the beam (commonly oxygen, cesium, argon or a liquid metal), typically with energies from 1 to 20 keV, continuously hit the sample transferring energy and provoking collisions with sample's atoms which results in sample's particles been ejected from a region called the mixed zone. This region's depth limits the depth resolution (z) of the SIMS technique usually from 2 to 30 nm (the lateral resolution x,y is between 50 nm and 2 μm). Therefore, SIMS resolution will depend on the energy, mass and angle of incidence of the ions and on the sample's material. As a result of the continuous sputtering, the mixed zone increases with time creating a crater whose advance is defined by the sputtering rate, with values usually ranging from 10 nA to 15 μA. The secondary ions ejected from the sample are then measured in a mass spectrometer, which physically separates these ions depending on their masses either using electrostatic analyzers and magnets, or AC and DC voltages.

SIMS is a technique that allows to analyse the impurities present in the sample as well as the intentional dopants created in the specimen, creating a distribution of these components along the sample (both depth and lateral distributions). The detection limit of the instrument varies upon the different elements, mainly because their different ionization efficiency known as ion yield. The ion yield is affected by the ionizing tendency of each element, the chemical composition of the sample and on the sputtering rate. However, although the detection limit of most of the elements is between 10^{12} to 10^{16} atoms/cm^3 precise quantification requires the use of standards as reference samples with similar composition as the sample to analyse.

In this thesis, the SIMS technique has been used to measure the concentration of nitrogen and silicon intentionally introduced in diamond films. The operational mode used was the depth profile mode, in which the concentration of the different species is represented as a function of depth (z) considering the sample's surface as the origin. The information collected is the secondary ion counts per second versus the sputtering time, then transformed to concentration versus depth calculating the depth measuring the depth of the crater and assigning concentrations based on comparisons to the standards.

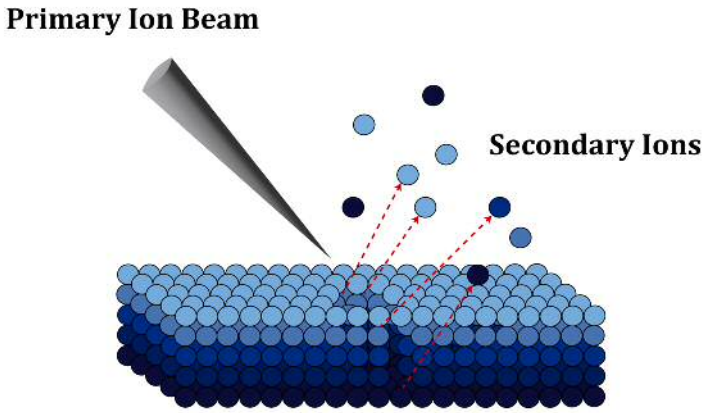

Figure 3.11: Schematic representation of the SIMS principle showing the sputtering process

Chapter 4

Surface charge manipulation on diamond nanoparticles

Abstract

It is well known that diamond nanoparticles' surface charges play a determining role in view of its subsequent material characteristics. Surface charges are determined by the surface functional groups present in the diamond nanoparticles, and can be controlled through different cleaning methods, annealing treatments or surface functionalization. The manipulation of these surface charges will be deeply important to control diamond nanoparticles adhesion and placement in different substrates and will have an important influence over colour centres fluorescence.

In this chapter, commercial diamond nanoparticles' surface groups will be modified following different annealing strategies. The study of the different surface groups present on the diamond nanoparticles will lead to a deeper understanding of nanodiamond surface-related properties.

In this chapter two main questions are addressed. In the first one, the mechanism behind low temperature hydrogenation in a molecular hydrogen atmosphere will be explained, for the first time, using detonation diamond particles (5 nm). Different reaction dynamics for the formation of the $C-H$ bond on the diamond nanoparticles' surface will be proposed. In the second part of this chapter, the main findings obtained with 5 nm particles are then applied to larger size diamond nanoparticles (50 nm), leading to the explanation of the controversial origin of the positive zeta potential.

4.1 Introduction

Diamond nanoparticles have been highlighted as important material for a wide range of applications. Due to diamond bio-compatibility [68,69] and non-cytotoxicity [70], diamond nanoparticles have been used in some biomedical applications such as optical bio-imaging or drug delivery. [1, 2] Diamond nanoparticles are also used as nucleation centres for synthetic diamond growth. [71] For instance, high quality nanocrystalline diamond films for Nano Electro Mechanical systems (NEMS) [72, 73] can be grown using diamond particles (3-5nm) as seeds. Another important application that will be deeply discussed throughout this thesis is the use of diamond nanoparticles as single photon sources (SPS). Defects present in the diamond lattice or defects intentionally created can act as single photon emitters. [74] SPS based on defects in diamond, known as colour centres, have attracted an increasing interest due to the fact that they can overcome the lack of practicability of many other SPS. They can operate at room temperature, and there is no need of high vacuum operation. [75] Many colour centres applications are based on optical properties, but some colour centres are also promising due to the spin properties. [76]

However, these diamond nanoparticles have to meet certain conditions to be useful for the different applications mentioned above. Their surface has to be as homogeneous as possible (same surface groups covering diamond surface), the presence of contaminants in the diamond nanoparticles' surface has to be minimised and large quantities of material must be available. Furthermore, for diamond nanoparticles' easy handling, it is important that diamond nanoparticles exhibit stability in colloidal systems. Unfortunately, 3-5 nm diamond nanoparticles tend to form aggregates making difficult to obtain a colloid with narrow size distribution. Great efforts have been made to overcome particles' aggregation, and all the methods will be described in the following sections.

Diamond nanoparticles' properties are also highly dependent on the particle size, and the choice of one definite particle size or another will be based on the ultimate application. Although different nanodiamonds structures are commercially available, the smallest one is known as ultra dispersed diamond (UDD) or detonation diamond and it is produced by a detonation synthesis. The mean size of these diamond nanoparticles is around 4 nm. Bigger particles, with sizes in the range from 10 nm to 100 nm, can be obtained transforming micron-sized monocrystalline diamond particles obtained from high pressure high temperature (HPHT) synthesis. In this chapter two different sizes of commercial diamond nanoparticles have been used, 4nm and 50 nm.

4.2 Nanodiamond Structures

Diamond and graphite are the most stable carbon allotropes (with an enthalpy difference between the two phases of 0.02 eV per atom [2]). However, graphite is thermodynamically favored over diamond at room temperature and pressures as is shown in figure 4.1. [77] To convert graphite into diamond, high activation energy barrier (0.4 eV per atom) must be overcome, thus requiring high temperatures and pressures (3000 K and pressures above 125 kbar) or the use of catalysts. Furthermore, due to this considerable activation energy, temperatures of 1800°C are necessary to reverse this process at atmospheric pressure, making diamond metastable.

From a structural point of view diamond is the result of a tetrahedral sp^3 bonding configuration and sticking to that structure, a diversity forms of diamond can be found, either obtained from natural sources or artificially created. [78]

According to a size-based classification, the smallest diamond structures known are diamondoids and consist on diamond cages in which carbon surface atoms are bonded to one hydrogen atom, with adamantane being the smallest diamondoid ($C_{10}H_{16}$) identified in 1933. [79] Diamondoids are isolated from petroleum [80] but are difficult to synthesize in a laboratory. It was not until much later, in 1987, when another source of natural diamond with sizes in the nanoscale (2-3 nm) was discovered, nanoscale diamond particles contained in interstellar dust. [81] However, these meteoritic nanoscale diamonds are formed by just few thousands of atoms, which makes difficult their analysis by standard mass spectroscopy methods and thus their true origin still remains unclear. [82]

As explained before, the high temperatures and pressures needed to produce natural diamond are non-viable to been reproduced in a laboratory and hence several methods to grow synthetic diamond were developed in the 1950s. In an attempt to mimic nature, the use of high pressures and high temperatures combined with catalytic materials, led to the development of one of this techniques, the High-Pressure High-Temperature (HPHT) method, explained in more detail in the next sections. Diamond particles obtained from this method are predominantly micron-sized and contain metal impurities from the process so are basically used for industrial applications. However, these micron-sized diamonds can be sized down to the nanoscale with high-energy milling techniques. [83]

A decade later, scientists from the URSS produced nanodiamond particles from the detonation of TNT and solid explosives based on CHNO, such as RDX ($C_3H_6N_6O_6$). [84]

After 20 years of inactivity, the possibility of scaling the production and the wide and increasing interest in nanodiamond particles led to improvements and optimization of the process, with up 80% of nanodiamond particles held in the detonation soot. [85]

Finally, with diamond being kinetically metastable, a third method of producing synthetic diamond came out almost in parallel to the development of the HPHT method, the Chemical Vapour deposition method (CVD) explained in the previous chapter. CVD is a low pressure kinetically governed process which produces high quality/purity diamonds. The control over the growth process, the possibility of doping diamond during growth and the possibility of growing diamond over large areas have made this method the preferred one among scientist for its unlimited capabilities towards applications.

In this thesis, commercial detonation diamond particles and commercial HPHT diamond nanoparticles have been used for different studies within this chapter.

Furthermore, the production of diamond nanoparticles from CVD grown films will be also discussed in the next chapter.

4.2.1 Detonation Diamond: Detonation synthesis

Detonation diamond particles (DND) were first synthesized in 1963 in the USSR. [84] DND are produced as a result of a detonation process in which TNT and hexogen with negative oxygen balance are used as explosive materials. [86] These materials are detonated in a chamber, usually in a N_2 atmosphere, that acts as a cooling medium, preventing the transformation of DND into graphite. [27]

Figure 4.2a) represents the carbon phase diagram. As it is well-known, at low temperatures and low pressures the most stable phase of carbon is graphite, so high temperatures and high pressures are necessary for diamond formation. [2] Usually high temperatures (>3500 K) and high pressures (>20 GPa) are generated in the detonation process as a result of the detonation wave propagation through the medium. The point at which such conditions are reached is known as Jouguet point (point A in 4.2a). [87] When both temperature and pressure drop (red line), liquid carbon atoms coalesce and crystallize forming nanodiamonds' agglomeration 4.2b). [2]

The material obtained in the detonation process, known as detonation soot, contains not only the diamond phase (from 40 to 80 wt%), but also graphitic carbon and metal impurities and oxides. [88] Figure 4.2b) represents the detonation soot components. Purification

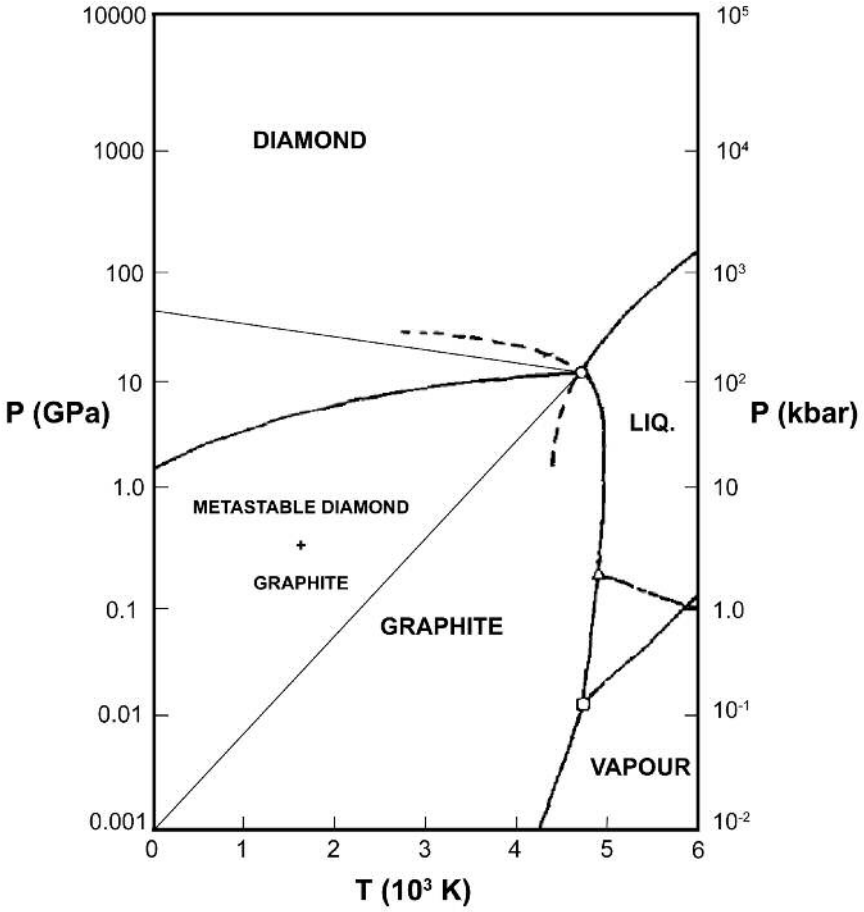

Figure 4.1: Carbon phase diagram detailing the regions in which graphite and diamond are thermodynamically more stable. Modified and reprinted from Physica A: Statistical Mechanics and its Applications, **156**, F.P. Bundy, 'Pressure-temperature phase diagram of elemental carbon', 169-178, Copyright (1989), with permission from Elsevier.

of diamond soots is a decisive step for most practical applications. The most general method to remove non-diamond phases is to use several acids (HCL) in a purification process or to use liquid oxidants (HNO_3, a mixture of H_2SO_4, or KOH/KNO_3). These methods dissolve metals present in the detonation soot and also oxidize the sp^2 carbon. [2] Nevertheless, industrial purification methods are not enough for certain applications as nanodiamonds (ND) tend to form aggregates and ND exhibit low dispersivity in liquid medium.

Ozone and air oxidation have probed to be feasible methods for deeper DND purification. [89, 90] Ozone-purified particles have an aggregate size in liquid medium of around 190 nm.

Diamond nanoparticles can be further de-aggregated in aqueous media by milling the nanodiamonds with micron-sized ceramic beads [91] or by microbead-assisted ultrasonic disintegration. [92] Stable colloids with 5 nm diamond nanoparticles are obtained. The main drawbacks of these techniques are the contaminants produced by the beads and nanodiamonds' surface graphitization.

Struggles with additional purifying methods lead to re-aggregation of core particles. [93,94] Nevertheless, additional methods such as borane-reduction of nanodiamonds in ultrasonic treatment [95] or nanodiamonds hydrogen annealing followed by centrifugation processes, can result in small aggregates (20 nm) or in complete nanodiamonds core isolation (3 nm-5nm) respectively. [96] After de-agglomeration processes, diamond nanoparticles' surface functionalization is essential to ensure surface uniformity and to understand the processes behind colloids behaviour.

Detonation diamond particles used in this work were sourced by PlasmaChem GmbH (G01 grade).

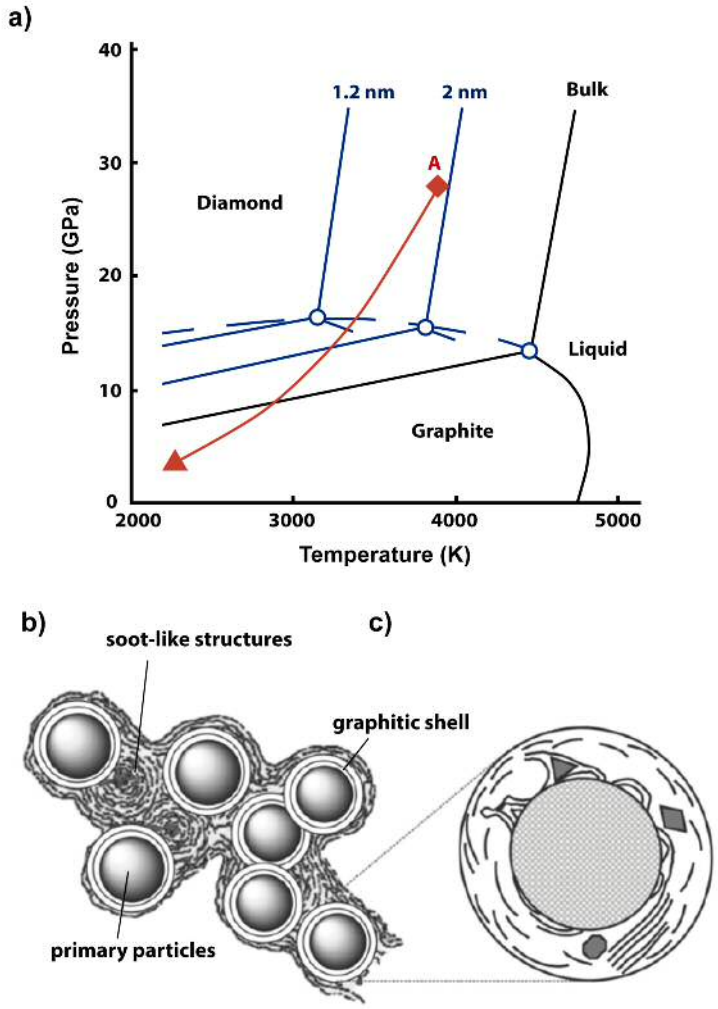

Figure 4.2: Detonation process for diamond nanoparticles synthesis. a) Carbon phase diagram showing diamond and graphite phases at their respectively stable conditions. Both diamond and graphite phases melt at 4500 K. During this process temperatures and pressures increase immediately, reaching the Jouguet point (marked as point A in the graph). With the temperature and pressure decreasing along the red line, carbon atoms condense into nanoclusters, coalescing then into larger liquid droplets and crystallizing. If the pressure drops below the diamond–graphite equilibrium line (black line), the formation of onion-like shells in enhanced, with this graphitic carbon binding the nanodiamond particles to form aggregates. Panel a) reprinted by permission from Macmillan Publishers Ltd: Nature Nanotechnology, V. N. Mochalin et al., **7**, 'The properties and applications of nanodiamonds', Copyright (2011). b) Scheme of the detonation soot components which include primary diamond particles, soot-structures and graphitic material surrounding the particles. Panel b) reprinted from Physica Status Solidi (a), A. Krueger et al., **204**, 'Deagglomeration and functionalisation of detonation diamond', 2881-2887, Copyright (2007), with permission by John Wiley & Sons, Inc.

4.2.2 Monocrystalline Diamond Particles: High-Pressure High-Temperature process

Apart from detonation diamond particles, 50 nm monocrystalline diamond particles obtained by synthetic HPHT were subjected to different annealing treatments and studied during the thesis. Micron size diamond particles created by the HPHT process can be processed and milled down to the nanometer scale.

As briefly introduced, the high-pressure high-temperature process was developed in an attempt to grow synthetic diamond, reproducing the pressures and temperatures needed to produce natural diamonds. Early experiments performed during the 1950s by the General Electric (GE) company, successfully produced synthetic diamond with a graphitic carbon source and catalytic solvents such as nickel, chromium, cobalt or iron, placed inside a belt press. [97] With the use of catalytic solvents, a reduction in the activation energy allowed the diamond formation by HPHT, proved for the first time in 1955. [97] Diamond seeds, a graphitic source and the a catalytic solvent inside the press were subjected to pressures around 10 GPa and temperatures exceeding 2300 K. [97] As such temperatures, the solvents are melted and the carbon bonds break apart from the graphitic source. Carbon is then transported to the diamond seeds and precipitates, forming a larger diamond. During the HPHT process, nitrogen present in the empty spaces of the chamber, in the solvent metals and in the carbon source material, is incorporated (up to 200 ppm) into the diamond, affecting some of the diamond properties. Attempts to reduce this incorporation include the addition of nitrogen getters (Al, Ni) which results in metal inclusions, hence reducing the diamond quality and the range of applications. [98]

The 50 nm monocrystalline diamond nanoparticles used in the thesis were produced by HPHT and were sourced by Microdiamant (MSY 0-0.05).

4.3 Diamond nanoparticles' surface groups

As seen in the previous section, synthetic diamond can be grown by different techniques including detonation synthesis, HPHT and CVD processes. Diamond nanoparticles can then be obtained directly from the detonation process, crushing the micron-size particles from the HPHT or milling down CVD grown diamond films. The particles thereof obtained will have different characteristics and hence will be used for different applications, which can be divided attending intrinsic bulk properties or properties arisen from the surface. For

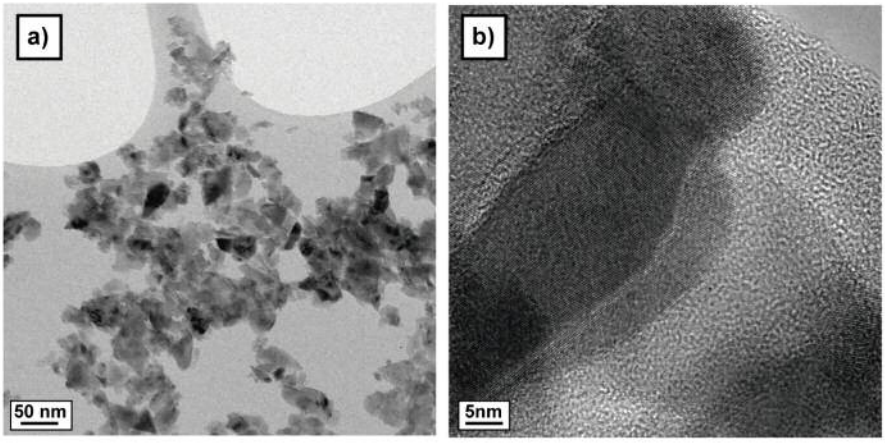

Figure 4.3: BFTEM and HRTEM images of 50 nm monocrystalline diamond particles a) Bright Field TEM image of 50 nm diamond nanoparticles and b) high resolution (HRTEM) image of a detailed 50 nm diamond nanoparticle.

example, bulk properties of detonation diamond are attractive for diamond-based cutting tools or as a polishing abrasive among others. On the other hand, surface properties have attracted an increasingly interest. As diamond is non-toxic, a large area of applications is focused in cell labeling and optical biomarking, however, what will be more important for this thesis is the use of diamond nanoparticles as single photon sources, discussed in chapter five. [99]

One of the decisive characteristics influencing material's properties is the diamond surface termination, strongly determined by the production method. For example, as briefly mentioned in subsection 4.2.1 the detonation soot is subjected to acids treatments and further purification processes before getting the commercially available detonation diamond particles, yielding to/generating an initially oxidized surface. This oxidized surface is a mixture of carboxyl, carbonyl, hydroxyl and some other oxygen groups, shown in figure 4.4 and can cause particle agglomeration. Particles extracted from the HPHT process will also present oxygen groups attached their surfaces due to the harsh conditions used to crush them after the HPHT process. On the other hand, films grown by CVD will be hydrogen-terminated due to an excess of hydrogen in the feed gas that etches away sp^2 bonds preferentially over sp^3 ensuring diamond formation.

Other properties to be considered before surface modification are the particles' size, shape and their surface orientation. Small particles such as 5 nm detonation diamond particles will have higher reactivity over bigger particles (the ones produced by HPHT or milling down CVD diamond films), as they have a large surface area, with more than 15% of UDD

particle carbon atoms located at the surface. On the other hand, bigger particles will behave as bulk diamond, due to they have less amount of atoms on the surface compared to the ones in the bulk. Furthermore, the detonation process produces highly spherical particles over the faceted particles obtained in the HPHT process which will also imply differences on their properties.

As seen before, the starting nanodiamond particles' surface can contain different groups attached which will have an influence over their properties. However these surface terminations can be controlled following several annealing treatments or more complicated functionalization procedures. The last are not under the scope of this thesis and will not be discussed, but can be found elsewhere. [100, 101]

Notwithstanding, annealing treatments involving oxygen termination, hydrogen termination and vacuum annealing have been deeply used within this thesis and hence are discussed in the following section.

4.3.1 Oxygen termination

An oxidized surface is the most common diamond surface termination usually generated from wet-chemical treatments used in particles production methods, purification and deagglomeration processes. These treatments involve the use of acids such as HCL or a combination of HNO_3/H_2SO_4 or H_2O_2/H_2SO_4, known for being strong oxidants. [100]

However, this does not ensure a homogenized surface and a mixture of oxygen-containing groups are usually present, including carboxyl, carbonyl and hydroxyl groups, shown in figure 4.4. Carboxyl groups are formed by the aforementioned acids treatments whereas carbonyl groups can preferentially be created combining ozone treatments under UV radiation. [89]

In the search for a more homogeneous surface, air annealing treatments at different temperatures were studied. This technique efficiently removes the sp^2bonded carbon, [102] producing a more homogeneous surface, mainly formed by carbonyl and ether functions, [100] while producing diamond anisotropic etching. The size reduction is clearly observed in detonation diamond under temperatures higher than 460°C. [103] However, lower etching rates have been observed for bigger size diamond particles with reported average high reductions (in 100nm particles) of less than 1nm/h at 500°C. [104]

The air annealing treatment is the method selected in this thesis to carry on diamond

nanoparticles surface oxidation, as it is efficient and does not involve the use of hazardous chemicals. Furthermore, it has been reported that air annealing substantially improve the luminescence properties of nanodiamonds' color centers as will be discussed in chapter five. [105] However, annealing temperatures have to be carefully chosen to avoid diamond etching. Detonation diamond particles were subjected to temperatures no higher than 460°C whereas 50 nm diamond particles were annealed at 480°C.

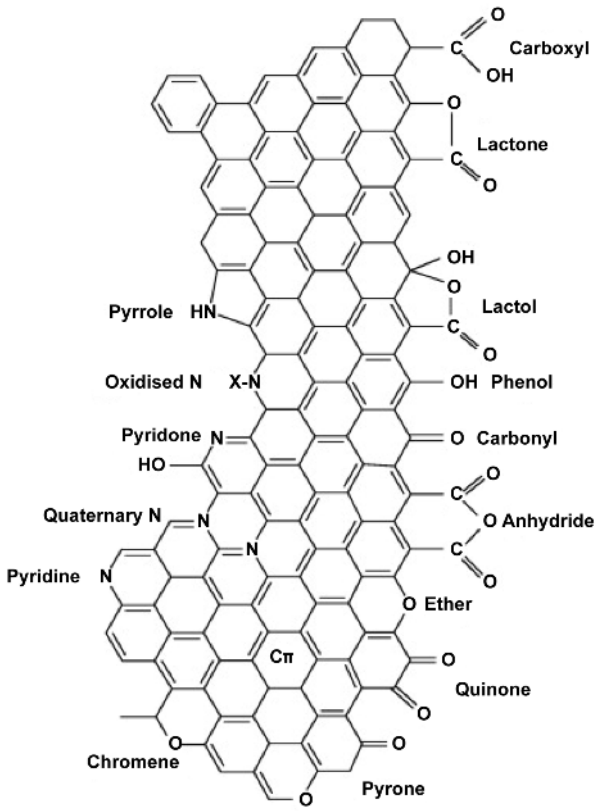

Figure 4.4: Scheme representing Nitrogen and Oxygen groups on carbon. Reprinted from Catalysis today, 150, 1-2, José Luís Figueiredo, Manuel Fernando R. Pereira, "The role of surface chemistry in catalysis with carbons", Copyright (2010) with permission from Elsevier.

4.3.2 Hydrogen termination

With oxygen groups covering in most of the cases diamond particles' surfaces, the reduction and substitution of these groups by hydrogen ones was a major challenge. While the production of a hydrogen terminated surface is straightforward for diamond films, it is not for diamond nanoparticles, where the main hindrance is to achieve a complete hydrogenated surface, avoiding the formation of hydroxyl groups. [106]

Different hydrogen annealing procedures have been discussed in the literature, and can be divided into 2 groups, which depend on if atomic hydrogen or molecular hydrogen are used for diamond nanoparticles hydrogenation. Atomic hydrogen can be created in a hydrogen plasma [107] or by breaking the hydrogen molecules at sufficient temperature using a tungsten filament. [108] Atomic hydrogen is more reactive than molecular hydrogen, however, obtaining a complete and homogenized hydrogenated surface is not easy using a microwave plasma reactor. Incomplete and or inhomogeneous hydrogenation can occur as some particles' surfaces, although nanoparticles are placed inside the reactor sitting flat on top of a holder, could be hidden and not completely exposed to the hydrogen plasma. Some progress to overcome the inhomogeneous hydrogenation was achieved by repeating the hydrogenation process twice, [107] or by rotating the diamond particles inside a quartz tube in a plasma reactor. [109]

On the other hand, the use of molecular hydrogen at high temperatures (900 °C) also leads to C-H bond formation, as well as an unavoidable sp^2creation. [110] However, the formation of sp^2carbon can be prevented using molecular hydrogen at low temperatures (500 °C), first proposed by Williams et al. [96] This last method for nanoparticles hydrogenation is the one used during this thesis, and the complete explanation behind the low temperature hydrogenation process can be found in section 4.5.

4.3.3 Vacuum Annealing

At was discussed at the beginning of this section, the high activation energy barrier (0.4 eV per atom) between graphite and diamond phases prevents the conversion from diamond to graphite at atmospheric pressures and temperatures as shown in the carbon phase diagram in figure 4.1. Nevertheless, when reducing particles' size to the nanoscale the conditions change enabling phase transformation. *Danilenko et al.* [87] and *Viecelli et al.* [111] determined the change in the carbon phase diagram for detonation particles formed during the detonation process, taking into account the higher surface energy of smaller particles over bulk diamond. As can be observed in figure 4.2a), the triple point of the phase diagram shifts to lower temperatures and higher pressures compared to bulk diamond, or in other words, the region in which diamond is thermodynamically stable move to lower pressures and higher temperatures. [112] This means that sp^2 formation and diamond graphitization is possible when annealing the diamond particles at different temperatures. However, the conditions to form graphite will depend not only on the particle size and crystal orientation but also on the surface groups covering the diamond

surfaces and will depend on the atmosphere the particles are annealed under and the process time.

Before any diamond surface functionalization or surface treatment, pristine diamond nanoparticles are covered by several groups or surface atoms which removal or decomposition will lead to surface reconstruction through creation of sp^2 bonds. [112] The amount of sp^2 created can vary from a monolayer or few monolayer of sp^2 carbon to a complete surface graphitization with the formation of carbon nano-onions. [113] For commercial detonation diamond particles, although up to 6% of the pristine surface contains sp^2, the initial sp^2 formation temperature is considered to begin above 750°C, [114] with a meaningful graphitization above 1000°C. [106] On the other hand, larger particles can also be graphitized but higher temperatures are needed.

A special care must be taken as too much sp^2 content created surrounded diamond core particles, can completely governed the particle's characteristics over diamond properties. As both detonation particles and 50 nm particles will have uncontrolled sp^2 content at the beginning, it is wise to first removed this content by air annealing and proceed to diamond graphitization afterwards.

In this thesis 50 nm diamond nanoparticles have been subjected to vacuum annealing treatments and results are discussed in section 4.6

4.4 Colloidal systems

After diamond nanoparticles have been subjected to different annealing treatments with the aim of ensuring a homogenised surface, it is desirable to be able to disperse these particles in different aqueous medium. The metastable mixture containing the suspended particles in the liquid medium, establishing two different phases, is known as a colloid. However, the co-existence of three different phases within the colloid is possible.

In this thesis, the word *colloid* will refer to solids (particles) dispersed in liquid (water), but in general, both dispersed substances and dispersing medium can be in gas, liquid or gas phases. [115] In a first approximation, a system can exhibit properties of colloidal character if the phases are within the range of 1 nm to 1000 nm and hence, surface-volume ratio would be high, with surface chemistry playing a decisive role. [116] If the particles in the dispersing medium are about the same size, the colloid is refer as been monodisperse, whilst if a different range of sizes is present the colloid is polydisperse.

Although the nature of some colloids is being stable (no presence of aggregates), instability is common in colloidal systems, as in thermodynamics terms, an entity tends to transform into states that lower its free energy. However, a suitable mechanism that allows this transformation has to occurred. Stable colloids are in a state of high energy, and would remain in that state for long time in the presence of an energy barrier that prevents transformation to unstable colloid. Thus, conditions to ensure high energy barrier have to be pursued.

Particles in a dispersion have a "natural" kinetic energy, producing collisions with other particles in the colloid (Brownian motion). A particle undergoing Brownian Motion will have a kinetic energy of $3/2KT$ with K being the Boltzmann's constant an T the system temperature. Thus, energies arisen from two particles' collision will be in the order of few KT. With energy barriers sufficiently high compared to KT, the colloid will remain stable as these particles' collisions do not have enough energy to overcome the barrier, which decrease will depend rather on medium/sample composition, temperature and pressure. However, this energy can have values up to $10KT$ which in the presence of attractive interactions between particles can lead to the formation of bigger aggregates. [117]

Therefore, in most of the cases what stabilizes or destabilizes a colloid are the intermolecular forces between the particles suspended in the colloid, explained in the next subsection.

The total free-energy curves in a colloidal system resulting from different interactions are shown in figure 4.5. Briefly, a stable suspension will contain particles repelling between each other whereas if this electrical repulsion is diminished, particles will start aggregating and finally sedimenting. In other words, a colloidal dispersion will be stable if repulsive forces are large enough to prevent aggregation.

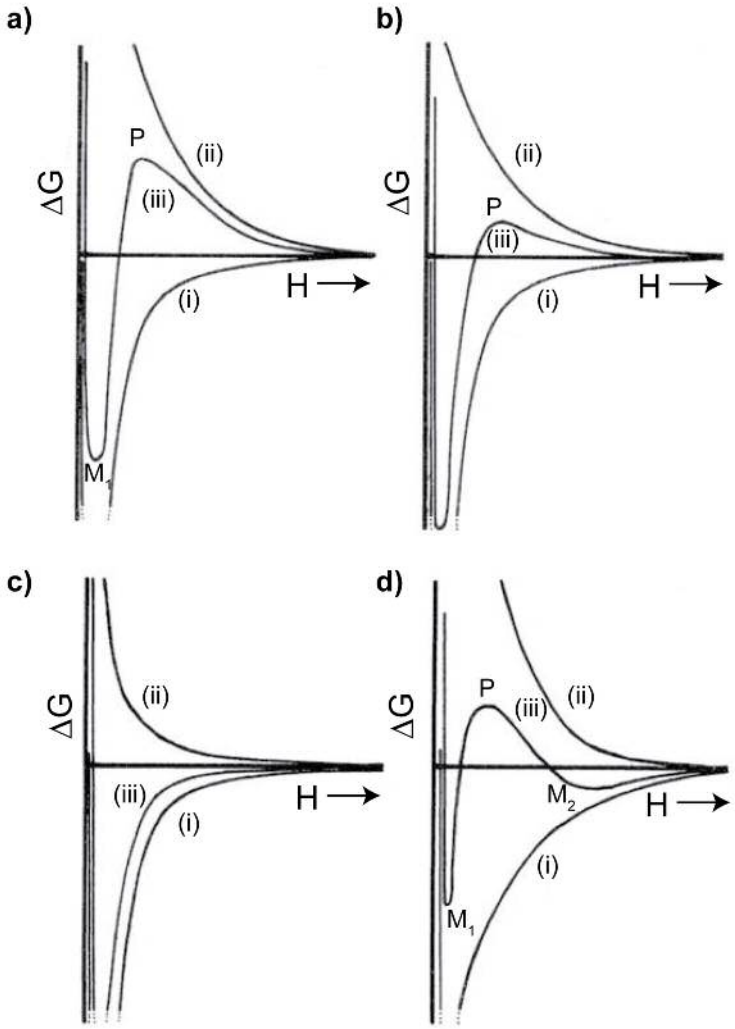

Figure 4.5: Curves representing the total free energy (ΔG) as a function of particles' separation (H) (iii) which results from attractive (i) and repulsive (ii) interactions. a) State representing a system with a high energy barrier, with a primary maximum denoted as P due to a strong repulsive interaction, and a minimum, denoted as M_1. b) System in which the energy barrier is lowered by a reduction of repulsive interactions. If the system energy barrier is reduced to few KT, the system is able to overcome the minimum M_1. c) Complete removal of the energy barrier. d) System in which a second minimum exits (M_2). If the depth of this minimum is in the order of few KT, aggregates can form, being weakly bounded.

4.4.1 Colloids stability: Zeta Potential

To study the stability of diamond nanoparticles in an aqueous medium, it is necessary to introduce the zeta potential concept. The zeta potential (ξ) is a parameter that describes the interfaces charging behaviour, which includes solid-solid interfaces, liquid-liquid interfaces or even liquid-gas interfaces. When talking about colloids (particles in a suspension), the zeta potential value is an indicative of the colloid stability. Standard approved zeta potential values to define stability are $\pm 30mV$.

As seen in the previous section, particles' behaviour in a liquid medium is governed by the electrical charges on the different interfaces. If electrostatic repulsion forces between two particles in the colloid are strong enough, the particles would remain separated. On the other hand, if these electrostatic repulsion forces are not strong enough, the particles can collapse, aggregating and eventually forming precipitates. Many theories have been developed to explain the stability of colloidal systems, but the most commonly used is the DLVO theory. The DLVO theory was developed in the 1940s by Boris Derjauin, [118] Lev Landau, Evert Vervey and Theodoor Overbeek. [119] This theory explains the colloidal stability assuming two forces contributions between particles in liquid medium: the London Van der Waals attractive interaction, and the electrical double layer forces (explained below). [120] Forces induced by the electrical double layer or due to the interaction of electrical double layers of neighbouring particles are long-range repulsive forces, and dominate over the van der Waals forces, preventing aggregation. However, this theory is not complete as it only takes into account two isolated particles in a liquid, separated few nanometers and far from the walls in which the colloid is contained. When the concentration of the colloidal solution is higher, particles become closer and the discrete nature of the different molecules is now involved. Therefore, long-range attractive forces are also involved in colloids stability, [121] hence why, non-DLVO equilibrium forces (i.e solvation forces) and Brownian forces have also been studied for a better understanding of colloidal particles interaction. [122] The interpretation of these forces requires a deeper explanation but it is not under the scope of this thesis. The origin of the charges involved in the DLVO theory, is of diverse nature, and it is discussed in the next sub-section.

Origin of surface charge formation

One way of ensuring electrostatic repulsive forces is controlling the surface charges on the diamond nanoparticles. When particles are introduced in a liquid medium, they immedi-

ately acquire a surface charge. The charges' formation at the interfaces concerns different mechanisms. These mechanisms include the adsorption/desorption of ions, ionization of particles' surface groups, isomorphic substitution and the accumulation and depletion of electrons. The isomorphic substitution involves certain minerals with different valence ions, and the accumulation/depletion of electrons is believed to be related to interfaces between metals and solutions with spontaneous polarization. [123] For these reasons, only the ionization of particles or the ions' adsorption will be considered in this thesis.

In the previous section, the different groups present in diamond surfaces were explained. Acidic groups (such as carboxylic acid) and basic groups (such as amine) undergo proton exchanges known as de-protonation and protonation respectively. Both processes are represented in 4.6a) and 4.6b). The carboxylic acid is dissociated in water, de-protonated, leaving a negatively charge surface. On the other hand, amine groups get protonated, leaving a positively charge surface.

The charging process is not that simple as it also depends on the surface groups density, the strength of the acidic groups (pk_a) and strongly on the pH of the aqueous medium. Furthermore, if two carboxylic acid groups are close enough, an interaction between them and a proton-interchange can occur.

$$pH = pk_a + \log \frac{[A^-]}{[HA]} \tag{4.1}$$

Equation (4.1) is known as the Henderson-Hasselbalch equation and relates the acid dissociation constant (pk_a) to the pH of the solution, with $[A^-]$ and $[HA]$ the deprotonated and protonated form of the acids respectively. The lower the value the pk_a is, the stronger the acid and therefore, the greater capacity to donate a proton. However, at low pH there is a high concentration of protons in the solution so the dissociation of the carboxylic acid is not auspicious. Lets consider a nanodiamond surface covered completely by carboxylic acid. Carboxylic acids are relatively strong acids, and their pH usually ranges from 2 to 5. [124] Dissociation of carboxylic acid is given by equation (4.2).

$$(CH_3)_3CCOOH + H_2O \rightarrow (CH_3)_3CCOO^- + H_3O^+ \tag{4.2}$$

If the diamond surface is covered by the $(CH_3)_3$CCOOH (pk_a=5.05), at pH 4, applying the Henderson-Hasselbalch equation, the acid will be dissociated 10%. As a rule of thumb,

an acid remains protonated until the pH reaches its pk_a. At high pH, the concentration of protons in the solution is low and the dissociation of acidic groups will be enhanced. The behaviour of basic groups will be the opposite, at low pH basic groups will become protonated. Different techniques to calculate the pka values can be found in the literature. [124–126] Notwithstanding, the presence of just one surface group is an ideal situation as usually there will be an heterogeneous combination of surface groups.

The second mechanism responsible for charge formation is the adsorption of ions or charged particles onto uncharged surfaces, represented in 4.6c).

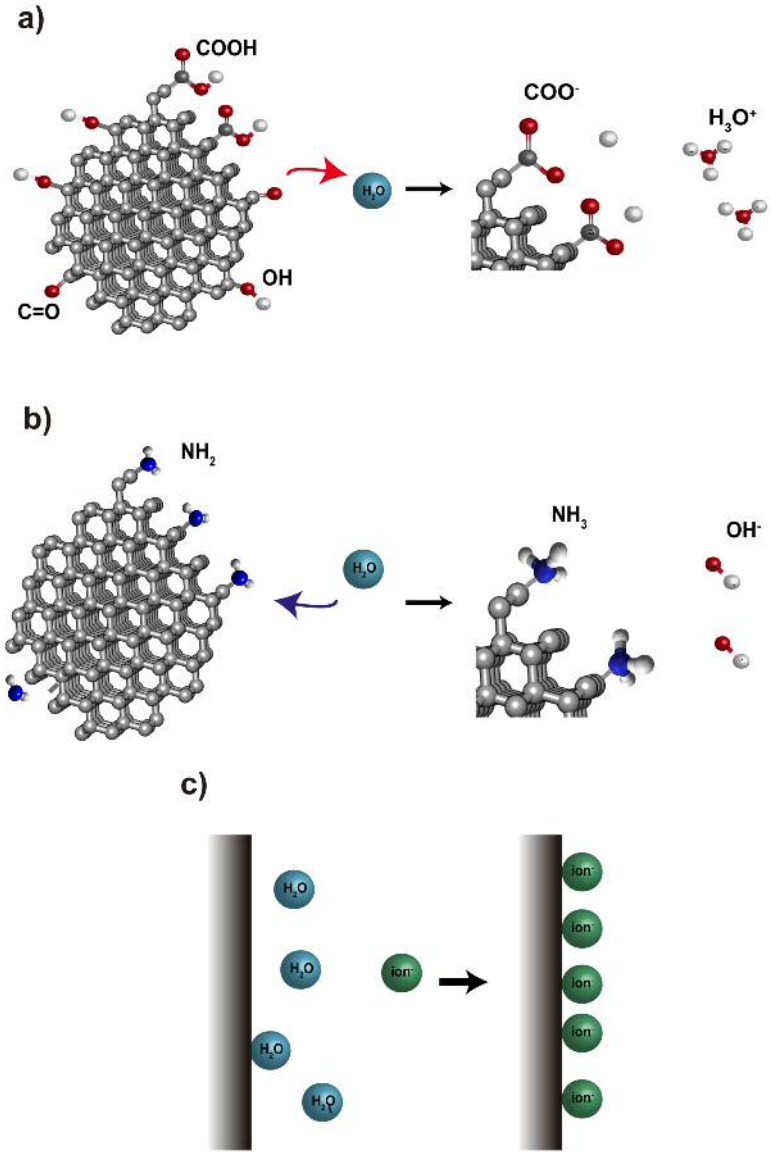

Figure 4.6: Representation of charge formation on nanodiamond surface. a) Deprotonation of carboxylic acid in water, b) protonation of the amine group in water and c) adsorption of water ions onto an uncharged surface.

The Electrical Double Layer (EDL)

The charge formed on the diamond surfaces, would be compensated by the excess of vicinity ions of opposite charge (counterions) in the aquous medium (the colloid is electrically neutral as a whole). The structure formed is known as Electrical Double Layer (EDL). Close to the surface, the counterions' concentration is high, but this concentration decrease with increasing distance from the solid surface establishing a diffuse layer of counterions. The counterions that form the closer layer, the stationary layer, are tightly bounded, whereas the ions in the diffuse layer are loosely bounded. The surface charge and the charge in the diffuse layer will produce a potential variation in the solution. The zeta potential ξ is defined as the potential measured in the border of the two planes, named as the shear plane. The potential in the particle's surface is denoted as ψ_S and this potential would be zero far from the surface. This is just a simplistic version of the EDL, a more complex model was developed in the 1900s.

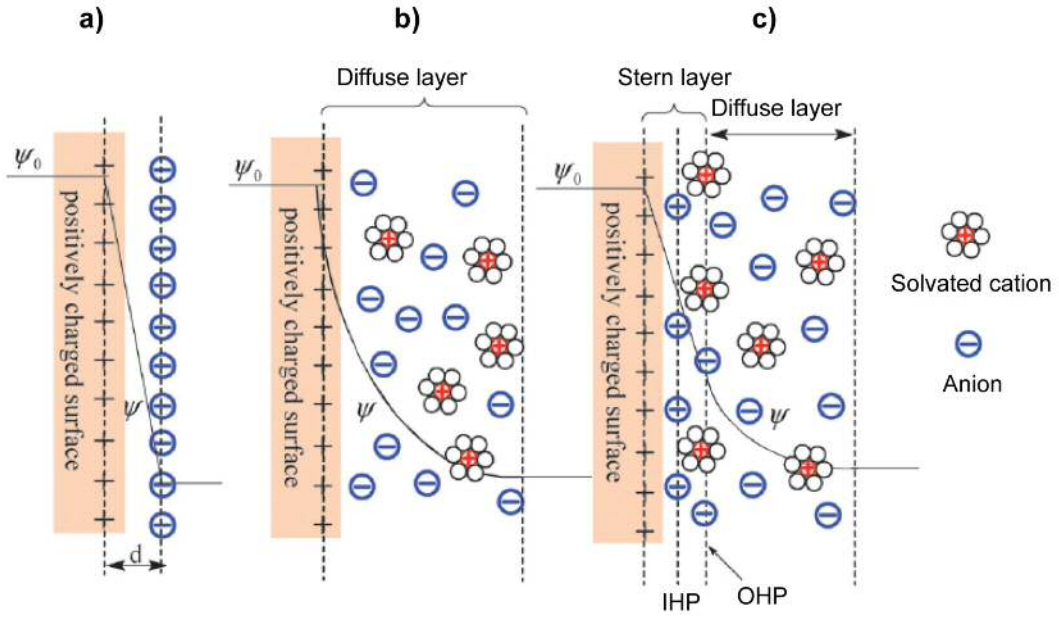

Figure 4.7: Schematic models of the Electrical Double Layer considering a positively charged surface. a) Helmholtz model b) Gouy-Chapman model and c) the Stern model showing the inner Helmholtz plane (IHP) and the outer Helmholtz plane (OHP). Reproduced from ***J. Mater. Chem. C***, 2015, 3, 6445-6470, with permission of The Royal Society of Chemistry. http://dx.doi.org/10.1039/C5TC00755K

The first theory to explain the EDL was given by Helmholtz in 1853. This theory explains the electrostatic interaction between a charged surface and a layer of counterions. This

double layer behaves as a capacitor with linear dependency when a voltage is applied. However, this theory does not consider essential factors such as thermal motion, ion diffusion or adsorption onto the surface. In the early 1900s, Gouy, Chapman, and Debye and Hückel developed a theory that took into account the previous factors, but failed into the assumption of considering ions as point charges. Finally, in 1924, Stern proposed a model combining the Helmholtz and the Gouy-Chapman models, considering the finite size of ions and defining two different regions for ions' distribution: the compact stern layer and the diffuse layer. [120] In the compact layer, two different types of adsorbed ions can be distinguished, distributed in the inner Helmholtz plane (IHP) and the outer Helmholtz plane (OHP). [127]. In figure 4.7 a), a schematic figure showing the different EDL models can be observed. [128, 129]

Measuring the Zeta Potential: electrokinetics effects

As explain in the previous sections, particles in a colloid carry different electrical charges on their surfaces, and these charges can interact with an applied electric field. Effects arisen from that interaction are defined as electrokinetic effects and the Zeta potential can be determined experimentally by measuring different electrokinetics effects.

Electrokinetic effects account for the tangential fluid motion close to a charged surface [129] and can be classified depending on the driving force that produce the movement, either of electrical or mechanical character. Electrophoretic mobility or electro-osmosis are electrokinetic phenomena in which an electric force leads to mechanical motion, whereas streaming potential or sedimentation potential are phenomena in which is a mechanical force what produces an electric current. A brief description of these electrokinetics effects can be found in *Delgado, A. V. et al.* [129]. Electrophoretic mobility is explained in more detail below, and streaming potential will be discussed in chapter six.

When charged particles are immersed in a liquid and an external electric field is applied, these particles will move toward the electrode with opposite sign. The velocity of these particles divided by the electric field is known as electrophoretic mobility, and is related to the zeta potential as follows:

$$\frac{V_{ep}}{E} = u_e = \frac{\varepsilon\xi}{\eta} f(\kappa a) \tag{4.3}$$

where V_{ep} is the particles' velocity, E the electric field, u_e is the electrophoretic mobility,

ε is the dielectric constant, ξ is the zeta potential, η is the viscosity and $f(\kappa a)$ is a dimensionless quantity known as *Henry's Function* where a is the particle radius and $\kappa - 1$ is the Debye length and measures the EDL thickness.

To determine the zeta potential, two approximations to the Henry's function can be applied, considering either large κa values (large particles in a high electrolyte concentration solution) or small κa values (with particles in a nanometer size range or in a solution with low electrolyte concentration). The first approximation leads to the *Helmholtz-Smoluchowski (HS)* equation:

$$u_e = \frac{\varepsilon \xi}{\eta} \tag{4.4}$$

And the second approximation can be simplified in the Hückel equation:

$$u_e = \frac{2\varepsilon \xi}{3\eta} \tag{4.5}$$

However, in most of the cases real systems are not represented in those approximations, as they required much more complex $f(\kappa a)$ functions. [130]

As previously mentioned, electrophoretic mobility is the parameter measured experimentally to calculate the zeta potential and it is determined by the Laser Doppler Velocimetry technique (LDV). [131] Two coherent lasers are used to measure a shift in frequency, with one frequency produced by the moving particles and the other one characteristic of the incident laser. The combination of both frequencies produced a modulated beam whose frequency would be proportional to the velocity of the moving particles, as stated by the Doppler principle.

In the following sections, zeta potential measurements performed on detonation diamond particles and 50 nm diamond particles are studied.

4.5 Ultra-dispersed diamond particles results

As explained in the CVD diamond growth process in chapter 2, hydrogen plays an important role not only during the diamond growth itself, but also in the diamond surface termination (hydrogenation), through C-H bond formation or by CH_2 groups. [100, 132] The use of atomic hydrogen (H) during diamond growth (i.e. formed dissociating molecular hydrogen via microwave plasma activation) will allow a preferentially sp^2carbon etching over sp^3carbon etching, preserving the latest electronic configuration on the diamond' surfaces and hence preventing surface reconstruction. [133] Among the hydrogenation mechanisms or methods (described in detail in previous sections), plasma hydrogenation has been a well established technique for diamond films hydrogenation. However, it is harder to get an homogeneous hydrogenation for nanodiamonds using a plasma in a CVD reactor as most of the particles' surface will be cover by another particles, as the nanodiamond powder will not sit completely flat on the substrate holder. Furthermore, particles also tend to overheat as they have poor thermal contact with the substrate. For that reason, other methods have been used for nanodiamonds hydrogenation (i.e. annealing in hydrogen gas), involving in most of the cases high temperatures which produce undesired graphitic structures. [106, 109]

In order to avoid sp^2 formation and a massive nanodiamond particles etching, hydrogenation at relatively low temperatures (500°C) using hydrogen gas was successfully performed in detonation nanodiamond by *Williams et al.* [96] Notwithstanding, the mechanism behind hydrogenation as such low temperatures was still uncertain and limited to small particles ($< 10nm$). [96] As detonation diamond particles have a significant and a higher amount of non-diamond carbon (sp^2) than larger diamond particles, [85] it was thought that sp^2 could have a catalytic effect, being desorbed as carbon radicals (C_2, C_3), reacting with the molecular hydrogen and thus producing the C-H bond formation on the nanodiamond surface (sp^3). [134]

To study the interaction between hydrogen and diamond surfaces (C-H bond formation), studies using low energy electron diffraction (LEED), [132, 135] temperature programmed desorption (TPD) [132] or IR spectroscopy [136] have been used, with the latest been the most extensively used as it provides a higher spectral resolution. Therefore, to study the mechanism responsible for low temperature hydrogenation and to prove the previous idea about the hydrogenation involving C_2, C_3 species, commercial detonation diamond powders were subjected to hydrogen annealing treatments at different temperatures, and

the powders were studied in FTIR and in a mass spectrometer.

The annealing treatments were carried out in our laboratory, at Cardiff University, in a vacuum chamber ($10^{-3}mbar$). FTIR and mass spectrometry measurements were performed at the National Dong Hwa University, in Taiwan, and the experiments were conducted by Ashek-I-Ahmed under the supervision of Professor Chia-Liang Cheng.

Detonation diamond particles (5nm) used for the experiments detailed in this section were sourced by PlasmaChem GmbH, Germany, and were annealed in molecular hydrogen at 100°C, 200°C, 300°C, 400°C and 500°C, as previously described. [96] Untreated detonation diamond particles were also measured for comparison.

4.5.1 Fourier Transform Infrared Spectroscopy

For the first FTIR measurements, the detonation diamond powder annealed at 500°C was transfered to an ultra high vacuum chamber (UHV) (see FTIR section in *Experimental Methods* chapter for a complete equipment description). The powder was first dispersed in deionized water, drop cast onto silicon substrates and then dried in vacuum for 24 hours before starting the IR measurements, as detailed in [134]. The hydrogenated detonation diamond particles were heated inside the UHV chamber, at temperatures ranging from 100°C to 800°C, using an electrically controlled heating device and without the addition of H_2. All samples were cooled down to room temperature prior to the start of the FTIR measurements.

Figure 4.8 shows the FTIR spectra of the hydrogenated detonation diamond particles for the different range of temperatures. Spectra from 800 cm^{-1} to 3200 cm^{-1} were recorded with special emphasis in the band ranging from 2800 cm^{-1} to 3000 cm^{-1}, shown in detail in figure 4.8b). C-H stretching features appear in this band and hence can be used to confirm the H-termination on diamonds. [136]

There are numerous studies in the literature investigating the interaction between hydrogen and diamond that conclude that this interaction is anisotropic and dependent on the crystal orientation. [135] Consequently, C-H peaks at different wavenumbers within the band ranging from 2800 cm^{-1} to 3000 cm^{-1}, will be attributable to the C-H adsorption on different facets or diamond surfaces. [135–138] In figure 4.8, the spectrum for the hydrogenated UDD at room temperature shows two evident and broad peaks at 2878 cm^{-1} and at 2945 cm^{-1}. As explained by *Cheng et al*, [136] these peaks are associated with hydro-

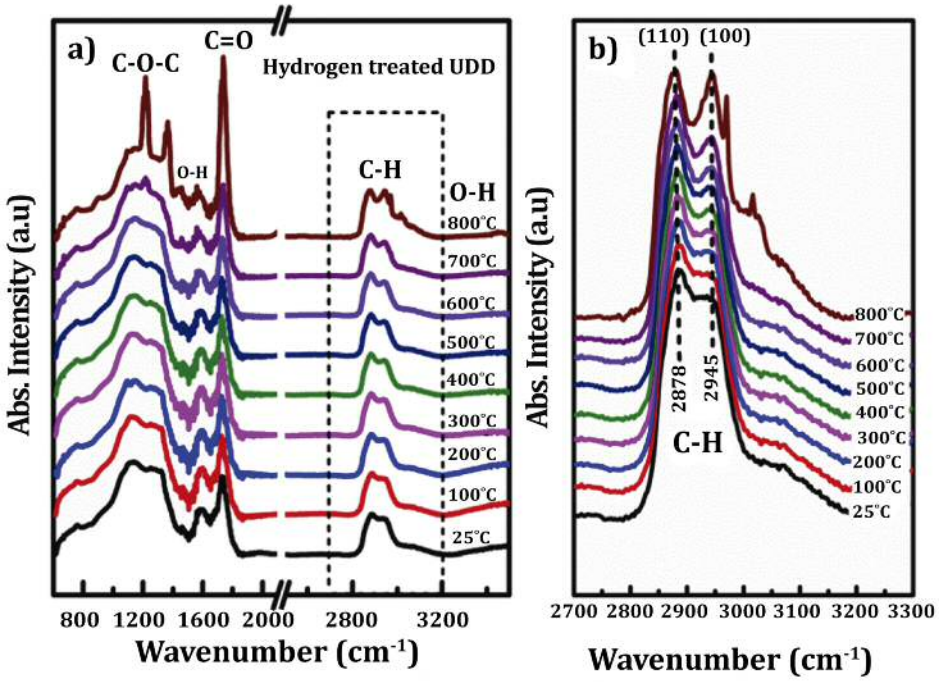

Figure 4.8: FTIR spectra of the hydrogenated detonation diamond annealed at different temperatures, from 100°C to 800°C. b) Detail of the C-H stretching mode. Reprinted from [134] under a Creative Common License, http://creativecommons.org/licenses/by-nc-nd/4.0/. https://doi.org/10.1016/j.carbon.2016.09.019

gen bonded to the C(111) and C(100) surfaces on diamond particles, more specifically, the peaks correspond to C(110):H mixed with C(111):H and C(100):H respectively. However, these values depict a slight mismatch in comparison with the values of 2870 cm^{-1} and at 2940 cm^{-1}reported for similar 5 nm size diamond particles. [136] This difference can be explained by variations in grain size. [134]

When measuring the C-H peaks in FTIR, it is extremely important to avoid organic surface contamination with hydrocarbons, as it will cause similar peaks to CH adsorbed on diamond samples, misrepresenting the measurement. An example of hydrocarbon surface contamination is shown in figure 4.9.

Figure 4.9 represents different spectra of the CH bond in 100 nm diamond powders. Figure 4.9a) shows the CH spectra for a sample left a long time under ambient conditions and transferred and measured in the UHV chamber, previous plasma hydrogenation treatment. After annealing the same sample for 30 min at 500°C (figure 4.9b), the intense peak around 2940 cm^{-1} decreases, indicating the desorption of the contaminated hydrocarbon. Hot filament hydrogenation at higher temperatures and for longer durations, does not change

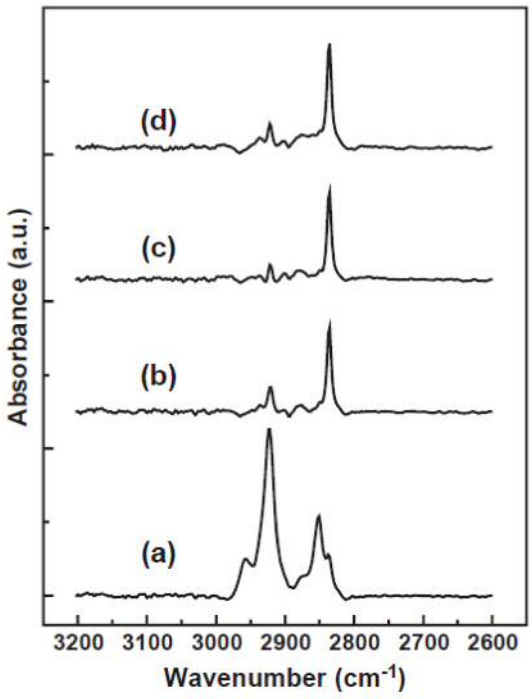

Figure 4.9: FTIR spectra showing the CH features from 100 nm diamond powders. a) Direct adsorption on contaminated sample, showing similar CH features. b) Further hot filament hydrogenated sample at 900 °C after an annealing at 500 °C for 30 min. c) Hydrogenation/etching 1 h at 300°C, and (d) hydrogenation/etching 2 h at 900°C. Reprinted from Diamond and Related Materials, 14, C.-L. Cheng et al., "The CH stretching features on diamond of different origins", 1455-1462, Copyright (2005), with permission from Elsevier

the CH spectrum (4.9c) and 4.9d)), showing the typical CH peaks. For that reason it is crucial to be really careful when preparing and measuring the samples by FTIR.

As described before, our hydrogenated UDD (500°C) was annealed at different temperatures (without addition of H_2). As the temperature is increased, the disordered or loosely bounded carbon is desorbed from the surface, sharpening CH peaks as can be observed in figure 4.8b). However, the C(111):H peak (usually at 2835 cm^{-1}) is not visible because of the effect of domain size. The size of C(111)-1x1 facets is too small to allow CH stretching features. [136] Nevertheless, the C(111):H peak will be present in the 50 nm nanodiamond particles, studied in the following sections.

As is evident from the results, it can be concluded that UDD particles are hydrogenated.

To further investigate this hydrogenation process, and to check whether carbon radicals are desorbed during the annealing and hence confirm the previous statement, an untreated

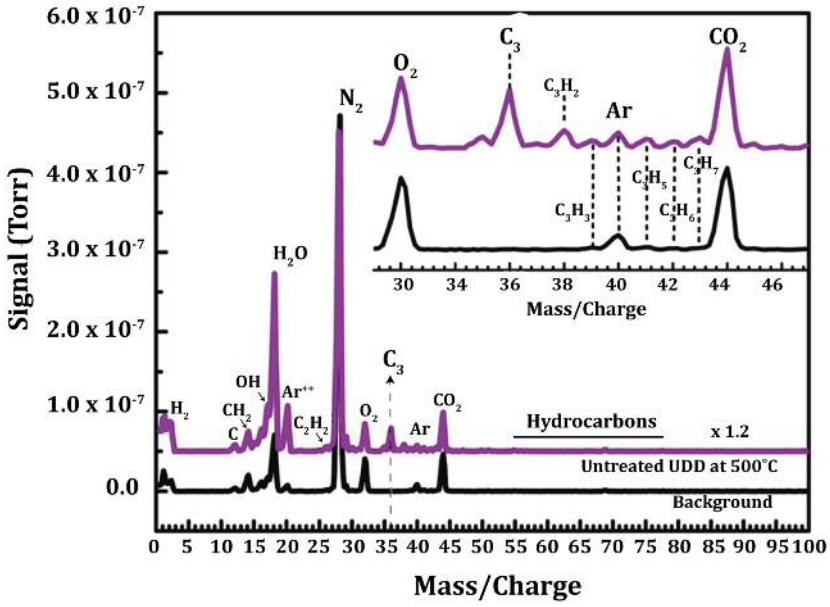

Figure 4.10: Mass spectrum of an untreated UDD sample annealed at 500°C and a silicon substrate used as background. The inset shows in detail the range in which C_3 and other carbon species of interest are produced. Reprinted from [134] under a Creative Common License, http://creativecommons.org/licenses/by-nc-nd/4.0/. https://doi.org/10.1016/j.carbon.2016.09.019

detonation diamond powder sample was introduced in an UHV chamber with an *AMETEK Dycor System 200 Residual Gas Analyzer (RGA)* attached. The vacuum was kept at $4x10^{-8}Torr$ during the measurements. The UDD sample was annealed at 500°C for 30 min. A silicon sample was also introduced into the chamber and annealed at 800 °C and its spectrum was used as a background signal. Figure 4.10 shows the mass spectrum for the UDD sample and the background signal, where peaks related to gases commonly found at low vacuum ($10^{-8}Torr$) were detected. Gases such as $H_2(m/z = 2, 1)$, $CO/N_2(m/z = 38)$, $H_2O(m/z = 18, 17)$ and $CO_2(m/z = 44)$ were observed in both background and untreated UDD samples. Other species such as double charged ions (^{40}Ar) and heavy hydrocarbons($C_3H_3(m/z = 39)$) were also present, explained in [134] in more detail. If the background and the untreated UDD signals are compared, two different peaks are observed in the latest at m/z=36 and at m/z=38 and are attributed to C_3 and its hydrocarbon C_3H_2.

In figure 4.10, the desorption of the C_3 radical is clearly observed in the untreated UDD sample annealed at 500°C. However, this desorption could also occur at lower temperatures. To further investigate the C_3 desorption, the untreated UDD sample was annealed

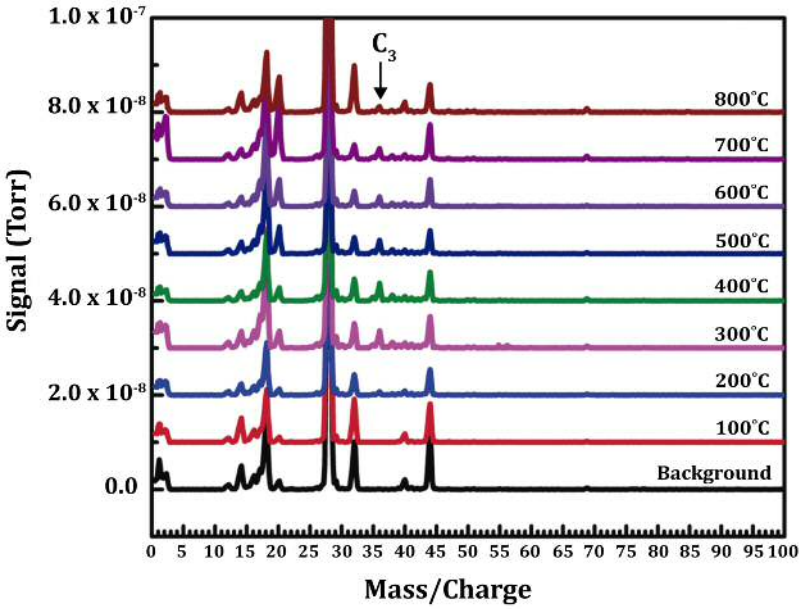

Figure 4.11: Mass/charge spectrum of untreated UDD sample annealed at different temperatures, ranging from 100°C to 800°C. Reprinted from [134] under a Creative Common License, http://creativecommons.org/licenses/by-nc-nd/4.0/. https://doi.org/10.1016/j.carbon.2016.09.019

at different temperatures (from 100°C to 800°C), for 30 min, increasing 100°C in each step. As can be observed in figure 4.11, the C_3 desorption starts at 200°C, with an intensity peak decrease at 500°C. As temperature is increased, more species are desorbed inside the vacuum chamber, producing an increase in the chamber pressure. As the chamber pressure was kept constant during the whole experiment, that means that a significant amount of C_3 could be pumped out.

According to the previous results, if the C_3 radical has a influence in the hydrogenation process, hydrogenation could also be possible as temperatures as low as 200°C, temperature at which C_3 begins to be desorbed from the nanodiamond particles surface. To confirm this effect, FTIR measurements were also conducted in hydrogenated UDD at 100°C, 200°C, 300°C and 400°C, and the spectra are shown in figure 4.12. As expected, CH stretching features are present in the hydrogenated UDD at 300°C and 400°C. However, hydrogenation at 200°C is not observed, maybe due to an incomplete C_3 desorption i.e., not enough to produce the C-H reaction.

The mechanism behind low temperature hydrogenation can be explained (further details

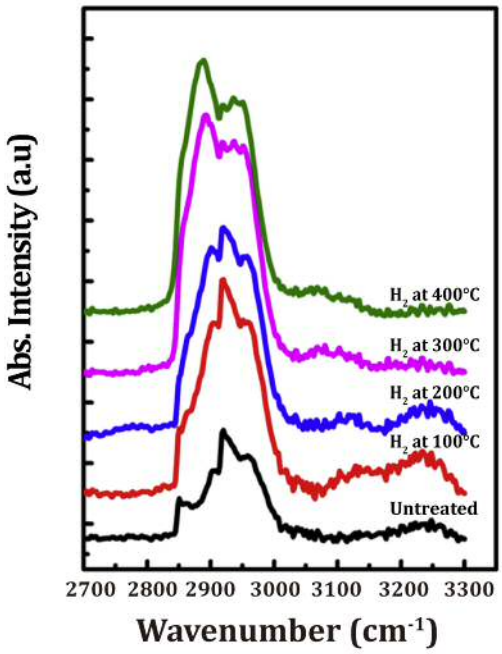

Figure 4.12: FTIR spectra of the CH features of untreated UDD and hydrogen annealed UDD at different temperatures, ranging from 100°C to 400°C. Reprinted from [134] under a Creative Common License, http://creativecommons.org/licenses/by-nc-nd/4.0/. https://doi.org/10.1016/j.carbon.2016.09.019

can be found in [134]) by the following free-radical reaction, proposed by *Ahmed et al.* [134]:

$$\cdot C \equiv C - \bar{C} \cdot + H - H \;\rightarrow\; HC \equiv C - \bar{C} \cdot + H \; or \; H \cdot \tag{4.6}$$

As can be observed in equation 4.6, the product resulting from this reaction gives two possible free radicals so different reactions can take place, given by equation 4.7 and equation 4.8:

$$HC \equiv C - \bar{C} \cdot + H - H \;\rightarrow\; HC \equiv C - \bar{C}H + H \; or \; H \cdot \tag{4.7}$$

$$H \cdot + H - H \;\rightleftharpoons\; H_2 + H \cdot \tag{4.8}$$

However, there are three possible contributors of C_3 [139] which will slightly affect the proposed reaction. [134]

To conclude, the C_3 radical is desorbed from the UDD diamond surface at temperatures from 200°C. At 500°C, enough C_3 is present in the vacuum chamber when hydrogen gas is introduced to dissociate the molecular hydrogen, producing atomic hydrogen (H). With H reaching high kinetic energy, it interacts with the carbon surface dangling bonds, producing the C-H bond formation.qwwq

4.5.2 Particles' size characterization

As was briefly mentioned in the abstract and in section 4.3, nanodiamond particles have attractive characteristics for applications in drug delivery and imaging among others. [1,2] A specific requirement or condition that nanodiamond particles have to meet to be used in that kind of applications is that their surface has to be as homogeneous as possible (with the least surface contamination, including the presence of graphitic carbon), and have to be stable in a colloid (present a narrow size distribution). The narrow size distribution can be compromised if different charges or surface groups are present on nanodiamond particle surfaces, yielding particle agglomeration.

One of the main advantages of surface hydrogenation from the gas phase (method described above) is that hydrogenation produces a homogenised surface and a narrow particle size distribution driven by high zeta potential values. The hydrogenation process described above was the process used while this thesis was conducted and ensures the narrowest size distribution.

To check the particles' size distribution, colloids from the treated nanodiamond particles are prepared as described in *Williams et al.* [96] Figure 4.13 shows the DLS size distribution for untreated nanodiamond particles and hydrogenated nanodiamond particles (taken from [96]), after being subjected to different centrifugation accelerative forces. As seen in figure 4.13a), for untreated nanodiamond particles the prevailing particle'size measured by DLS is over 100 nm, independently of the centrifugation speeds or cycles whereas the hydrogen treated particles present a size distribution around 2nm-4nm after centrifugation at 10000 rpm. This result confirms the particles' deagglomeration with the effective low temperature hydrogenation process.

Colloids prepared using hydrogen treated diamond nanoparticles are used in our laboratory for applications involving particles and diamond film growth, so the particles' size distribution should be frequently checked. Although these colloids are stable over long durations, it is wise to measure the particles' size, as further centrifugation can be required

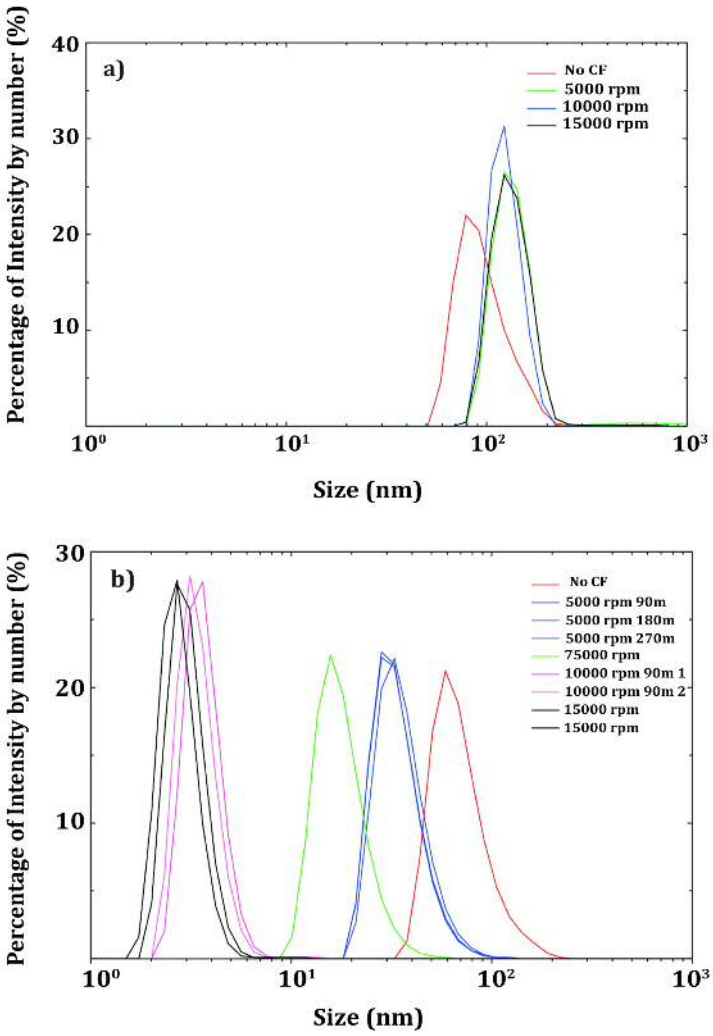

Figure 4.13: Particles' size distribution of the detonation diamond particles. a) Size distribution of the untreated detonation diamond particles after centrifugation at different acceleration speeds and b) size distribution of the hydrogenated detonation diamond particles. Reprinted from ACS Nano, 4 (8), Williams. O. A. et al., "Size-Dependent Reactivity of Nanodiamond Particles", 4824-4830, Copyright (2010), with permission from American Chemical Society

from time to time to remove aggregates. Although dynamic light scattering is the most standard and accurate method to check particles' size distributions, is limited to highly spherical nanoparticles with narrow size distributions. [49] For detonation diamond particles and commercial nanodiamond particles, size is determined by DLS as these particles produce a quite narrow size distribution. However, for particles produced following milling strategies, another techniques could also be used for comparison as particles obtained with these techniques will have broader size distribution.

As was detailed in the *Experimental Methods* chapter, in DLS, the particle size is determined from intensity fluctuations in the Rayleigh scattering off a volume of the particles (assuming particles' sizes below the wavelength). As the intensity of Rayleigh scattering is proportional to d^6, being d the particle's diameter, the presence of large particles or aggregates can mask the measurement over smaller particles in the same colloid. [140] According to *Bryant G. et al*, for a bimodal distribution of particles, the ratio limit (diameter ratio) for accurately size detection is 2:1. [141]

Scanning probe techniques such as AFM have proved to be powerful techniques in terms of resolving capabilities, and three dimensional resolution. [142] However, artifacts produced from the tip convolution can lead to inaccurate size' values and if two separate size distributions are present in the sample, an unreliable ratio of nanoparticle sizes used in the nanoparticle mixtures could be measured, as deposition/drying methods may skew the size distribution. On the other hand, microscopy techniques like TEM, allow measurements with high resolution allowing accurate and detailed morphology and structure characterization at the same time. [143] However, in TEM the sample observed only represents a small fraction of the total sample.

As a consequence, size calculation from samples containing bimodal or multimodal size distributions is a challenge and the use of different techniques for size determination can reveal remarkable differences. [144] For all these reasons, the use of alternative methods for the particles' size characterization is important, mostly for colloids in which polydisperse sizes' distribution are present. A method in which particles' size can be determined in a colloid, would be desirable as we will have information from a wider distribution. Such a method is known as nanoparticle tracking analysis or NTA (explained in the experimental methods chapter) [144] and relies on the simultaneous tracking of particles in a colloid.

Both DLS and NTA have been extensively used during this thesis and particles' size measurements will be specially important in chapter five, based on the production of diamond nanoparticles with colour centres from diamond films.

4.5.3 Zeta Potential

As introduced in 4.4, the zeta potential value over a pH range is a clear indication of the stability of a colloid, and depends on the surface groups bonded to the nanodiamond particles' surface. As a reminder, colloids' stability is defined as absolute zeta potential values greater than 30mV.

Figure 4.14 shows the zeta potential versus pH for air annealed and hydrogen annealed diamond nanoparticles, as well as for SiO_2 nanoparticles. The graph has been obtained from [71]. High positive zeta potential values are observed for hydrogenated detonation diamond nanoparticles from pH values ranging from pH 3 to pH 8, being stable in that range. On the other hand, air treated detonation diamond nanoparticles show strong negative zeta potential values that results in high colloid stability from pH 4 to pH 11. For SiO_2 particles, a slightly basic behaviour is seen at low ph values ($< pH4$) whereas these particles have an acidic behaviour for $pH > 4$.

Negative zeta potential values are well understood. For example, in untreated powders, most of the diamond surface is covered by oxygen containing groups, such as carboxyl, carbonyl, alcohol and ethers, generated during particles' production and cleaning methods. The negative zeta potential can be explained due to the dissociation of these carboxyl (COOH) and carbonyl (C=O) groups in the diamond particles' surface. [106]. Negative zeta potential values are also present in air annealed particles. Air annealing treatments have been thoroughly used not only to remove the non-diamond content on the particles' surface, but also to oxidize diamond particles' surfaces. [102, 106] This treatment allows the creation of the aforementioned oxygen containing groups. The dissociation of these COOH and C=O groups present on the diamond particles' surface lead to negative zeta potential values, which become less negative at low pH due to a higher hydrogen ion concentration at acidic pH values.

On the other hand, the origin of positive zeta potential has been controversial, and several models have been proposed to explain it. However, in this section this origin will not be explained. A complete explanation supported by different techniques will be studied in the following section 4.6.

Finally, negative zeta potential values are also observed for SiO_2 nanoparticles, as will be observed for any silicon dioxide surface (Si substrates, quartz substrates). The awareness of the zeta potential values will have profound implications for CVD diamond growth and subsequent applications. As it is well known and was explained in previous chapters, the use of diamond seeds on non diamond surfaces is mandatory to create high nucleation density allowing the coalescence of thin diamond films. [145, 146] The commonly used silicon substrates will repel particles with negative zeta potential whereas particles with positive values will be electrostatically attracted to surfaces presenting negative zeta potential ones.

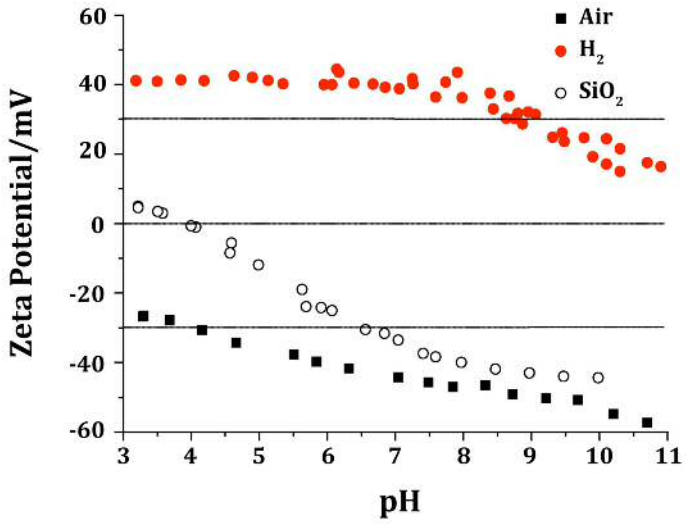

Figure 4.14: Zeta potential measurements over a pH range, for hydrogen and air annealed detonation diamond particles and untreated SiO_2 nanoparticles, measured by dynamic light scattering. Reprinted from Chemical Physics Letters, 509/1-3, Hees. J et al., "Electrostatic self-assembly of diamond nanoparticles", 12-15, Copyright (2011), with permission from ElSevier

4.6 Microdiamant 50 nm particles results

As was previously described in section 4.5, the low temperature hydrogenation process for detonation particles deagglomeration was proved and an explanation for the mechanism behind low temperature hydrogenation was proposed and corroborated for the first time. However, the mechanism was only seen on detonation diamond particles, but not on larger size nanoparticles.

Furthermore, positive zeta potential values seen in hydrogenated UDD at low temperature, were to date, poorly understood within the literature. To try to overcome these issues, commercial 50 nm diamond nanoparticles were subjected to six different annealing treatments.

The first treatment consisted of an air treatment which was performed heating the diamond particles in a furnace under air atmosphere at 480°C for 5 hours. The second treatment was a molecular hydrogen gas treatment in which the diamond nanoparticles were annealed in hydrogen gas (hydrogen gas was flowed at 100 sccm) at 500°C and at 10 mbar for 5 hours. [96] As the hydrogenation process at low temperature was previously shown to be possible because of the sp^2carbon presence, sp^2carbon was intentionally created on 50 nm diamond nanoparticles by annealing the particles at high temperatures in vacuum in the third treatment. The diamond particles were heated in vacuum ($1x10^{-3}$mbar) at 1000°C for 2 hours. The same vacuum annealing treatment was performed to another set of nanodiamond powder, but after the 2 hours of vacuum annealing treatment, the particles were cooled down to 500°C and a molecular hydrogen treatment under the same conditions as explained before was performed. In the last treatment, the diamond particles were first annealed in air (480°C, for 5 hours) and then the vacuum annealing followed by hydrogen treatment was conducted. Finally, untreated diamond nanoparticles powder was also studied.

In order to characterize diamond nanoparticles, some powder from each different treatments was kept and some powder was used to prepare colloidal dispersions. Aqueous colloids were prepared from the above-mentioned treated powders by dispersing 0.1 g of powder in 200 ml of deionized water. The colloids were dispersed via high power ultrasound (Sonics Vibra-cell VCX 500) at 200W (3 s on 2 s off duty cycle) for five hours and the colloids temperature was kept below 20°C. All the solutions were decanted after been settled for 24 hours, to remove any large sonotrode contaminants. The solutions were centrifuged at 20000 g at 10°C in a Sigma 3-30 KS centrifuge. Once the colloids for the

different powders were prepared, the powders were characterized by the methods detailed in the following sections.

4.6.1 Particles' size characterization

Particles' size distribution was obtained from the colloid prepared from the air treated diamond powder. All the colloids were prepared from powders with the same particles'size distribution, and as particles' aggregation is not expected for the standard pH (5.8), for the rest of the colloids only quick dynamic light scattering (DLS) measurements were performed. The colloid was prepared as explained in the previous section. Two different methods for the determination of the particles' size were used. In the first one, the particles were characterized by dynamic light scattering (DLS) after 10 minutes centrifugation at 20000g. Several accelerative forces (from 5000g to 50000g) were also applied to the samples with identical results, confirming the monodisperse nature of the colloid. The *Malvern Zetasizer Nano ZS* (described in the experimental chapter) equipped with a 633nm laser in backscattering configuration (173°C) was used.

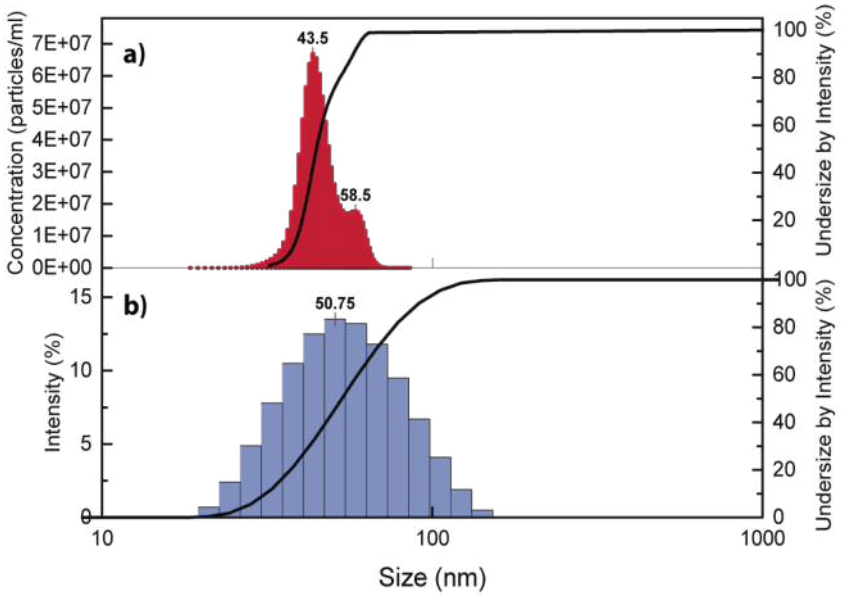

Figure 4.15: Particles' size distribution of the air treated colloid. a) NTA size distribution and b) DLS size distribution. Reproduced from [147] with permission from the Royal Society of Chemistry.

As can be seen in 4.15b), the sample's size distribution median is 50.75 nm. To confirm the particles' size distribution, a second characterization method based on nanoparticle tracking analysis (NTA) was used. A *Malvern Nanosight LM10* (described in the experimental chapter) equipped with a 635 nm laser was used. NTA gives a more precise measure as individual particles can be tracked. The particle size distribution measured by NTA is plotted in 4.15a). A slightly bimodal distribution can be observed, with two clear particles' size distributions at 43.5 nm and 58.5 nm. The concentrations of particles in the colloid is in the order of 10^7 particles/ml. The colloid was previously diluted until the required concentration was achieved usually between 10^7-10^9 particles/ml). [49,50] In both DLS and NTA graphs, the cumulative undersize distribution is also represented on the right axis. This distribution reflects the percentage of particles below the corresponding size, indicated in the x-axis, and it is quite useful if a multimodal distribution of particles' sizes is present.

In both methods, the obtained size is the hydrodynamic radio, usually bigger than the size measured in the dried particles. Notwithstanding, the particles' size value is in accordance with the value given by the commercial powder supplier, 50 nm.

4.6.2 Transmission Electron Microscope (TEM)

TEM measurements were also performed to confirm the particles' size and the structural change in the diamond nanoparticles' surface. TEM specimens were prepared by dispersing the powders in ethanol via ultra-sonication and the solutions were drop cast onto a perforated-carbon TEM grid. Bright field and high resolution transmission electron microscopy images were recorded in a *FEI Titan*^{3} with a spherical aberration corrector. Low working voltage (80 kV) was used in order to avoid undesired diamond nanoparticles' surface graphitization or sample contamination. As is well known, the electron beam can induce the formation of a graphitic-like outer shell, [148] and can also promote volatile carbon species present in the sample to be re-absorbed into other areas of the sample. [143, 149] In this thesis, TEM measurements were performed in order to observe diamond nanoparticles' surface graphitization (intentionally created), so the working voltage must be selected carefully, avoiding high voltage values.

As the particles that will present more morphological changes in their surface will be the ones after the vacuum annealing, just three of the treated powders were imaged. The first one was the untreated diamond powder, the second one the vacuum annealed powder, and

the last one was the powder after the vacuum annealing treatment followed by hydrogen annealing.

4.16a) shows a bright field image of the dispersed untreated particles with sizes ranging from 30 nm to 50 nm. As can be observed, particles exhibit facets. These results are in accordance with the particles' size measured previously by DLS and NTA. In 4.16b), a HRTEM image of an oriented diamond nanoparticle's detail is shown. Most of the particles imaged presented a crystalline diamond core, however some of them showed an amorphous outer shell surrounding the diamond core. Diamond nanoparticles' surface strongly depends on their production methods (as described before) and non-diamond areas (sp^2) are commonly present on the surface, particularly in detonation diamond (DND), [85, 96] but also larger particles. For most applications, such as improvement of the optical properties of colour centres in diamond, [105] a homogenised diamond surface is desirable. A lot of studies have been performed to control the sp^3/sp^2 ratio, trying to remove all the sp^2 carbon for subsequent diamond's surface functionalization. [102]

On the other hand, the presence of sp^2 carbon can lead to the diamond surface's reconstruction. sp^2 carbon in the form of graphitic-like carbon or amorphous carbon is highly reactive and can promote the diamond nanoparticles' surface functionalization. [106] It has been demonstrated that the presence of sp^2 carbon on diamond nanoparticles surfaces plays an important role in the diamond surface hydrogenation at low temperature. [96] The C-H bond formation in the diamond nanoparticles surface at low temperature (500°C) was rather unusual as the conventional methods require high temperatures (>2000°C) to dissociate the hydrogen gas. [150] However, it was recently proved that even at low temperatures the sp^2 carbon can be desorbed as a gas phase of carbon radicals such as C_2 or C_3, allowing the reaction between the C_3-H_2 and so promoting the production of atomic hydrogen and C-H bond formation. [134] Previous results showed detonation diamond nanoparticles' surface hydrogenation at temperatures low as 300°C, but the same treatments were unsuccessful for larger particles, as they present less sp^2 on their surface, and sp^3 bonds are not reactive at such low temperatures.

However, vacuum annealing at high temperatures (1000°C) can promote surface graphitization [151] around the diamond nanoparticles core, allowing the subsequent low temperature surface hydrogenation. 4.16c) shows the second sample, the diamond nanoparticles powder after the vacuum annealing treatment. The TEM image shows several diamond nanoparticles after being vacuum-annealed at 1000°C. The particles present a well-defined diamond core and an outer shell in which graphitization (arrows' marked) can be clearly

observed, with a space between the graphitic layers of 0.34 -0.35 nm. The last image, 4.16d), corresponds to the particles after the vacuum annealing and the hydrogen atmosphere treatment at 500°C. Not much change can be seen, and the TEM image also shows diamond nanoparticles covered by a graphitic shell.

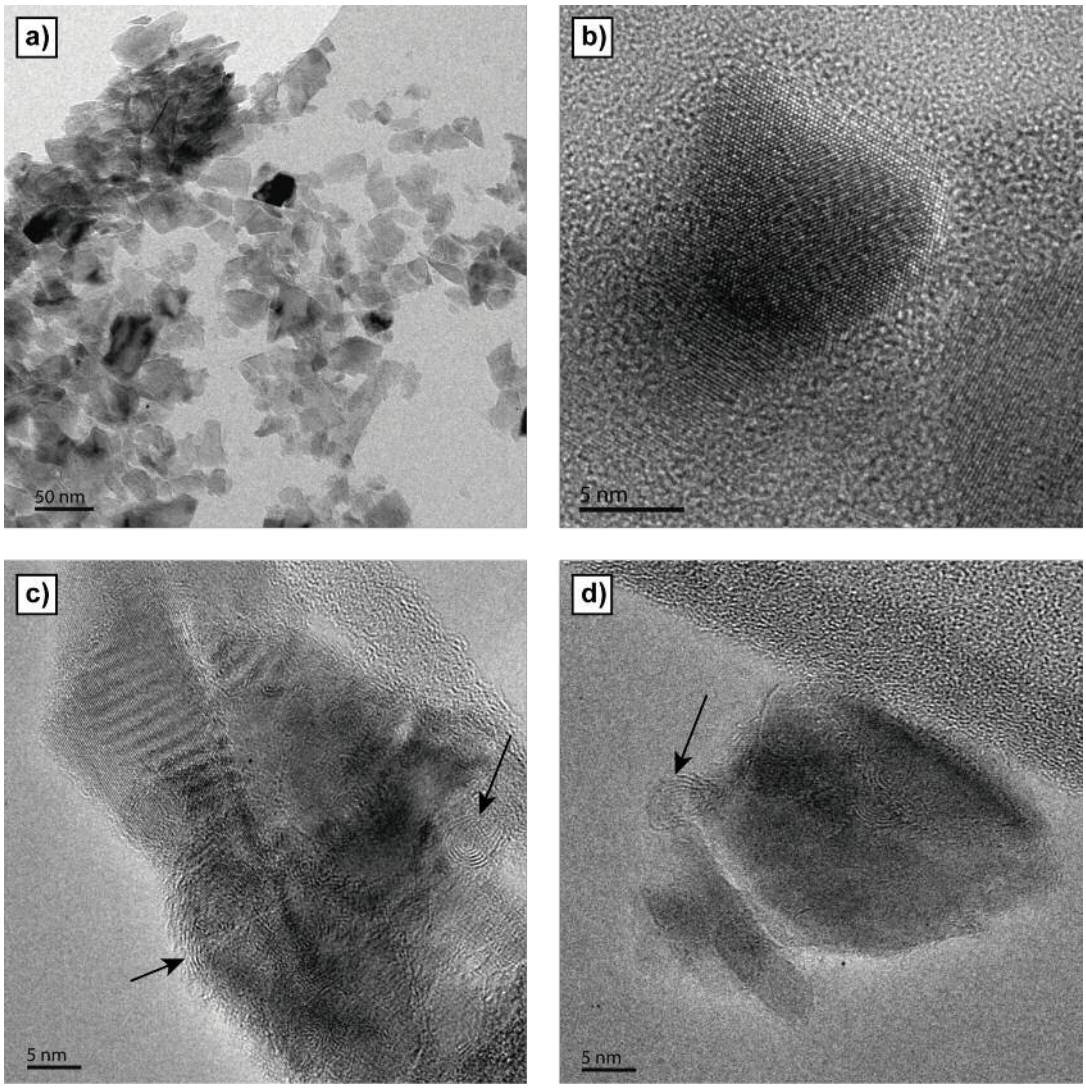

Figure 4.16: Unfiltered Transmission Electron Microscope images of the particles. a) Bright field image of the as received 50 nm particles, b) high resolution (HRTEM) image of the as received 50 nm particles, c) HRTEM of the vacuum annealed particles and d) HRTEM image of the hydrogenated particles. Reproduced from [147] with permission from the Royal Society of Chemistry.

TEM is a powerful tool to resolve the atomic structure of materials, but the main purpose of using TEM in this thesis was to confirm particles' size and surface' graphitization.

However, in general, the major aim of performing different annealing treatments to diamond nanoparticles is to change the surface groups present in the particles' surface and

to study how these groups affect diamond nanoparticle properties. The easiest way of identifying different surface functional groups is by FTIR technique (described in the experimental method chapter). In section 4.5, FTIR measurements were performed to study the hydrogenation process and will be explained in the following subsection.

4.6.3 Raman Spectroscopy and Fourier Transform Infrared Spectroscopy

Raman studies were also performed on the samples to confirm diamond quality and surface graphitization. As it is well-known, diamond can be graphitized at elevated temperatures. The graphitization temperature will change with particle' size. [152, 153] For instance, detonation diamond particles (5nm) can be fully transformed from diamond to onion-like carbon at 1400 °C, and this temperature will increase with size. The annealing treatment conducted in our samples was performed at 1000°C as we wanted to intentionally introduced sp^2 carbon but preserve the diamond properties.

The graphitization of the diamond nanoparticles was confirmed by Raman measurements. Raman measurements were recorded in an inVia Renishaw confocal Raman microscope equipped with a 532 nm laser. All the measurements were acquired using the same parameters: 10 seconds acquisition time, 50 accumulations, and 10% laser power. Figure 6.10 shows the Raman spectra of the different treated diamond powders.

All spectra show a clear first-order diamond peak at 1332 cm^{-1}, broader and less intense for the powders that have been vacuum annealed. Figure 4.17a) shows the Raman spectrum for the untreated powder. Apart from the intense and narrow diamond peak at 1332 cm^{-1}, a broad band at 1550 cm^{-1} confirms the presence of sp^2 sites. This band, known as G-band, is due to the bond stretching of all pair of sp^2 atoms in both rings and chains. [154, 155] In figure 4.17b) the diamond powder after the air annealing treatment is shown. As can be seen in the graph, the G-band is still present in this sample although air annealing treatments promote the sp^2 bonds removal in diamond particles' surface. [102, 106] Sp^2 bonds removal is dependent on air annealing temperature. For detonation diamond, successful graphitic sp^2-bonded carbon removal is accomplished between 425°C and 460 °C. [102, 156] Higher temperatures will result in material's weight loss due to sp^3 carbon burning. However, higher temperatures are needed for sp^2 carbon removal of 50 nm diamond nanoparticles. The air annealing treatment in this case was performed at 480 °C so it is possible that sp^2-bonded carbon is still present in the sample, as confirmed by Raman. Hydrogen gas treatment (figure 4.17c) also shows a prominent G-band.

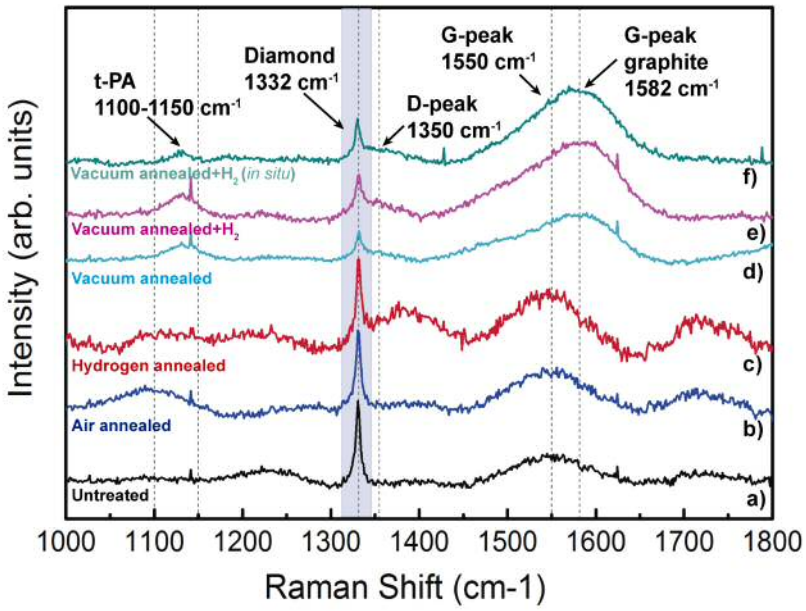

Figure 4.17: Raman spectra of the different treated powders. a) Untreated diamond powder, b) Air annealed powder, c) hydrogen treated powder, d) vacuum annealed powder, e) vacuum annealed powder followed by molecular hydrogen treatment and f) same as e) with the powder kept in vacuum between the vacuum annealing and the hydrogen treatments. Reproduced from [147] with permission from the Royal Society of Chemistry.

Different Raman characteristic peaks are present in the samples that have been previously vacuum annealed (figure 4.17 d)-f)). The diamond peak is still present although it is slightly shifted to lower frequencies and is less intense and broader than in the previous treatments. This is because diamond powders can undergo a phase transition from diamond to graphite under annealing processes, as explained before. [157] Three different peaks arise. The first and broad peak appears between 1100 cm^{-1} and 1150 cm^{-1}, and has been related to sp^2 structures known as trans-polyacetylene structures. [158] Trans-polyacetylene modes are related to the presence of hydrogen. [159] Although molecular hydrogen wasn't introduced in the chamber while annealing the sample (figure 4.17d)), hydrogen was present in the vacuum annealed sample as molecular hydrogen can be desorbed from the vacuum chamber walls. [160] The second peak, around 1350 cm^{-1}, corresponds to the well-known D-peak, and is due to breathing motion of sp^2 rings. [155] The third emergent peak is located at 1582 cm^{-1} and is characteristic of graphitic-like materials, clearly indicating that graphitic structures have been formed after the annealing at 1000°C. [161]

FTIR measurements were performed to determine the surface complexes, and all the spectra are shown in figure 4.18 and figure 4.19. For the FTIR measurements all the treated powders were prepared as previously described and were transferred to a UHV chamber. [134] FTIR measurements were conducted *in-situ* and chamber base pressure was maintained around 5x10^{-7} Torr. In order to eliminate loosely bonded hydrocarbons originated from air exposure, all the samples were annealed using electrically controlled heating device under UHV at 200°C and 550°C and the spectra were collected using a Bomem MB154 FTIR with MCT-liquid nitrogen cooled detector. The resolution was set to be 4 cm^{-1}, and 400 scans were used. To avoid IR background signal from the elevated temperatures, annealed samples were cooled down to room temperature for the measurement. All the measurements were performed in Taiwan, in National Dong Hwa University, by our collaborators Prof. Chia-Liang Cheng and Ashek-I- Ahmed.

Room temperature samples' spectra were also measured to compare hydrocarbon contamination.

In figure 4.18, FTIR measurements for the different powders at the three different temperatures recorded are shown. As samples were exposed to air between the annealing treatments and the FTIR analysis, hydrocarbon-related C-H features are present. These features appear for the non-treated sample, the air-annealed sample and the hydrogen treated sample. The C-H peaks disappear after heating at 550 °C, clearly indicating that this peak is hydrocarbon related.

As can be observed, there is a significant difference between the powders annealed in vacuum at 1000°C (figure 4.19 d-g) and those that were not annealed (figure 4.19 a-c). For all the samples, the first band region with noticeable peaks is between 1000 cm^{-1} and 1300 cm^{-1}. This broad band is generally associated with C-O-C stretching vibrations of cyclic ether. [162] Moreover, two distinguishable broad peaks are observed in the region between 1250 cm^{-1} and 1500 cm^{-1}. The peak at 1265 cm^{-1} is attributed to CO bending vibration, and the peak between 1380 cm^{-1} and 1440 cm^{-1} corresponds to the asymmetric –CH bending vibration. These two peaks are due to the presence of the ester group (CH_3-COOR), which is evident in the sample shown in 4.19 (b). The CO intensity is significantly reduced in the samples annealed in vacuum and thus followed by hydrogen treatment (figure 4.19 d-g). This peak's intensity reduction indicates the -CO desorption / substitution by H during ND annealing at elevated temperature. [163] As is well known. at high temperatures, oxygen containing groups can be desorbed and decomposed, resulting in formation of CO and CO_2. [164] However and although different techniques such as

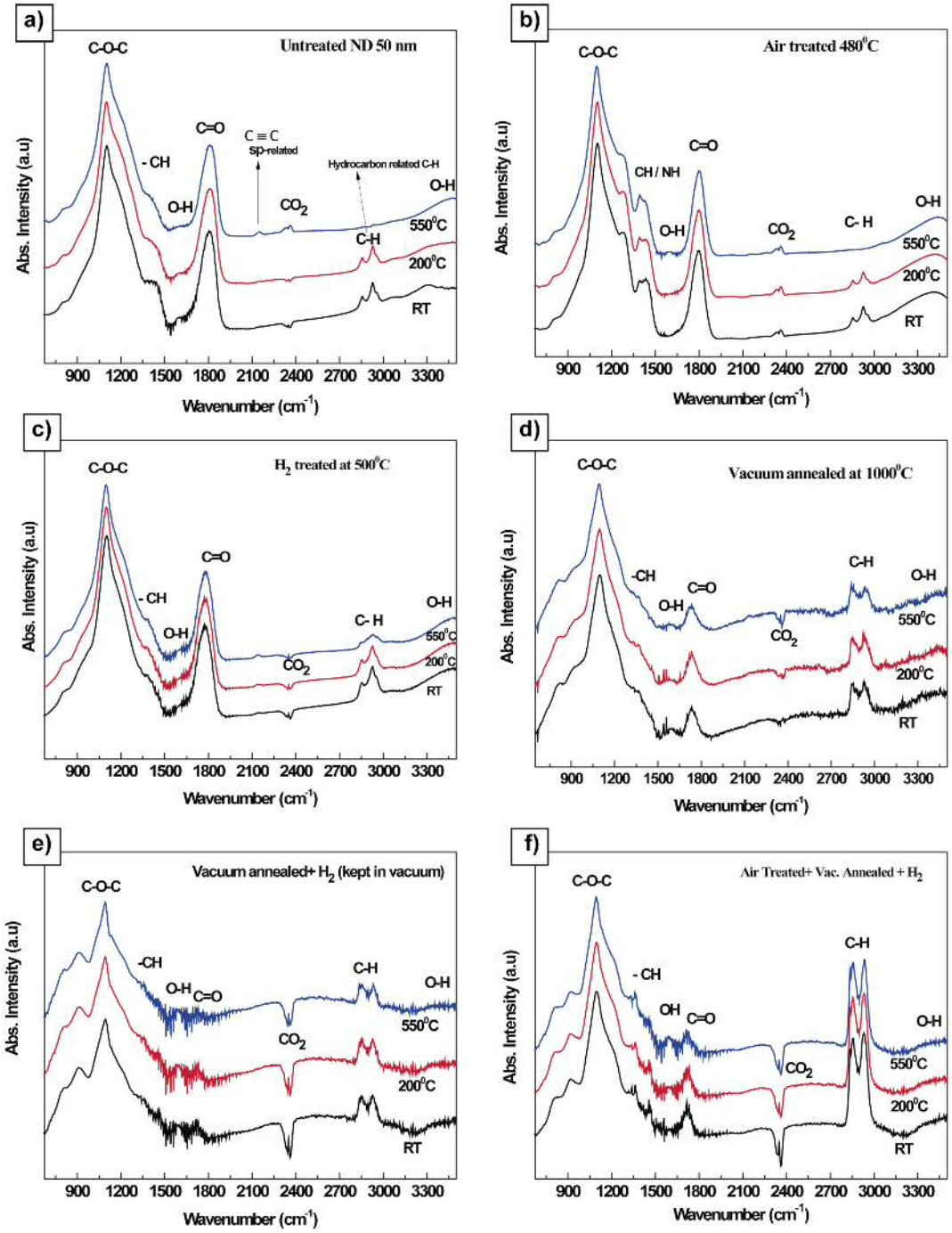

Figure 4.18: FTIR spectra of the different treated diamond powders for three different temperatures. a) Untreated diamond powder, b) Air annealed powder, c) hydrogen treated powder, d) vacuum annealed powder, e) vacuum annealed powder followed by molecular hydrogen treatment (kept in vacuum) and f) air treated followed by e) treatment. Reproduced from [147] with permission from the Royal Society of Chemistry.

FTIR, XPS or temperature programmed desorption (TPD) have been used to identify the groups from which CO and CO_2 are desorbed, the identification of such groups remains a challenging task, with the main conclusions summarized in [112]. Furthermore, the range of thermal desorption/decomposition of each oxygen-related surface group (ranging from 500K-1100K) [165] will depend on both surface group environment and on the crystal or facet orientation (in the case of diamond particles).

Another remarkable difference in the form of peak reduction is observed between vacuum annealed samples followed by H treatment and the non-vacuum annealed samples. This is observable in the band range from 1600 cm^{-1} to 1800 cm^{-1}. The broad peak centred at 1778 cm^{-1} corresponds to C=O stretching modes, and demonstrates the presence of carboxyl groups mainly. As what happened with the peak corresponding to the CO bending vibration, the C=O peak intensity is reduced in the samples after the vacuum annealing treatment. If the C=O peak's maximum of the non-vacuum annealed samples and the vacuum annealed one is compared, the latest presents a peak maximum around 1711 cm-1 which was also observed by *V.L Kuznetsov and Y.V. Butenko* who assigned this peak to C=O stretches in ketonic groups. [112] The C=O peak completely disappears after the vacuum annealing/hydrogenation process as explained for the -CO peak intensity reduction. [163, 166]

A small intensity peak appears also at 1620 cm^{-1}. This peak is associated with –OH bending vibration due to the presence of water outside environment or due to the carboxyl group (-COOH) on ND surface. The corresponding –OH stretching mode is a wide band observed between 3200 cm^{-1}-3600 cm^{-1}.

Another meaningful change is observed on the band ranging from 2800 cm^{-1}-3000 cm^{-1} shown in figure 4.19 (b). The hydrogenation of nano-diamond particles surfaces is confirmed with the presence of the C-H stretching modes. However, strictly speaking, this band region contains information not only about the interaction between hydrogen and diamond (sp^3), but also includes information about hydrogen bonded to different carbon species (different electronic configurations such as sp^2). The C-H stretching characteristics are observed in the 50 nm diamond nanoparticles after vacuum annealing, so C-H peaks could correspond to hydrogen bonded to sp^3 or sp^2carbon. As mentioned in section 4.5, for hydrogenated particles, the carbon-hydrogen interaction/bonding is anisotropic and depend on crystal orientation, which translated into frequencies results in a frequency shift. Frequency shifts also result from H bonded to different local environments or for the presence of different CH_x groups. [167] According to the literature, C-H stretching

features of H bonded to sp^2appear above 2950 cm^{-1} whereas H bonded to sp^3 signatures appear below 3000 cm^{-1}. [167, 168] However, this distinction is quite ambiguous and the C-H stretching features corresponding to sp^2or sp^3 carbon is not clear in the community.

In this case, two clear peaks at 2860 cm^{-1} and at 2934 cm^{-1} are observed in figure 4.19 d-g. In detonation diamond, these peaks appear at 2870 cm^{-1} and 2940 cm^{-1}. [136] The peak at 2860 cm^{-1} corresponds to C(110):H mixed with C(111):H, and the peak at 2934 cm^{-1} for C(100):H. [134] Besides those peaks, a clear sharp peak of C (111): H, plane adjacent with C (110): H, is also present at 2835 cm^{-1} and it is relevant for large size ND.

As previously mentioned, the mechanism responsible for diamond particles hydrogenation is the catalytic reaction between carbon radicals and hydrogen molecules. [134] C_2 and C_3 carbon radicals are available after desorption of intentionally created sp^2 carbon through vacuum annealing at 1000°C. This result indicates the effect of sp^2 carbon on hydrogen dissociation as –CH peaks are not formed on the sample shown in figure 4.19 (a-c). It is noted that for the sample in figure 4.19 d) annealed at 1000°C in vacuum without the external source of hydrogen in chamber, -CH is formed through the interaction of hydrogen desorbed from chamber wall at elevated temperature (> 500°C).

Besides the low temperature hydrogenation shown by the samples after the vacuum annealing treatment, the most interesting result is the change in zeta potential observed in the same samples, explained in the following subsection.

4.6.4 Zeta potential

As briefly advanced in section 4.5, while the origin of negative zeta potential is well understood, the origin of positive zeta potential is controversial and few examples were found within the literature. It has to be clarified that this thesis has been focused only on positive zeta potentials on nanodiamonds surfaces without the addition of any functionalised groups, or molecules.

The positive zeta potential in nanodiamonds is both controversial and unusual. Although there are some models that try to explain this positive zeta potential origin, they generally assume a pristine (sp^2free) diamond surface. [169,170] However this assumption is directly contradicted by *Härtl A. et al.* as positive zeta potential is never seen on bulk diamond surfaces. [171] *Härtl A. et al.* measure the surface zeta potential by streaming potential measurements demonstrating that the zeta potential of both hydrogen and oxygen

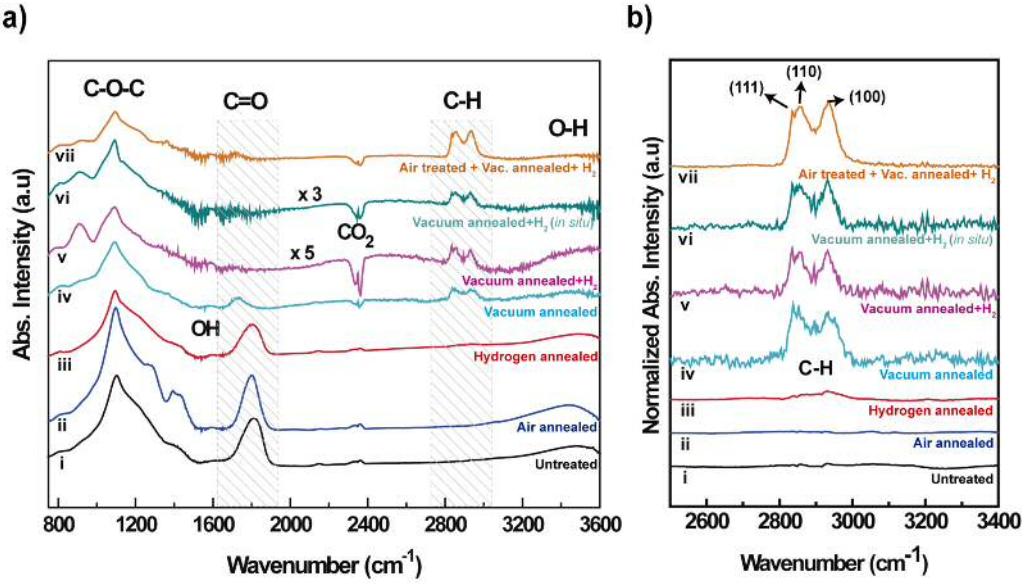

Figure 4.19: FTIR spectra of the different treated diamond powders. a) Untreated diamond powder, b) Air annealed powder, c) hydrogen treated powder, d) vacuum annealed powder, e) vacuum annealed powder followed by molecular hydrogen treatment, f) same as e) with the powder kept in vacuum between the vacuum annealing and the hydrogen treatments and g) air treated powder followed by e) treatment. Reproduced from [147] with permission from the Royal Society of Chemistry.

terminated bulk diamond is negative over the whole pH range. [171]

Figure 4.20 shows the zeta potential versus pH for the different colloids, prepared as detailed in 4.6. Zeta potential measurements and pH titration measurements were made in the *Malvern Zetasizer Nano ZS*, using the MPT-2 autotitration accessory. 0.1 M HCL and 0.1 M of NaOH were used as acid and base titrants. Zeta potential measurements are the average of 3*100 scans. The colloids were de-gassed by nitrogen flow.

The zeta potential value is strongly dependent on the particles' treatment used, due to the presence of different functional groups in the diamond nanoparticles' surface. [91,172]

In this thesis, negative zeta potential values were measured in the colloids prepared from powders previously annealed in air, in molecular hydrogen, and after a vacuum annealing at 1000°C. The colloid obtained from air treated powder shows the most negative zeta potential, with values ranging from -35mV at pH 3 to -55mV at pH 11, being stable in the whole range of pH (colloids stability is defined as absolute zeta potential values greater than 30mV).

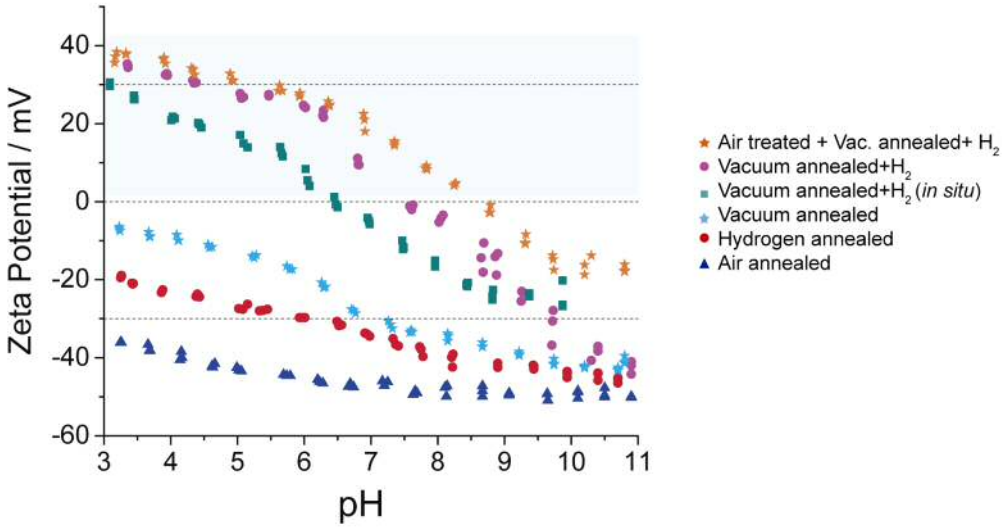

Figure 4.20: Zeta Potential vs pH of the different colloids prepared. a) Air annealed powder, b) molecular hydrogen treated powder, c) vacuum annealed powder, d) vacuum annealed powder followed by molecular hydrogen treatment kept in vacuum e) same as d) but the powder was taken from the vacuum chamber after the annealing treatment, and f) air treated powder followed by a vacuum annealing treatment and a molecular hydrogen treatment. Reproduced from [147] with permission from the Royal Society of Chemistry.

Air annealing treatments have been thoroughly used not only to remove the non-diamond content in the particles' surface, but also to oxidize diamond particles' surfaces. [102, 106] This treatment allows the creation of the aforementioned oxygen containing groups. The dissociation of these COOH and C=O groups present in the diamond particles' surface lead to negative zeta potential values, which become less negative at low pH due to a higher hydrogen ion concentration at acidic pH values.

A similar trend is observed for the hydrogen annealing treatment. As confirmed in FTIR spectra, oxygen groups (C=O mainly) are still present after the hydrogen treatments, resulting in negative zeta potential values. Nevertheless, it has to be taken into account that previous works on detonation diamond show a positive zeta potential after the same molecular hydrogen treatment, but was proved to be ineffective for larger particles. [96,156] Again, this is due to the difference in non-diamond content (sp^2) present in the detonation diamond particles 'surface, and in the 50 nm diamond particles' surface, and can be explained in terms of the basicity of carbon surfaces. [173] Last, the vacuum annealed

sample also shows a slightly less but still negative zeta potential. As mentioned before, annealing the sample at high temperatures, produces the desorption of oxygen containing groups (preferentially in nanodiamond particles) with subsequent nanoparticles' surface reconstruction/graphitization. However, an incomplete oxygen group desorption can occur as well as a re-deposition process in the form of graphitic carbon, leading to the observed values of zeta potential. [100, 112]

On the other hand, positive zeta potential values were observed in the samples subjected to vacuum annealing followed by hydrogen annealing treatments. The origin of positive zeta potential values observed can be explained and further understood and sustained by back titrations measurements, explained below.

Reverse titrations were measured preparing aqueous colloids of mass/volume concentration 1% and diluting by 1:10 seven/eight times whilst monitoring the pH versus time until it stabilised. The pH was measured by a Mettler Toledo. The colloids were de-gassed by nitrogen flow as was the de-ionised water used for dilution.

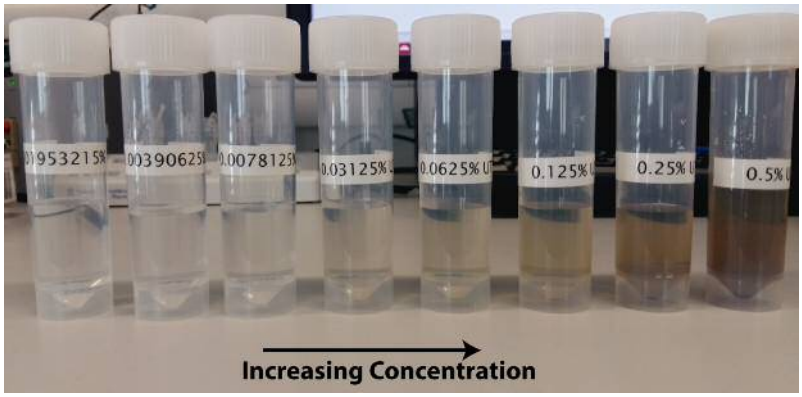

Figure 4.21: Photography of different dispersions prepared for back titration measurements. The image corresponds to the untreated diamond powder, with increasing concentration from left to right.

Back titrations of the various surface treatments are shown in figure 4.22 a). It is clear that the air annealed sample shows the strongest acidity vs concentration, which is easily explained by its low concentration of sp^2 and high concentration of COOH groups. These COOH groups become de-protonated making the solution more acidic with increasing concentration of particles as well as generating a negative zeta potential as seen in 4.20. The concentration of these COOH groups is somewhat depleted by vacuum annealing or annealing in molecular hydrogen and is evidenced by their reduced acidity vs particle concentration. However, upon vacuum annealing followed by hydrogen annealing the samples exhibit clear basicity.

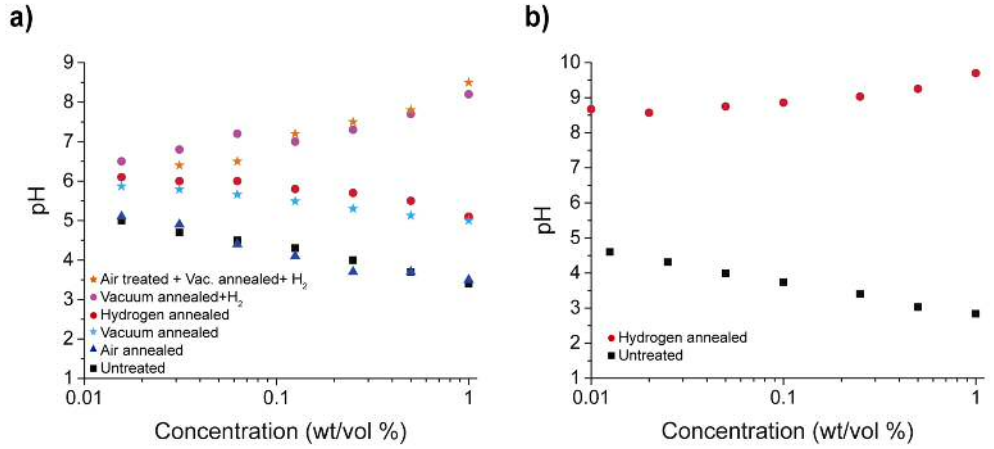

Figure 4.22: Back titrations of the different colloids prepared. a) Back titrations measurements for 50 nm particles and b) back titrations for detonation diamond particles. Reproduced from [147] with permission from the Royal Society of Chemistry.

The origin of the basicity of carbon surfaces and therefore the origin of the positive zeta potential remains unclear. An explanation found in the literature binds the basicity in carbon black and carbon-based materials with the absence of oxygen containing groups, driving off by hydrogen. [174] Nevertheless, another explanation suggests that are the oxygen-containing surface groups structures, such as pyrone-type, the ones that confer the carbon basic properties. [173, 175, 176] The strength [177] or weakness [175, 178] of pyrone-type structures as basic sites is controversial, but a relatively high amount of these structures are necessary to explain the carbon basicity, which is not the case here, as confirmed in FTIR. The positive zeta potential can also be associated with the protonation of amino groups in acidic environment. [179] But amino groups are not present in the diamond particles.

One of the most generally accepted explanation regarding the carbon basicity comes from the electron-donor-acceptor (EDA) complex. In this complex, π electron-rich regions located in the basal planes, can interact with oxonium (H_3O^+) ions. [180, 181] In other words, oxygen-free carbon sites can absorb H_3O^+ ions to provide a diamond's surface with positive charge and so basic properties. However, as these ions are bound within the slip plane they cannot explain the simultaneous positive zeta potential.

But certainly the closest explanation for carbon basicity is related to oxygen-free Lewis base sites on the basal planes within the graphene layers. [182] After annealing the powders in vacuum at high temperature (1000°C), graphite is created forming an outer-shell of the diamond core particles, and leaving oxygen-free Lewis base sites. As the graphite created

is highly reactive, the diamond powder after annealing and exposure to air can reabsorb oxygen, hence explaining the negative zeta potential of the vacuum annealed sample. However, the same samples after the vacuum annealing and hydrogen treatment present a stable basic surface, which means that after the hydrogen treatment, active sites are no longer present for the oxygen absorption. [182] This leaves particles with little or no COOH on the surface with graphitic planes exposed to the aqueous solution. These planes can become protonated by H^+ from the solution, which would simultaneously generate a positive zeta potential whilst rendering the solution basic. This would only work with samples with little oxygen and some sp^2 on the surface, as evidenced by the vacuum annealed / hydrogenated samples. A model for the positive zeta potential explanation is shown in figure 4.23.

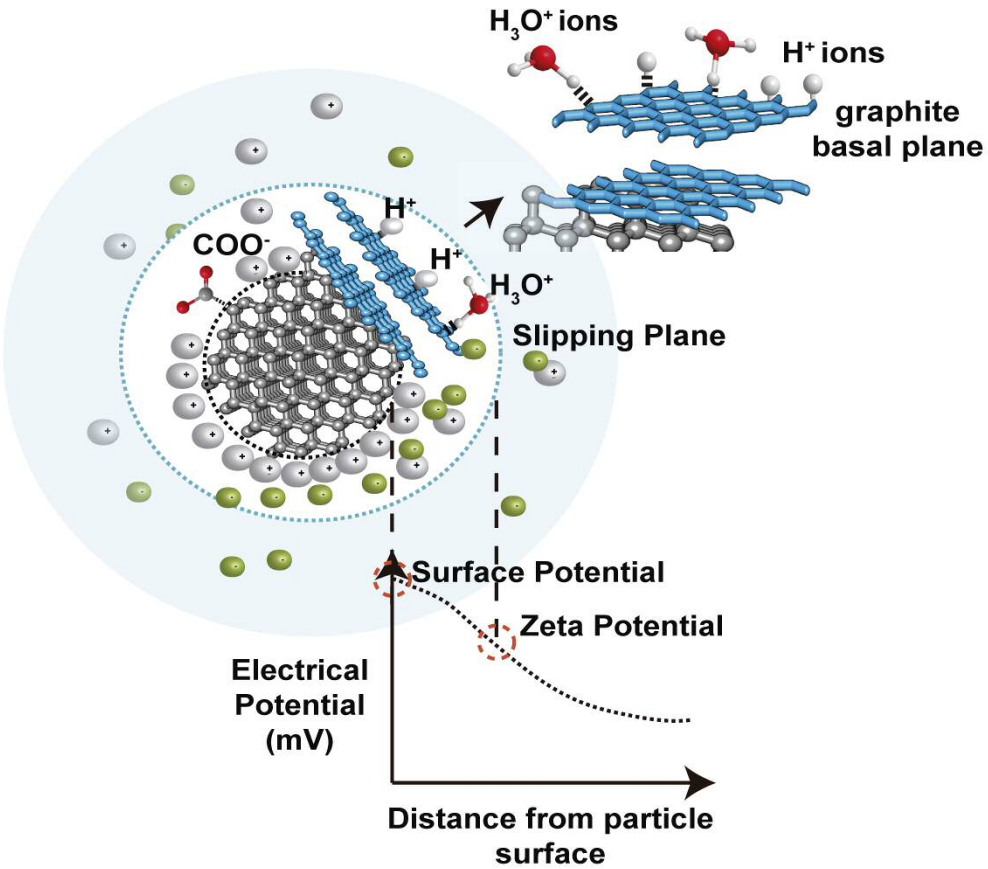

Figure 4.23: Positive zeta potential explanation model based on Oxygen-free Lewis base sites. Reproduced from [147] with permission from the Royal Society of Chemistry.

This is further evidenced by the enhanced basicity seen on detonation nanodiamond particles which have a much higher concentration of sp^2 at the surface, as seen in 4.22b). Far stronger basicity is seen, which correlates with the higher concentration of basal planes for protons to diffuse into. These detonation nanodiamond particles also exhibit a strong

positive zeta potential as previously reported. [96] The air treated particles were vacuum annealed and hydrogen treated and a colloid from this powder was also prepared. This air annealing treatment ensures that no other surface groups present in the pristine diamond particles where involved in the positive zeta potential. After the air annealing treatment, the diamond particles' surface present a homogenized surface, formed by oxygen-related groups. The subsequent vacuum annealing and hydrogen treatment allow the creation of oxygen-free basal planes and the stabilization of these sites.

4.6.5 Absorbance

As explained in the experimental method chapter, diamond is optically transparent due to its wide bandgap. However, if diamond presents high doping levels or sp^2sites, diamond absorption is increased with the creation of a pseudogap due to π-bonded carbon. [183] The formation of this pseudogap in hydrogenated amorphous carbon (a-C:H) films is widely known, with the π-π^* model originally developed for amorphous carbon.

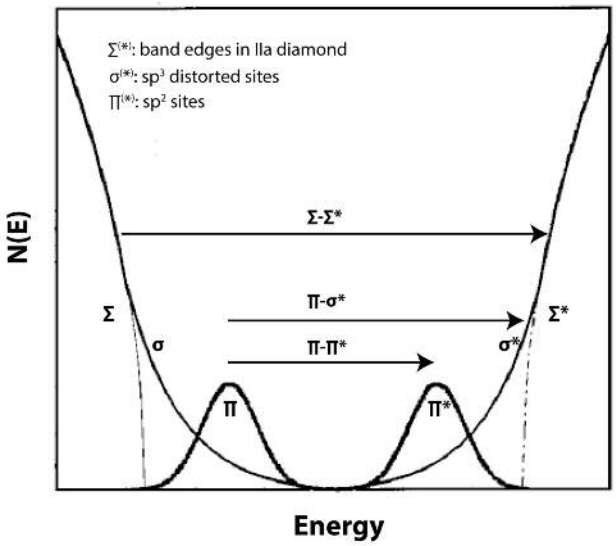

Figure 4.24: Scheme representing the density of states in diamond's gap. Optical transitions between different electronic states are marked by arrows. π and π^* bands are due to the presence of sp^2sites. "Reprinted figure with permission from : M. Nesládek, K. Meykens, L.M. Stals, M. Vaněček and J. Rosa, Physical Review B, 54, 1996. Copyright (1996) by the American Physical Society". https://doi.org/10.1103/PhysRevB.54.5552

Figure 4.24 shows a schematic model based on molecular-dynamics simulations. [61] In this model, three different transitions are considered, π-π^* and π-σ^* in amorphous carbon

regions and Σ-Σ^* which is the indirect transition between the valence band and the conduction band in diamond. This model can be extended to diamond nanoparticles containing sp^2bonded carbon.

With high detection sensitivities allowing the detection of absorbances up to 10^{-5} ppm, techniques such as Photothermal Deflection Spectroscopy (PDS) are better to measure the sp^2content, [61, 184] but sp^2can also be detected by UV-Visible Spectroscopy. [185] The π-π^* transitions and hence the presence of sp^2bonded carbon will be translated into the appearance of absorbances in the range of 180– 260 nm in carbon materials. [186]

UV-Visible measurements for 50 nm diamond nanoparticles were conducted in a *GENESYS^{TM} 10S UV-Vis Spectrophotometer* choosing scanning wavelengths from 190nm to 1100nm. 1ml of slurry was taken out of each dispersion prepared for the reverse titration measurements and was introduced in a quartz cuvette. A cuvette with DI water was used to measure the background signal. Five different slurries were measured, prepared with the untreated powder, the vacuum annealed powder, the air treated followed by a vacuum annealing and a hydrogen annealed powder, an air treated sample, and a hydrogen annealed sample. As too concentrated dispersions produce saturation in the UV-Visible detector, it was necessary to further dilute the dispersions for all the samples, following the same procedure as for the reverse titrations preparation.

Figure 4.25 and figure 4.26 show the absorbance versus wavelength for the different samples at different concentrations. A common characteristic for all of them is the absorbance increase with increasing concentration, observed for all measured wavelengths. Furthermore, the absorbance is higher in the UV region, becoming close to zero in the visible region for low concentrated samples. Two different behaviours were observed and have been represented separately in figure 4.25 and figure 4.26. Figures 4.25 a) and 4.25 b) show the absorbance for high concentrations and low concentrations respectively for the untreated sample, figure 4.25 c) and 4.25 d) represent the high and low concentrations for vacuum annealed samples, and figure 4.25 e) and figure 4.25 f) correspond to the same concentrations for the air treated followed by vacuum annealing and hydrogen annealed samples. A clear peak around 230 nm is observed in all of them, corresponding to the sp^2bonded carbon, and a peak at 960 nm, which has not been reported in the literature, also appears. However, peaks at 230 nm and 960 nm are more pronounced in the vacuum annealed sample. As seen in TEM clear graphitized areas were observed in this sample.

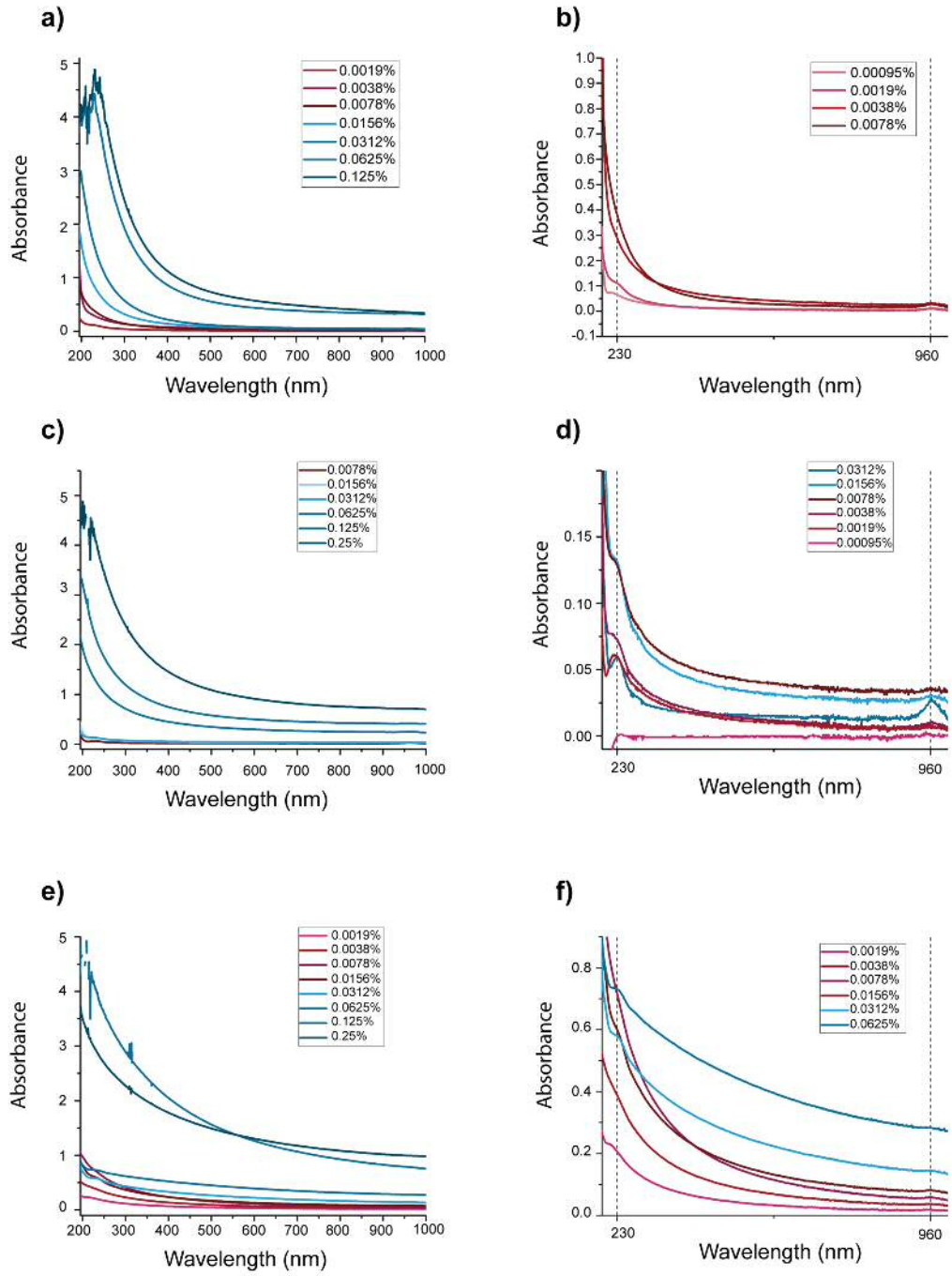

Figure 4.25: UV-Visible spectra as a function of wavelengths for different concentrations. Sample prepared with untreated 50 nm diamond powder for a) high concentrations and b) lower concentrations. c) Vacuum annealed sample for high concentration and d) vacuum annealed sample for low concentration. e) and f) absorbance measurements for the air annealed followed by vacuum annealing and hydrogen annealing sample, for high concentrated and low concentrated slurries respectively.

On the other hand, the air treated sample (figure4.26a) and figure4.26b))and the hydrogen annealed sample (figure4.26c) and figure4.26d)) have a less pronounce peak/shoulder around 220 nm, with the absence of the 960 nm peak.

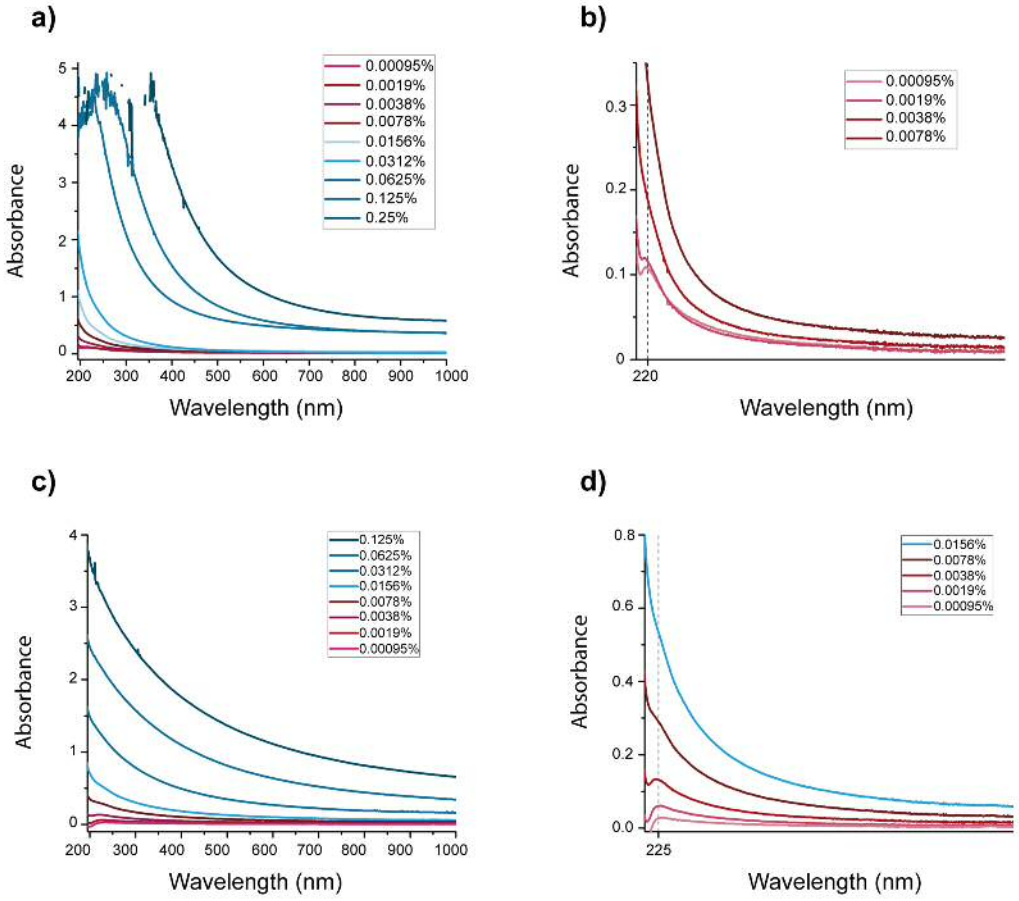

Figure 4.26: UV-Visible spectra as a function of wavelengths for different concentrations. Slurry prepared with the 50 nm air treated diamond powder for a) high concentrations and b) lower concentrations. Detector saturation is observed in highly concentrated slurries in figure a). c) and d) hydrogen annealed dispersions for high concentrations and low concentrations respectively.

4.7 Conclusions

In this chapter, surface charge manipulation on diamond nanoparticles has been performed. Detonation diamond particles (5 nm) and 50 nm commercial diamond nanoparticles were subjected to different annealing treatments. For DND particles, hydrogen annealing treatments were conducted in order to explain the hydrogenation of diamond surfaces. It was proved that Sp^2 carbon content plays an important role in diamond nanoparticles' surface hydrogenation, as sp^2 carbon can be desorbed as C_2 or C_3 allowing the C_3-H_2 reaction.

On the other hand, for larger particles (50 nm), the low temperature hydrogenation was not effective due to the reduced sp^2 content available on the surface. Different annealing methods were performed with 50 nm diamond nanoparticles and sp^2 was intentionally created on the nanodiamonds' surface, allowing subsequent low temperature hydrogenation. Colloidal properties of the treated powders were studied, and evidences for the positive zeta explanation were proved.

Chapter 5

Production and characterization of diamond particles with SiV colour centres

Abstract

Due to the emergence of quantum communication, quantum computation and quantum cryptography (specifically quantum key distribution), photons have been highlighted as promising candidates for developing new devices. Photons can serve as secure and fast carriers of quantum information allowing the propagation of coherences over long distances. Single photons can also be used as quantum bits for quantum computers because of their demonstrated quantum entanglement. Different sources have been used for single photon creation and although single photon sources (SPS) were developed more than a decade ago, the realization of a useful device remains challenging. Many SPS lack practicability, as some SPS need high vacuum operation, low temperature operation, and they present low collection efficiency. SPS based on defects in diamond, known as colour centres, have attracted an increasing interest due to the fact that they can overcome all these challenges.

In this chapter, different approaches to create colour centres in diamond will be studied, based all of them in the *in situ* incorporation of defects into the diamond lattice during CVD growth. In the first approach, nanodiamonds of different sizes will be grown on quartz and sapphire substrates with the aim of removing the nanoparticles from the substrate, isolating them for subsequent manipulation.

The second part of this chapter will be focused on a different strategy to create nanoparticles containing colour centres. First, diamond films will be grown, with defects being incorporated into the diamond lattice during the CVD growth, as was done during the first approach. After

the diamond film growth, nanoparticles will be obtained following milling strategies. Finally, the milling of commercial single crystal diamond samples will also be studied, considering different milling materials, in order to choose the appropiate one according to the ultimate application.

5.1 Introduction

Whereas the importance of manipulating and controlling nanodiamond surface groups was demonstrated in the previous chapter, in this one, the control over diamond single defects, with high impact for quantum applications, will be examined.

The study and understanding of diamond defects and the huge developing of nano-engineering technologies opened a new field of applications based on quantum diamond. As diamond has a wide indirect bandgap (5.5 eV), the intrinsic optical properties of diamond, result in diamond being transparent from the UV region to the far infrared due to diamond inversion symmetry and hence the lack of a dipole moment. [187] Although defect-free diamond does not show the one-phonon absorption at 7.5 μm it has minor adsorptions from 2.5 μm to 6.7 μm (4000-1500 cm^{-1}) due to two and three phonon processes. [188]

However, diamond having just intrinsic optical properties is not common, as most of the available diamonds, both natural or artificially created contains some defects. These defects will induce new discrete energy levels in the diamond bandgap, which will produce absorptions at energies below 5.4 eV, causing the colour of some natural diamonds, and hence the name of colour centres. [187]

Several classifications of diamond defects can be found in the literature, but the classification used in this thesis will only attend to either intrinsic defects due to an interstitial carbon or a missing carbon (vacancy), or to extrinsic defects, which comprise non carbon atoms that have been incorporated into the diamond lattice. The most common defects in diamond are nitrogen-related ones, present in natural diamond and synthesized HPHT or CVD diamond and lead to the well-known 'Type' classification. Diamond can then be classified into four types, known as Type Ia, Type Ib, Type IIa and Type IIb. The first two types contain nitrogen either as isolated or aggregated impurities whereas the last two (type IIa and type IIb) have very low concentration (type IIa $< 5ppm$) or no measurable nitrogen concentration. [189]

Nitrogen is not the only impurity that can be found in the diamond lattice, but due to the tightly packed diamond lattice, only small size atoms will fit. Nevertheless, the increasing interest in colour centres properties covering the most demanding quantum applications, has led to a determined search of new colour centres.

5.2 Single Photon Sources: Why diamond?

With the establishment of the first quantum principles in 1900 with the quantization of the electromagnetic radiation and the postulation of light consisting on individual 'quantum' particles (photons), the era of quantum mechanics began. It was not until few decades later that researchers realized the full potential of manipulating these single photons. [190] However, a new handicap arose, how to produce and detect single photons on demand? Before answering that question is important to establish some consideration about what an 'ideal' single photon is.

Unlike classical light sources in which photons are emitted randomly following Poisson distributions, 'ideal' single photon sources will emit one photon at each time. [75] However, real photon sources deviate from this assumption as there is a probability for the emission of either zero or multiple photons, hence requiring photon statistics to define a single photon source. Other important parameters that define single photon sources are the second-order autocorrelation function $g^{(2)}(0)$, the system quantum efficiency η and the spectral line width or wavelength uncertainty $\Delta\lambda$. [191] The intensity autocorrelation function can be measured experimentally through the Hanbury Brown and Twist (HBT) experiment, and represents the probability of detecting two photons separated by a certain time difference τ and will be more extensively discussed in this chapter. The second one, the quantum efficiency, represents the probability of a photon emission after an excitation cycle. In an ideal single photon source, this probability should be one, but it is often smaller than 1. This probability can be reduced if the system presents a three level or a multilevel system with shelving states or if a non-radiative transition takes place. Another important parameter of a single photon source, closely related to the quantum efficiency, is the collection efficiency. Once the photon is emitted, is it extremely important to be able to collect that emission with minimal loses. However, with diamond having high refractive index (2.4), high collection efficiencies can only be achieved with structures such as cavities. Finally, null or small inhomogeneous spectral line widths are needed in systems in which photons need to be generated massively in parallel.

Most of the single photon sources are atom-like systems, that is, systems in which electronic transitions can occur only at discrete energies. These transitions are usually induced either through electrical or optical excitation (a laser pulse). There are many systems that have been studied over the last decades. [75] The first studied single photon emission was observed in 1977 in sodium atoms that were continuously excited by a dye-laser

beam. [192] Single photon sources consisting on single atoms have also been reported in the literature, [193] and require single atoms to be trapped into a high-finesse optical cavity. The main advantages of this system is that the quantum efficiency is close to one and photons could be produced in quantity for a scalable system. On the other hand, the limited trapping time along with the possibility of decoherence effects due to atom-cavity coupling fluctuations made this system not ideal for certain quantum applications. Similar single photon sources use single ions instead of atoms to produce single photons. With a better confinement than the one achieved with single atoms, the main drawback of these single photon sources is the low collection efficiencies. Single molecules [194] and quantum dots [195] have also shown single photon emission and have been studied as single photon sources. Semiconductors quantum dots have been by far the most extensively studied systems. Quantum dots can be created by growth techniques such as molecular beam epitaxy (MBE), embedding a semiconductor with a small gap in between another one with a larger bandgap, or through chemical synthesis, creating colloidal quantum dots. The creation of quantum dots can be perfectly engineered and controlled. Nevertheless, the high vacuum conditions needed during MBE growth along with cryogenic temperatures needed to limit the phonon band scattering effects which lead to, most of the times, non-vanishing $g^{(2)}(0)$ values and non-indistinguishable photons, reduce the practical potential devices.

Nowadays, some of the most promising single photon sources are colour centres in diamond. A colour centre is an optically active complex which involves impurity atoms and/or defects, such as interstitials, and vacancies. But why is diamond a good candidate for a single photon source? Because diamond can overcome the main common sources of decoherence (the loss of information from a system into the environment). The decoherence sources include nuclear spins, low electron concentration and phonon scattering at room temperature. [196] In addition and as mentioned before, an ideal single photon source should be one with 100% probability of emitting a single photon, with 0% probability of multiple photon emission and need to be able to produce indistinguishable photons. [190] Diamond colour centres can fulfill all these requirements.

5.3 Colour Centres in Diamond

Hundreds of colour centres have been reported in the literature, [197] with Ge being the last discovered, just a couple of years ago. [198] The most important characteristic that

defines a colour centre is the energy associated to the pure electronic transition, which is in most of the cases unique for each impurity and is known as the zero phonon line (ZPL). Furthermore, the diamond lattice affects the electronic structure of the different impurities, producing for each defect, exclusive vibration-assisted electronic transitions (vibronic sidebands) which are due to interactions with intrinsic lattice phonons and local vibrations. [197] In general, the broad sidebands will be a drawback for single photon sources. However, and as will be explain below, the silicon-related colour centre, presents low phonon coupling which leads to emission mostly concentrated in the ZPL with a narrow emission line.

The most studied and known colour centres are the nitrogen-related, not surprising considering that nitrogen is the most common defect in diamond. As briefly mentioned in 6.1, there are different defects associated with nitrogen: a single substitutional nitrogen, nitrogen aggregates or the nitrogen-vacancy complex which gives rise to the well-known nitrogen-vacancy colour centre (NV), produced by a substitutional nitrogen atom and a vacancy at an adjacent lattice position in diamond. Single photon emission from the NV centre was observed in 1997 for the first time. [199]

Colour centres can also show different charge states. For nitrogen, the one that presents more interesting properties for single photon experiments is the negatively charged NV^- centre. From now, it will be denoted as NV for simplicity. However, a neutral charged NV^0 centre with a ZPL at 575 nm has also been observed and can be produced (temporarily) exciting the negatively charged NV centre with a green laser. [200] The optical transition of the NV centre can be modelled as a three-level energy system and its purely electronic transition, the zero photon line (ZPL), is located at 637 nm (1.945 eV). [74] The NV centre can be described using the generally accepted six-electron model. [201, 202] Apart from the ZPL emission, a NV centre can decay by emitting a photon and several phonons, giving rise to phonon sidebands, and making interference impossible. This is the major limitation of NV centres, although NV centres are one of the most important centres for magnetic sensors, [76, 203, 204] and as spin quantum bits [205, 206] .

5.3.1 The SiV Colour centre

Whilst NV is the most common colour centre in natural diamond, SiV is the one that can be incorporated more easily during CVD growth. As the nitrogen-vacancy colour centre, the silicon-vacancy colour centre also presents different charge states, the negatively charged

(SiV^-) being the most interesting.

Goss et al. [207] first proposed that the structure of the silicon-vacancy centre consists of a Si atom splitted into two vacancies aligned along the <111> direction (shown in figure 5.1a), with a D_{3d} symmetry. However, further symmetries have also been considered and are still under debate (deeper discussion can be found in [63]). Figure 5.1b) and figure 5.1c) show the electronic structure and the spectrum of the SiV centre. The SiV^- (SiV from now) has a zero-phonon line energy of 1.68eV (738 nm), which splits into a four line structure when it is cooled down [208]. The origin of this splitting is due to a split ground and excited state caused by a strong spin orbit coupling. [209] The SiV centre shows a high Debye-Waller factor (DW) [210] which indicates that most of the emission (70%) is produced in its narrow ZPL (down to 0.7 nm). [211] Furthermore, high emission count rates (6000 kcps) and his lifetime of 1.8 ns, made this colour centre spectral properties superior as those of the NV centre.

Apart from the superior optical properties, due to the ZPL splitting at low temperature without the application of a magnetic field, the SiV centre offers much more possibilities in quantum information processing (QIP) systems. The SiV allows an ultrafast optical coherent control, faster than the one achieved for the NV centre. [212]

For these reasons, this chapter will be focused on SiV fabrication processes and improvements to achieve better optical properties and a a better control over diamond nanoparticles containing this colour centre.

5.4 Colour centres Fabrication processes: CVD Approach

As seen in 6.1, the presence of impurities in diamond nanoparticles, leads in many occasions to the formation of colour centres. For example, the existence of NV centres is common in detonation diamond nanoparticles due to the presence of nitrogen during the purification processes, as seen in the previous chapter. [214] However, the amount of nitrogen and hence the number of NV colour centres per diamond nanoparticle is not controlled, being necessary different approaches to control these colour centres and therefore be useful for different applications. Most diamond colour centre applications require quantum control hence demanding both high quality material and fine control over intrinsic and extrinsic defects such as impurities. Therefore, synthetic diamond growth processes, CVD mainly, are required to provide such a quality level and control in the doping level, usually

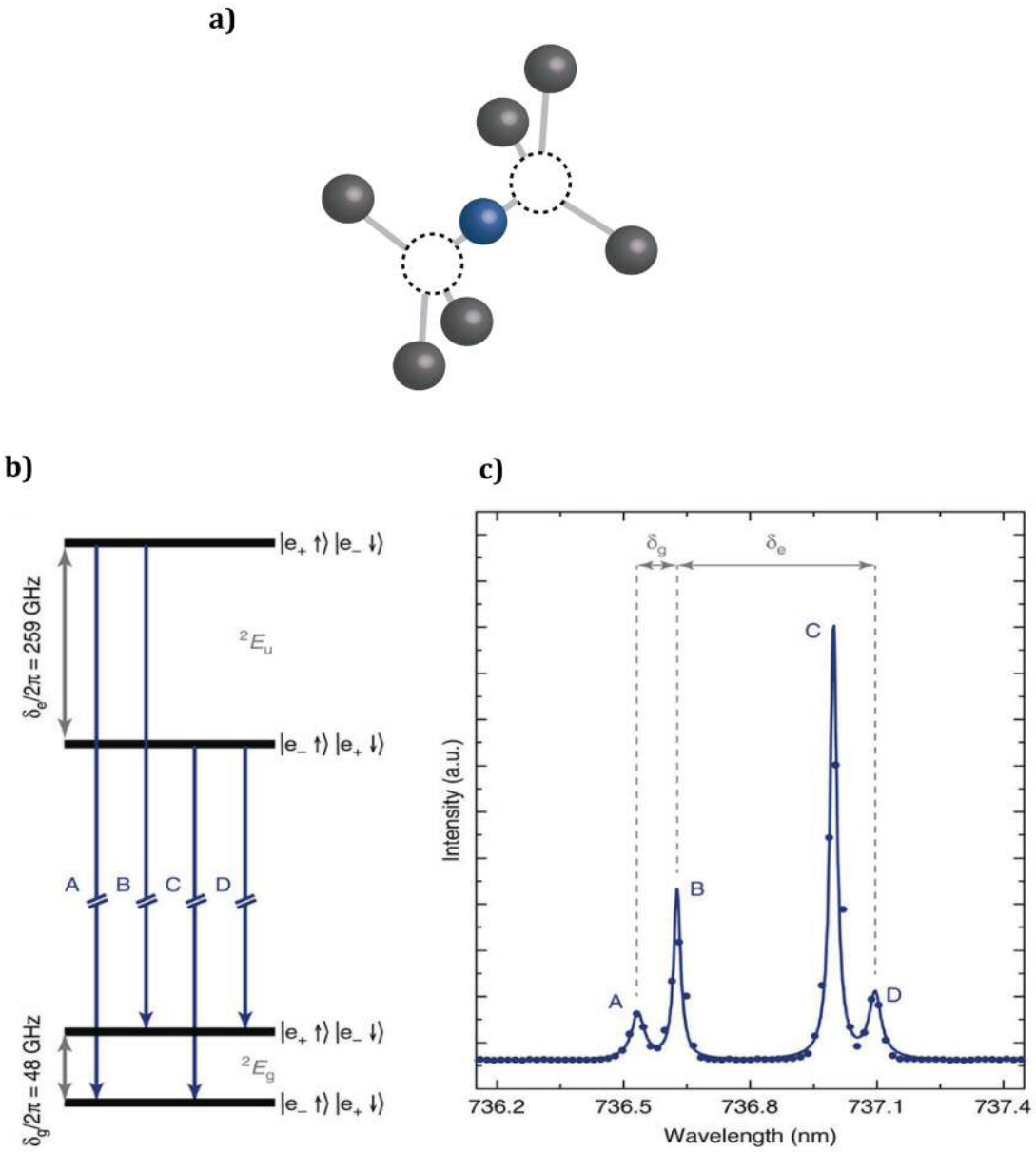

Figure 5.1: Scheme, spectrum and Electronic Structure of the SiV. a) SiV scheme showing the silicon atom in blue between two vacancies. Illustration modified from reference [213]. b) Scheme of the electronic structure of the SiV at zero magnetic field. Large level splittings of 48GHz in the ground and 259GHz in the excited state, mainly caused by spin orbit coupling, are characteristic for the SiV. c) Photoluminescence spectrum of the four zero phonon line transitions of the SiV centre. The spectrum is obtained under non-resonant excitation at 690nm and at 4K. Panel b) and c) reprinted from Nature Communications, (**7**), Becker, J.N. et al., 'Ultrafast all-optical coherent control of single silicon vacancy colour centres in diamond'.

minimising the number of impurities. Common impurities sources in the CVD process are the chamber walls, impurities present in the gases or impurities introduced from the atmosphere.

Several strategies to create diamond colour centres have been reported within the literature. [215] Nitrogen (and other impurities) can be intentionally introduced in the diamond lattice by electron irradiation or ion implantation. [216, 217] With acceleration energies necessary to implant the ions within the diamond lattice ranging from few KeV to MeV, a vacuum annealing process (usually performed at temperatures between 600°C and 1000°C) is necessary to repair the damaged diamond surface and allow the colour centre activation. [218] Ion implantation is usually performed in high quality type Ib HPHT diamond. However, it has to be noticed that most HPHT diamonds already have a non-negligible amount of nitrogen (100 ppm approximately) from the atmosphere or from the materials used during the growth and can provoke the presence of a high density of NV centres. This high density of NV ensembles is preferred for magnetometry applications, [204] but not if control down to the single optical centre level is needed. Therefore, in order to reduce the impurities before the ion implantation process, it is necessary to synthetically produce high purity diamond by CVD. The CVD process also allows the creation of high-quality isolated diamond nanoparticles with small crystal sizes in which the sp^2 content can be reduced.

Similar strategies have been used to produce the SiV centre. Several reports show the efficient creation of SiV centres by ion implantation [219] but also by hot filament CVD and plasma-assisted CVD. [220] In microwave plasma-assisted CVD growth, these centres can be created incorporating silicon during the diamond growth, using either a silicon containing substrate as the Si source, or a Si solid source placed inside the reactor. In both cases, the plasma etches the Si and incorporates it into the diamond lattice. However, for single photon applications, low densities of SiV centres are required and hence low doping concentrations are demanded. The best way to control the silicon incorporation is introducing silicon in the gas phase, as will be explained in the next chapter.

For SiV centres to be useful in quantum applications, it is important to be able to isolate the single-photon system. For this reason, the growth or production of isolated diamond nanoparticles containing the colour centre will be preferred over centres embedded in the bulk diamond. In this chapter two different approaches to create diamond nanoparticles containing colour centres have been performed, both based on CVD growth. In the first one, diamond nanoparticles are directly grown onto different substrates, and in the second

one, silicon substrates are used to grow polycrystalline diamond films with subsequent substrate etching and diamond film milling.

5.4.1 CVD growth of nanodiamonds on Quartz Substrates

The choice of quartz and sapphire as substrates for diamond nanoparticles (with SiV centres) growth, is linked to their good optical and thermal properties. With a transparency that extends from the ultraviolet (UV) to the near infrared (IR) both are excellent materials for the subsequent development of optical devices. As seen in the previous section, SiV centres can be produced *in situ* during CVD growth, due to the presence of silicon impurities coming from substrate etching, chamber walls or intentionally introduced either in a solid or in a gas phase. Therefore, the use of quartz substrates will produce large amounts of silicon impurities and hence the formation of SiV ensembles instead of single SiV centres as described in the following sections.

As previously described, the main goals are to control and to reduce the nanodiamonds (NDs) density, and to control their size and placement. A controllable density is needed to try to isolate and place a ND in an optical microcavity. Due to imposed confocal aperture size (around one μm), the optimal density is one diamond nanoparticle or seed per μm^2.

Quartz substrates seeding

The density of diamond nanoparticles on a substrate is determined by the electrostatic interaction between the diamond seeds and the substrate. This density can be controlled/manipulated changing the surface groups and hence the zeta potential of diamond nanoparticles, as described in chapter two. As a reminder, silicon substrates or silicon dioxide substrates present a negative zeta potential over the whole range of pH. Hydrogen terminated diamond seeds possess positive zeta potential values over the same pH range, thus ensuring densities $> 10^{-11} cm^{-2}$ in these substrates [156] with a complete diamond film coalescence after 10 minutes of growth (0.6% of CH_4/H_2). [221] On the other hand, seeding the substrates with colloids containing air annealed particles will produce densities in the order of $> 10^{-9} cm^{-2}$ due to electrostatic repulsion caused by identical zeta potential values between the quartz substrate and the diamond seeds. [156] Further dilution of colloids containing these air annealed particles will lead to the desired densities. As the obtainment of isolated nanodiamonds is pursued, colloids with air annealed diamond seeds will be used avoiding the formation of a continuous diamond film during CVD growth.

Quartz substrates were seeded with an air annealed nanodiamond colloid in an ultrasonic bath for 10 minutes, previous cleaning with acetone, isopropanol and deionised water (DI water). Substrates were spun dry. The air treated slurry was prepared as detailed by *Hees et al.* [156] and contains 0.5 gr of commercial Plasmachem GmbH G01 grade powder in 250 ml of DI water, representing in terms of concentration, 0.2% mass (g) / volume (ml). More diluted slurries were also prepared by diluting the original one 1:10 and 1:100.

AFM measurements were performed in the seeded substrates with a *Park Systems XE-100* AFM operating in non-contact mode and equipped with TESPA silicon AFM tips (320 kHz resonant frequency, 42 N/m spring constant, and 8–12 nm tip radius).

Figure 5.2 shows 5 μm x 5 μm AFM images of quartz substrates seeded with the three different slurries, non-diluted, 1:10 diluted and 1:100 diluted. AFM images were analysed with the WsxM programme. [222] Low nucleation densities are observed, with seeds sizes varying from 4 nm to 7 nm as determined by a height profile in figure 5.3b). However, larger lateral sizes around 50 nm are observed, due to tip-sample convolution as shown in figure 5.3b). Figures 5.2 a), c) and e) show the quartz substrates seeded with the original slurry, the 1:10 diluted and the 1:100 respectively. After repeating the seeding and the measurements on different samples, and different areas, reproducibility was poor. In addition contradictory results were found due to the highest density was observed for the 1:100 diluted colloid.

Another cleaning and seeding method investigated deal with the inconsistent results. A standard SC-1 cleaning consisting of a mixture of $H_2O_2 : NH_4OH : Deionised H_2O$ (1:1:5) at 75 °C for 10 min., was performed, [223] followed by a DI H_2O rinse, and finally spun dry. After substrates cleaning, few drops of the different slurries were drop cast on the quartz substrates and the samples were spun dry. In this case, reproducible samples were found, shown in figures 5.2 b), d) and f). However, particle aggregation was observed in the original colloid, independently on the cleaning method used, thus this slurry was not used for subsequent CVD growth.

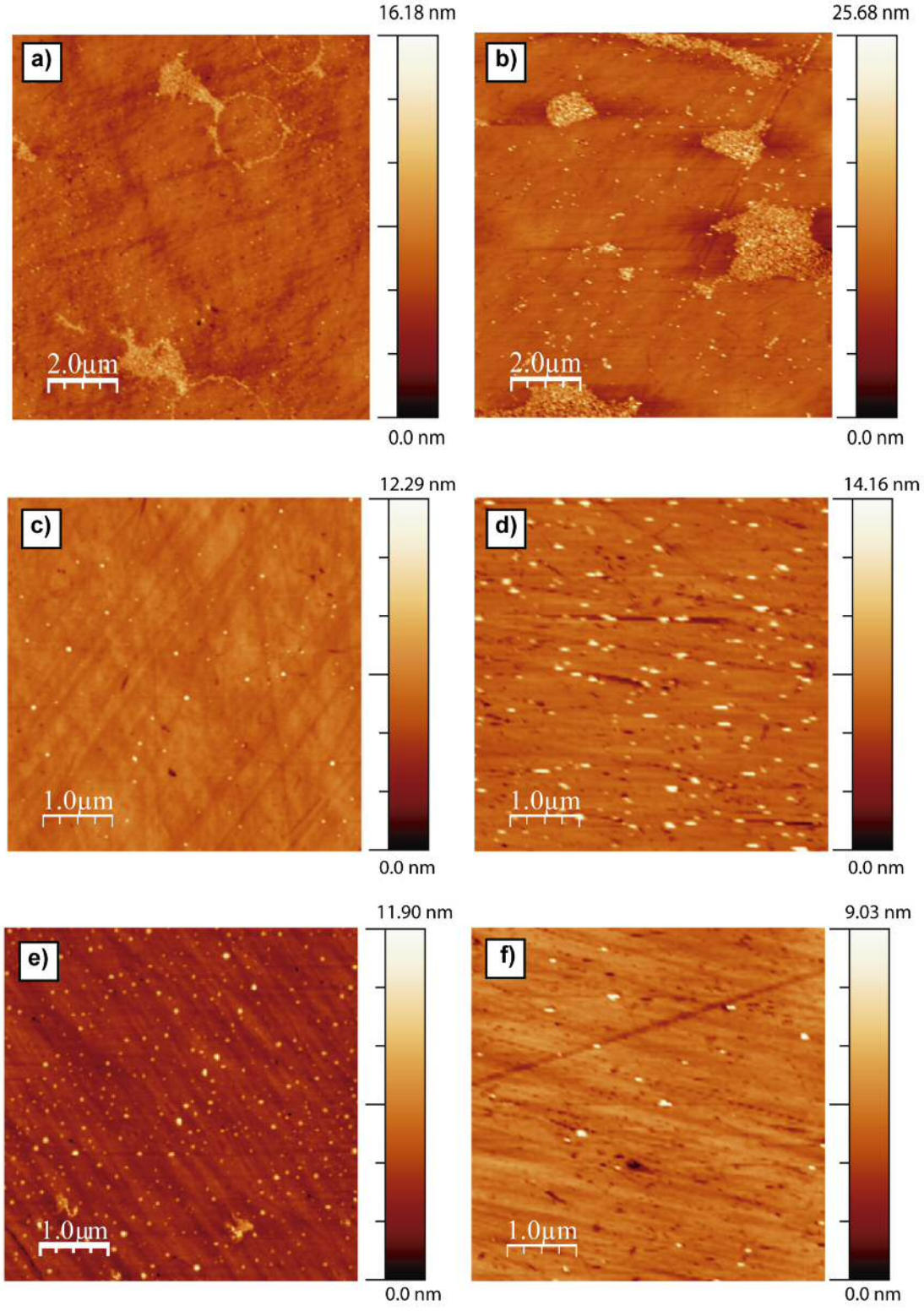

Figure 5.2: AFM images of seeded quartz substrates. a) and b) represent the quartz substrate seeded with the original slurry using the ultrasonic bath or the spin coating method respectively, c) and d) quartz substrates seeded with the 1:10 diluted slurry and the same seeding methods and e) and f) 1:100 diluted slurries

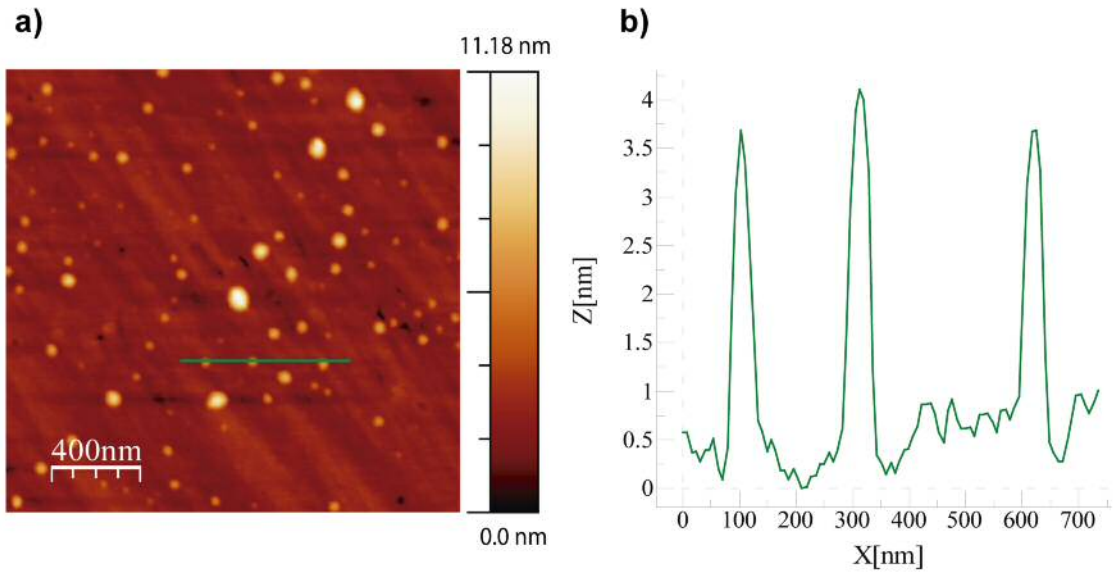

Figure 5.3: a) AFM image of the 1:10 seeded quartz substrate and b) height profile indicating 4-7 nm size particles with 50 nm lateral size caused by tip-sample convolution.

Quartz growth

Whereas nanodiamonds' densities are determined by the selection of differently treated particles seeds with opposite zeta potential, the growth conditions have repercussions on nanodiamonds' size. The size of the diamond crystals is an important parameter and it is desirable for this size to be less than the emission wavelength of the embedded colour centre. This requisite arises to eliminate internal reflection of the light and enhance the collection efficiency of the emitted photons. [224] So it is of a real importance to conveniently choose the growth parameters. The most important parameters are H_2 and CH_4 gas flow (CH_4 percentage), microwave power and chamber pressure (microwave power density), and growth duration. A plasma with high CH_4 concentration prevents seeds from being etched, ensuring the growth and also increasing this growth rate . [225] However, higher CH_4 concentrations also lead to an increase in the disordered carbon (sp^2) content. [22] For this reason an intermediate methane concentration should be chosen. Microwave power density has a strong influence for the crystal morphology. Higher microwave power density values yield better nanodiamond quality, so a high density regime is preferable. [226] Both methane concentration and microwave power density were fixed, but the growth duration was the parameter being changed in the studied samples.

Samples were grown in a *Seki 6550 Microwave Plasma Enhanced Chemical Vapour Deposition (MWPECVD) reactor*, with a microwave frequency of 2.45 GHz. Samples were placed in a molybdenum substrate holder, on top of a water cooled copper stage. The gas flow was measured in Standard Cubic Centimetres Minute (sccm). The flow for the quartz samples was 285 sccm of H_2 and 15 sccm of CH_4, so $CH_4 : H_2$ was 5% of a total flow of 300 sccm. The microwave power was set to 3.5 kW and the chamber pressure was 40 torr. Substrate temperature was measured using a *dual wavelength Williamson pyrometer* (475°C-1475°C) and adjusted by tuning the pressure between the molybdenum holder and the cooper stage. Temperatures from 630°C to 800°C were recorded.

Two quartz samples seeded with the 1:10 and 1:100 diluted colloids were placed inside the reactor each time. Growth duration was 60 min, 15 min, 5 min, and 1 min. Scanning Electron Microscope (SEM) measurements were performed in a *Veeco FEI (Philips) XL30 ESEM* (Environmental Scanning Electron Microscope) equipped with a Field Emission Gun (FEG).

Figure 5.4, shows nanodiamonds on quartz substrates after 60 minutes growth, with figures a) and b) corresponding to the quartz substrates seeded with the 1:10 diluted slurry and

figures 5.4 c) and d) corresponding to the 1:100 diluted slurries. Lower nanodiamonds densities are observed for the quartz substrates previously seeded with the 1:100 slurry. The same trend is observed in figure 5.5 for the samples after 15 min. growth duration, with figures 5.5a) and 5.5b) seeded with the 1:10 diluted slurry and figures 5.5c) and 5.5d) seeded with the 1:100 diluted slurry. SEM images show an increase in particles size for longer growth duration as well as an increase in crystallinity. Particles mean size for the 60 min growth is around one micron, and half this size for the 15 min growth. SEM resolution was not good enough to resolve the 10, 5, and 1 minutes growth images and charging effects appeared on the substrates even after gold coating, so AFM measurements were also performed, showing in most of the images just the quartz substrate.

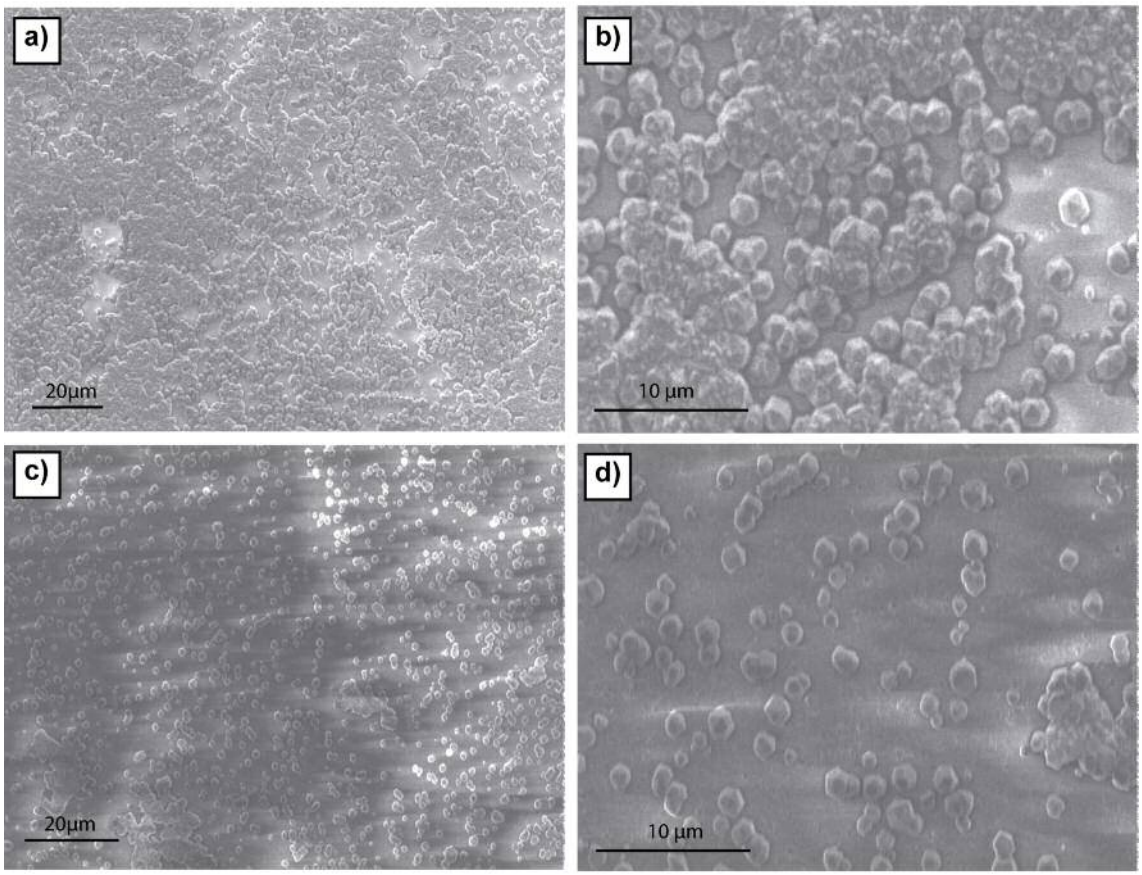

Figure 5.4: SEM images of nanodiamonds grown on quartz substrates for a growth duration of 60 minutes. Panels a) and b) correspond to the 1:10 diluted seeding slurry and panels c) and d) show quartz substrates previously seeded with the 1:100 diluted slurry. In both cases, higher magnifications were used in order to analyse the particles size.

AFM measurements showed surface deterioration with increasing growth duration due to the effect of plasma etching. New plain substrates were placed inside the reactor during 2, 5, and 10 minutes, to characterise the surfaces, shown in figures 5.7 b) c) and d)

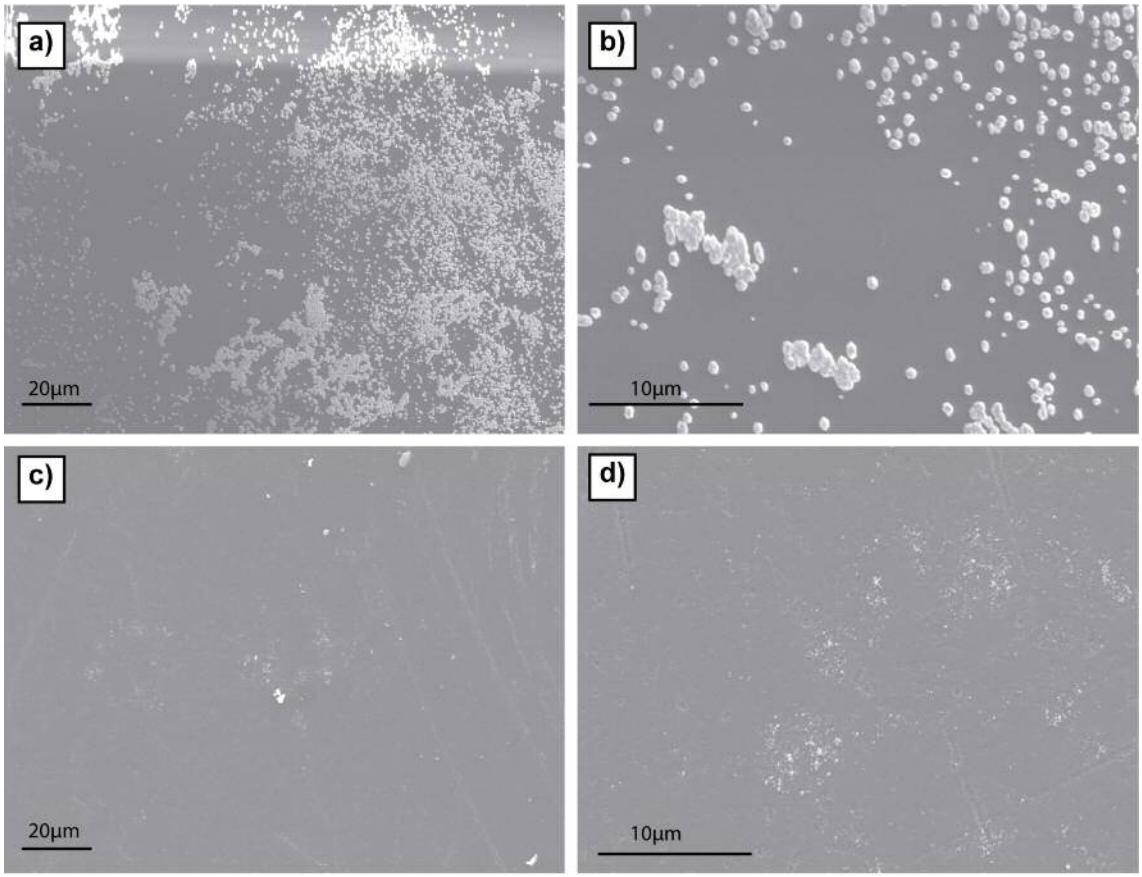

Figure 5.5: SEM images of nanodiamonds grown on quartz substrates for a growth duration of 15 minutes. Panels a) and b) correspond to the 1:10 diluted seeding slurry and panels c) and d) show quartz substrates previously seeded with the 1:100 diluted slurry.

respectively. The growth parameters were the same as the ones described previously. Figure 5.7 a) corresponds to a plain quartz substrate that was not introduced in the CVD reactor and was used as a reference. As observed in the AFM images and in the profile graphs below each image, substrate degradation is clearly observed with increasing RMS roughness from 0.5 to 4.5 nm.

With Colour centres luminescence properties clearly influenced by the nanodiamonds surroundings, such damaged surface could have a negative influence over colour centres stability, being necessary either the use of a different substrate or a change in the growth parameters. Nanodiamonds grown on sapphire substrates are discussed in the next section and low temperature growth was also studied. The standard SC-1 cleaning was repeated in quartz substrates and plain and seeded quartz substrates were introduced in the CVD reactor. Growth rate differences of 9.5 times were observed between samples grown at 800°C and at 500°C, so this growth rate difference would be approximately 10 times at 400°C, the selected temperature for the low temperature growth. Methane flow rate was

10 sccm and was diluted in 190 sccm of hydrogen ($CH_4 : H_2$=5%) and chamber pressure and power were 14 Torr and 1500 kW respectively. The resulting temperature was 420 °C. The growth duration was selected to be 50 min. and was compared with the equivalent one at high temperature, the 5 min. growth duration.

AFM images of both high temperature and low temperature growth are shown in figure 5.6 with a clear improved substrate quality with 0.6 nm RMS.

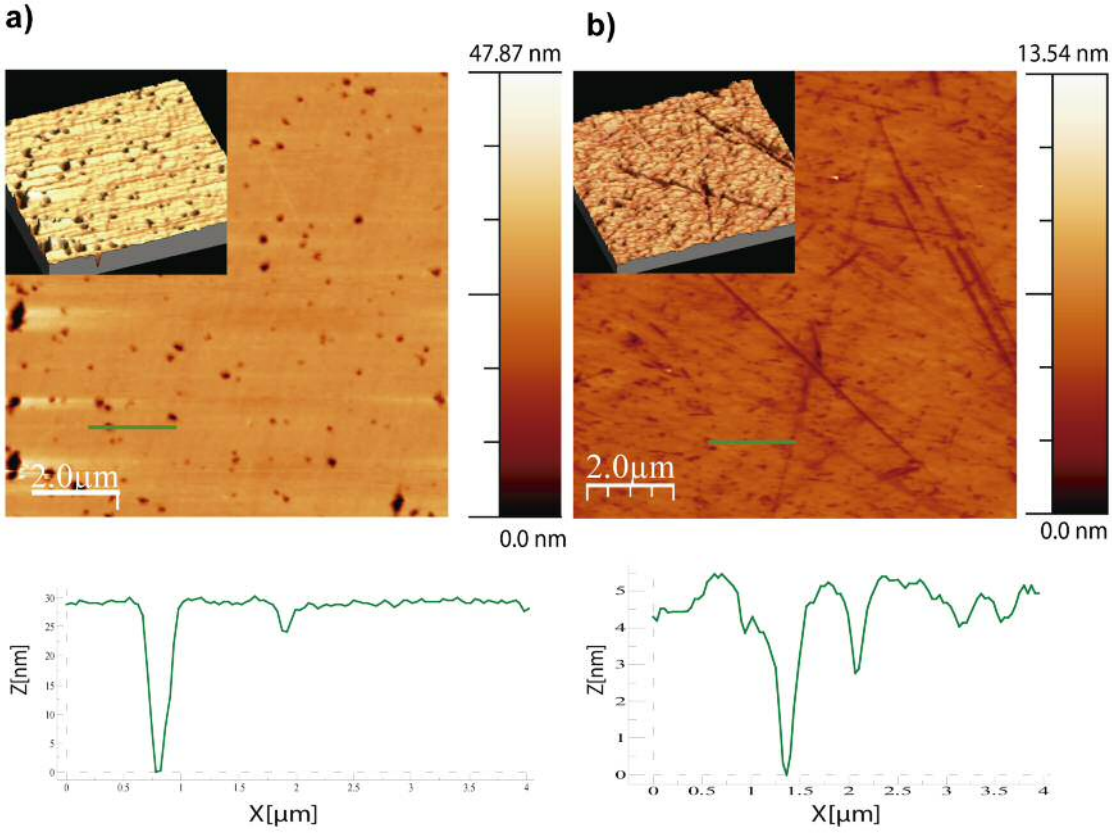

Figure 5.6: AFM images of non-seeded quartz substrates for equivalent growth durations at a) high temperature (800°C) and b) low temperature (420°C).

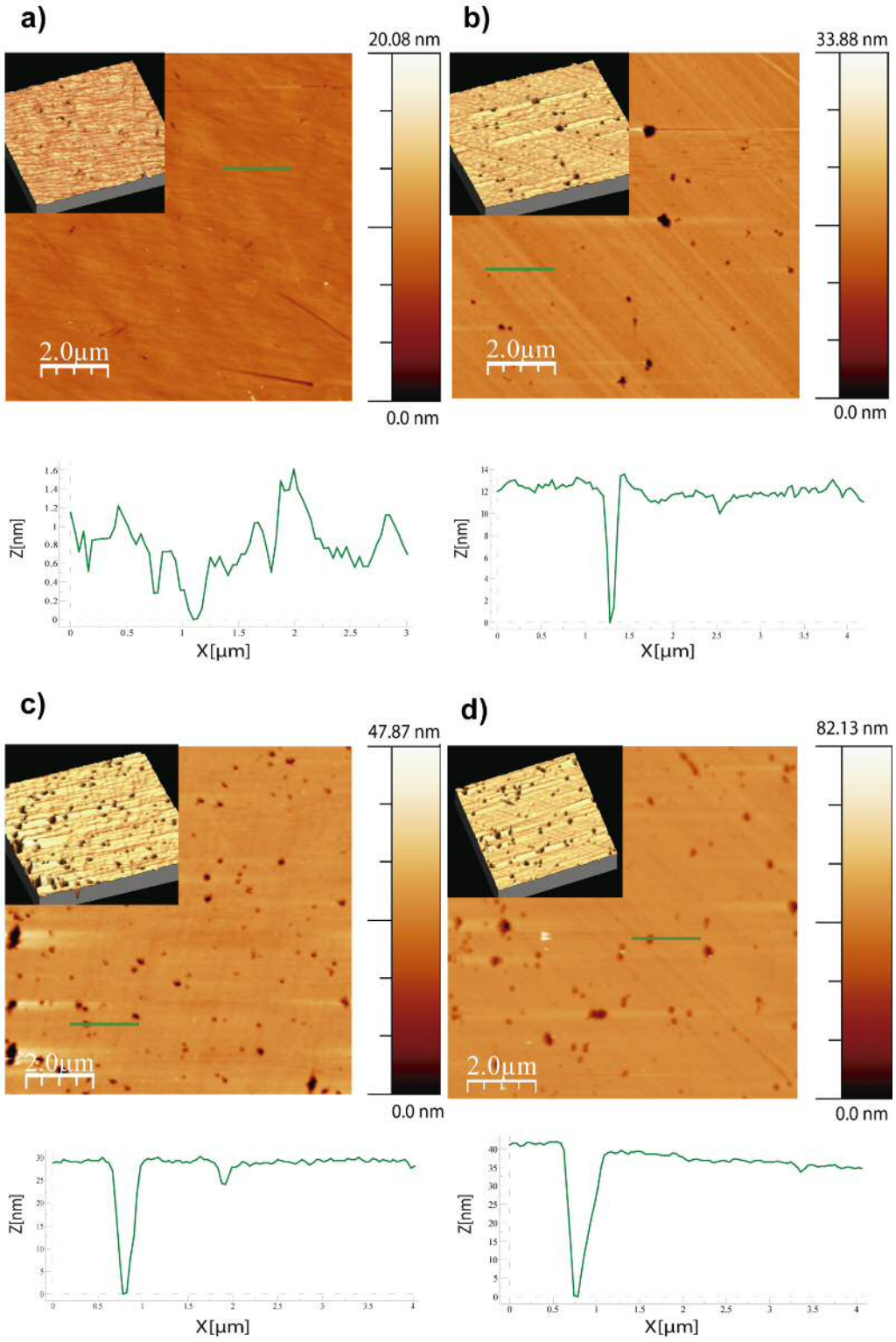

Figure 5.7: AFM images of non-seeded quartz substrates with their respective height profiles below each image. Insets represent 3D images of the substrates. a) Plain quartz substrate with 0.45 nm RMS, b) quartz substrate after 2 min. of growth, c) quartz substrate after 5 min. growth and d) after 10 min. growth. Surface damage is clearly observed and increases with growth duration.

Photoluminescence measurements

Photoluminescence measurements on the quartz substrates were conducted by Dr. Philip Dolan in the Department of Materials in Oxford University (UOXF). A suitable excitation method is necessary for using nanodiamond colour centres as single photon emitters, being a laser optical excitation the preferred method employed. Two different wavelengths are typically used, 532 nm for NV excitation and 690 nm for SiV centres. An excitation wavelength shorter than the fluorescent wavelength of the colour centre is needed to separate the excitation light and the single photon fluorescence. [63]

As was formerly mentioned, no additional silicon or nitrogen was included in the reactor. Nevertheless, both SiV and NV colour centres are present in the quartz samples. SiV emission comes from the surface etching process and NV emission is really common in nearly all natural and synthetic diamond due to the favourable energetical incorporation of nitrogen. Photoluminescence from the samples was imaged in a purpose-built scanning confocal microscope with excitation switchable between 532 nm and 690 nm, and PL spectra recorded with the two excitation wavelengths. This dual wavelength excitation allows the identification of emission from NV centres and SiV centres to understand the relative concentrations of the two defects in the as-grown material. Figure 5.8 shows data recorded from two samples with different seeding concentrations (1:10 and 1:100 dilutions) and growth durations (15 mins and 60 mins respectively). Both samples show strong SiV emission along with evidence of NV and sp^2carbon in the PL spectra. [227] The sample seeded with a 1:100 dilution and 60 minutes growth duration has larger diamond particles, $1\mu m$ in diameter, that show a sharp Raman signal under 532 nm excitation, and less sp^2 carbon emission at wavelengths between 700 and 800 nm. In both samples strong SiV emission is seen in a large fraction of the nanodiamonds as evidenced by recording two images of the same region using the two laser excitation wavelengths.

As explained in 5.3 and although we are interested in SiV and NV colour centres, the SiV centres are more promising due to their narrow ZPL at room temperature, with a Full Width Half Maximum (FWHM) down to 0.7 nm. [211] On the other hand, the NV centre has a spectrally broad emission band and it also has a broad emission wavelength (at room temperature). Although Hanbury Brown and Twist experiments (HBT) were not performed in these samples to test if these colour centres are real "single" photon emitters, the fact that quartz substrates were used, already indicates that a lot of silicon impurities would be incorporated producing SiV ensembles rather than single photon emitters.

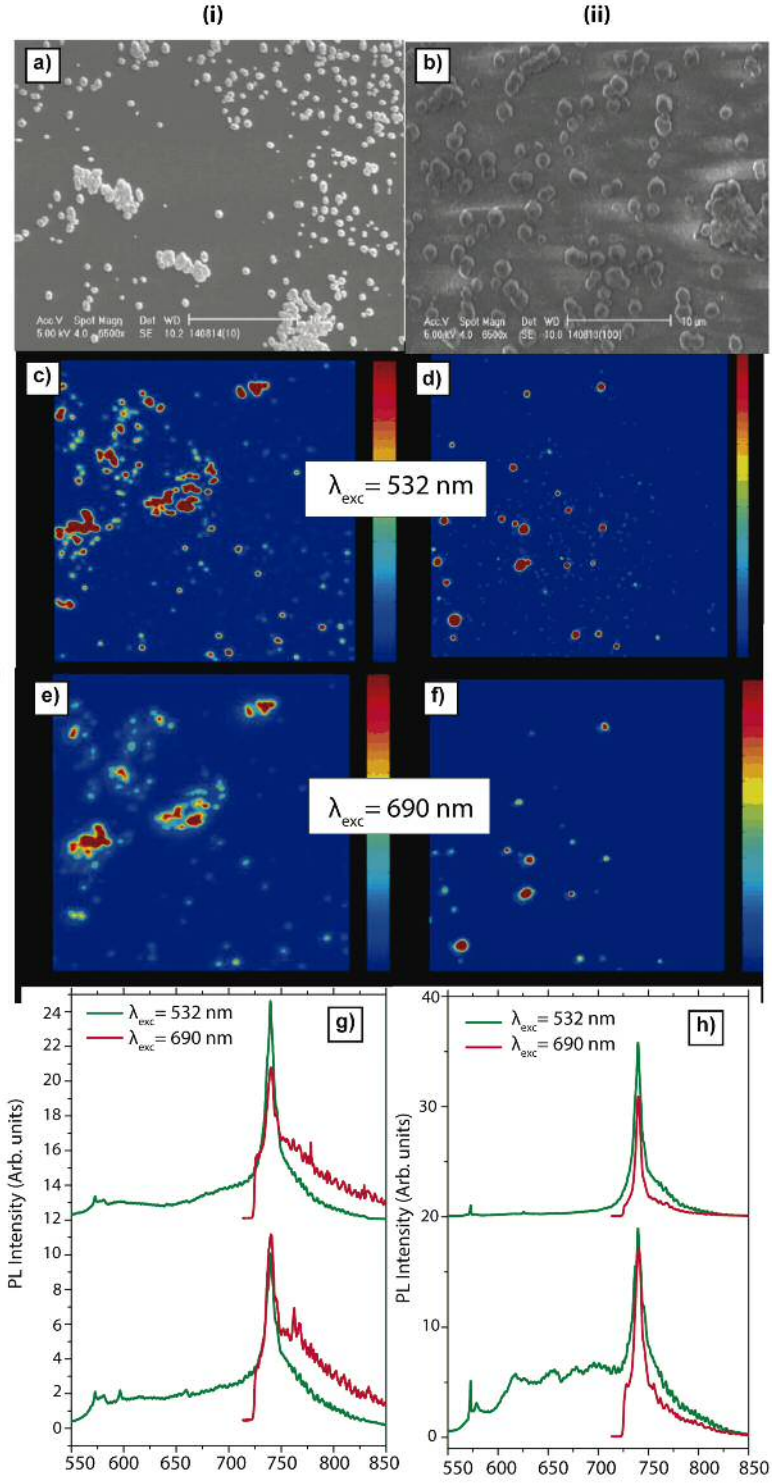

Figure 5.8: Characterization of nanodiamonds containing SiV centres grown on quartz substrates. a) SEM micrographs, b) PL images and c) Two examples of PL spectra taken in different nanodiamonds. Images b) and c) show data recorded with both 532 nm and 690 nm laser excitation. Sample (i) on the left column corresponds to the substrates seeded with the 1:10 diluted slurry and 15 min. growth. Sample (ii) on the right column was seeded with the 1:100 diluted colloid and grown for 60 min.

5.4.2 CVD growth of nanodiamonds on Sapphire Substrates

As briefly mentioned, unintentionally introduced silicon impurities can be incorporated during CVD growth, with silicon containing substrates and reactor chamber walls as the main sources of 'contamination'. Nevertheless, some silicon incorporation from the reactor chamber can be avoided controlling the chamber pressure and microwave power and hence the size of the plasma formed. Non-silicon substrates can also be chosen, introducing silicon as a solid source [228] or in the gas phase to create SiV centres. SiV centres formation in nanodiamonds have already been studied in sapphire substrates, [228] molybdenum, [228] copper, [228], HPHT diamond [229] and Iridium substrates. [210, 230]

In this thesis, growth onto sapphire substrates was also performed. Sapphire, also known as alumina, is aluminium oxide (Al_2O_3) in the purest form. Several sapphire substrates were seeded with both Air and H_2 annealed particles colloids, following the same procedure as for quartz substrates. However, poor particles-surface adhesion was found, making image acquisition challenging. Nevertheless, sapphire substrates seeded with the air treated nanodiamond colloid resulted in higher seeding densities. Although sapphire zeta potential is highly dependent on the crystal orientation, [231] low absolute zeta potential values for pH ranging from pH 5 and pH 7, with isoelectric points (IEP) in the same range, [232] could have an influence in the low particles adhesion. As it is shown in the next part, sapphire substrates were then grown without any previous seeding, and spontaneous nucleation was found, ensuring the lowest density values. Taking into account the necessity of transferring the as-grown nanodiamond into open-access resonators, choosing sapphire could be helpful as nanodiamond can be easily dissolved in colloidal suspension ready for spin coating.

Growth on Sapphire

As previously mentioned, controllable density conditions with seeded particles are difficult to achieve due to low nanodiamond particles adhesion to sapphire substrates, so plain sapphire samples were studied. In order to control the nanodiamond particles' size, different growth duration of 240 min, 120 min, 30 min and 15 min were selected and SEM images of nanodiamonds onto the sapphires substrates are shown in figure 5.10. The growth was performed in the *Seki AX6500 CVD* reactor, with a methane gas flow of 5 sccm diluted in 495 sccm of hydrogen ($CH_4 : H_2 = 1\%$). The microwave power was set to 3.5 kW and the chamber pressure was 40 torr. Temperatures between approximately 830°C and 900°C were obtained as determined by the dual wavelength pyrometer. Spontaneous nucleation

was observed in the samples, and well faceted nanoparticles were achieved, with crystalline size increasing with growth duration. The Nanodiamond size presents a linear behaviour and is represented in figure 5.9, resulting in particles of $2.2\mu m$ for 240 min growth, $1.1\mu m$ for the 120 min growth, 181 nm for growth durations of 30 min and 106 nm for the growth carried out during 15 min.

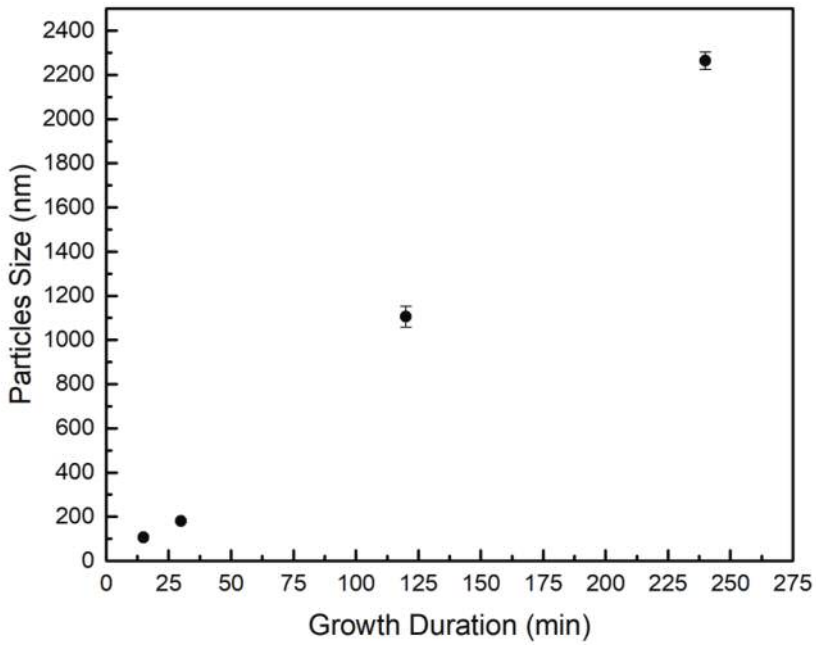

Figure 5.9: Nanodiamonds' size as a function of growth duration, measured from the SEM images shown in figure 5.10. Nanodiamonds were grown onto sapphire substrates without previous nucleation processes, showing a linear rate increase with increasing growth duration.

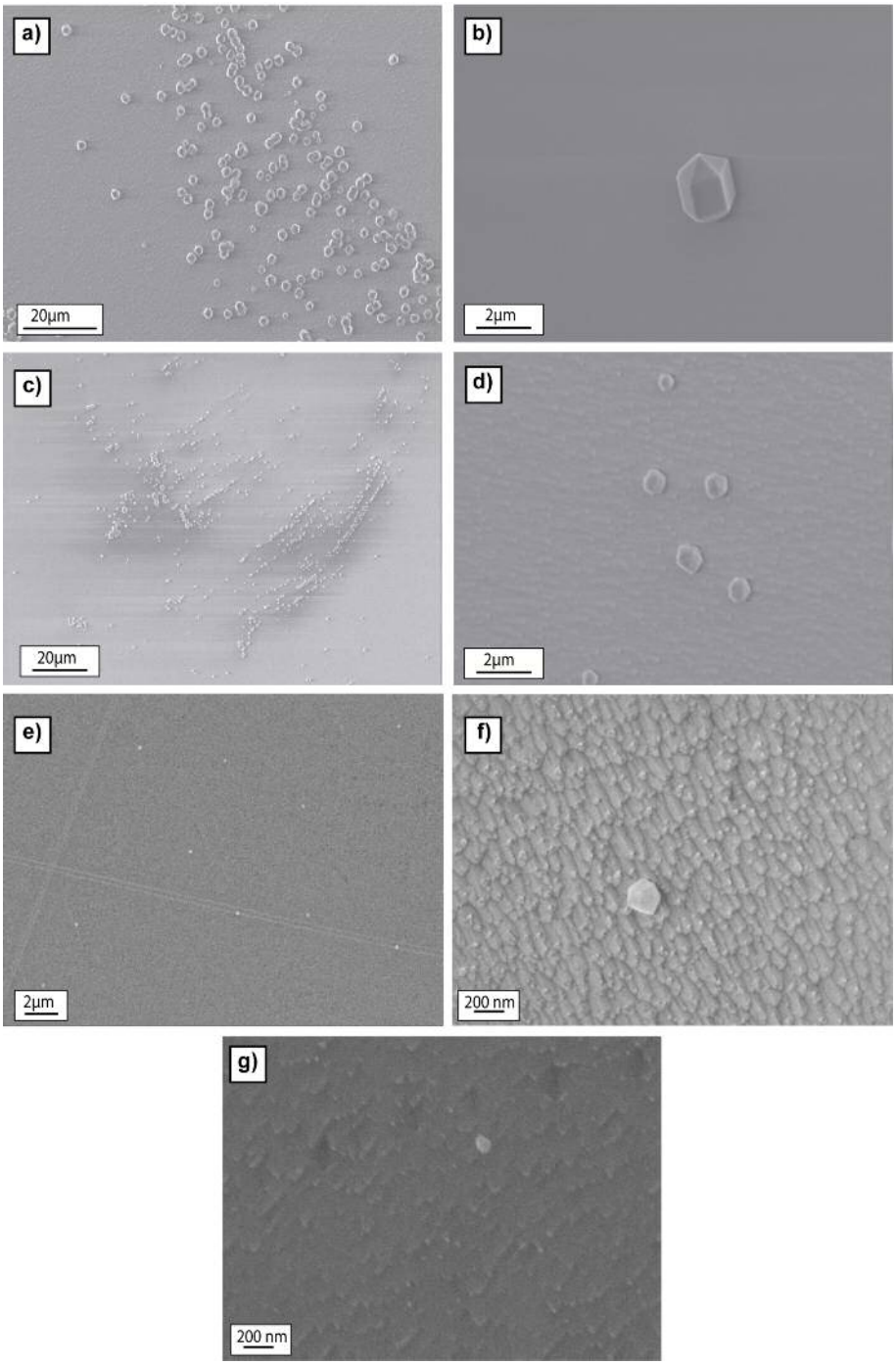

Figure 5.10: SEM images of nanodiamonds grown on sapphire substrates for different growth durations. Panels a) and b) show nanodiamonds after 240 min growth. All the nanodiamonds analysed presented well defined facets and a mean size of 2.2 μm. c) and d) images correspond to growth duration of 120 min. with nanodiamonds sizes around 1.1 μm. Panels e) and f) show nanodiamonds after 30 min growth and g) after 15 min growth.

Photoluminescence measurements

In order to study the optical properties of the nanodiamonds grown on sapphire, photoluminescence measurements were also performed at Oxford University, using the same laser excitation wavelengths, 532 nm and 690 nm. In this case, the growth onto sapphire substrates was repeated including pieces of silicon, to create SiV centres, around the holder in which the sapphire was placed. Samples with and without silicon incorporation were studied.

Figure 5.12 shows an example PL measurement obtained in one of the samples. As seen in figure 5.12c), the PL image shows nanodiamonds aggregation with the PL spectra shown in figure 5.12a). As can be observed, the difference between the signal from the nanodiamond aggregation and the substrate is too low to distinguish any SiV emission. Figure 5.12b) shows the background signal taken on the sapphire substrate. A broad band is observed between 700 nm and 850 nm due to substrate luminescence, as well as narrow peak around 700 nm. These findings are in agreement with *Sedov et al.*, [228] who reported similar PL results for sapphire substrates, shown in figure 5.11.

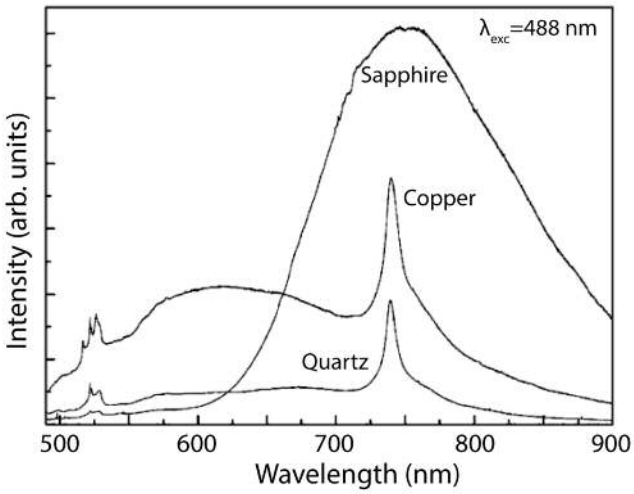

Figure 5.11: Photoluminescence spectra of isolated nanodiamonds on sapphire, copper and quartz substrates. Nanodiamonds grown onto copper and quartz substrates show a narrow emission line at 738 nm wavelength indicating the presence of SiV centres. Sapphire substrate presents a broad band between 700 nm and 850 nm due to the strong substrate luminescence. Reprinted by permission from Springer Nature, Bulletin of the Lebedev Physics Institute, 'Gas-phase growth of silicon-doped luminescent diamond films and isolated nanocrystals', V. S. Sedov, I. I. Vlasov, V. G. Ralchenko et al., 38, Copyright (2011).

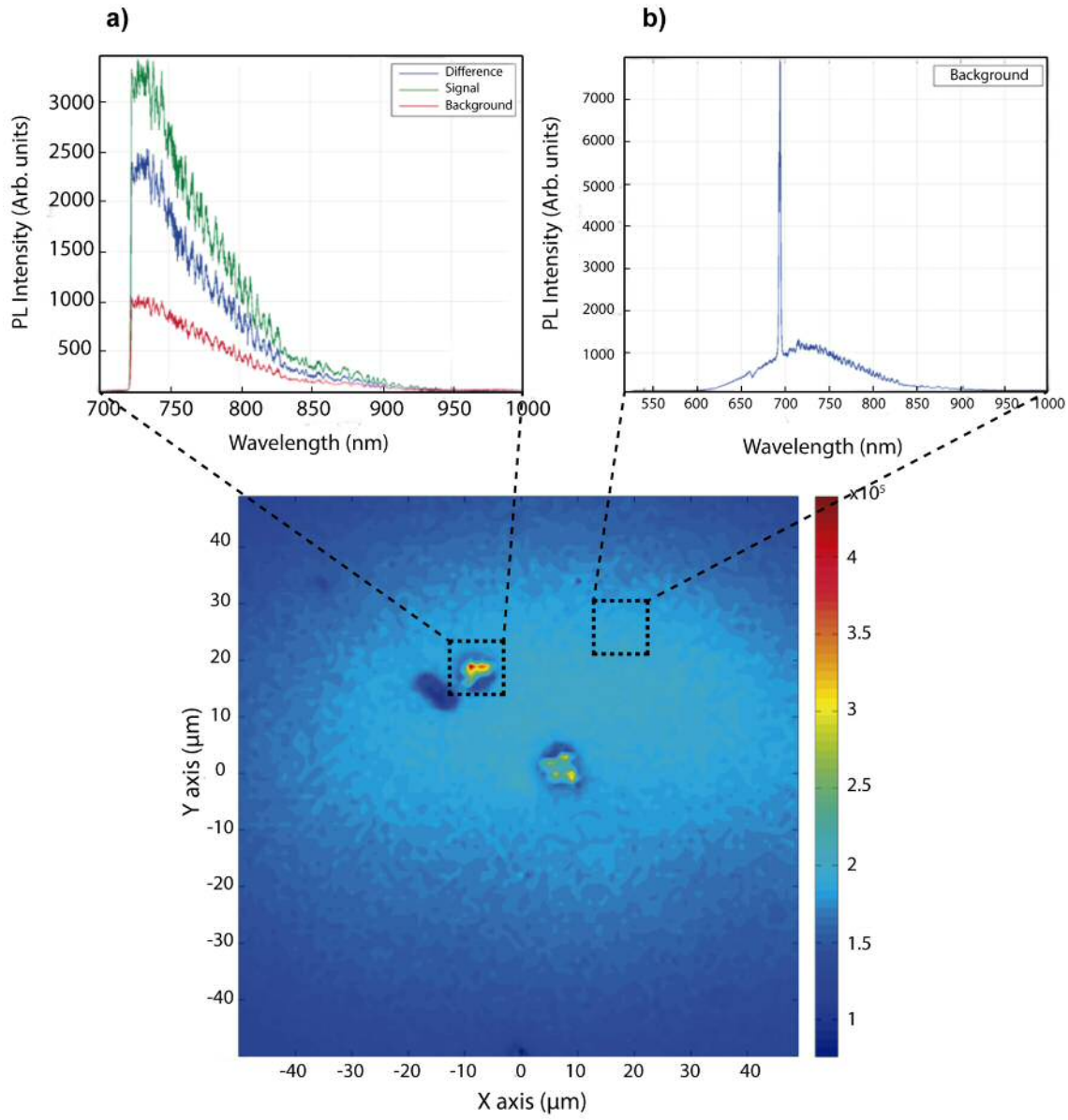

Figure 5.12: PL spectra and PL image of nanodiamonds grown on sapphire. a) PL spectrum of a characteristic nanodiamond showing the PL signal coming from the nanodiamonds, the background signal and the difference between both signals. b) Substrate luminescence signal and c) PL image of the scanned area.

5.5 Colour centres Fabrication processes: Milling strategies.

Single Crystal samples milling

As stated in chapter two, the outstanding properties of diamond nanoparticles have led to an increasing search and study of novel diamond nanoparticles properties. The importance of diamond nanoparticles containing colour centres has been highlighted throughout this chapter, with special emphasis in the NV centre and in the SiV centre as good candidates for quantum computing and quantum cryptography applications. The NV centre is probably the most investigated diamond colour centre, with interesting applications related to its spin properties. [76] Spin manipulation possibilities make this colour centre attractive as a magnetic field sensor and for magnetic imaging. [233] Furthermore, recent studies in levitated diamond nanoparticles containing the NV centre have been proposed to detect quantum superposition states, [234, 235] and as a method to detect quantum gravity. [236] On the other hand, the spin related properties of the SiV centre are not so well-known, although there are several studies in the literature.

In the previous section, the *in situ* CVD growth of nanodiamond particles containing colour centres was explained, and bright and photostable SiV centres on nanodiamonds growth by CVD on different substrates have also been achieved. Nevertheless, to enhance the emission from these colour centres it is necessary to couple these centres to a cavity or resonator, hence being necessary techniques to obtain nanodiamonds containing those centres. Several approaches such as pick and place methods involving AFM techniques [237] or the immersion of the substrates into an ultrasonic bath to obtain the nanodiamonds have been performed, but the first technique is challenging and time consuming. Therefore, it would be preferable to somehow obtain nanodiamond particles containing colour centres directly available to spin coat onto the desired substrate.

The creation of colour centres by doping commercial nanoparticles available (ion irradiation for instance), is feasible. However, increasingly demanding applications make necessary the use of high quality and contaminants-free diamond nanoparticles. Non-diamond carbon (sp^2) is commonly present in commercial diamond nanoparticles. The presence of such carbon on diamond surfaces leads to particle aggregation [96] and reactive sp^2species are detrimental for biological applications. Additionally, amorphous carbon and impurities are adverse for diamond nanoparticles levitation in high vacuum. The non-diamond

content absorbs the trapping laser light, heating and burning the diamond nanoparticles. [238] Apart from the adverse sp^2content, a non neglectable amount of metal contaminants [239, 240] is also present in commercially available nano-particles, hence reducing the possibilities of magnetic-related applications.

For these reasons, it is highly important to be able to create customized diamond particles. Several methods for particles' production are known up to date. The most versatile one is the production of diamond nanoparticles crushing CVD diamond or bulk diamond by milling techniques. [241] This approach enables particle size distribution control and offers the possibility of creating custom colour centres as well as particles from bulk diamond with low nitrogen concentration. Nevertheless, deep cleaning methods are required after the milling process.

This section is focused on different milling approaches, using different materials according to the final application. In the first subsection commercial single crystal diamond samples are milled using two different materials. The second subsection is then aimed at the production of diamond nanoparticles containing SiV centres milling CVD grown diamond films with different silicon content.

5.5.1 Milling and acid cleaning processes

Commercial CVD grown single crystal (SC) diamond samples (2.6 mm $\times$ 2.6 mm sized) sourced from Element six, with boron and nitrogen concentrations < 0.05 ppm and < 1 ppm respectively, were used in this study. Two different grinding bowls, one made of tempered steel and one made of silicon nitride, were used for crushing the SC plates. XPS, Raman, DLS and NTA and TEM measurements were performed to study the differences between the two grinding materials.

12 SC plates (95 mg approximately) were introduced in each grinding bowl with 5 ml of DI water and 30 and 40 grams of silicon nitride and tempered steel grinding balls (d=3mm) respectively. Samples were milled in a *Fritsch, Planetary Micro Mill Pulverisette 7*, following 6 cycles of 5 min on/15 min off at 1100 rpm. After the milling process, the samples were cooled down and taken out of the grinding bowls and several acid cleaning processes were performed. For iron removal, the cleaning was performed as described by *Heyer et al.* [241] Briefly, 30 ml of HCL was added to the slurry while continuous stirring in a condenser for 24 hours at 140°C bath temperature. For the silicon nitride cleaning, 20 ml of sample was mixed with 30 ml of orthophosphoric acid (H_3PO_4) and the mixture was

stirred continuously in a condenser during 24 hours at 180°C bath temperature. To remove the acids, both solutions underwent washing and centrifugation cycles at 30000g until the pH reached a value of 5.8. The slurries were dried in a hot plate to obtain the powders. For the silicon nitride grinding process, the obtained powder was introduced again in the condenser after being dissolved in water, and 30 ml of concentrated sodium hydroxide (NaOH) solution was added. The washing and centrifugation cycles were repeated until pH 5.8 was reached. After the cleaning and centrifugation cycles, both powders were treated in a furnace under air atmosphere at 600°C for 5 hours.

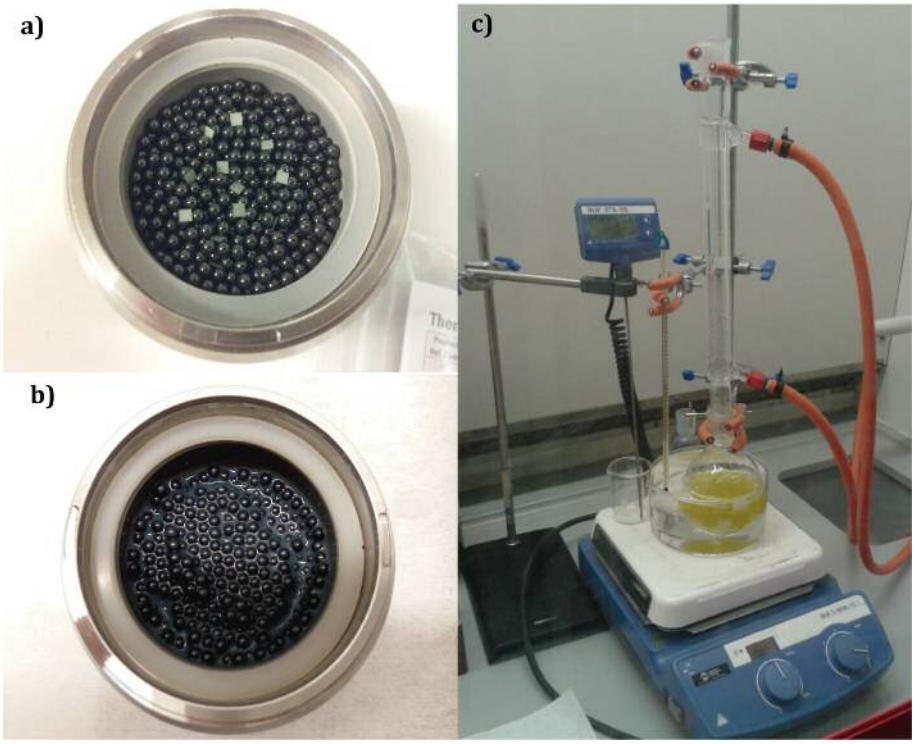

Figure 5.13: Single crystal milling process. a) SC plates inside the tempered steel grinding bowl before the milling and b) after the milling. c) Acid cleaning of the solution obtained in b).

5.5.2 XPS measurements

To compare the surface chemistry and the composition of each powder after the tempered steel and the silicon nitride milling process, X-ray photoelectron spectroscopy (XPS) data were taken using a *Thermo Scientic*^{TM} *K-Alpha*$^{+}$ *spectrometer*. A monochromatic Al source operating at 72 W (6 mA emission current x 12 kV anode potential), was used to acquire a survey spectra and high resolution scans of the interesting peaks obtained at pass energies of 150 eV and 40 eV respectively. Pass energy was achieved using a K-

Alpha charge neutralization system, which employs a combination of both electrons and low energy argon ions.

The elemental composition of the single crystal samples after the milling processes was measured by XPS. XPS measurements were taken in various steps. 1) On pristine SC substrate, 2) after tempered steel milling, 3) after tempered steel milling followed by acid cleaning and 4) after the silicon nitride milling followed by its corresponding acid cleaning treatment.

Figure 5.14 shows the XPS survey for the mentioned processes with all the detectable elements present in the samples. All XPS spectra were calibrated with the carbon C1s peak at 285 eV as will be explained below.

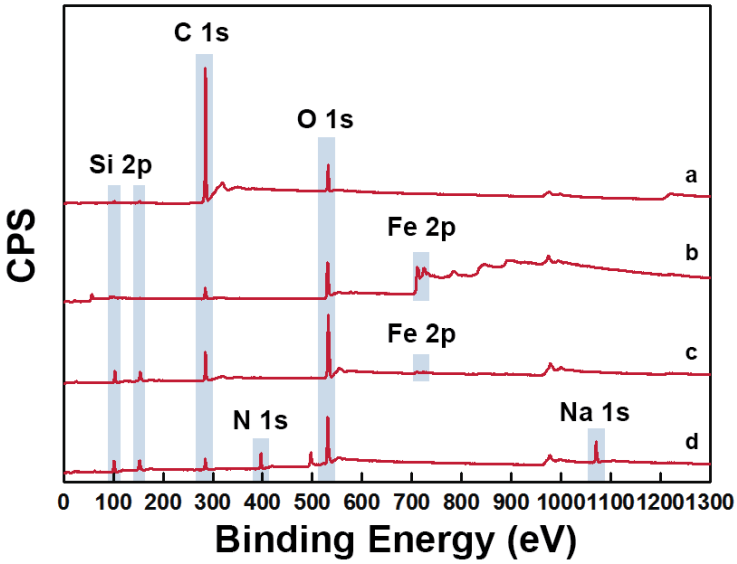

Figure 5.14: Survey XPS spectrum of the different samples. a) SC raw material just before the milling, b) powder after milling using tempered steel grinding bowl, c) powder after the tempered steel milling and the acid cleaning to remove the metal contaminants and d) powder after silicon nitride milling.

Figure 5.14a) shows the XPS spectrum of the as received SC substrate. The XPS spectrum shows two clear peaks corresponding to carbon (C1s peak) and oxygen (O1s peak) elements at 285 eV and 531.8 eV respectively. A small third peak (Si2p) also appears. No silicon should be present in the sample, so to check that this silicon was from some sample surface contamination, cluster argon ion cleaning was performed. After the cluster cleaning, the silicon peak disappeared completely. Survey XPS spectrum in figure 5.14b), shows four elements for the sample milled with the tempered steel grinding bowl, before the acid

cleaning: carbon (C1s), oxygen (O1s), iron (Fe2p) and silicon (Si2p). The Fe2p peak confirms the presence of iron in the sample. Although acid cleaning was performed to the sample in order to remove all the metallic components, non-negligible amounts of iron were detected (XPS detection limit is 10ppm), as shown in figure 5.14c). The Si2p peak presence can be ignored as this silicon is due to contamination present previous to the milling process and can be removed with argon ion cleaning inside the XPS chamber.

The C1s, O1s, Si2p, N1s and Na1s peaks are present in the SC sample milled with the silicon nitride grinding bowl (figure 5.14d). In this case, the Si2p and N1s peaks are related to silicon and nitrogen contamination due to insufficient cleaning of the silicon nitride produced in the milling. The Na1s peak is due to sodium contamination in the cleaning process, as NaOH was used in the cleaning. Nevertheless, iron (Fe2p peak) was not detected, making the use of a silicon nitride grinding bowl extremely important in magnetometry applications.

To obtain more information about the elements present in the samples, high resolution scans were performed over specific peaks. The data was deconvoluted using a Gaussian fit in the CasaXPS program, after subtraction of a Shirley type background. All the data has been normalized by dividing the intensities by the maximum value of the raw data. In XPS, the photoemission produces core holes in the sample, which induce surface charge. Photoelectrons ejected from the sample have to overcome this charge thus resulting in higher binding energies. While this is not an issue for conductive samples, the use of a charge compensator prevents surface charge accumulation for non-conducting samples, delivering a flux of low energy electrons at the surface and hence shifting the photoelectron peaks to lower energies. [66] For this reason, the shift in energy must be 'corrected' typically calibrating the C1s signal with a value of 285 eV, although other peaks can also be used as reference (e.g. Si2p). [242]

When analysing diamond and in general carbon containing samples, careful fitting procedures must be done as nanodiamond particles will present numerous carbon bonds attached to their surface, with small binding energy shifts between the components. The main component of the C1s peak is attributed to bulk and surface sp^3 C-C bonds, and it is usually calibrated at 285 eV or 284.8 eV. [242,243] There are several ways of assigning the different components of the C1s peak. The first one is to consider that the different components can be fitted at fixed known BE values (shifted in energy). The second one consists on fitting the C1s peak with different Gaussians and then looking for the resulting values in the literature assigning these values to the corresponding components. Both analysis were

performed for comparison, but the first one was the selected one as works better when different samples need to be compared. Nevertheless, similar results were obtained.

BE shifts were taken from the literature and used to deconvolute the C1s peak into its different components. Shifts of -1, +1, +2.5, and +4 eV were assigned to graphitic carbon, hydroxyl (C-OH)/ether(C-O-C), carbonyl (C=O), and carboxyl groups (COOH), respectively, providing an adequate fit to the data. [244] A peak at a BE shift of -3 eV was also added for the silicon nitride milled sample, which corresponds to Si-C, not present in the tempered steel one. Although these values have been used to deconvolute the C1s peak, [244] there is no consensus in the literature, as different BE values have been reported for the same chemical species, and small differences in the shifts assigned to each carbon component are also used. [245–248]

C1s and the iron Fe2p peaks are shown in figure 5.15. The C1s peak for the SC sample before any milling process shows a clear peak at 285 eV, attributed to the C-C bond which corresponds to sp^3 bonded carbon. In the same figure, the C1s peak of the SC diamond sample milled with the tempered steel grinding bowl presents a symmetric peak and although fitted with six peaks, consists basically of four Gaussian peaks, centred at 284 eV, 285 eV, 286 eV and 287.5 eV. The first peak at 284 eV correspond to C=C bonds. The peak at 285 eV corresponds to sp^3 bonded carbon, the peak at 286 eV is attributed to –C-H/C-O bonds [249] and the peak at 287.5 eV is assigned to the C=O bonds.

The C1s peak of the SC diamond sample milled with silicon nitride grinding bowl presents in contrast an asymmetric peak with a tail towards higher binding energies, characteristic of samples with higher sp^2carbon concentration. This peak can be deconvoluted into six Gaussian peaks, centred at 285 eV, 284 eV, 286 eV, 287.5 eV, 289 eV and 283 eV. The peak at the lowest energy, 283 eV confirms the presence of C-Si, also present in the high resolution Si2p peak shown below. The peak at 284 eV can be assigned to sp^2C=C carbon, the peak at 286 eV can be attributed to C-O sp^3, the peak at 287.5 eV is assigned to carbonyl (C=O) although can be neglected for the small content and the peak at 289 eV, that can be assigned to carboxyl groups (COOH) or the $\pi - \pi^*$ transition. [250, 251]

Therefore, clear differences are observed in the C1s peak between the tempered steel milling and the silicon nitride milling, observing a priori, further graphitization produced with the silicon nitride grinding balls, which will be detrimental for SiV photoluminescence stability.

The percentage of the relative contents of the C1s peak are shown in figure 5.16. In

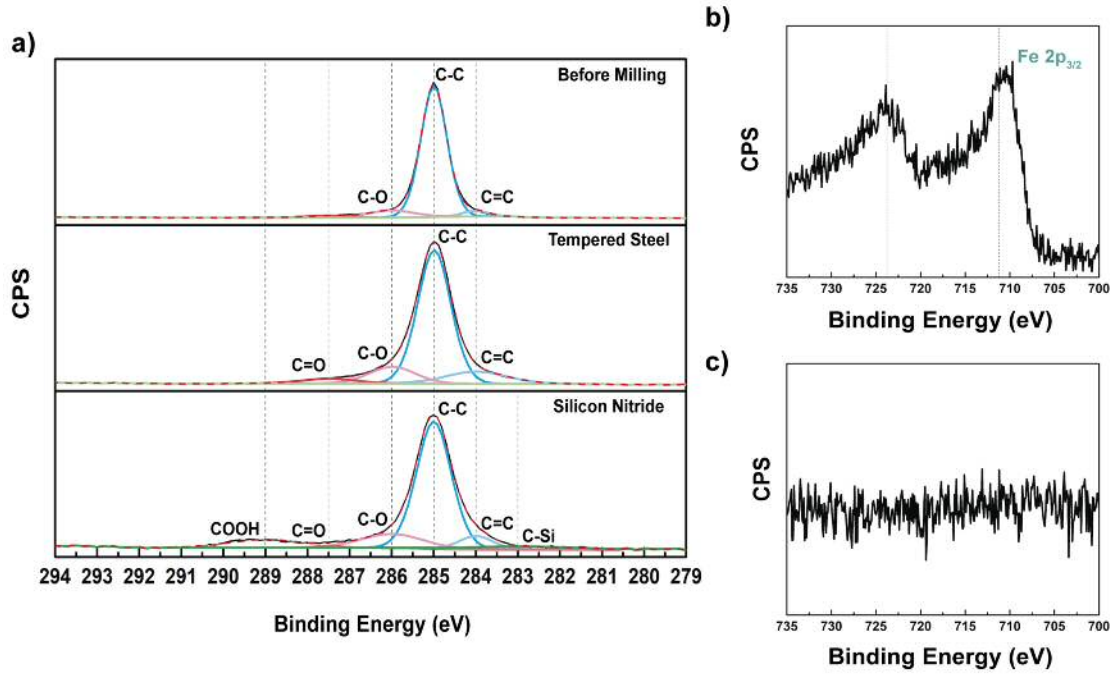

Figure 5.15: High resolution XPS scans for the carbon and iron elements. a) Carbon (C1s) deconvoluted peak for the as received SC, and the powders after been milled with the tempered steel and the silicon nitride grinding bowls respectively. b) Iron (Fe2p) peak for the SC samples milled using a tempered steel grinding bowl and c) Fe2p peak of the SC sample milled with the silicon nitride grinding bowl.

this case, five samples are represented: the SC sample before the milling process, the same sample after an argon cluster cleaning, the sample just after the milling with the tempered steel material and then the samples after the milling and cleaning processes, with the tempered steel and the silicon nitride materials. From the histogram it is clear that the sample with the highest sp^3 content (85.6%) is the SC sample before the milling process and suggested to an argon cluster cleaning, whilst sp^3 content decreases to 65.8% after the milling with the silicon nitride grinding bowl. On the other hand, the appearance of peaks related to COOH groups with an 8.68 % and C-Si (2.8 %) in the sample milled with the silicon nitride material, compensate the total C1s content.

Another important difference between the two milling processes is the detection of iron in the tempered steel sample. High resolution scans for the Fe2p peak were performed on both the tempered steel and the silicon nitride samples. Figure 5.15b) shows the Fe2p for the tempered steel sample. The binding energy of $Fe2p_{3/2}$ was observed at 711.2 eV and corresponds to the core level spectra of Fe^{3+} ions in their oxide form. Although iron was not detected in the SC sample milled with the silicon nitride grinding bowl, a more

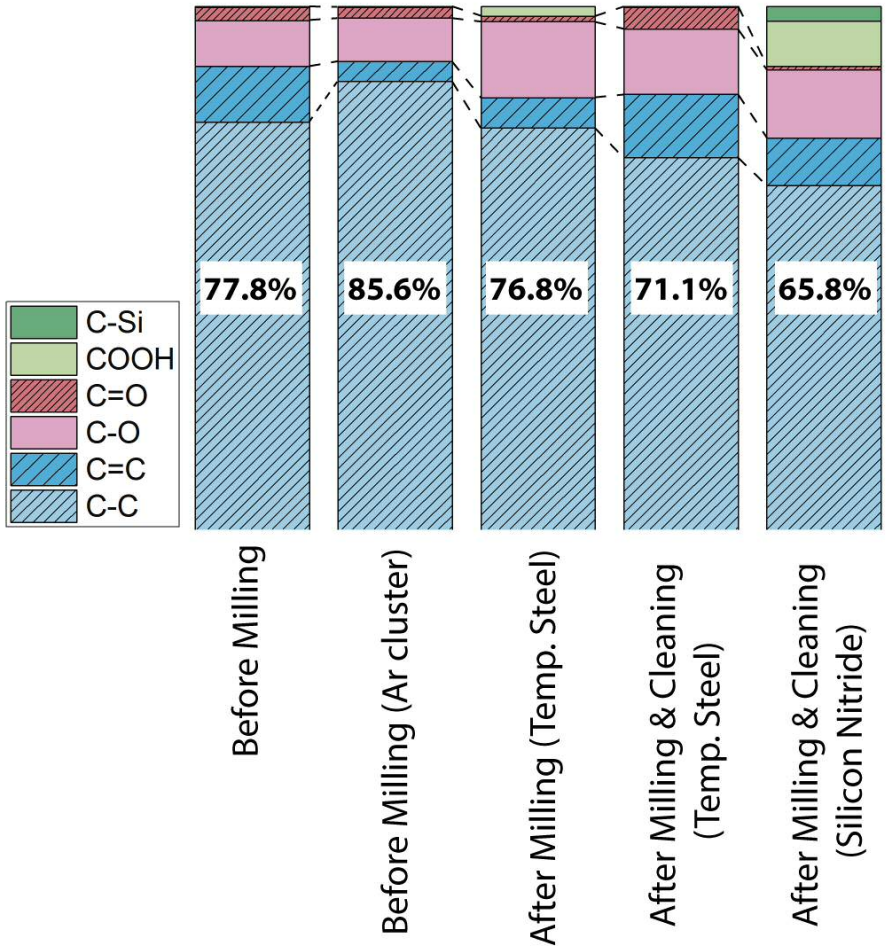

Figure 5.16: Histogram showing the percentages for the different components of the C1s peak for the SC samples.

detailed scan for the Fe2p peak was also performed is this sample for comparison. Figure 5.15c) shows the XPS measurement of this peak in which iron was not distinguished.

Even though silicon nitride milling seems to be the best method to avoid any metal content in the diamond particles produced, the silicon nitride material generated in the milling process is difficult to remove. Also the asymmetry in the C1s peak suggests a further surface graphitization of the particles when compared to the tempered steel milling process, and will be confirmed by the TEM measurements in the following subsections.

High resolution scans for the O1s peaks and the Si2p peaks were also performed. Oxygen was detected in the XPS analysis in both samples. The high resolution spectra for the

O1s peak is shown in figure 5.17.

For the SC sample milled with the silicon nitride grinding bowl (figure 5.17a)), the O1s peak consists of three Gaussians, centred at 531.1 eV, 532 eV and 535.8 eV. The peak at 531.1 eV with a FWHM= 2.18 eV, is associated with C=O. [245] The peak at 532 eV, with a FWHM= 2 eV, is due to C-O, and the peak at 535.8 eV can be attributed to carboxyl groups (COOH) or can also be due to atmospheric O_2 or CO_2 absorbed. [252, 253] The presence of the 289 eV peak in the C1s spectra also confirmed the presence of these COOH groups.

The O1s peak for the tempered steel sample is represented in figure 5.17b) and consists of a symmetric Gaussian distribution fitted with three Gaussians centred at 530 eV, 532 eV and 533 eV. The peaks are associated with metal oxide bonds (Fe=O, 530 eV), with organics bonds such as C-O (532 eV) and finally the peak at 533 eV can be associated to hydroxyl compounds or SiO_2. [253]

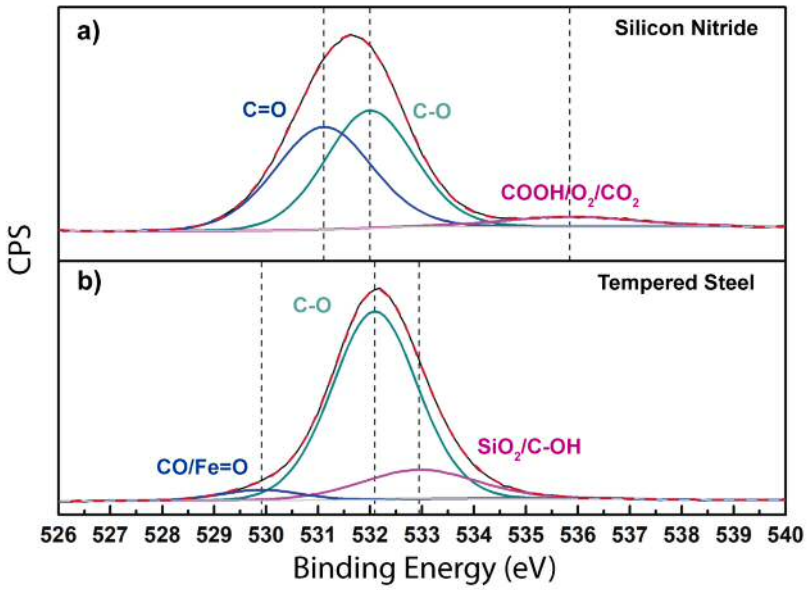

Figure 5.17: Deconvolution of the O1s peak, showing three Gaussian peaks in both the a) silicon nitride sample and b) tempered steel sample.

The high resolution Si2p spectra of SC milled with silicon nitride and tempered steel samples are shown in figure 5.18. A clear shift in the Si2p peak shows different Si bonding species for both samples. The data was fitted with two peaks in both cases.

For the sample milled with the silicon nitride grinding bowl and balls, the peak at 101.1 eV binding energy (FWHM= 1.64 eV), is associated with silicon carbide (SiC). This presence

was also observed in the C1s spectra with the appearance of a peak at 283 eV. [254, 255] The second peak at 102.4 eV, FWHM=1.92eV, corresponds to silicon bonded to nitrogen (SiN).

For the sample milled using the tempered steel grinding bowl, two completely different peaks are observed. The peak at 103.2 eV clearly shows the binding energy for the silicon dioxide, with FWHM= 2.2 eV, and the peak at 102.7 eV, FWHM= 1.6 eV, can be attributed to silicon sub oxides. Previous work based on both high resolution XPS spectra and theoretical calculations, investigate the different SiOx species. [256,257] These species consist of four Si oxidative states, Si^{1+}, Si^{2+}, Si^{3+} and Si^{4+}, with the Si2p core level shifts of 0.6, 1.5, 2.8 and 4.5 eV respectively. These results are in accordance with these studies, showing a difference of 1.2 eV between the Si^{3+} (Si_2O_3) and the Si^{4+} (SiO_2) states. [258,259] The O1s peak from SiO_2 at 533 eV was also observed in the O1s spectra.

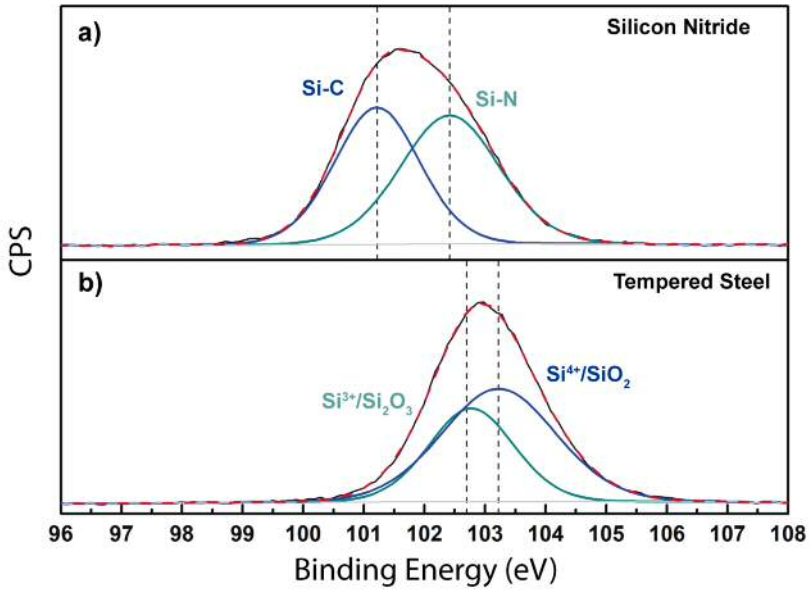

Figure 5.18: Deconvolution of the Si2p peak, showing two Gaussian peaks in both the a) silicon nitride sample and b) tempered steel sample.

Finally, a high resolution spectra was also taken on the N1s peak, confirming the presence of nitrogen. A single peak with 396.2 eV binding energy was fitted and is related to Si=N as shown in figure 5.19.

To summarize and compare the different elements that constitute the samples, atomic percentages were calculated from the XPS survey spectra considering the appropriate sensitivity factors. [260]

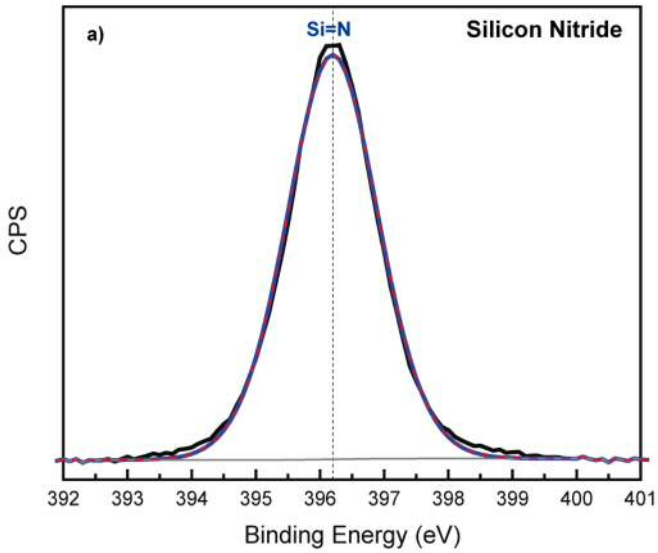

Figure 5.19: Deconvolution of the N1s peak

Samples	**Composition**				
	$C1s$	$O1s$	$N1s$	$Fe2p$	$Si2p$
Before Milling	90.6%	7.4%	0.29%	-	1.60%
Before Milling (Ar cluster)	96.5%	3.41%	-	-	0.05%
After Milling (Temp. Steel)	27.5%	40.1%	-	16.6%	15.85%
After Milling and cleaning (Temp. Steel)	38.8%	40.3%	-	0.20%	20.6%
After Milling and cleaning (Si_3N_4)	18.2%	38.2%	15.6%	-	28.1%

Table 5.1: Composition of the different samples in atomic percentages.

The SC sample before the milling and after a cluster Ar ion cleaning, shows the highest C1s content (96.5%) followed by a 3.41% of oxygen and almost negligible amount of silicon (0.05%). Just after the milling with the tempered steel grinding bowl, the amount of carbon decreases considerably (27.5%), with the appearance of the Fe2p peak due to the milling process, which represents up to 16.6%. It is clear that after subjecting the sample to an acid cleaning, the iron content is reduced (0.20%), being arduous the complete removal of it. Finally, the SC sample after the milling with the silicon nitride grinding bowl shows the lowest carbon content (18.2%) and a high nitrogen (15.6%) and silicon (28.1%)content due too insufficient cleaning after the milling.

5.5.3 ICP-MS

After the milling processes, a qualitative study of the elements present in the samples was performed with Inductively Coupled Plasma Mass Spectrometry (ICP-MS). The instrumental detection limit (IDL) for iron ranges from 1-10 ppt and 0.1-1 ppb for silicon. The samples analysed were the SC after been milled with both the tempered steel and the silicon nitride materials.

Nanodiamond samples were weighed into polypropylene 2 ml centrifuge tubes and treated with 200μL of 50% (99.99% purity) hydrofluoric acid. The samples were allowed to stand for 1 hour with occasional sonication prior to centrifugation at 16,700 rcf in an *Eppendorf R5154 centrifuge* for 10 minutes. 100 μL of the supernatant was taken and made up to 5 ml with 2% nitric acid in ultrapure water. The samples were analysed for ^{28}Si using an *Agilent 7900 series ICP-MS* equipped with an 'Inert Kit' glass free sample introduction system. All samples were repeated in triplicate and all sample runs were performed 5 times each. Calibration used 7 dilution points from 0.01mg/l up to 100mg/l. Spectrometer calibration was independently checked for acceptable (+/- 10%) linearity against a 6 Li standard. The results obtained are shown in the table below.

	Sample Mass (mg)	Sample Digest	%Si (ICP-MS)	Blank corrected	%Si	Mean	Abundance Corrected (^{28}Si=92.22%)
TS	3.15	1.575	0.1716	0.1647	10.4577	11.48	**12.45**
	2.69	1.345	0.1471	0.1401	10.4196		
	2.21	1.105	0.1568	0.1498	13.5596		
SN	3.09	1.54	0.2065	0.1995	12.9140	12.65	**13.72**
	2.20	1.10	0.1648	0.1579	14.3516		
	2.12	1.06	0.1203	0.1133	10.6924		
				Blank Average	1.38602		

Table 5.2: Si content in the samples after the tempered steel (TS) and the silicon nitride (SN) milling and after the respective acid cleaning processes.

From the results, it is clear that a lot of Si is still present in the silicon nitride sample, as was also detected in XPS. The silicon presence is due to an insufficient acid cleaning and was expected as the material retrieved after the whole process was more than the starting material. Nevertheless, the Si detection after the tempered steel cleaning does not have a particular explanation. Si measured in the sample in XPS after the tempered steel milling was related to surface contamination and was removed after a cluster argon ion cleaning

and according to the commercial distributor data sheets, Si is not present in the SC crystal samples. Furthermore cross contamination between both samples is not possible as new and different beakers were used for the acid cleaning. Nevertheless, the origin of the Si content detected can not be explained. Silicon has been detected however, in commercial detonation diamond samples. [239, 240] *Volkov et al.* performed a 68-elements analysis over 20 different commercial UDD samples, detecting relatively high amounts of Si in all them. [239] However, in this case, Si can be created due to the interaction of the explosion wave with the reactor chamber walls during the detonation synthesis process. [239]

5.5.4 Raman Measurements

To confirm the quality of the diamond powders obtained after crushing (and cleaning) the SC plates, Raman measurements were performed in an *in Via Renishaw* confocal Raman microscope equipped with a 532 nm laser. All the measurements were acquired using the same parameters: 10 seconds acquisition time and 50 accumulations.

Figure 5.20 represents the Raman measurements for the different SC powders. A sharp and clear diamond peak centred at 1332 cm^{-1} can be observed in both samples. However, in the silicon nitride sample, shown in figure 5.20b), a small G band between 1500 cm^{-1} and 1600 cm^{-1} is observed, which confirms the presence of sp^2 sites. Not much information can be determined from the Raman spectra.

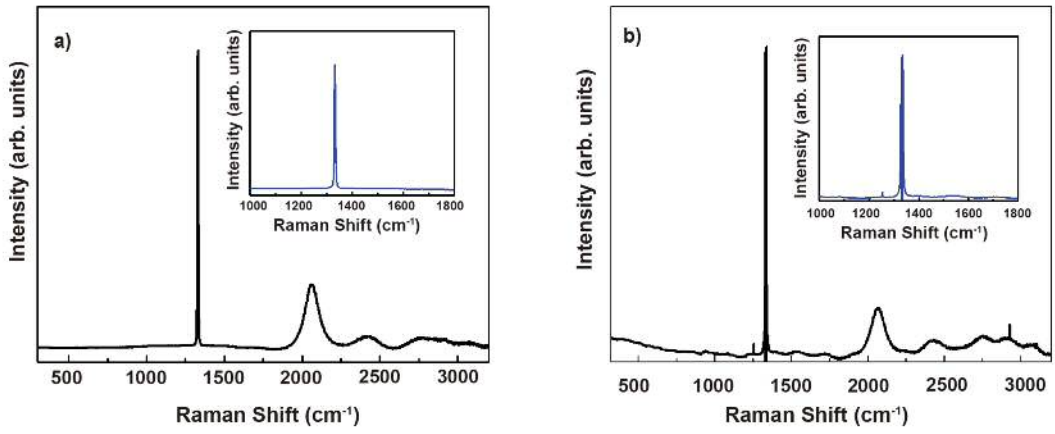

Figure 5.20: Raman measurements of the powders after the milling, acid cleaning and air annealing processes. a) SC powder after tempered steel milling process and b) SC powder after the silicon nitride milling process. Insets represent a zoomed image around the diamond peak.

5.5.5 Particles' size characterization

To have control over particles' size is highly important for the different applications. Particles with diameters of $< 70nm$ are desirable for quantum applications and particles with sizes below 10 nm being needed for most biological ones. For easier handling, it is also advantageous to be able to disperse the particles in different aqueous media, producing stable colloids. Particle sizes can then be controlled combining longer milling processes and colloid centrifugation at higher accelerative forces, collecting the stable supernatant. Once these colloids are produced, it is crucial to be able to accurately determine the particles' size.

As mentioned in chapter three, techniques such as dynamic light scattering and nanoparticle tracking analysis are among the most used ones due to size determination from colloids provides information from a wider distribution, as more material is analysed in a single measurement. Particles produced by milling techniques will have polydispersed size distributions and hence at least two methods are needed to confirm particles' size. However, drawbacks arisen from the method to determine the particles' diameter (intensity fluctuations in the Rayleigh scattering) will limit the DLS technique whilst the smallest particles (of less than 20 nm) can not be measured by NTA. TEM measurements in the next subsection will show these limitations.

To measure the size of the particles obtained milling the SC samples, colloids were prepared with the cleaned SC powders milled using both the tempered steel and the silicon nitride materials by dispersing 0.01 g of powder in 20 ml of deionized water. The colloids were dispersed via ultrasound and the solutions were centrifuged at different accelerative forces (5000 g, 10000 g, 20000 g and 30000 g) at 10°C in a *Sigma 3-30 KS centrifuge*. DLS and NTA measurements were performed to measure the particles' size distribution. A *Malvern Zetasizer Nano ZS* equipped with a 633nm laser in backscattering configuration (173°) and a *Malvern Nanosight LM10* equipped with a 635 nm laser were used respectively. Particles milled with both materials were measured, but only results obtained from the tempered steel milled sample are shown in figure 5.21. No difference in particles size was observed in DLS between the sample milled with the tempered steel grinding bowl and the silicon nitride one, but slightly smaller particles were detected by NTA.

Figure 5.21a) shows the distribution of particles after centrifugation at 5000 g. In the NTA analysis graph two different particles' sizes distribution peaks can be differentiated, 118 nm and 156 nm, whereas the particles' size distribution is broader for the DLS measurement.

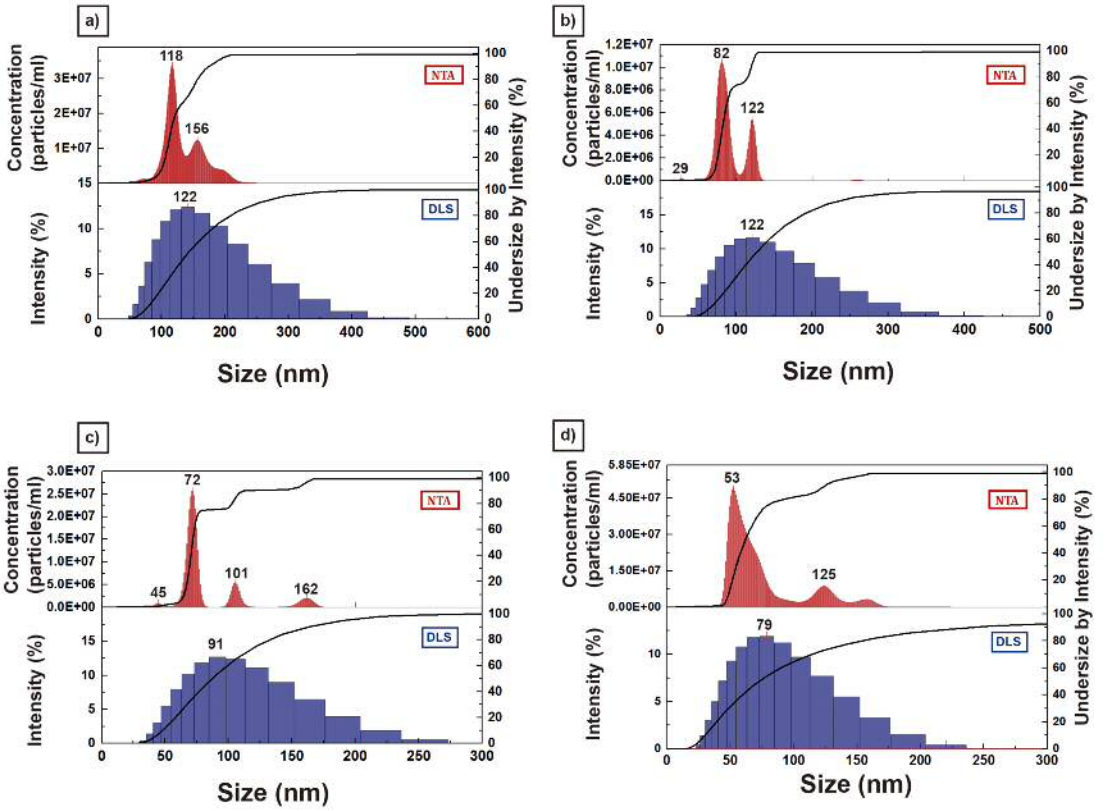

Figure 5.21: Particles' size distribution of the milled powder solutions measured by DLS and NTA after centrifugation at different accelerative forces: a) 5000 g b) 10000 g c) 20000 g and d) 30000 g.

This difference increases with increasing centrifuge accelerative force as seen in Figures 5.21b)-d). Three particles' size distribution were distinguish at 10000 g (Fig. 5.21b), 29 nm, 82 nm and 122 nm, but in the DLS measurement a mean value of 122 nm was obtained. Centrifugation at higher rpm, results in smaller fractions of particles, and particles' size distribution down to 52 nm were collected.

5.5.6 TEM Measurements

TEM measurements were performed to study morphological changes in the two samples, due to milling processes with different materials. Appreciable changes in size, shape and composition were obtained.

The TEM measurements were conducted by Georgia Wood, under the supervision of Prof. Julie Macpherson at University of Warwick. Tempered steel milled samples were drop cast onto carbon coated Cu TEM grid (300 mesh, Agar Scientific) and silicon nitride milled samples were drop cast onto lacey carbon grids. Bright field emission images and high

resolution images were recorded in a *JEOL 2100* equipped with a LaB6 electron gun and operated at 200keV.

Figure 5.22 corresponds to the SC sample milled with the tempered steel grinding bowl and balls and centrifuged at 30000 g. Figure 5.22a) shows lots of small and spherical nanoparticles, around 10-20 nm, with no amorphous carbon. Size distribution analysis were also performed on these images (Fig. 5.22b)), confirming the abundance of particles with sizes mainly between 10 nm and 40 nm. As seen in the previous subsection, such small particles were not detected by DLS or NTA due to the presence of the larger ones. Some larger misshaped particles were also present with areas of diamond and areas of amorphous carbon. Figures 5.22 c) and d) show detailed HRTEM images of small spherical particles and a larger nanoparticles respectively. Different diamond planes can be observed in figure 5.22c). These HRTEM images were analysed by Fourier transform and the analysis of the diffraction spots gave the d-spacing of the lattice hence identifying the material. From the analysis, the presence of iron oxide (also suggested by the XPS measurements), is confirmed in some of the larger nanoparticles as detailed in figure 5.22d) even after the acid cleaning.

TEM measurements of the SC sample after milling with the silicon nitride grinding bowl are shown in figure 5.23. Particles with entirely distinct and faceted shapes were observed with the presence of lots of large agglomerates and small irregular shaped fragments. The size distribution analysis performed with the previous sample could not be applied due to agglomeration and thus inability to distinguish individual nanoparticles. Figure 5.23b) shows a HRTEM image of one of the large agglomerates, with clear marked diamond planes and the presence of amorphous carbon. Most of the nanoparticles imaged contain both sp^3 and sp^2 carbon.

From all the measurements carried out in the SC samples explained throughout this section, it can be concluded that milling the samples using the tempered steel material or the silicon nitride material will produce nanoparticles with completely different characteristics. Depending on the final nanoparticles application, one material will preferably be used over the other. Although both samples are subjected to acid cleaning, the complete iron removal was not achieved, being detrimental for magnetometry applications. On the other hand, tempered steel milled particles will produce particles with brighter and more stable emission from SiV centres as will be explained in the next section. Particles obtained from the silicon nitride milling present large amount of graphitic carbon quenching the emission from SiV, whilst milling the samples with this material will ensure metal-free

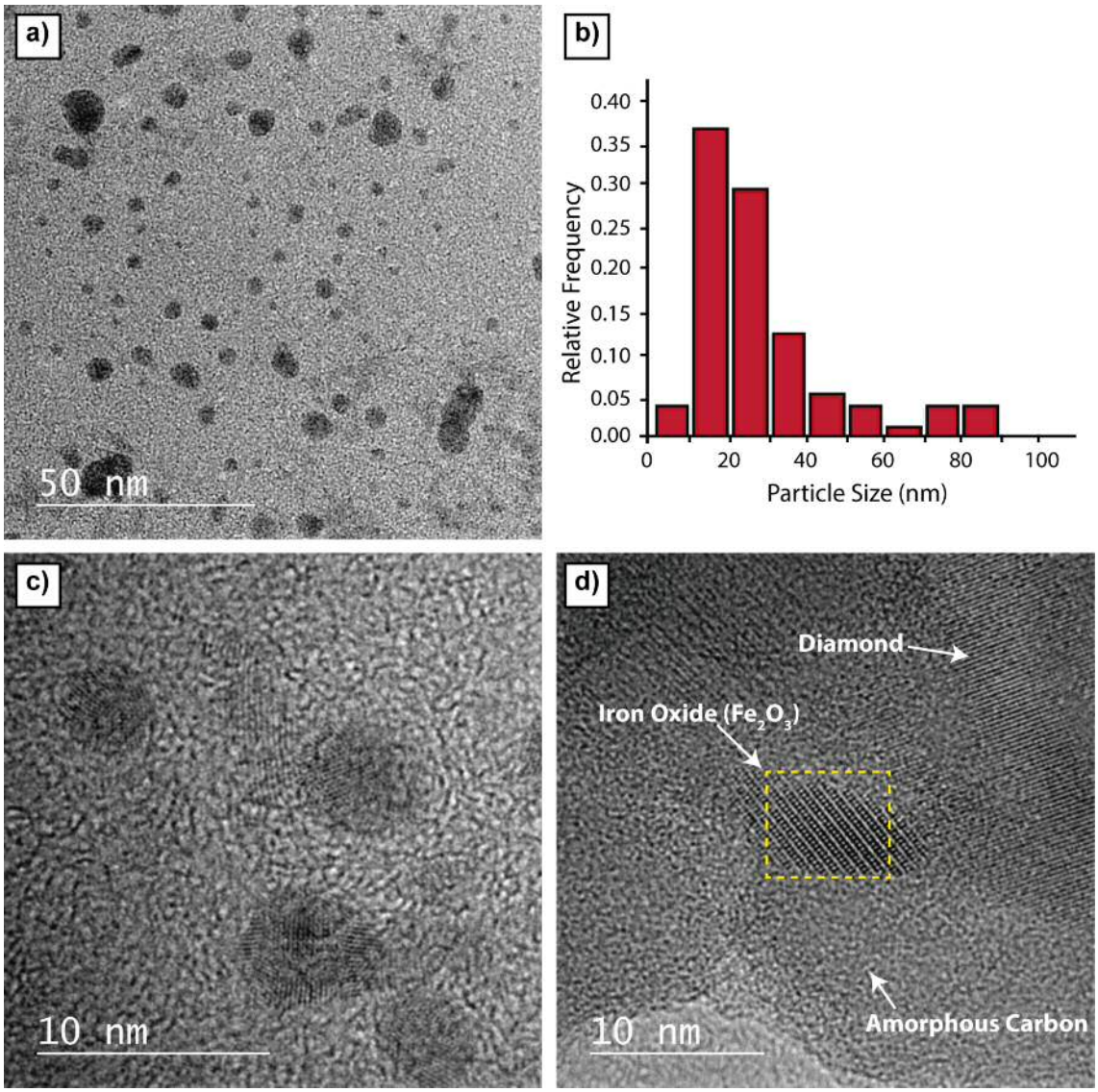

Figure 5.22: Unfiltered Transmission Electron Microscope images of particles obtained milling SC diamond samples with the tempered steel grinding material. a) Bright field image showing small isolated spherical particles. b) Size distribution analysis with particles sizes in the range between 10 nm and 50 nm. c) HRTEM image of small particles detailing different planes and d) HRTEM image of a large aggregate showing both the diamond lattice and the presence of iron oxide and amorphous carbon.

nanoparticles.

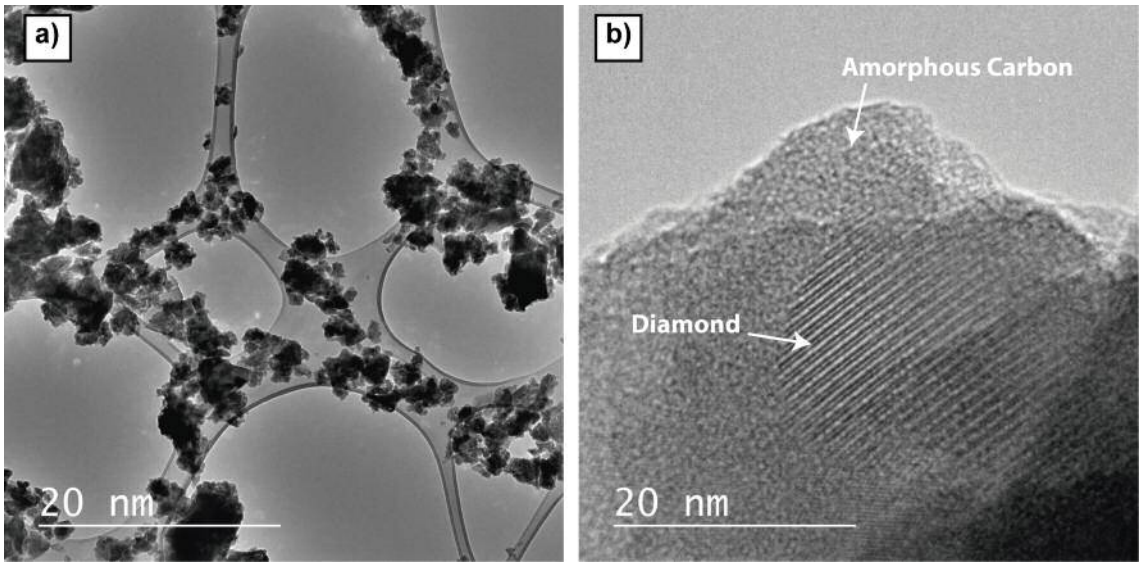

Figure 5.23: Unfiltered Transmission Electron Microscope images of particles obtained milling SC diamond samples with the silicon nitride grinding material. a) Bright field image showing the faceted and aggregated particles. b) HRTEM image of one of the agglomerates with diamond planes and amorphous carbon contents marked by arrows.

5.6 Colour centres Fabrication processes: Milling strategies.

Nanocrystalline Diamond Films Milling

At the beginning of this chapter, the production of nanodiamonds containing SiV centres grown by CVD onto different substrates was discussed. Whilst having superior collection efficiencies, the possibilities of tailoring these centres producing nanodiamonds ready for spin casting, open a much more interesting fabrication strategy through milling procedures.

In the previous section, the differences in morphology, composition and size seen between the two materials for milling diamond samples were discussed, in this section the results of diamond films milling with different Si content are presented. The faceted and graphitized particles (shown in figure 5.23) produced by the silicon nitride milling will have inferior optical properties as explained through this section.

Diamond film growth was performed either using Si wafers as substrates or growing directly onto the molybdenum holder to avoid time-consuming substrate etching. In both processes, six Si pieces were placed inside the reactor to allow the SiV formation, although in the case of using Si substrates, these centres are also created due to the substrate plasma etching. Figure 5.24 shows one of these growing procedures.

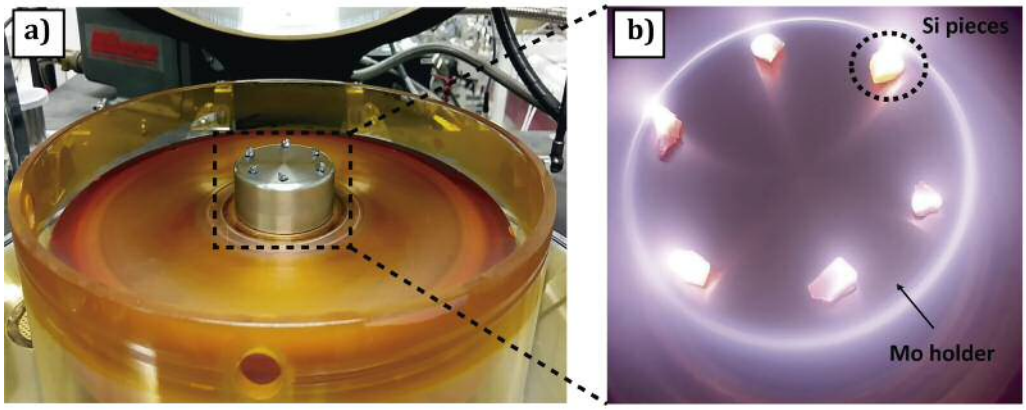

Figure 5.24: Diamond growth on top of a Molybdenum holder. a) Holder with Si pieces on top, placed inside the reactor chamber, to create diamond films with SiV centres. b) Plasma during CVD diamond growth.

5.6.1 CVD Growth onto Silicon substrates

The first samples were grown in a *Seki AX6500 CVD* reactor. Prior to growth, standard SC1 cleaning (as detailed before) was performed, using 2 inches p-type 100 silicon wafers of 500 μm thickness. Substrates were rinsed in DI water in an ultrasonic bath for 10 minutes and then spun dry. Si wafers were then seeded by placing the wafers inside a mono-dispersed colloid containing hydrogen terminated diamond nanoparticles (5 nm) in DI water whilst undergoing agitation in an ultrasonic bath for 10 minutes, thus ensuring high nucleation densities. [156] Following this treatment, the Si wafers were rinsed, spun dry and placed inside the reactor chamber. To prevent diamond seeds from etching during ramp up to growth conditions, an incubation process was performed. During the incubation period, the methane flow was kept at 20 sccm, diluted in 495 sccm of H_2 ($CH_4 : H_2 = 3.88\%$). The methane concentration was reduced to 5 sccm for the subsequent growth ($CH_4 : H_2 = 1\%$) in a total flow of 500 sccm. The microwave power was set to 3.5 kW and the chamber pressure was 40 torr. Temperatures of approximately 900°C were measured with a high temperature dual-wavelength Williamson pyrometer. To ensure hydrogen termination and to prevent non-sp^3 carbon to be deposited, samples were cooled down in a hydrogen plasma. Growth rate and samples thickness were *in-situ* monitored by laser interferometry and samples thickness was also *ex-situ* determined with a *Filmetrics F-20 Spectral Reflectance system*. The growth rate was 0.1 μm/hour and ten one-micron thick diamond films were grown.

SEM and Photoluminescence measurements before the milling

SEM and PL measurements were performed on two of these films to check the morphology and PL emission. In the other eight samples, the Si wafer was etched away and the diamond films remaining were milled. SEM measurements were performed at Cardiff University, in a *Raith e-Line* Scanning Electron Microscope (SEM), operating at 20 kV and a working distance of 10 mm, with an image of one of these films shown in figure 5.25a). The SEM images show complete coalescence of the film with 500 nm faceted diamond grains. PL measurements, shown in figure 5.25 b), were measured at Saarland University (Germany). Measuring single SiV centres is not possible in nanocrystalline diamond films as many SiV will be present and because of the high background fluorescence, hence the importance of obtaining nanodiamonds out of these films. However, peaks around 740-750 nm indicate the presence of SiV defects, which is a good start to produce nanodiamonds containing

these centres.

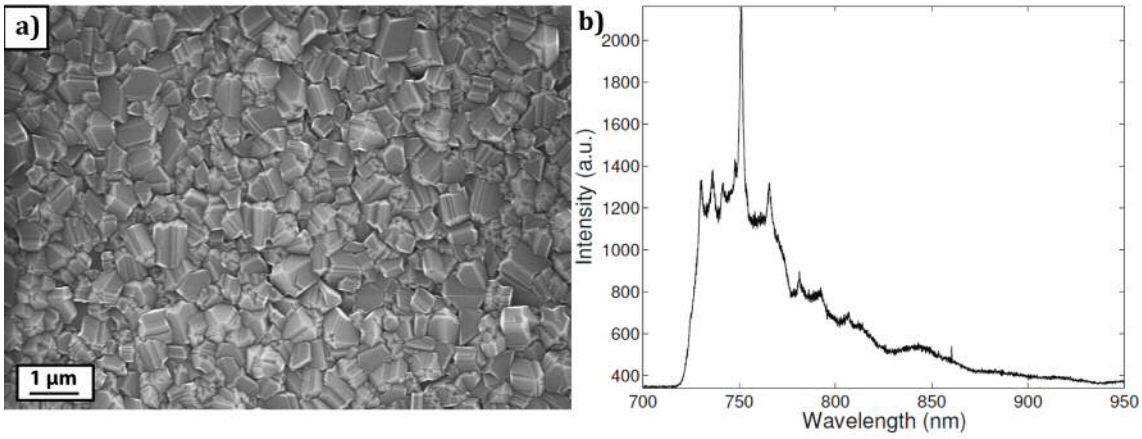

Figure 5.25: a) SEM image of the diamond film grown inside the CVD reactor and b) PL measurement of the same film showing the SiV emission with a prominent peak at around 750 nm.

The Etching, milling and acid cleaning processes

After the growth process, the silicon substrates were etched for subsequent diamond film milling. An isotropic wet etching was performed at Cardiff University in a 1000 class cleanroom. Standard methods for Si etching have been extensively reported in the literature, [261, 262] and the one used in this case consists of a mixture of Hydrofluoric acid (HF), Nitric acid (HNO_3) and Acetic acid (CH_3COOH), in a proportion of 3:5:3, [263] with an overall reaction shown below:

$$Si + HNO_3 + 6HF \rightarrow H_2SiF_6 + HNO_3 + H_2O + H_2 \tag{5.1}$$

While the HNO_3 drives the oxidation of the silicon and HF fluoride ions form the H_2SiF_6 (soluble), the acetic acid then prevents the dissociation of H_2SiF_6 into NO_3^- or NO_2^-. [263] Due to the impossibility of increasing the temperatures during the etching process because of cleanroom facility safety regulations, low etching rates were observed. For this reason, growth directly onto the molybdenum holder was also performed as explained later.

Once the first four silicon wafers were completely etched, 40 mg of diamond were obtained. The 40 mg of diamond film containing the SiV centres and 5ml of DI water were placed inside the silicon nitride grinding bowl of the *Planetary Micro Mill Pulverisette 7* with 80 silicon nitride grinding balls (d=3mm). The mixture was milled for two hours, with 12

cycles of 5 min on + 5 min pause at 600 rpm and 12 cycles of 5 min on + 5 min pause at 1100 rpm, with a centrifugal acceleration of 95g.

Roughly the same amount of diamond was obtained from the etching of the other 4 wafers. The diamond films were placed inside a tempered steel grinding bowl with 5 ml of DI water as well as 40 grams of tempered steel grinding balls. The milling process was the same as the one performed with the silicon nitride grinding bowl.

After the milling with the silicon nitride grinding bowl, a grey mixture slurry of diamond powder/DI H_2O and Si_3N_4 remains was obtained as well as a black slurry for the tempered steel sample. In the first attempt, the silicon nitride sample was not cleaned as the cleaning process was still under study. On the other hand, acids treatments for the tempered steel sample were performed as detailed in the section 5.5.

After the removal of the iron as described, the obtained slurries were dried out and the powders obtained were treated in an air oven at 400°C during 5 hours. As seen in chapter four, air annealing efficiently removes non-diamond carbon (sp^2) [102] which is present in the samples, first as a result of the milling process and secondly, because of non-diamond carbon preferentially present in the CVD diamond films grain boundaries. Also the nanodiamonds surface is partially oxidized previous any air annealing treatments due to the acid cleaning processes. However, annealing at too high temperatures can cause diamond etching, hence temperatures below 500°C were selected. [104] Furthermore, *Neu et al.* reported improvement in the crystalline quality after air annealing, with a narrowing of the Raman diamond peak as well as an enhancement of the single photon emission probability. [264] Figure 5.26 shows Raman measurements performed in ensemble NDs and PL measurements in both ensembles and single nanodiamonds, taken from reference [264]. Different air annealing processes at temperatures of 460°C and at 480°C as well as a hydrogen treatment are compared, showing a reduction in non-diamond content after the air annealing.

The amount of material collected after the oxidation process for the sample milled with the silicon nitride material weight around 20% more than the material before the milling process, concluding that a lot of contamination is created during the milling using the Si_3N_4 material. Conversely, there is a change in mass after the milling with the tempered steel grinding bowl as expected after all the processes conducted.

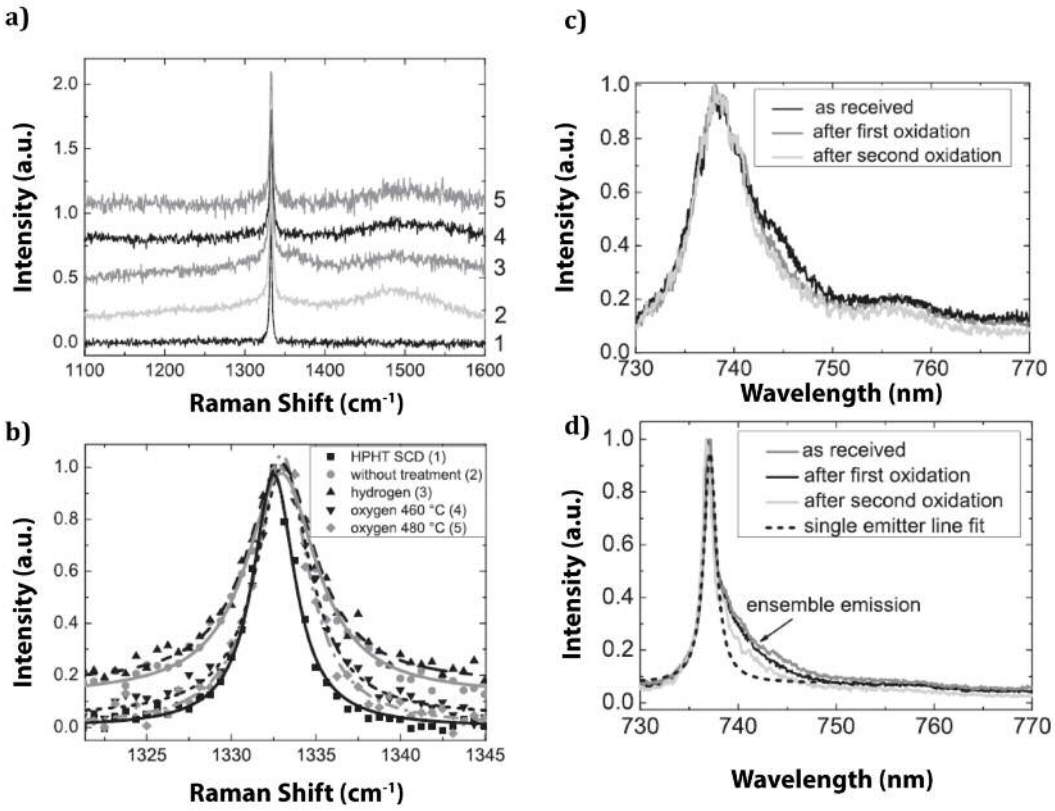

Figure 5.26: a) Raman spectra of an ensemble of nanodiamonds obtained via the BASD method from a polycrystalline CVD diamond film after different annealing treatments. Curve 1 shows an HPHT SC diamond spectrum for comparison. Curve 2 corresponds to a non-annealed sample, curve 3 shows a spectrum after a hydrogen annealing treatment, and curves 4 and 5 correspond to a sample treated at 460°C and a sample annealed at 480°C respectively. b) Detailed spectrum of the diamond Raman peak fitted with a Lorenztian curve. c) PL Spectra of a SiV ensemble of nanodiamonds after different oxidation steps. d) Single SiV emission spectra after the oxidation processes. Reprinted from E. Neu, F. Guldner, C. Arend et al., 'Low temperature investigations and surface treatments of colloidal narrowband fluorescent nanodiamonds', Journal of Applied Physics, 113, 20, Copyright (2013) with permission from AIP Publishing.

Photoluminescence measurements after the milling

0.01 grams of the oxidized powder (diamond sample) of each sample were mixed with 20 ml of DI water and the mixture was ultrasonicated for 10 min. Samples were drop casted onto quartz substrates and PL measurements were conducted at Oxford University. PL measurements were conducted at room temperature. A laser with a 532 nm wavelength operating in continuous wave mode was used as excitation source. The laser power was

1mW and a 0.9 N.A. lens was used. Figure 5.27a) shows a PL image of a scanned area with several nanodiamonds agglomerated, with PL spectra represented in figures 5.27b), 5.27c) and 5.27d). The PL spectrum in figure 5.27b) does not resemble SiV centres, rather a broad band between 600-750 nm. This signal can be due to in part background contribution and sp^2carbon still present in the samples. On the other hand, both spectra in figures 5.27c) and 5.27d) show some SiV broad peaks at around 750 nm, but still exhibit a broad band at longer wavelengths probably caused by sp^2carbon.

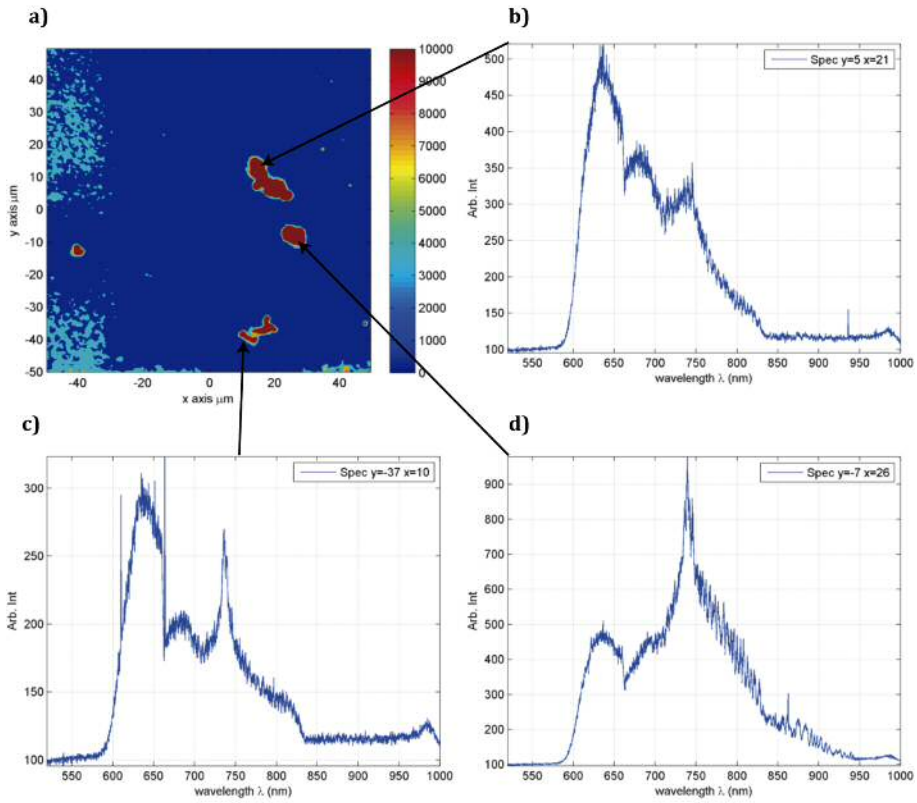

Figure 5.27: PL image and PL spectra of nanodiamond ensembles obtained from the milling of nanocrystalline CVD grown diamond films, with a tempered steel grinding bowl and balls. a) Nanodiamonds ensemble showing a broad band due to non-diamond carbon present in the sample. b) and c) several nanodiamonds with SiV signatures.

Similar PL set-up conditions were used to measure the samples milled with the silicon nitride grinding bowl, shown in figure 5.28. No SiV emission was found, probably due to an acid cleaning step not being performed, the presence of sp^2carbon on the nanodiamonds surfaces or the different properties of the nanodiamonds created using the silicon nitride grinding bowl.

Although some of the nanodiamonds produced show promising PL characteristics, further improvements are required, as well as efficient silicon nitride cleaning, as many of the

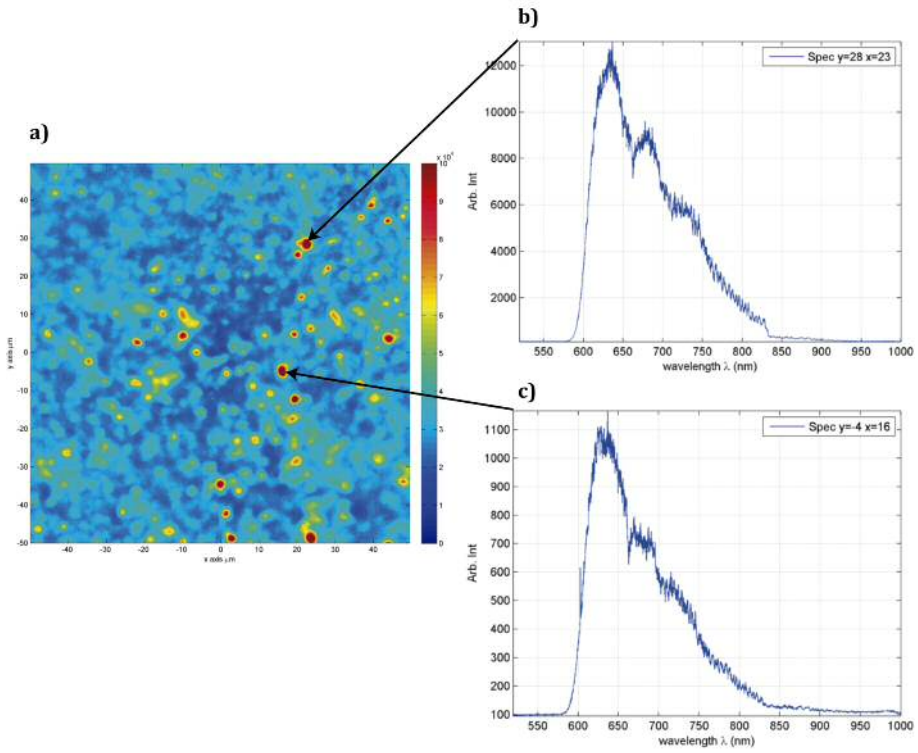

Figure 5.28: a) PL image and b) and c) PL spectra of nanodiamond ensembles obtained from the milling of nanocrystalline CVD grown diamond films, using a silicon nitride grinding bowl and balls.

nanodiamonds measured did not exhibit either a bright or stable SiV emission.

5.6.2 CVD growth onto Molybdenum holder

The CVD growth process was repeated, but this time the growth was directly conducted onto the molybdenum holder to avoid the necessity of etching the Si substrate. The Mo holder was seeded with the hydrogen-terminated diamond nanoparticles mono-dispersed colloid placing several drops of the slurry on top of the holder. The holder was dried in air and then placed inside the reactor for the growth process. Silicon pieces were also placed around the holder, as shown in figure 5.24 to create SiV centres. An incubation process was also performed to prevent diamond seeds etching, with a methane flow of 15 sccm, diluted in 285 sccm of H_2 ($CH_4 : H_2 = 5\%$) during this period. The methane concentration was then reduced to 9 sccm for the subsequent growth ($CH_4 : H_2 = 3\%$) in a total flow of 300 sccm. This time the methane percentage was increased to increase the growth rate. The microwave power was set to 4.5 kW and the chamber pressure was 50 torr. Higher temperatures, of approximately 1000°C, than the ones used for the previous growth were

measured with a high temperature dual-wavelength Williamson pyrometer. Diamond films with thickness of more than 10 μm need to be grown in order to delaminate the film from the Mo holder. The growth was stopped after 75 hours, and pieces of diamond were collected from the reactor up to a total of 400 mg.

Milling and acid cleaning process

An equal amount of diamond was placed in the tempered steel and the silicon nitride grinding bowls as well as 5 ml of DI water. As more material was placed inside the grinding bowl, 150 ball of silicon nitride were placed inside it, whilst 40 grams of balls were introduced inside the tempered steel bowl. 6 cycles of 5 min on/15 min off were performed at 1100 rpm in both cases. After releasing the pressure inside the bowl, another 6 milling cycles were performed.

For the cleaning process after the silicon nitride milling, DI water was added to the slurry resulted from the milling, up to a total of 20 ml, and the milled slurry/DI H_2O was mixed with 30 ml of H_3PO_4 and stirred continuously in a condenser at 180°C bath temperature for 24 hours. On the other hand, the slurry obtained after the tempered steel milling, was taken out of the grinding bowl with another 20 ml of DI water. 30 ml of HCL were added to the slurry while continuous stirring in a condenser for 24 hours at 140°C bath temperature. To remove the acids, both solutions underwent washing and centrifugation cycles at 50000g until the pH reached a value of 5.8. Both slurries were dried in a hot plate to obtain the powders. Nevertheless, the silicon nitride milled powder was dispersed in 30 ml of DI water and introduced again in the condenser with 30 ml of concentrated sodium hydroxide (NaOH) for another 24 hours at 140°C. The washing and centrifugation cycles were repeated until pH 5.8 was reached. The amount of powder recovered after the silicon nitride grinding was double than the material at the beginning, so a lot of silicon nitride must be present in the material. However, less powder was weighed after the tempered steel sample, indicating a further cleaning. The silicon nitride milled powder was treated in a furnace under air atmosphere at 400°C for 5 hours as was the tempered steel milled powder.

Photoluminescence measurements after the milling

The photoluminescence measurements were conducted at Oxford University, using the same set-up as for previous measurements (detailed in 5.6.1). After the air annealing,

both tempered steel and silicon nitride milled samples were drop cast onto quartz substrates. Similar results were observed for both materials. Unfiltered samples and filtered samples (filtered using a PTFE membrane filter with $0.1\mu m$ pore size) were measured. Figure 5.29 shows PL measurements performed on the unfiltered samples, all from large structures corresponding to either agglomerates or micron-size diamonds. Many bright features were observed. Most of the PL spectra obtained from the large structures present similar peaks as those represented in figures 5.29b), 5.29c) and 5.29d), with a broad band ranging from 600 nm to 700 nm suggesting sp^2presence on nanodiamonds and broad peaks around 740 nm, distinctive of SiV centres. Much more interesting results were obtained after filtering the samples, shown in figure 5.31. Filtering through 100 nm pore size reduces the concentration of agglomerates, producing a uniform consistency although it reduces the amount of material drastically. Most of the nanodiamonds analysed show a narrower SiV peak, centred between 738-740 nm. Peaks were fitted with both Lorentzian and Gaussian distributions, with FWHM values between 6 nm and 13 nm for the peaks analysed. The narrowest peak observed was centred at 700 nm (FWHM=1 nm) and was fully characterized to check if this SiV emission corresponds to a single photon emitter.

Saturation and Intensity autocorrelation measurements

Saturation measurements were performed on the narrowest peak, to determine the photon count rate, one of the key figures of merit of single photon sources. The count rate (I) can be estimated as a function of the incident optical excitation power given by:

$$I = \frac{I_{sat} P}{P + P_s} \tag{5.2}$$

where P_s is the saturation power, obtained measuring the power dependence of the fluorescence intensity [62] and I_{sat} the maximum photon rate. The emitter studied showed clear saturation (figure 5.31d)) with a count rate value of $I_{sat} = 6.2x10^3 cts/s$ and a saturation power of $P_{sat} = 0.025mW$.

The population dynamics and the single photon nature of this colour centre were established by measuring the second-order intensity autocorrelation function, $g^{(2)}(\tau)$ in the time

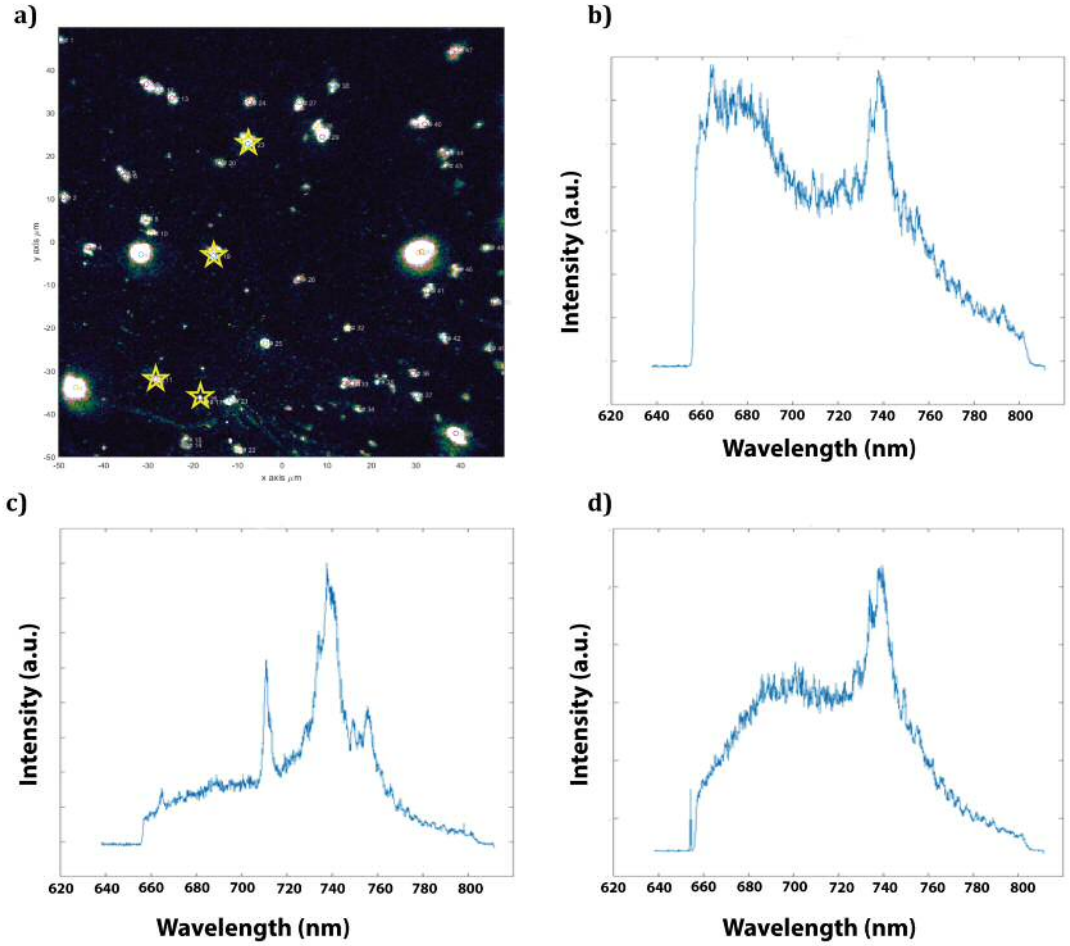

Figure 5.29: a) PL image and b), c) and d) PL spectra of unfiltered nanodiamond ensembles obtained from the milling of nanocrystalline CVD grown diamond films, using a silicon nitride grinding bowl and balls.

domain, defined by:

$$g^{(2)}(\tau) = \frac{\langle I(t)I(t+\tau)\rangle}{\langle I(t)\rangle^2} \tag{5.3}$$

Equation (5.3) can be rewritten as:

$$g^{(2)}(\tau) = \frac{\langle n(t)n(t+\tau)\rangle}{\langle n(t)\rangle^2} \tag{5.4}$$

where n is the photon detection event, proportional to classical intensity. However, for analysis of the autocorrelation function it is more common to express the equations as derived from the electronic structure of the system. For example, if a two-level system is

considered (an excited state and a ground state), equation (5.4) results in:

$$g^{(2)}(\tau) = 1 - e^{-\tau/\tau_0} \tag{5.5}$$

where τ_0 is a constant.

In a single quantum system, two photons can not be emitted simultaneously, and a spontaneous emission lifetime needs to occur before the emission of a new photon, which mathematically means that the autocorrelation function vanishes at $\tau = 0$ for an ideal single-photon source. However, in practise, systems with $g^{(2)}(0) < 0.5$ are also considered as single emitters. The statistics defining a single emitter are known as antibunched, in contrast to those for the coherent light (described by a poisson distribution) with values of $g^{(2)}(0) = 1$. Nevertheless, the appearance of an intensity-dependant bunching effect (with $g^{(2)}(0)$ exceeded one) is also possible, revealing the presence of a metastable excited state. [210] Hence, the electronic structure is described as a three-level system, including a shelving state. More complex three-level systems have also been proposed in the literature, but is beyond the scope of this thesis. [63] An example of bunching and antibunching effect of the autocorrelation function are shown in figure 5.30a) as well as a three level diagram, shown in figure 5.30b).

Resolving analytically the rate equations as described elsewhere, the autocorrelation function results in:

$$g^{(2)}(\tau) = 1 - (C+1)e^{-|\tau|/\tau_1} + Ce^{-|\tau|/\tau_2} \tag{5.6}$$

where

$$\begin{aligned}
\tau_{1,2} &= \frac{2}{A \pm \sqrt{A^2 - 4B}} \\
A &= k_{12} + k_{21}k_{23} + k_{31} \\
B &= k_{12}k_{23} + k_{12}k_{31} + k_{21}k_{31} + k_{23}k_{31} \\
C &= \frac{1 - \tau_2 k_{31}}{k_{31}(\tau_2 - \tau_1)}
\end{aligned}$$

and k_{12} is proportional to the excitation intensity. From the equation above, it is clear that if $C = 0$ the three level system results in the two level scheme, and hence C determines

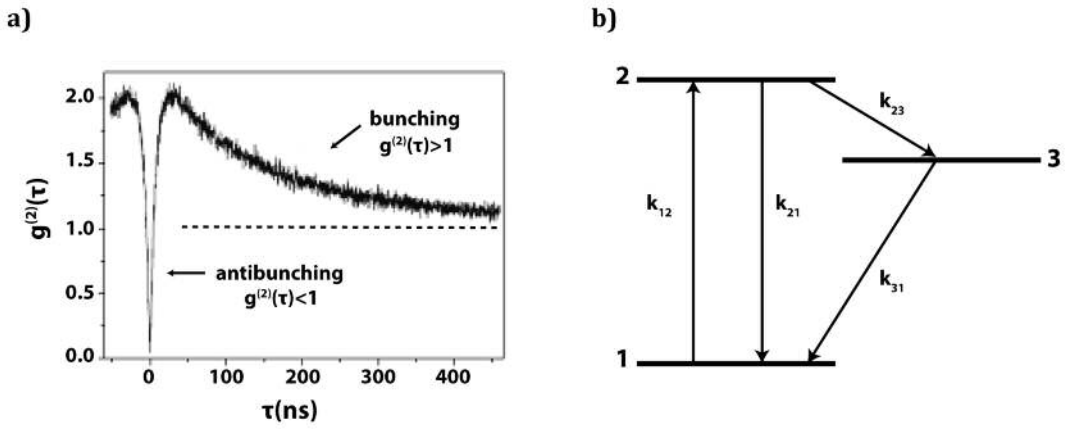

Figure 5.30: a) $g^{(2)}(\tau)$ autocorrelation function of single photon emitter showing the characteristic antibunching effect and b) three-level diagram of a SiV centre.

how important is to consider the three-level scheme in a given system.

This correlation function was measured in a Hanbury Brown and Twist (HBT) set-up [265]. The incoming signal is split by a 50:50 beam splitter onto single-photon detectors (two avalanche photo-diodes). The $g^{(2)}(\tau)$ autocorrelation function is then obtained from the normalized histogram of the delay times between successive photon detection events. High signal intensities are required, in practise, photon count rates need to be above $10^4 s^{-1}$. From these measurements, no clear single-photon emission from the emitter was detected, as shown in the inset of figure 5.31d). As previously reported, [63] there are several factors that can explain the non-vanishing $g^{(2)}(0)$ value. The most obvious one is the presence of several emitters in the nanodiamond under study although it is challenging to distinguish between emitters. The second one is due to the background fluorescence from the nanodiamond in which the colour centre is placed. This fluorescence (mainly in the 600 nm-800 nm spectral band region) in most of cases is attributed to sp^2 carbon and explained by the creation of electronic states within the bandgap. The third reason would be limited timing resolution of the experimental setup, which is less likely.

To summarize, some peaks with clear SiV emission were found after appropriate acid cleaning with both HCL or H_3PO_4 for the samples milled with the tempered steel and the silicon nitride materials. Although an improvement in the SiV emission from these peaks was observed after filtering them, a notable reduction on the material available and hence on the SiV emitters were found. Also, emitters with high intensity were not found, and many of the emitters imaged were not stable after some time.

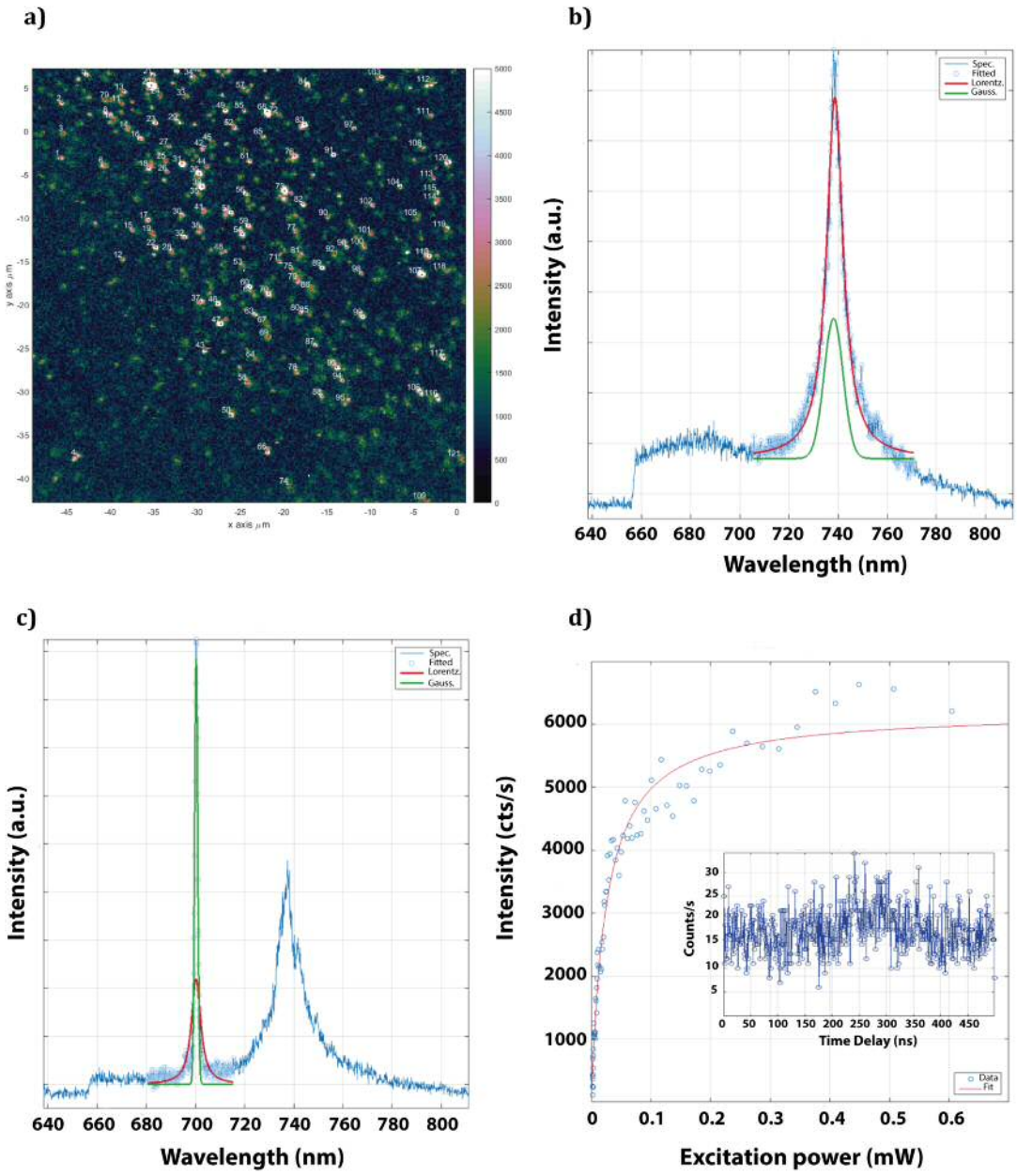

Figure 5.31: a) PL image showing a good spatial nanodiamonds distribution and b) and c) PL spectra of filtered nanodiamonds with a SiV emission peak centred at 739 nm and at 700 nm respectively. d) Saturation measurements performed in the SiV peak showed in c). Inset of figure c) shows HBT measurement with no clear antibunching.

5.6.3 CVD Growth onto Silicon substrates: increasing the Si incorporation

In an attempt to further improve the quality of the emitters and the number of emitters showing SiV features, the amount of silicon incorporated during the CVD growth was increased. As silicon was incorporated using a solid source (from the etching of the silicon pieces placed inside the reactor), the amount of silicon in the gas mixture can not be directly controlled. Nevertheless, previous studies demonstrated an increase in the SiV emission after the implantation of Si^{28} atoms in samples with high nitrogen concentrations. [266] *Zhang et al.* also observed and enhancement of the SiV-CL intensity after intentionally incorporation of nitrogen into the diamond growth in the gas phase. Nitrogen would act as electron donor, facilitating the formation of SiV centres. [267]

In order to study how nitrogen affects the SiV emission and to see if an increase in the silicon content would lead to the formation of more SiV centres, surviving after both the milling and the acid cleaning processes, nitrogen was incorporated in the gas phase during the CVD diamond growth.

Eight samples were grown in the *Seki AX6500* CVD reactor, after a SC1 cleaning, using 2 inches p-type 100 silicon wafers of 500 μm thickness. Substrates were rinsed in DI water in an ultrasonic bath for 10 minutes and then spun dry. Si wafers were then seeded as explained before. Following the seeding treatment, the Si wafers were rinsed, spun dry and placed inside the reactor chamber. Si pieces were also introduced inside the reactor chamber to create SiV centres.

Four wafers were grown varying the methane content. For the first sample, an incubation period of 3 min. was used, flowing 15 sccm of CH_4 diluted in 485 sccm of H_2 ($CH_4 : H_2 = 3\%$). The methane was then reduced to 5 sccm in a total flow of 500 sccm ($CH_4 : H_2 = 1\%$) for the growth process. For the next sample, the growth was performed without a previous incubation period, using 15 sccm CH_4 diluted in 485 sccm of H_2 ($CH_4 : H_2 = 3\%$). Incubation periods were also not performed in the following samples, with 25 sccm CH_4 diluted in 475 sccm H_2 ($CH_4 : H_2 = 5\%$) and 35 sccm CH_4 diluted in 465 sccm H_2 ($CH_4 : H_2 = 7\%$) respectively. The microwave power was set to 3.5 kW and the chamber pressure was 40 torr for all the growths. Temperatures of approximately 940°C were measured with a high temperature dual-wavelength pyrometer. To ensure hydrogen termination and to prevent non-sp^3 carbon to be deposited, samples were cooled down in a hydrogen plasma. Growth rate and sample thickness were *in-situ* monitored by laser interferometry and

samples thickness was also *ex-situ* determined with a *Filmetrics F-20 Spectral Reflectance system*, with thickness around $1\mu m$.

The next samples were grown with the same methane content (1%, 3%, 5% and 7%) but introducing 1 sccm of N_2 in a total flow of 500 sccm being $N_2 = 0.2\%$. Hence, for the first sample, 5 sccm of CH_4 were mixed with 1 sccm of N_2 and diluted in 494 sccm of H_2, for the second sample, 15 sccm of CH_4 were mixed with 1 sccm of N_2 and diluted in 484 sccm of H_2, for the third sample 25 sccm of CH_4 were mixed with 1 sccm of N_2 and diluted in 474 sccm of H_2 and in the last one, 35 sccm of CH_4 were mixed with 1 sccm of N_2 and diluted in 464 sccm of H_2. 1 sccm of nitrogen was selected as it was the minimum amount of nitrogen that can be reliably controlled using a 500 sccm mass flow controller. A growth enhancement was observed when small amount of nitrogen was incorporated, with a growth rate increase up to 5 times compared to the samples without nitrogen. This fact is well known and extensively studied in the literature. [268–270] The increase in the growth rate with nitrogen introduction was attributed to the change in the surface composition of adsorbed species. Nitrogen would be competing with hydrocarbon species (i.e. CH_3) for free radical adsorption sites and then, nitrogen catalyses the hydrocarbon species for their incorporation into the diamond lattice. [269]

Morphology

To study the change in morphology due to nitrogen and methane increase, all samples were SEM-imaged in a *Raith-e-Line* SEM operating at 20 kV and at working distance of 10 mm. Samples without nitrogen incorporation are shown in figure 5.32. Not much change in grain size (with (111) well faceted crystallites between 500 nm and $1\mu m$) is observed from samples in figure 5.32a), b), c) or d) with methane contents of $1\%, 3\%, 5\%$ and 7% respectively. These well faceted crystallites indicate a high quality diamond film. Nevertheless a grain size reduction was expected with increasing methane content due to re-nucleation processes becoming dominant, but was not observed. [22]

On the other hand, the morphology is largely affected by the nitrogen introduction as observed in figure 5.33. Pyramidal (100) facets with rough surfaces were observed. Crystallites between 150 nm to 300 nm were observed for the sample grown at $CH_4 : H_2 = 1\%$ and an increase in grain size, with sizes between 300 nm and 500 nm, was observed for the samples with 3% methane content. A further increase was observed in the sample grown at 5% with grain sizes between 500 nm and $1\mu m$. However a decrease in grain sizes was

observed for the last sample ($7\%CH_4$), with sizes again between 150 nm and 300 nm.

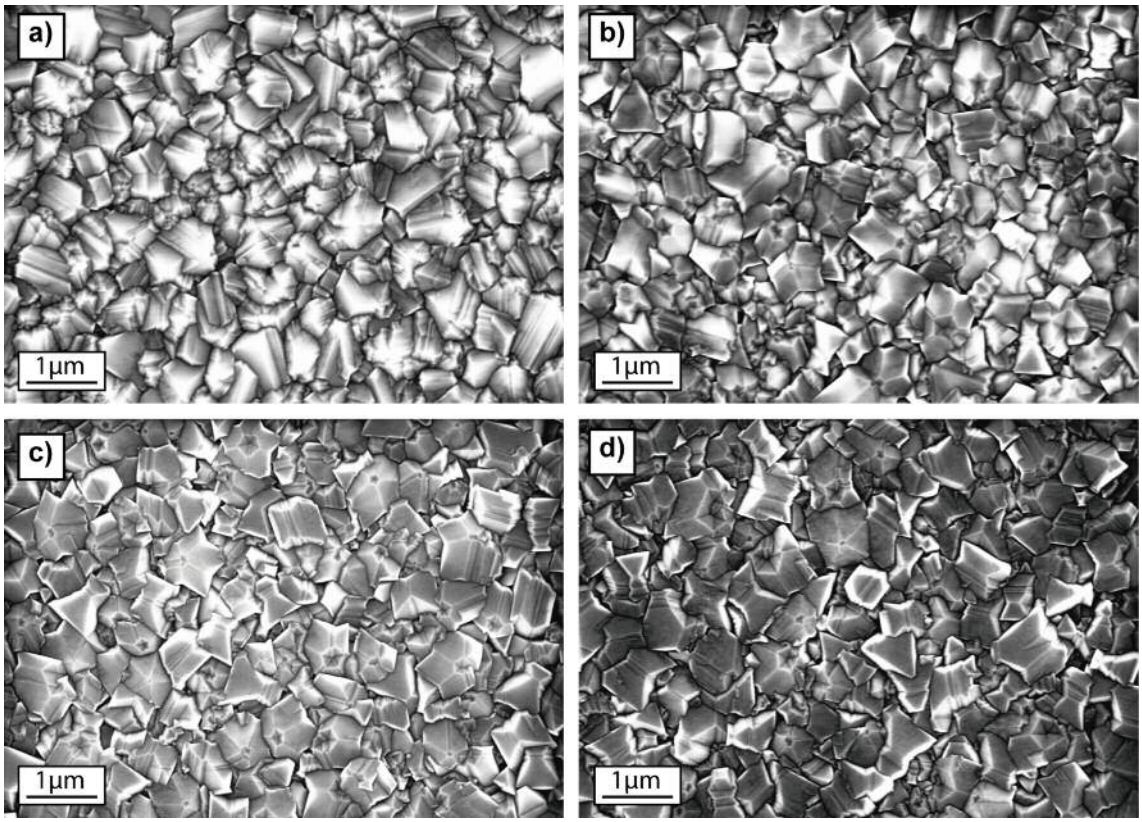

Figure 5.32: SEM images of CVD diamond films without nitrogen incorporation and with $CH_4 : H_2$ content of a) 1%, b) 3%, c) 5% and d) 7%.

Raman measurements

Raman spectroscopy measurements were performed in a *inVia Renishaw confocal Raman microscope* equipped with a 532 nm laser. Figure 5.34a) shows the spectra of the diamond films grown for different methane concentrations as indicated on the right above each curve, and with no nitrogen incorporation. All the spectra show a clear diamond peak at 1332 cm^{-1}. As the methane content is increased (3%-7%), the appearance of two broad bands around 1150 cm^{-1} and between 1450 cm^{-1} - 1580 cm^{-1} indicate the presence of sp^2 structures known as trans-polyacetylene structures and graphitic carbon respectively. Raman spectra of diamond films with 0.2% of N_2 in the total gas flow are shown in figure 5.34b). A broader diamond peak (compared to the samples with no nitrogen incorporation) is observed, as well as a more defined 1140 cm^{-1} peak and an also broader band from 1400 cm^{-1} to 1600 cm^{-1}, both due to sp^2 structures. These peaks are more intense as methane content increases. A peak around 1350 cm^{-1} corresponds to the D-peak due to breathing motion of sp^2 rings. Besides, a peak around 1250 cm^{-1} appears for the samples with 1%

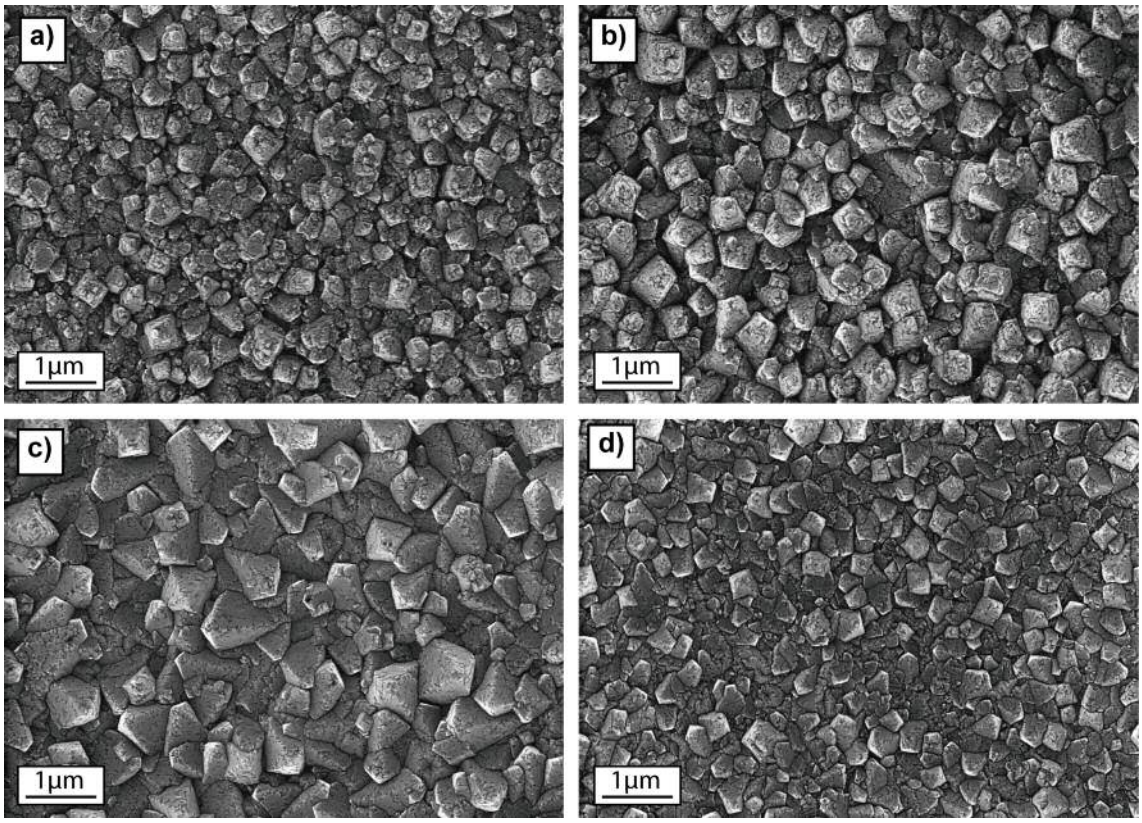

Figure 5.33: SEM images of CVD diamond films with N_2 : 0.2% incorporated and with $CH_4 : H_2$ content of a) 1%, b) 3%, c) 5% and d) 7%.

and 7% of methane. [271]. From the graphs, it is clear that sp^2 related peaks are more intense for the sample with 1% of methane, maybe related to smaller grain sizes.

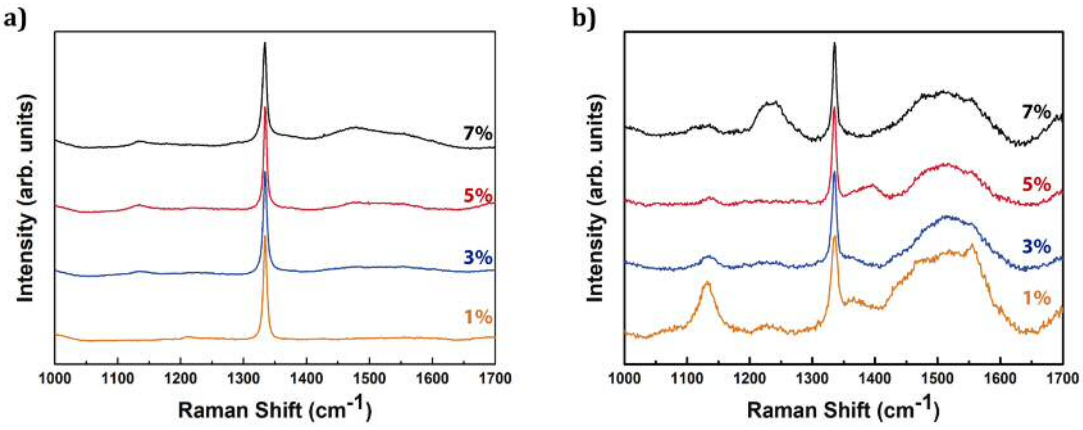

Figure 5.34: Raman spectra of diamond films grown a) without nitrogen in the gas phase and b) with controlled nitrogen doping for different $CH_4 : H_2$ content: 1%, 3%, 5% and 7%.

Photoluminescence measurements before the milling

The optical properties of the different films grown were performed by Alexander Boomer and Sarah Lindner under the supervision of Prof. Christoph Becher at Universität des Saarlandes, Saarbrücken (Germany). All the measurements were performed in a confocal microscope with a 640 nm wavelength, and using 50 μW as excitation power.

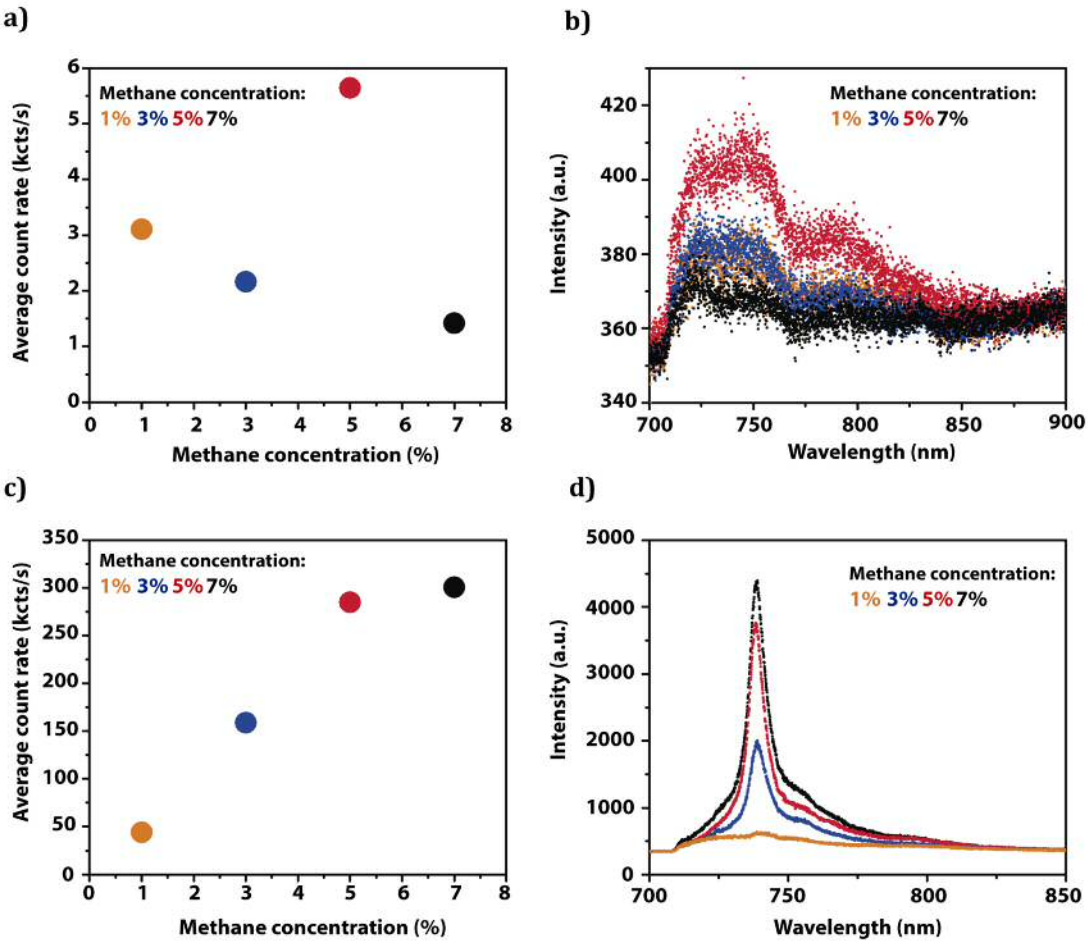

Figure 5.35: Average count rates and PL measurements respectively, of the CVD grown films a), b) without nitrogen and c) and d) with 0.2% of N_2 in the gas phase, for different methane content as indicated in the graphs.

Figures 5.35a) and b) represent the average count rate and the PL intensity of the samples in which nitrogen was not incorporated in the gas flow during the growth process, for different methane percentages. The average count rate in figure 5.35a) shows and average over 20 measurements taken. As it is observed, the sample with slightly higher count rates is the sample with $CH_4 : H_2 = 5\%$. In figure 5.35b) an increase in the PL intensity with a broad band between 700 nm- 750 nm, is observed, but no clear SiV peak can be

distinguished, as observed in previous PL measurements also performed in a sample with the same growth conditions (figure 5.25b)).

On the other hand, an increase in the average count rate as well as an increase in the PL intensity, with the SiV peak at around 740 nm, is observed after the nitrogen doping. SiV photoluminescence enhancement was also reported in the literature by *S. Singh et al.* [272] on diamond nanoparticles (250 nm size), after the incorporation of small amount of substitutional nitrogen into the feed gas during the CVD diamond growth. As pointed out briefly in 5.6.3, nitrogen atom act as donors, raising the Fermi-level closer to the conduction band and negatively charging the SiV centres, which become optically active.

SIMS measurements

At the beginning of this subsection it was stated that the aim of nitrogen doping was to try to increase the number of nanodiamonds with SiV centres after the diamond films milling. As the strongest PL emission intensity was observed for the sample with the 7% of methane and 0.2% N_2, SIMS measurements were performed on that sample to measure the real amount of Si incorporated into the films. Figure 5.36 shows a SIMS profile, with carbon and silicon concentrations, of a diamond film grown onto a silicon substrate. The diamond film thickness can be estimated from the graph, as the silicon concentration is higher in the Si substrate. The diamond film thickness is around $1.2\mu m$.

At the beginning of the CVD growth process, the silicon substrate is being etched and some silicon is incorporated into the diamond. When the diamond film starts coalescing, the Si content drops whereas the carbon content increases. The silicon content keeps dropping after coalescence, reaching a plateau, and then going down again as the diamond film thickness increases. However, the silicon content does not drop to zero as silicon is also being etched/incorporated from the Si pieces placed around the holder inside the reactor during the growth as well as in part from the lateral of the silicon wafers. Si concentrations between $3.5x10^{18}$ - $5x10^{18}$ (atoms/cm^3) were measured. Although the silicon content is higher than the residual Si measured in diamond films grown by CVD, [220] the creation of SiV centres using Si as a solid source is not the best. A higher Si incorporation can not be achieved, and what is more important, the Si content would not remain constant along all the diamond film thickness, which means that the Si content will decrease considerably after few microns of growth. In order to overcome that problem, silicon will be incorporated in the gas phase, as will be explained in the next chapter.

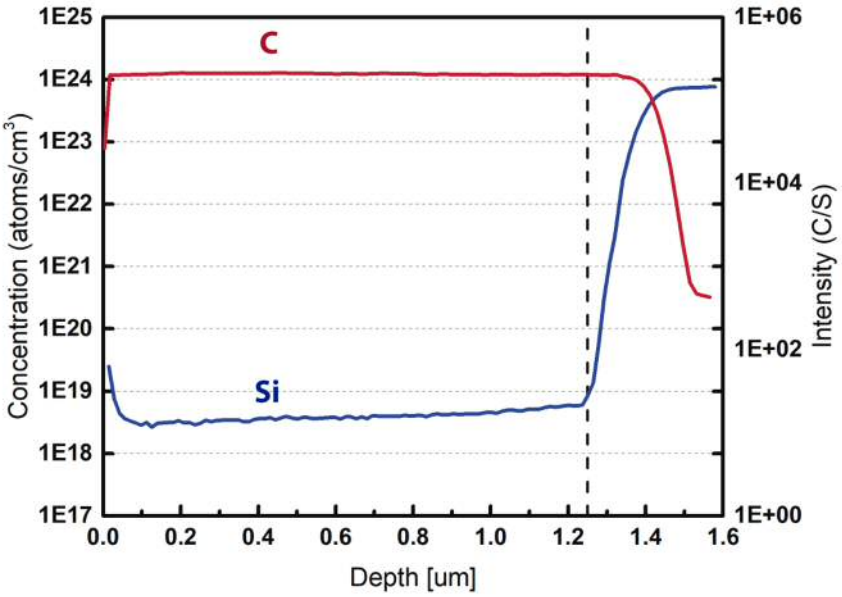

Figure 5.36: SIMS measurement of a CVD diamond film grown with nitrogen in the gas phase and with $CH_4 : H_2 = 7\%$.

After checking the Si content, 6 more diamond films $1\mu m$ thick were grown. Si wafers were seeded and cleaned as detailed in 5.6.3, and then were placed inside the reactor for the growth process. 35 sccm of CH_4 and 1sccm of N_2 were diluted in 465 sccm H_2 ($CH_4 : H_2 = 7\%$), while keeping the chamber pressure at 40 Torr, and microwave power at 3.5 kW.

The Etching, milling and acid cleaning processes

Si substrates were etched to obtain free-standing diamond films and the etching process was performed by Alexander Boomer at Universität des Saarlandes, Saarbrücken (Germany). An anisotropic wet KOH etching was performed, using two teflon tanks [262]. One of the teflon tanks was filled with KOH and holes were made into the bottom of the second one. Samples were then placed inside the teflon tank with holes and then it was immersed into the teflon tank containing KOH. With teflon having low heat conductivity, it was not possible to increase the bath temperature, hence resulting in low etching rates.

Once the substrates were etched, pieces of diamond films were collected and prepared for acid cleaning processes. Ethanol was used to extract the diamond film pieces from a plastic box used for transportation and after the film pieces were dried out, were mixed with 10

ml of DI water and sonicated for 10 minutes. 5 ml were then placed inside the tempered steel grinding bowl and the other 5 ml inside the silicon nitride one, for the subsequent milling processes. 40 grams of tempered steel balls were placed inside the tempered steel bowl whilst 30 balls were introduced inside the silicon nitride one. 6 cycles of 5 min on/15 min off were performed at 1100 rpm in both cases. After releasing the pressure inside the bowl, another 6 milling cycles were performed.

Acid cleaning processes were performed as detailed in 5.6.2. After these processes the obtained powders were air-annealed at 480°C. Colloids were prepared dispersing 0.01 g of the powders in 20 ml of deionized water and were centrifuged at different accelerative forces (5000 g and 10000 g).

Particles' size characterization

Particles' size distribution was measured by DLS and NTA in the samples before being subjected to any centrifugation cycle, and in the samples centrifuged at 50000 g and at 10000 g, using a *Malvern Zetasizer Nano ZS* equipped with a 633nm laser in backscattering configuration (173°C) and a *Malvern Nanosight LM10* equipped with a 635 nm laser respectively. From figure 5.37, it is clear that as explained in both the previous chapter and in section 5.5.5, the DLS technique is not capable of resolving small particles in the presence of bigger ones. On the other hand, NTA can distinguish between the different particles' size distribution present in the sample as it is based on the individual tracking of particles. Samples milled in the tempered steel grinding bowl are represented in figure 5.37a), b) and c) which corresponds to the sample before the centrifugation cycles, after centrifugation at 5000 g and after 10000 g respectively. A reduction in particles' size can be observed, with sizes as small as 18 nm after centrifugation at 10000 g, which is at the limit of resolution of the NTA equipment. Although further centrifugation cycles were also performed at 30000 g, no difference was observed by DLS or NTA.

Nevertheless, size differences are appreciable between the samples milled with the tempered steel or the silicon nitride bowl, as observed in figures 5.37d), e) and f). Smaller particles were obtained milling the diamond films with the tempered steel material. Size distributions between 18 nm and 99 nm were measured after the tempered steel milling, with the majority of the particles having sizes of 63 nm, whereas the sizes distributions were observed between 62 nm to 157 nm for the silicon nitride one.

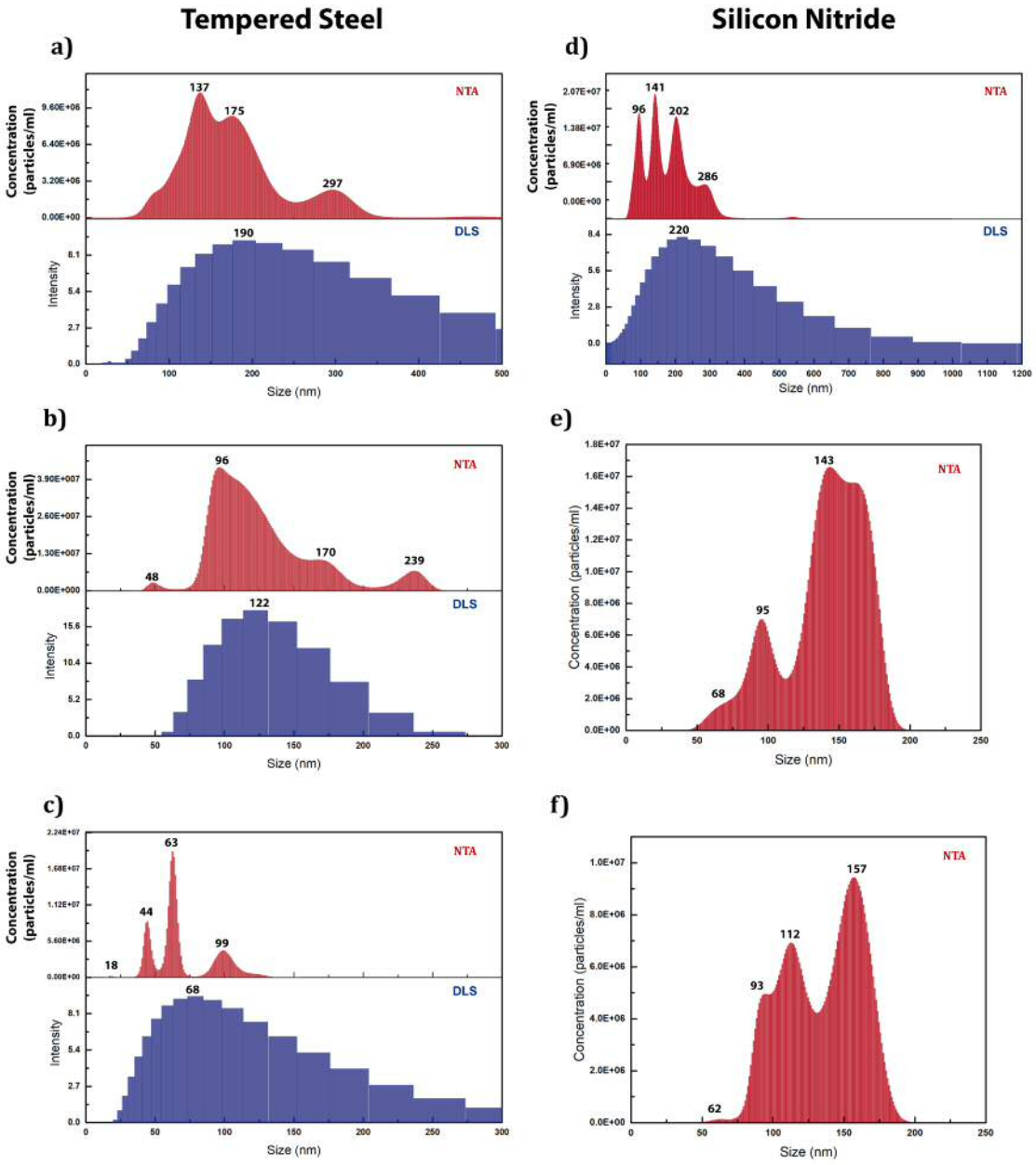

Figure 5.37: Particles' size distribution of the milled powder solutions measured by DLS and NTA after centrifugation at different accelerative forces: a) 5000 g b) 10000 g c) 20000 g and d) 30000 g.

Photoluminescence measurements

The slurries were sent back to Germany, and all the samples were drop cast onto iridium substrates before PL characterization. All samples were measured using a 640 nm wavelength and an excitation power of 1 mW. As the nanodiamond density was too high in the original slurries, all of them were diluted, 10^5 particles/μl being the final concentration.

PL measurements of the particles obtained after the tempered steel milling are shown in figure 5.38. All the graphs show four characteristic spectra corresponding to four different nanodiamonds, representatives of all the nanodiamonds measured in the samples. Figure 5.38a) represents the PL emission of the nanodiamonds before any centrifugation cycle. As observed in the graph, a clear SiV emission peak is observed, with a ZPL centred around 740 nm. Small SiV ZPL peak shifts (± 5 nm) can be appreciated in the same figure for the individual nanodiamonds measured. Count rates of several 10^6 counts per second were measured in all the nanodiamonds, and the SiV emission was very bright, stable and reliable in all samples. However, broad ZPL widths ranging from 12-20 nm indicate the probable presence of ensembles. Besides, the asymmetry of the ZPL peak and the broad side-band emission shifted towards longer wavelengths, clearly confirms this presence. Similar photoluminescence characteristics were observed in the sample after centrifugation at 5000 g, shown in figure 5.38b). SiV ZPL were also centred around 740 nm and broader ZPL width distributions were observed. Finally, figure 5.38c) shows the SiV PL emission for the sample after centrifugation at 10000 g. Less emitters were found, and some nanodiamonds measured were empty, but the count rates were still in the range from $2x10^5$ counts per second to several 10^6 counts per second. ZPL was centred at 740 ±2 nm and broader ZPL widths were measured. All the measurements were performed at room temperature, and the broadening of the ZPL was due to phonon processes. [273]

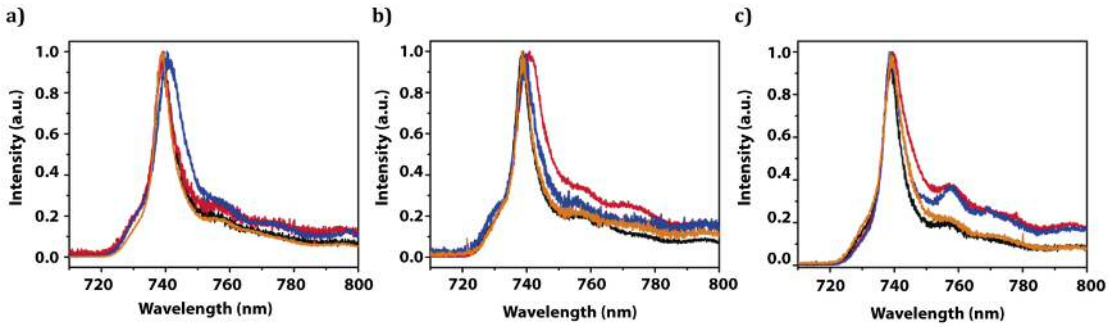

Figure 5.38: Photoluminescence spectra of several nanodiamonds with SiV emission centred at 740 nm, produced by the milling of CVD diamond films with a tempered steel grinding bowl. All the emitters were excited at 640 nm. Nanodiamonds were subjected to a) no centrifugation cycles, b) several centrifugation cycles at 5000 g and c) centrifugation cycles at 10000 g.

Figure 5.39 shows the SiV PL emission for the samples milled with the silicon nitride bowl, and after centrifugation cycles at a) 5000 g and b) 10000 g. Very bright SiV emitters were also found, with several 10^5 counts per second and PL emission spectra typical of a

nanodiamond ensemble as was observed for the samples milled with the tempered steel grinding bowl. Nevertheless emitters with broader ZPL and photobleaching effects were observed for the sample after centrifugation at 10000 g.

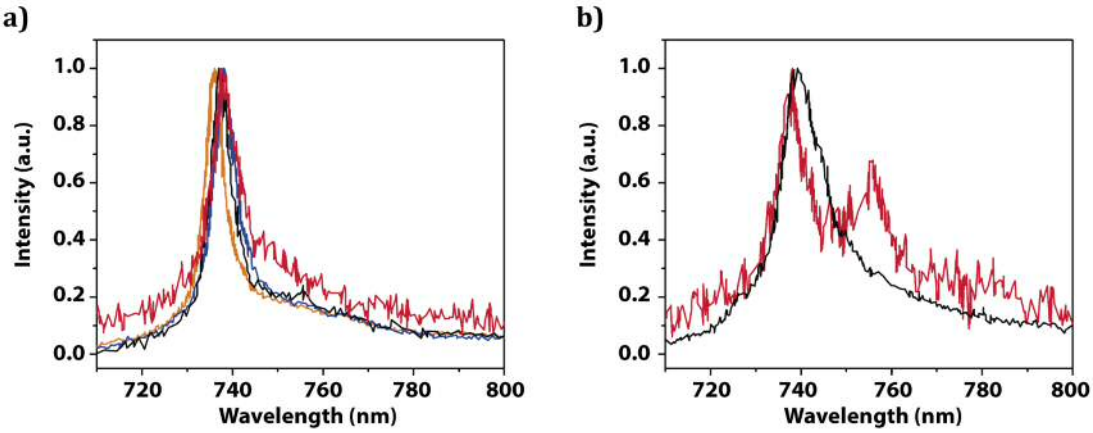

Figure 5.39: Photoluminescence spectra of several nanodiamonds with SiV emission centred at 740 nm, produced by the milling of CVD diamond films with a silicon nitride grinding bowl. All the emitters were excited at 640 nm. Nanodiamonds were subjected to a) several centrifugation cycles at 5000 g and b) centrifugation cycles at 10000 g.

Intensity autocorrelation measurements were not performed in these samples. Due to the high density of nanodiamonds and the nanodiamonds small sizes, it was difficult to distinguish isolated nanodiamonds so it is not clear if several nanodiamonds were measured in the confocal spot and hence responsible for the ensemble-like PL emission. First, it would be necessary to define by lithography techniques some marks or patterns in the substrates, deposit the diluted slurry and check under SEM the nanodiamond size. After ensuring that there is just one isolated nanodiamond, measure in the confocal the PL emission, aligning the mark to ensure that the same nanodiamonds is measured.

5.7 Conclusions

In this chapter, different strategies for SiV creation were followed, using in all of them Si as a solid source for SiV emitters creation. First, nanodiamonds were directly grown onto non-diamond surfaces inside a CVD reactor. Nanodiamonds with stable SiV centres and a narrow ZPL were grown controlling both the density and the size by changing the seeding slurry concentration and the growth duration process respectively. Although having low background fluorescence, crucial for PL characterization measurements, these substrates were, however, damaged by the exposure to the hydrogen an methane plasma even after few minutes of growth. The damaged substrate in addition to the small collection efficiencies and stress induced by the heteroepitaxial growth, does not make this process promising for obtaining single photon emitters. On the other hand, sapphire substrates have such a high fluorescence background that completely masks the SiV emission.

The second strategy that has been followed in this chapter is the creation of these colour centres by milling down diamond films with Si incorporated, either obtained growing onto Si substrates with subsequent etching processes or onto Molybdenum holders. The use of different materials for the milling process has demonstrated the advantages and drawbacks of the two different materials: tempered steel and silicon nitride. Milling the diamond films with the first material resulted in smaller nanodiamonds with better photoluminescence properties. XPS measurements performed in commercial SC diamond samples milled with both materials, confirm the presence of non-sp^3 carbon and silicon nitride in the nanodiamonds after the milling with the silicon nitride bowl, with can negatively influence the PL properties. Furthermore, TEM measurements show faceted particles. On the other hand, 'cleaner' and rounded nanoparticles were observed in the XPS and TEM measurements, after the tempered steel milling. TEM measurements show however, Fe_2O_3 remains, impossible to remove and detrimental for magnetometry applications. Thus silicon nitride milling is a better choice for metal-free diamond nanoparticles creation.

In summary, promising methods towards the creation of really bright and stable nanodiamonds with sizes smaller than 50 nm have been achieved. Furthermore, having the nanodiamonds with SiV centres dispersed in a solution, ready for drop cast onto any devices, makes them extremely useful in quantum applications.

Chapter 6

A Quartz tube reactor design for controlled Si doping

Abstract

In this chapter, the design of a simple, NIRIM type chemical vapour deposition reactor for diamond growth is detailed. The reactor discharge tube consists of a quartz tube placed in a 2.45 GHz waveguide in which the conditions for the metastable growth of diamond are created. Most of the reactor components rely on commercially available KF fittings, providing reactor easy modification and repair. Furthermore, the interchangeability of the quartz tube enables the use of different dopants ensuring no cross contamination between them, as well as easy cleaning between growth runs. The incorporation of Si into the diamond films using silane as a gas source will be studied. The quality of nanocrystalline diamond films produced will be analysed by SEM, Raman and PL spectroscopy. The clear faceting of diamond crystallites observed and a large diamond fraction indicated in Raman, demonstrate the design offers deposition of diamond with minimal complexity and cost.

6.1 Introduction

In the previous chapter, the production and characterization of diamond particles with SiV colour centres was explained. Several strategies for SiV centres creation were successfully followed. Nevertheless, due to silicon doping being performed using a solid source, the silicon incorporated was not well controlled as the amount of silicon in the gas phase was unknown. For quantum applications such as quantum computing or applications regarding photon entanglement, the presence of ensembles instead of single photon emitters is not tolerable, so a method to control the Si content ensuring the formation of just one SiV centre is desirable.

As seen in the previous chapter, the generation of SiV centres is related to the amount of Si that is favourably incorporated into the diamond lattice. As a general assumption, the more Si incorporated, the less probability of finding single photon emitters. Furthermore, PL quenching of SiV centres is also observed if a high content of Si is incorporated, although the reason behind it is still not clear. [274] Hence, the majority of the studies reported, pursue the incorporation of as little silicon as possible (but enough for SiV centres creation).

Studies have demonstrated the formation of single SiV centres by the incorporation of silicon solely from the etching of the substrate. Although single photon emission was observed, not all the emitters measured produced single photon emission probably due to the presence of more than one emitter in a single nanoparticle, so further studies are needed to try to overcome this problem and to control more accurately the Si concentration.

As briefly described, one way of controlling precisely the Si concentration is by ion implantation techniques. *Wang et al.* [219] and *Steinmetz et al.* [275] reported SiV single photon emission in type IIa diamond windows and in single crystalline type IIa CVD diamond respectively after an ion implantation. Whilst the location and the density of these impurities can be controlled by this technique, the lattice damage produced in the process can affect the PL properties, reducing the PL efficiency. [276] Furthermore, the possibility of producing particles containing these centres that can also be dispersed in a liquid, would be advantageous over either bulk diamond SiV centres or particles attached to a surface.

The production and control over particle sizes was demonstrated in chapter five. However, as the diamond nanoparticles obtained from the milling process originated from different areas of the diamond films (with non-uniform Si concentrations as shown in figure 5.36),

it is probably that the diamond nanoparticles would have a different Si content and hence different SiV concentrations.

An alternative to overcome this issue is to introduce silicon in the gas phase, using silicon precursors/gases such as silanes ($SiH_4, CH_3SiH_3, C_{12}H_{36}Si_5$). [276, 277] This will ensure silicon homogeneity throughout the diamond growth process permitting long growth durations and hence the possibility of producing more diamond material. Several studies have been reported in the literature with silane effectively incorporated into diamond films and diamond particles, grown onto different substrates such as Si, [278] sapphire, [279] aluminium nitride (AlN) [276] and single crystal diamond (SC). [280] The silane introduction will be discussed within this chapter.

The high quality level and doping control necessary to produce single photon emitters or even new colour centres in diamond require clean CVD systems in which the sources of contamination can be minimised. It would also be ideal to use one CVD reactor for each doping source or contaminant present/introduced, according to the ultimate application. For instance, if boron is introduced in a system for growing superconducting diamond films, the boron present even after a oxygen reactor cleaning process would be detrimental for growing SiV colour centres as boron is believed to quench the SiV PL emission.

Although a considerable variety of CVD reactors are available commercially, their significant complexity and cost, rule out the use of the CVD technique for many research laboratories. For that reason, we developed a simple quartz tube CVD reactor for diamond growth (with CAD files, parts list and control program freely available to download and modify) [281]. Apart from its simplicity, the reactor deposition camera consists of an interchangeable quartz vacuum tube. This means that the reactor can be easily cleaned after growth runs, or the quartz discharge tube can be replaced if needed, avoiding cross contamination of unwanted dopants in the reactor chamber. The reactor design will be discussed in the next section.

6.1.1 The history of reactor design

The compelling and unique properties of diamond [2] led to the development of new reactors and methods to synthesize the material either pursuing industrial or academic purposes. [282] First attempts on synthetic diamond growth were performed in the early 50's by high pressure-high temperature (HPHT). [97] In the same decade, and in order to avoid the extreme conditions required for the HPHT growth, a new low pressure and

kinetically governed growth process was established. Diamond growth from the gas phase by Chemical Vapour Deposition (CVD) was successfully developed for the first time by *Eversole* and independently by *Angus et al.* and *Deryagin et al.* [13] CVD method allows diamond growth upon more suitable conditions than HPHT and not only on diamond substrates but also on a wide range of non-diamond substrates. In the first published CVD growth work, Eversole deposited diamond on natural diamond powder by chemical vapour deposition using hydrocarbons or carbon monoxide. [283–285] However, it was with the introduction of hydrogen in the gas phase in 1966 [286] and its role as etchant of non-diamond sp^2 carbon that facilitated the low pressure diamond growth and a flourishing interest in CVD diamond growth. Following hydrogen introduction, the decisive breakthrough came with the use of atomic hydrogen [287] obtained from the dissociation of diatomic hydrogen either thermally produced, with the use of a hot filament, [288] or as a result of plasma activation. [289]

The subsequent development of CVD reactors' design and the studies accomplished in the 1980s by a Japanese group led to the decisive expansion of CVD diamond growth. [290] Japanese researchers from the National Institute for Research in Inorganic Materials (NIRIM), reported crystalline diamond growth on non-diamond substrates from a mixture of hydrogen and methane gases under plasma conditions. [289] The ongoing work and the design of the NIRIM-type reactor led to its promptly commercial availability by New Japan Radio Co. Ltd Company, which resulted in CVD as being the most extensively used technique for diamond growth using a gas phase. However, those CVD deposition systems, presented low deposition rates of about $1\mu m/h$ (low deposition rates for industrial purposes and to scale-up the production).

Additional methods for CVD diamond growth were proposed in 1988. An oxy-acetylene combustion flame proposed by *Hirose et al.* [291] and the direct current Arc plasma jet described by *Kurihara et al.*, [292] provided higher deposition rates, up to $40\mu m/h$ and $900\mu m/h$ respectively. Another important achievement was accomplished in the late 1980s. Large-areas deposition was possible with the development of new commercial CVD systems by ASteX (explained in chapter two). [15] Furthermore, the ASTeX design, with reactor quartz walls away from the plasma and the substrate, entailed a reduction in possible contaminants sources. Finally, during the 1990s, further improvements were made in reactor design, which with the development of higher-power magnetrons, resulted in important progresses in cost reductions as well as an increase in the deposition rate and plasma stability.

6.1.2 The NIRIM reactor: TE modes

Microwave plasma reactors are based on plasma cavities or waveguides with different geometric configurations, and were developed for the low-loss transmission of power at high frequencies. [293] The microwave signal can be propagated through these waveguides, and this propagation will depend on the dielectric and magnetic properties of the medium. The variation of electric and magnetic field wave components within the waveguide can be derived from the Maxwell equations, subjected to boundary conditions. [293] Plasma reactor waveguides can support the propagation of transverse electric (TE) and/or transverse magnetic (TM) modes depending on the presence of longitudinal magnetic or electric field components. A finite number of modes can propagate within the waveguide, as long as the operating frequency is above the lowest frequency for which a mode can propagate, known as cutoff frequency. TE and TM modes are also usually denoted as TE_{mn} and TM_{mn} where the m and n index represent the number of electric field maxima (or lobes) in the radial and axial directions, respectively. [294] The mode with the lowest cutoff frequency is known as the dominant or fundamental mode. [295]

The NIRIM type reactor consists of a quartz tube that acts as vacuum deposition chamber, inserted into a hollow rectangular waveguide. Hydrogen and methane gases are introduced in the reactor chamber. Microwave power, produced by a high frequency microwave plasma source (2.45 GHz magnetron), is coupled into the reactor chamber through a dielectric window and creates a discharge. The free electrons generated, then transfer their acquired energy to the gases within the reactor chamber, dissociating the molecules and forming the active species, hence establishing the appropriate conditions for diamond growth. The reactor chamber is an electromagnetic cavity with known microwave electric fields modes that allow control over the location of the plasma. In the NIRIM reactor the dominant TE_{10} mode propagates in the waveguide with sinusoidal dependence along the x direction (long dimension of the waveguide). A sliding short circuit is used to adjust the maximal electric field and hence the plasma position. [19] The deposition areas are limited to one-inch wafers due to the reactor design and the small plasma generated by the only presence of the TE_{10} mode. However, studies on doped diamond layers grown onto single crystal diamond substrates in NIRIM type reactors, reported by *Mortet et al.* [296] confirm the suitability of NIRIM reactors for high quality diamond growth.

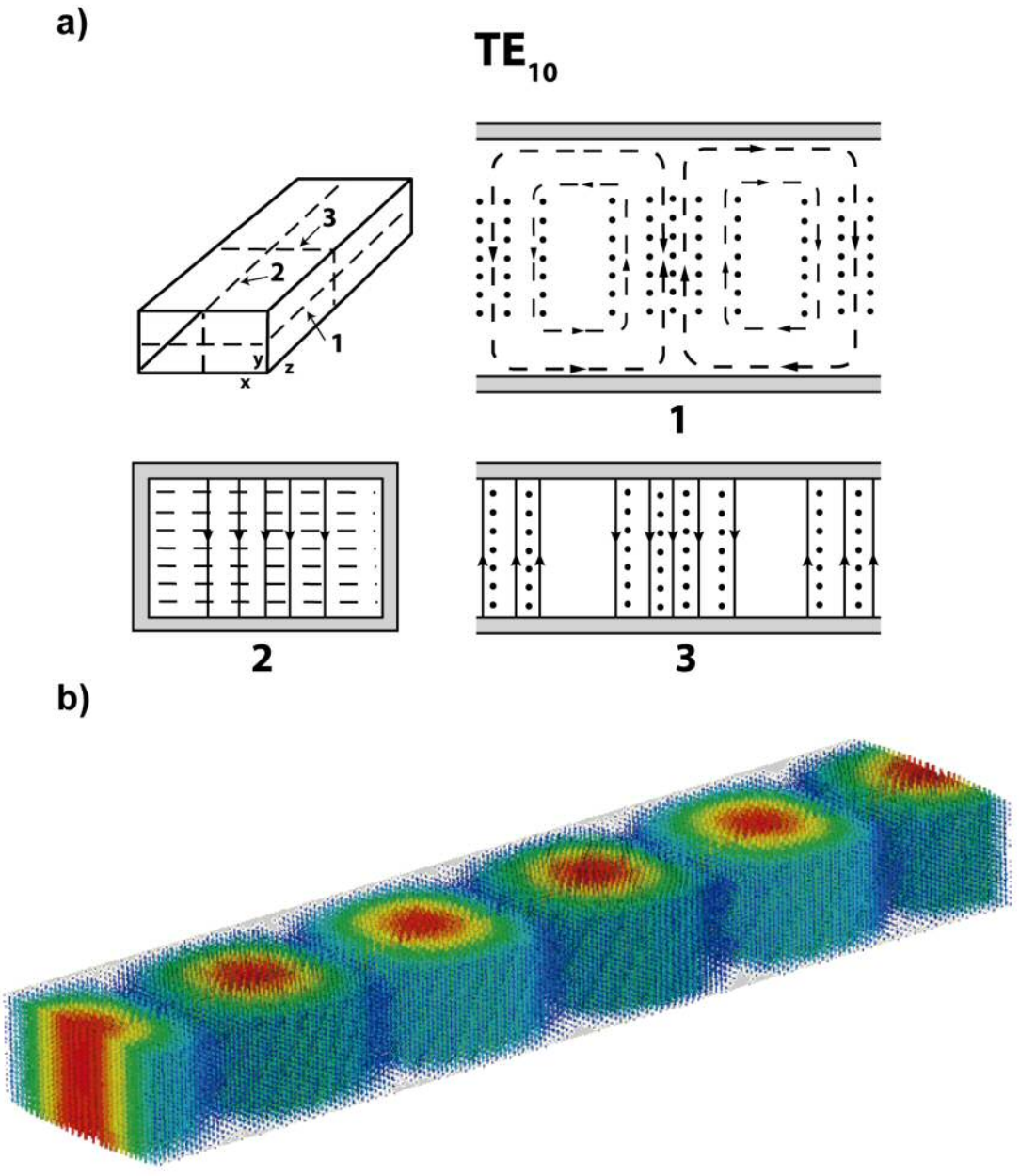

Figure 6.1: The TE_{10} fundamental mode of a rectangular waveguide of a NIRIM reactor. a) Field lines for the fundamental mode. Reprinted with permission from John R. Whinnery, Simon Ramo and Theodore Van Duzer, *Fields and Waves in Communication Electronics*. Copyright ©1965 by John Wiley and Sons. b) E-field phase in a rectangular waveguide. Reprinted from [295].

6.2 System Overview

6.2.1 Reactor Design

The reactor is based on the design by NIRIM, [288] and consists of a quartz vacuum tube placed within the anti-node of a 2.45 GHz rectangular waveguide to create a plasma discharge suitable for CVD diamond growth. While the vacuum tube has been designed around an easily replaceable quartz tube relying on available KF fittings, all the microwave components are within the standard WR340 series by *Sairem*, minimising both complexity and costs. An overview of the complete reactor is shown in figure 6.2 (c). In the same figure, in panel (b) a side view of the reactor is represented, detailing the different microwave and reactor components and finally panel (a) shows a cross section of the discharge tube, indicating the substrate holder and its position.

As seen in figure 6.2, the reactor is built around a downstream source, supplied by *Sairem*, composed of a water cooled cavity (A) and two interchangeable chimneys to the top and bottom (B). The quartz discharge tube is placed within the waveguide through two holes at the top and bottom of the metallic cavity, and the protruding sections of the tube are covered by the metallic chimneys to prevent microwave leakage. The discharge tube is cooled with compressed air through two fittings at both ends of the chimneys to prevent overheating. To ensure that the discharge tube is in place, two compressed springs run around the circumference of the inner wall of the chimneys, providing mechanical support. The sample is placed within the downstream source as detail in figure 6.2 (a). A one inch sample holder (C), is positioned on top of a quartz rod within the quartz tube. The hydrogen and methane gaseous precursors and any other gases such as silane for Si doping, are fed into the quartz tube through the KF40 x KF25 reducing cross to the top of the reactor (D) (also indicated in figure 6.4a)). The gas flows are controlled by a series of *MKS πMFC Mass Flow Controllers (MFCs)*. The gas supply is also controlled through pneumatic solenoid valves, which are placed in between the MFCs and the reactor inlet. The chamber pressure is monitored using a *Vacuubrand capacitive VSK3000* pressure gauge which is connected to the lower KF25 cross (F). The pressure is controlled with a variable speed *Vacuubrand MV 2 NT VARIO* diaphragm pump, which is connected with a flexible hose to one of the lower KF flanges (E) and a CVC 3000 controller. As a security measure (prevent over pressurisation of the quartz tube) and hence being able to perform long growth durations leaving the reactor unattended, a *MKS 51A* baratron pressure switch with a setpoint of 70 Torr is connected to the top tee (D)) and an above

atmosphere *Pfeiffer AVA 016 X* pressure relief valve is also connected to a KF25 cross (F). To allow venting to atmospheric pressure (to introduce or remove the sample from the reactor previous/after CVD growth processes), a manual diaphragm valve is also connected to (F). Finally a *Williamson DWF-24-36C* dual wavelength pyrometer is attached at the top of the reactor on the reducing tee to a custom made tilt stage with vacuum tight quartz window, to monitor the temperature of the sample during growth (G).

The microwave radiation is generated by a *2 kW 2.45 GHz Sairem magnetron* (H), positioned in a support structure. To prevent or minimise damage to the magnetron from both power reflected from the vacuum chamber and unintended breakdowns, the microwaves are first fed through an isolator and arc detection flange (I) before entering the TE_{10} waveguide (J). For space considerations, two 90° E-bends were installed to the topside of the support structure. After passing through the E-bends and the TE_{10} waveguide, a series of tuning stubs (K) are used to match the impedance of the discharge tube to the magnetron source to ensure the power is delivered effectively with minimal reflection. The tuning stubs were adjusted before the first diamond film growth, and kept essentially unchanged during the subsequent growths. The microwaves then finally pass through a quartz window (L) which prevents the ingress of dust into the waveguide and any associated damage to the microwave components to the bottom of the support structure. When microwaves enter the downstream source, ionise the hydrogen and methane gaseous precursors fed inside the quartz discharge tube, creating the conditions necessary for diamond growth. A sliding short-circuit (M) positioned approximately a quarter of a wavelength from the centre of the discharge tube, is used to adjust the location of the electric field maximum within the downstream source. To perform high quality diamond growth, the sliding short-circuit is displaced along the strucutre (M) until the plasma is positioned to coincide with the centre of the sample within the waveguide, as shown within the cross section of figure 6.2(c). To simplify operation, the section of waveguide between the quartz window and the magnetron are kept at atmospheric pressure.

More details of the quartz tube and the sample rod are shown in figure 6.3. Panel (a) gives an overview of the vacuum chamber with the quartz tube sectioned, and panels (b) and (c) show cross sections of the chamber and sample loading mechanism respectively. As shown in figure 6.3(b), the vacuum chamber consists of a 50 mm O.D. x 46 mm I.D. x 480 mm long quartz tube (A). At the end of the tube, BS1806 50.17 mm ID x 5.33 mm thick Viton O-rings (B) are compressed against the quartz tube, ensuring the chamber sealing by two custom made 304 stainless steel tube ends (C and D), tightening three M5 screws

(E). Alignment of the axis of the components to that of the quartz tube is maintained through the use of a further inner O-ring (F), ensuring flush contact with the chimneys at either side of the downstream source, minimising microwave leakage.

To prevent the formation of a trapped volume between the two pairs of O-rings ((B) and (F) in figure 6.3 (c)) and allow leak testing of the reactor, the inner O-rings (F) are grooved. As the quartz tube constitutes mostly of the length of the vacuum tube and extends far beyond the plasma, absorbates and film deposition on the stainless steel components are minimised. As will be detailed later, the reactor can then be easily kept clean either cleaning the quartz tube in an air furnace or replacing the economical quartz tube, which also aids the prevention of cross-contamination upon switching dopants within the feed gas. A Shapel M aluminum nitride sample holder (G) sits on top of a 30 mm OD quartz rod (G). As detailed for the quartz tube, a series of BS1806 28.17 mm ID x 3.53 mm thick Viton O-rings seal the loading flange (H) against the quartz rod. The sample can be easily loaded and extracted due to the loading flange slides along a pair of 8 mm D guide rails bolted to the top and bottom of support structure (I). The joint (J) between the loading flange and the flange on the bottom of the lower tube end, is sealed with an inset 50.17 mm I.D. x 5.33 mm thick Viton O-ring, compressed between both and with further tightening with three M5 bolts. Finally, the upper and lower tube ends are terminated by a KF50 and two KF25 flanges respectively to allow connection to the KF fittings detailed previously. Once complete, mechanical support of the quartz tube is then facilitated through the combination of the uppermost tube end sitting flush against the upper chimney, the compressed springs within the chimneys, and finally the bolting of the lower tube end to the guide rails.

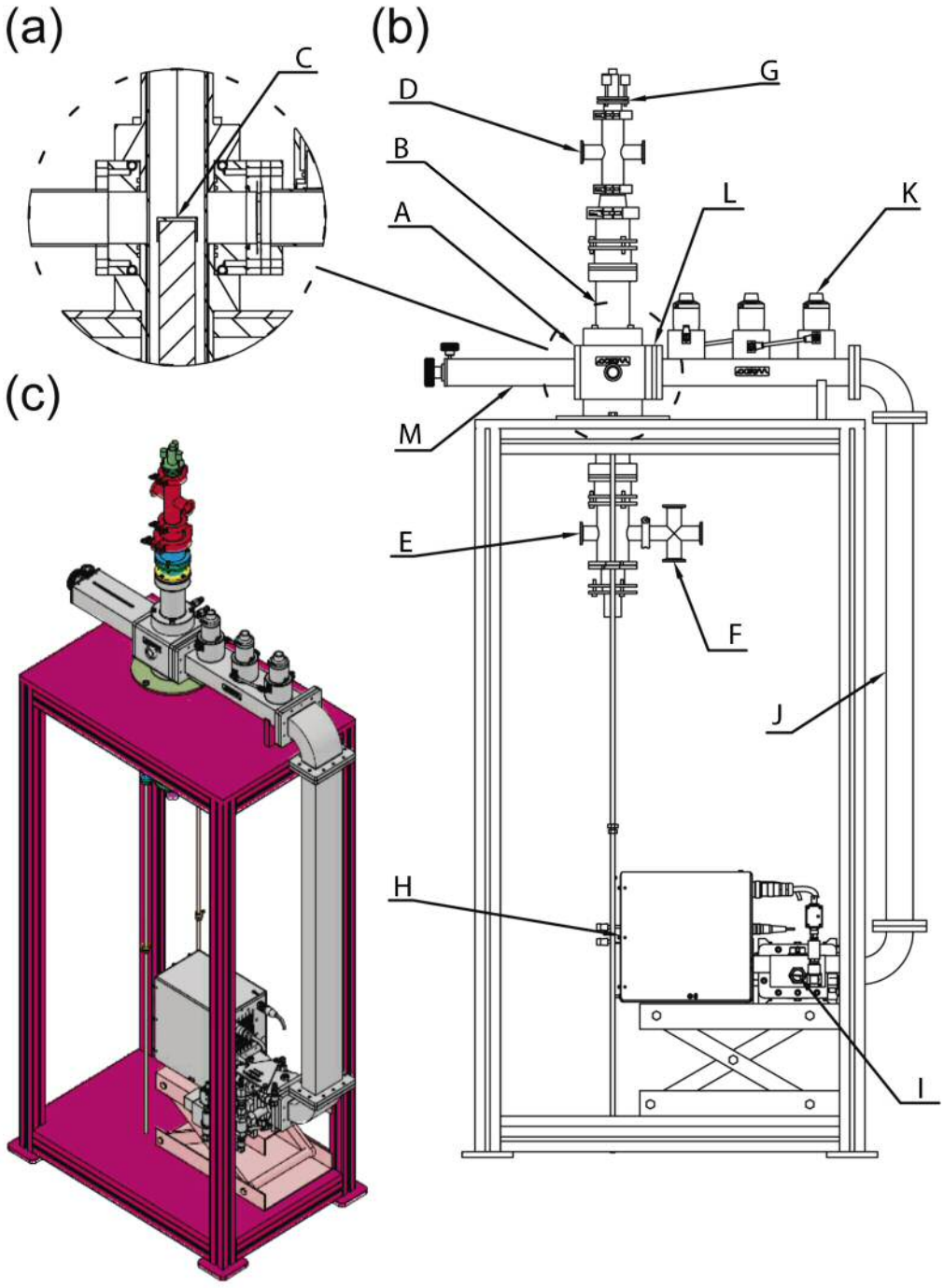

Figure 6.2: NIRIM reactor overview. (a) Cross section of the reactor chamber, showing the placement of the sample holder on top of the quartz rod in the middle of the downstream source. (b) Side view of the reactor indicating all the important components, and (c) isometric view of the reactor.

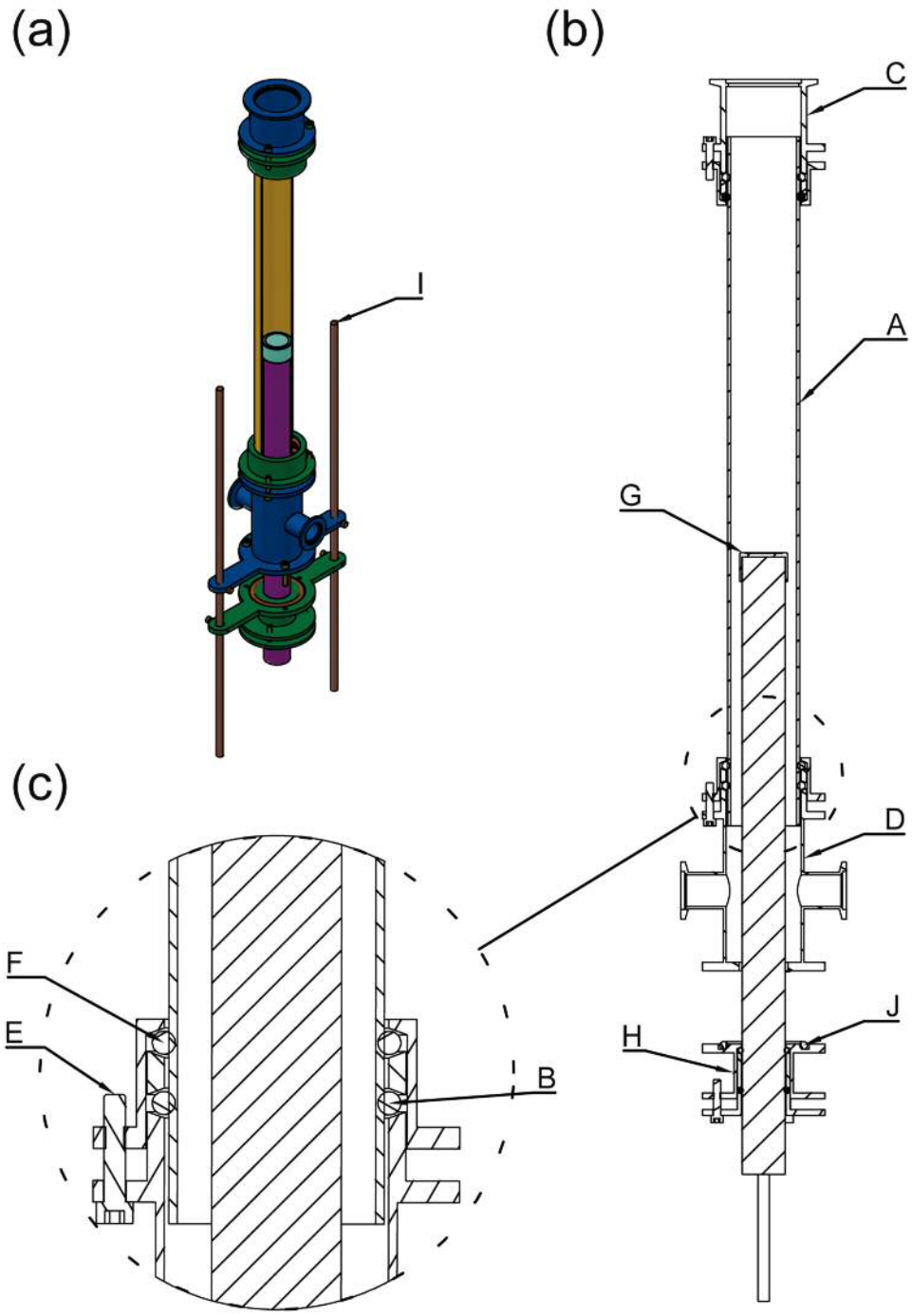

Figure 6.3: Vacuum discharge tube. (a) Overview and (b) section of the discharge tube detailing the components, and (c) cross section detail of the sealing an alignment mechanism around the quartz tube.

6.2.2 Reactor Control and Safety Implementations

To control and run the reactor allowing automated operation and also to facilitate safety, the MFCs and the CVD 3000 pump controller are interfaced with Labview through a series of National Instruments USB-6001 multifunction I/O DAQs and a USB-232 serial instrument controller respectively. Each USB-6001 DAQs is controlling two MFCs as detailed in figure 6.5 b). The way a MFC works is by comparing the flow reading to the setpoint, and positioning a valve to maintain, or achieve, the setpoint rate. [297] The MFCs and DAQs are interconnected through a cable to a 15 pin D-connector (observed in figure 6.4 b)), and powered through a +12 V power supply. The virtual instrument (VI) created in Labview (figure 6.5 c)) allows dynamic control and records the feed gas flow rates while preventing the selection of combustible hydrogen/oxygen mixtures. Finally, the temperature of the sample is recorded passing the 4-20 mA signal of the Williamson pyrometer remote interface through a 500 Ω resistor mounted in a panel close to the MFCs (figure 6.5a)) and measuring the potential with one of the inputs of the DAQs.

Additional safety measurements were implemented. For example, if the flow rate of a MFC deviates from its set point for an extended period of time, the VI will shut off all MFCs and will evacuate the discharge tube. Furthermore, if the pressure within the discharge tube is no longer able to sustain a plasma, the reflected power will increase towards to the magnetron. This increase will be detected by the Sairem components, and the magnetron will be switched off. Moreover, if the reactor pressure exceeds 70 Torr, a hardwired Baratron pressure switch (figure 6.4 a)) will shut off the gas supply through the pneumatic solenoid valves placed in between the MFCs and reactor inlet. Finally, the water flow to the reactor and microwave components is controlled through a flow switch. It is installed so that if the water flow falls below 6 L/min, the magnetron will switch off to prevent overheating of the reactor components.

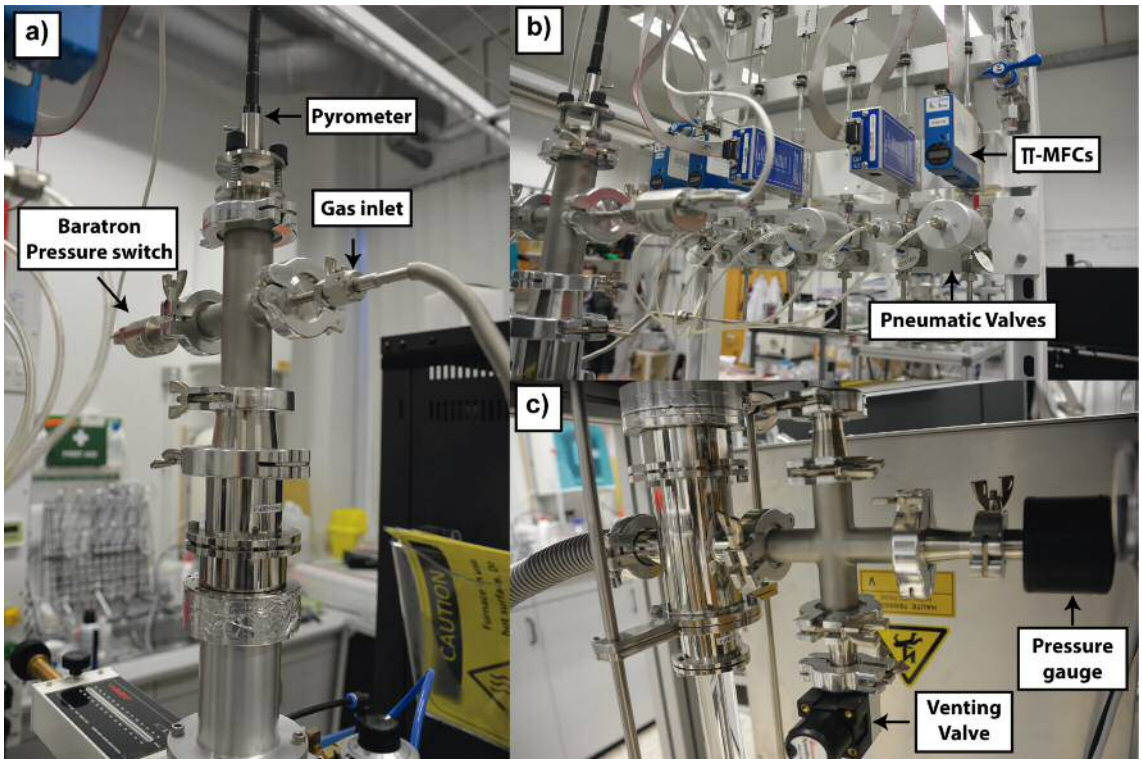

Figure 6.4: Different components of the NIRIM reactor. a) Top part of the reactor, detailing the tilt stage for mounting the pyrometer, the gas inlet and the baratron pressure swicth. b) MFCs, gas lines and pneumatic valves. c) Bottom part of the reactor, with the guide rails at both sides of the quart tube to facilitate the removal of the quartz rod and the pressure gauge and venting valve connected through a tee and KF fittings. All the images have been reproduced from [281]

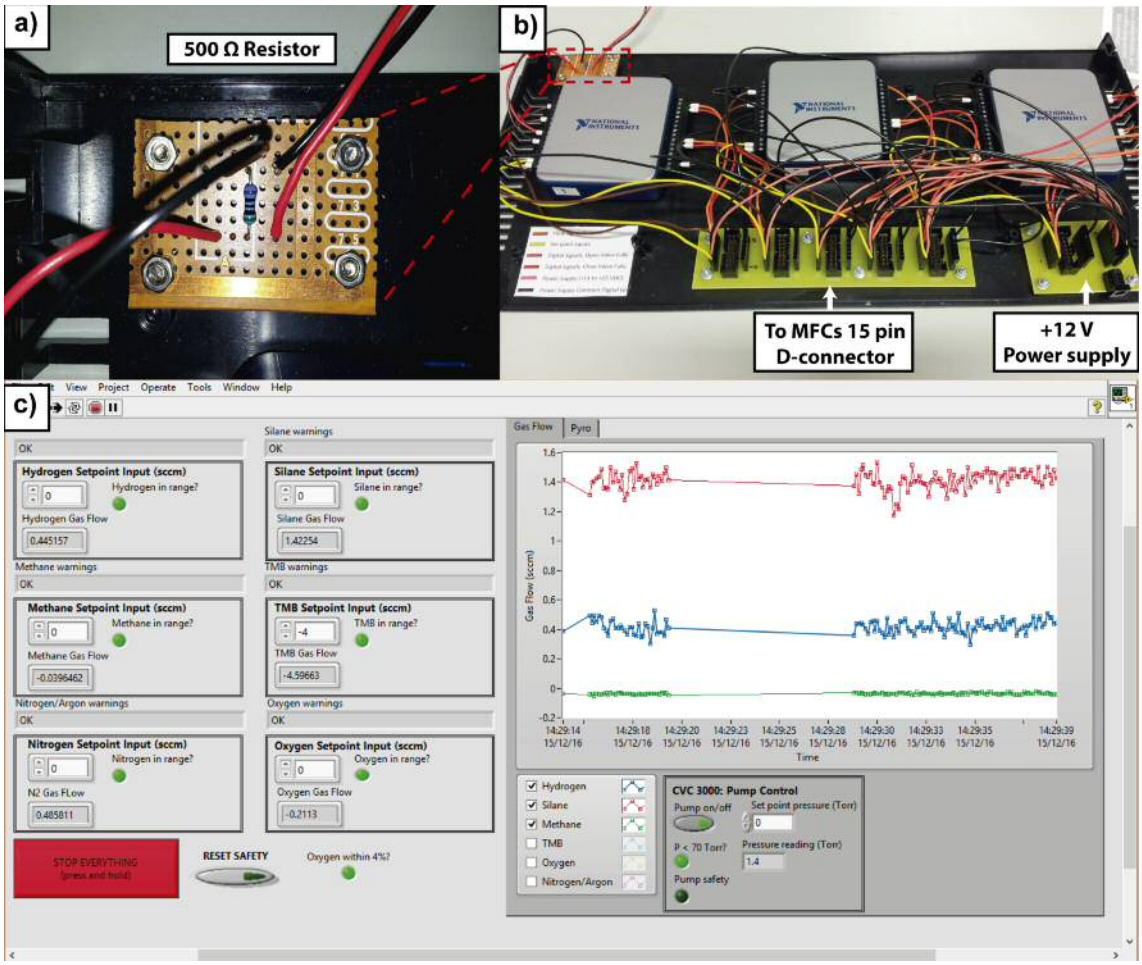

Figure 6.5: Reactor control. a) Resistor to convert the 4-20 mA signal of the pyrometer into a potential, measured in a DAQ input. b) DAQs wired to the 15 pin D-connector of the MFCs and c) main reactor VI with all the gas flow controls and the CVC 3000 pump control.

6.3 Reactor Usage

6.3.1 Improving the optimal growth conditions

Several attempts of diamond growth on the NIRIM reactor were performed before establishing the optimal conditions. Two main parameters were changed. First, the height the quartz rod enters inside the quartz tube and hence the height of the sample and substrate holder within the downstream source and second, the methane-hydrogen flow rate (CH_4/H_2). It is well established that an increase in the methane concentration produces a deterioration of diamond films properties as a result of a reduction in grain size. [22] Therefore, methane concentrations diluted in hydrogen were kept low and set to 3%, 1%

and 0.5%.

Other operation parameters such as reactor chamber pressure and forward power, were kept between 52 and 57 Torr and between 0.52 and 0.57 kW respectively hence growing at high power density conditions. *Williams et al.* [22] demonstrated that diamond growth with a high power density regime produce high quality diamond films, while growth under a low power density regime leads to a deterioration of diamond films properties, producing appreciable changes in film morphology. Controlling the chamber pressure and the forward power, the size of the plasma was also modified, ensuring a large enough high density plasma while minimising contact with the quartz tube walls.

Two different substrate holders were also used for the samples growth, a molybdenum holder and an aluminium nitride one, with no appreciable changes between them.

For the first series of growth, the quartz rod height (sample height) was varied, keeping the rest of the growth parameters the same, as detailed below. For the first growth, the rod height was adjusted so that the sample sat on top of the holder, just at the entry of the waveguide. That sample height was selected as a reference and denoted as 0 mm. Before the growth, the dual wavelength pyrometer was also adjusted to fall on within the middle of the sample, turning the screws in the pyrometer custom made tilt stage, shown in figure 6.2 (G). Four more samples were grown varying the rod height. From the reference point (0 mm), the the rod was moved up, + 5mm and +10 mm, and down, -5 mm and -10 mm and several samples were grown in each position.

Nanocrystalline diamond (NCD) films were grown using (100) Si one-inch wafers as substrates. Prior to growth, the wafers were cleaned following a standard RCA (SC-1) cleaning. The silicon wafers were also seeded in a mono-dispersed colloid containing hydrogen terminated diamond nanoparticles (5 nm) in DI water whilst undergoing agitation in an ultrasonic bath for 10 minutes, thus ensuring high nucleation densities. The seeded sample was then placed in the ceramic holder, on top of the quartz rod and introduced inside the reactor as detailed previously. To prevent diamond seeds from etching during ramp up to growth conditions, an incubation process was performed. In this incubation period, the methane flow was kept to 15 sccm and was diluted in 285 sccm of hydrogen ($CH_4/H_2 = 5\%$). The methane flow was then set to 9 sccm and the hydrogen flow was 291 sccm ($CH_4/H_2 = 3\%$) during the growth process. The chamber pressure was kept between 52 and 57 Torr in all the samples, while maintaining the microwave power in the range of 0.52-0.57 kW. The substrate growth temperature was measured by dual wave-

length pyrometry resulting in temperatures around 740°C. After the growth process,the samples were cooled down in a hydrogen plasma to prevent the formation of non-sp^3 carbon. For comparison, all the samples grown in this chapter are one-micron thick, with thickness determined by *in-situ* laser interferometry and *ex-situ* with a *Filmetrics F-20 Spectral Reflectance* system.

SEM images were performed on all the samples to observe the surface morphological changes due to variations in the sample position within the downstream source. SEM images were acquired in a *Raith e-Line SEM*, at 20kV operation voltage and 10 mm working distance, and are shown in figure 6.6. In the reference sample, shown in figure 6.6 c), no clear diamond faceted crystallites are observed, indicating *a priori* not a good quality diamond film. Moving the quartz rod up, and hence introducing a bit more the sample to sit just above the waveguide entry, produces a further deterioration of the diamond film as observed in figures 6.6 d) and 6.6 e). However, situating the rod/sample -10 mm (figure 6.6 a)) or -5 mm (figure 6.6 b)) below the reference height, generates diamond films with some faceted diamond grains with sizes between 100 nm and 200 nm showing an improvement in diamond film quality.

For this reason, -5 mm was the chosen height for subsequent diamond films growth.

Once the holder position was adjusted such as the sample sits just below the entry of the waveguide, the methane flow rate was varied. As explained below, the methane flow rate was kept low in order to avoid the deterioration of the diamond films, so CH_4/H_2 ratios of 3%, 1% and 0.5% were selected. In the first one, a methane flow of 9 sccm diluted in 291 sccm of hydrogen was used, whereas the methane flow was set to 3 sccm and 2 sccm and the hydrogen flow to 297 sccm and 398 sccm for the second and the third one respectively. To check reproducibility, several samples were grown for each CH_4/H_2 ratio. Samples sitting on top of both the aluminium nitride and the molybdenum holder were also grown, shown in figure 6.7. SEM images on the left column correspond to the samples grown using the aluminium nitride holder (figures 6.7 a), 6.7 c) and 6.7 e)), whereas samples grown using the molybdenum holder are shown on the right column (figures 6.7 b), 6.7 d) and 6.7 f)). A clear improvement on the quality of the diamond films is achieved when reducing the methane-hydrogen ratio from 3% to 1%. Completely coalesced diamond films with clear faceted 100 nm grains are obtained. A further reduction in the methane ratio also results in good quality diamond films with slightly reduced crystallites sizes.

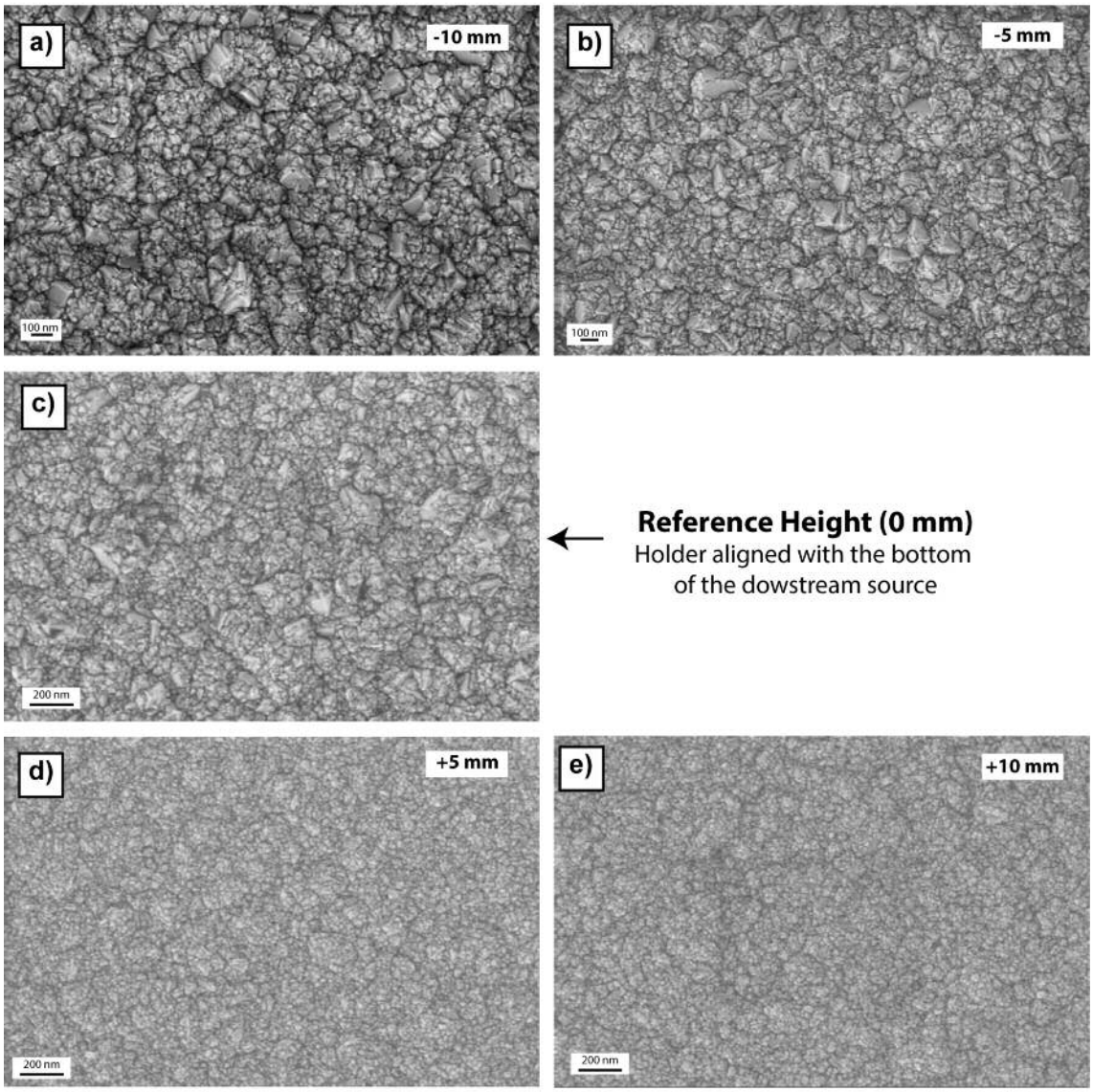

Figure 6.6: SEM images of one-micron diamond films grown onto Si substrates in the NIRIM reactor. Diamond film grown with the quartz rod situated below the entry of the waveguide at a) -10 mm and b) -5 mm in respect to the reference sample. c) Diamond film grown with the sample sat just at the entry of the waveguide, used as a height reference. d) and e) Diamond films grown with the sample sat just above the entry of the waveguide at +5 mm and +10 mm above the height reference respectively.

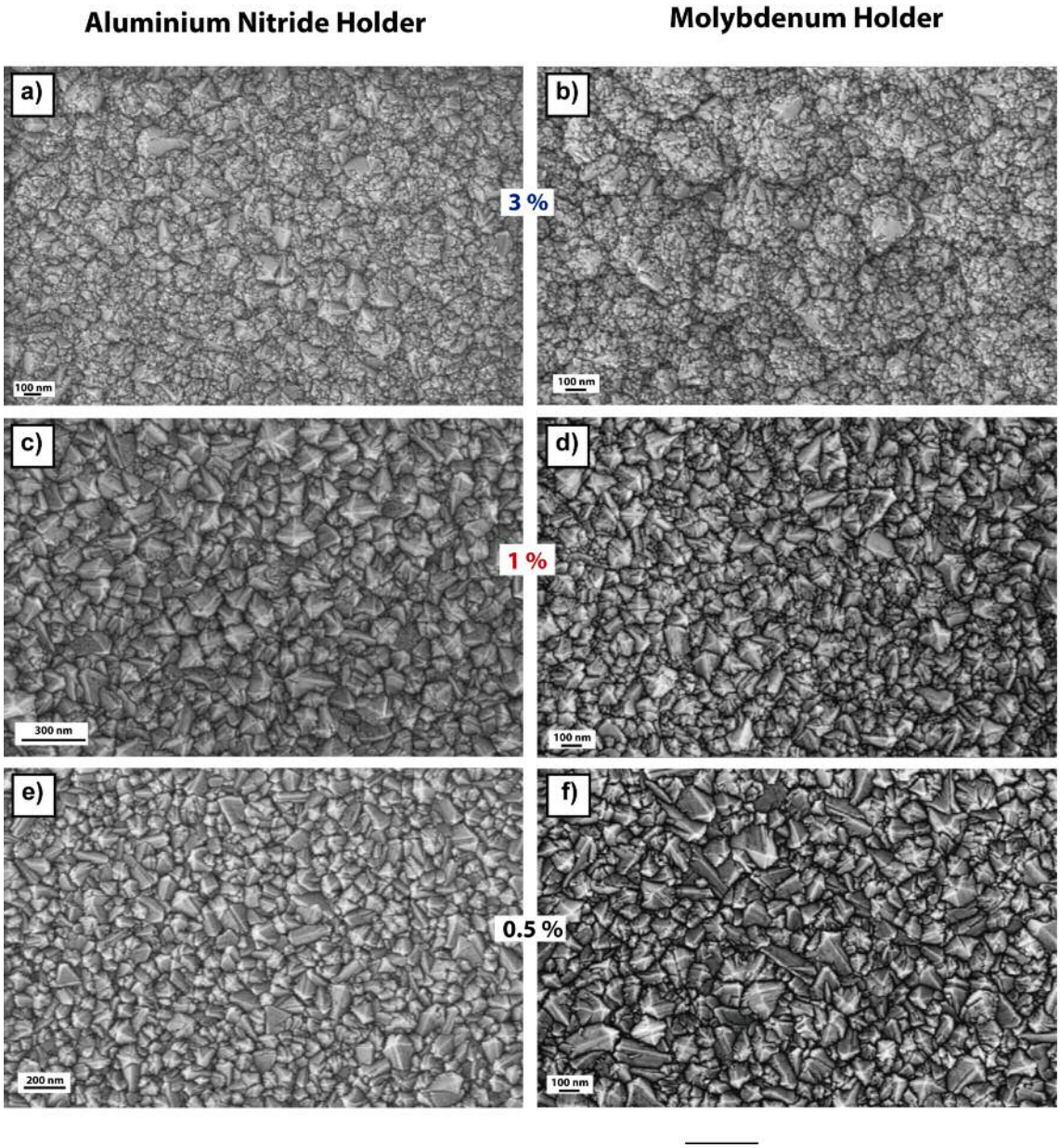

Figure 6.7: SEM images of the diamond films grown onto Si substrates in the NIRIM reactor.

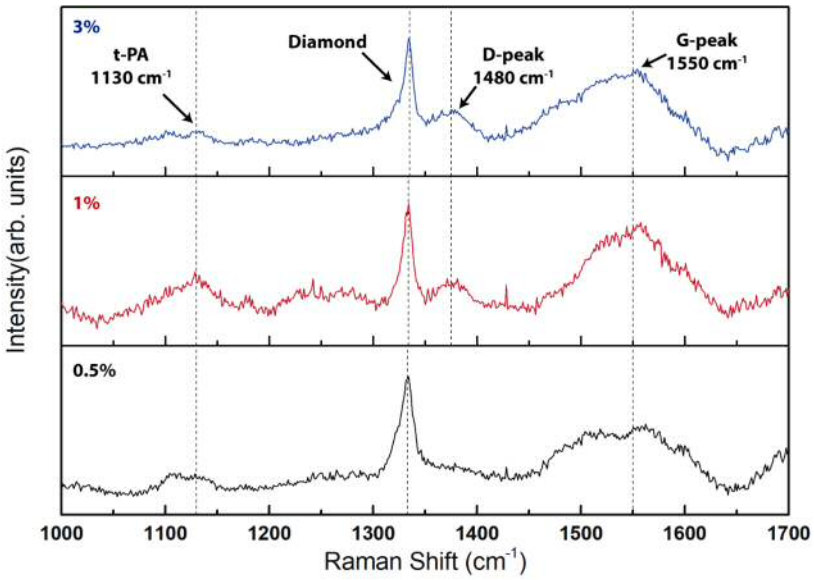

Figure 6.8: Raman spectrum of the one-micron diamond film for different CH_4/H_2 flow rates, as indicated in each graph.

Raman measurements were performed to confirm the quality of the films grown with the different methane-hydrogen flow ratios, and the measurements were carried out in a *in Via Renishaw* confocal Raman microscope, equipped with a 532 nm laser. As shown in figure 6.8, all the spectra show the first-order diamond peak, with peak positions and FWHM detailed in table 6.1. These peaks are broadened due to the small size of the crystallites. A pronounced broad G-band is located between 1450 cm^{-1} and 1650 cm^{-1}, and it is due to the bond stretching of all pair of sp^2 atoms in both rings and chains. [298] Furthermore, a peak at 1130 cm^{-1} appears, which has been related to the presence of C-H bonds in trans-polyacetylene structures (TPA). [158] A less pronounced peak at 1380 cm^{-1} is attributed to the well-known D-peak, and is due to breathing motion of sp^2 rings.

CH_4/H_2 (%)	**Raman peak** (cm^{-1})	**FWHM** (cm^{-1})
3	1335	10.12
1	1334	11.29
0.5	1333	15.50

Table 6.1: First-order diamond Raman peak positions and FWHM values for diamond films with increasing methane-hydrogen flow ratios.

Due to higher growth rates were obtained with higher methane-hydrogen flow ratios, $CH_4/H_2 = 1\%$ was selected for subsequent diamond films growths.

Finally, the last film with the selected growth parameters was grown to check reproducibility. Thus, the flow rates of methane and hydrogen were initially set to 15 sccm and 285 sccm for 5 min during the incubation period and then the methane flow was reduced to 3 sccm ($CH_4/H_2 = 1\%$). The hydrogen flow was increased to 297 sccm ensuring a constant gas flow of 300 sccm. The pressure used was 55 Torr and the microwave power was 0.52 kW, resulting in temperatures around 740°C. The film thickness was one-micron, with a growth rate of 0.5 $\mu m/h$.

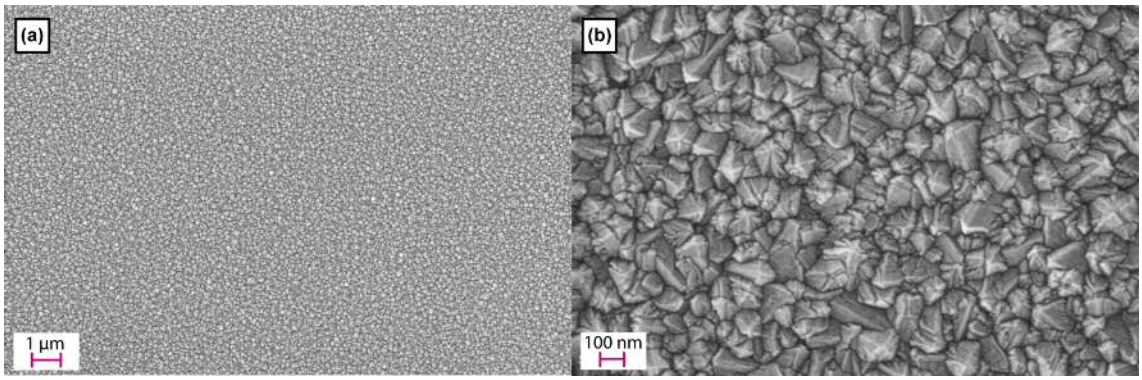

Figure 6.9: SEM images of the one-micron diamond film grown onto a (100) silicon substrate. (a) Lower and (b) higher magnifications showing the coalescence of the diamond film and the size of the diamond grains respectively.

SEM images and Raman measurements were performed in the sample. The SEM image in figure 6.9 (b), shows clear faceting of the diamond grains whereas the low magnification image (figure 6.9 (a)), confirms the coalescence of the film without pinholes in the substrate. Meanwhile, Raman spectra shown in figure 6.10, shows a clear first-order diamond peak at 1332 cm^{-1}, the TPA peak at 1130 cm^{-1} and a less pronounced G-band at around 1550 cm^{-1}. It is well-known that the scattering efficiency of graphite is approximately 50 times larger than the diamond one considering an excitation of 514 nm. This means that in combination with the diamond film morphology observed, a high diamond fraction is observed in the NCD film.

6.3.2 Reactor cleaning

Although reactor quartz rod and substrate holder are cleaned with isopropyl alcohol and DI water after each growth run, it is not necessary to clean the reactor quartz tube so often. Nevertheless, after approximately 20 hours of operation, an amorphous carbon band is deposited in the interior of the quartz tube adjacent to the plasma which can affect the microwave propagation within the waveguide. For this reason, it is mandatory to then

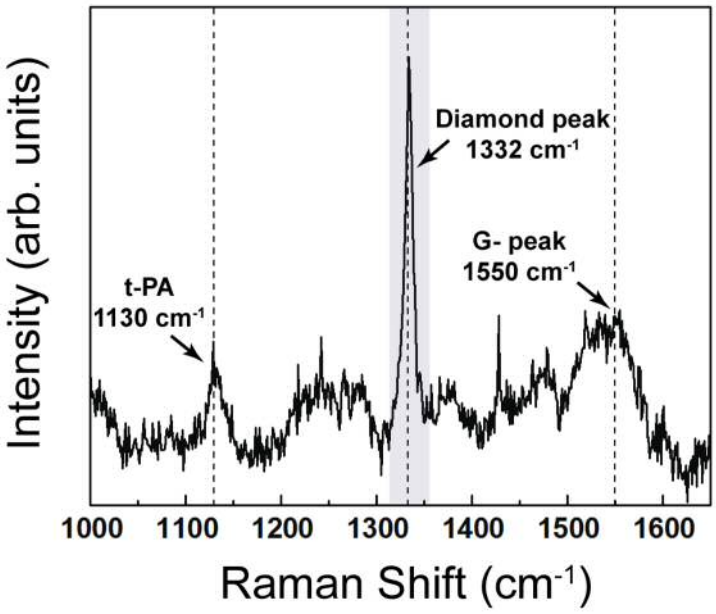

Figure 6.10: Raman spectrum of the one-micron diamond film.

remove the quartz tube. The quartz tube is cleaned by heating it in air at 600-700°C inside a furnace for 5-6 hours or until clean. The quartz tube can also be replaced if a dopant is changed.

6.4 Silane Incorporation

Once the optimal conditions for diamond growth were established, studies changing the silane flow rate were performed. A series of nanocrystalline diamond (NCD) films were grown using silicon (100) one-inch wafers. These wafers were previously cleaned following a standard RCA (SC-1) cleaning. The silicon wafers were also seeded in a mono-dispersed colloid containing hydrogen terminated diamond nanoparticles (5 nm) and DI water whilst undergoing agitation in an ultrasonic bath for 10 minutes, thus ensuring high nucleation densities. The seeded sample was then placed in the ceramic holder, on top of the quartz rod and introduced inside the reactor as detailed previously. Initially, an incubation process was performed, with methane flow set to 15 sccm diluted in 285 sccm of hydrogen ($CH_4/H_2 = 5\%$). The methane flow rate was then reduced for the growth process and set to 3 sccm. Hydrogen was set to 291 sccm to ensure a methane-hydrogen ratio of $CH_4/H_2 = 1\%$ during the growth while silane flow rate was varied, keeping the total flow rate at 300 sccm. Silane flow rates were selected according to the minimum gas flow that

can be controlled and measured in the silane mass flow controller (500 SCCM). Silane flow rates were set to 0 sccm, 10 sccm, 15 sccm, 20 sccm, 25 sccm and 30 sccm, representing silane-methane ratios (SiH_4/CH_4) of 0%, 0.16%, 0.25%, 0.33%, 0.42% and 0.50% respectively. The chamber pressure was kept between 52 and 55 Torr in all the samples, while maintaining the microwave power in the range of 0.52-0.55 kW. The substrate growth temperature was measured by dual wavelength pyrometry resulting in temperatures around 740°C. After the growth process, the samples were cooled down in a hydrogen plasma to prevent the formation of non-sp^3 carbon. The diamond films thickness was kept at $1\mu m$ and was determined by *in-situ* laser interferometry and *ex-situ* with a *Filmetrics F-20 Spectral Reflectance* system. Different growth rates were obtained as shown in figure 6.11. A growth rate of 0.5 $\mu m/h$ was found for the sample without silane incorporation and a reduction in growth rate was observed as the silane content was increased. Finally, a growth rate of 0.27 $\mu m/h$ was measured for $SiH_4/CH_4 = 0.5\%$.

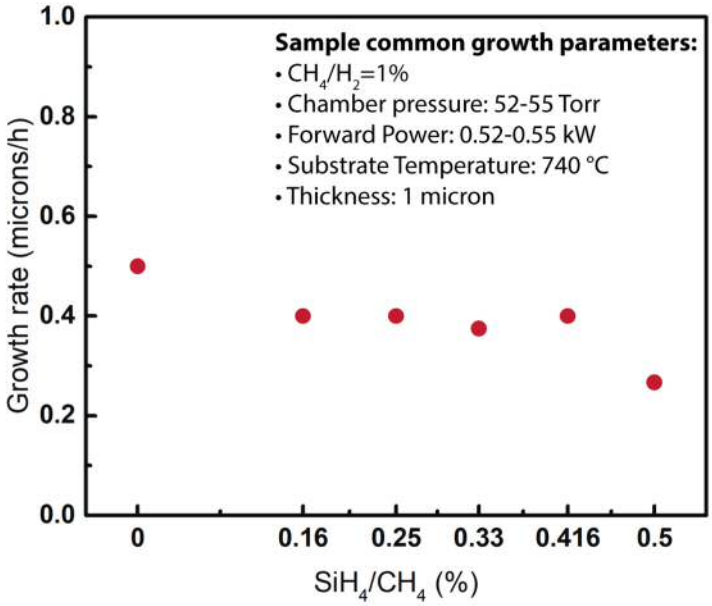

Figure 6.11: Diamond films growth rates as a function of silane-methane concentration ratios, determined by laser interferometry.

6.4.1 SEM measurements

SEM measurements were performed to study changes in morphology and grain size. The samples were characterized in a *Raith e-Line* SEM, at 20kV operation voltage and 10 mm working distance. SEM images are shown in figure 6.12. Figure 6.12a) shows a diamond

film without silane incorporation. The faceted diamond grains with sizes between 100 nm-200 nm indicate high quality material. Low magnification images were also taken to prove the coalescence of the diamond film, and similar images as the one in figure 6.9a) were obtained. As the silane flow rate was increased, a deterioration in the crystalline quality was obtained, with re-nucleation processes observed. This deterioration in crystalline quality is clear in figure 6.12c), where not many clear faceted diamond grains are visible. Further increase in the silane content results in a further noticeable diamond film surface morphology deterioration, with rough surfaces, as seen in figure 6.12e). Nevertheless, well-faceted (100) diamond crystallites are observed in figure 6.12d) which corresponds to a silane flow rate of 0.33%.

6.4.2 Raman measurements

The quality of the diamond films grown was measured by Raman spectroscopy, in a *in Via Renishaw* Raman spectrometer equipped with a 514.5 nm Ar^+ laser. The normalized Raman spectra in figure 6.13 show a clear first-order diamond peak at around 1332 cm^{-1} for all the samples (exact values for the diamond Raman peak are shown in table 6.2). As seen in figure 6.10, the peak broadening is due to the small size of the crystallites. [298]. In the sample without silane incorporation (figure 6.13a)) a peak at around 1130 cm^{-1} also appears, due to the presence of trans-polyacetylene structures. [158] The presence of this peak is however not observed in the rest of the samples. In the same curve, the broad G-band ranging from 1400 cm^{-1} to 1600 cm^{-1}, confirms the presence of sp^2 bonds. [159] Apart from the sample in figure 6.13c), which corresponds to a silane-methane ratio of 0.25%, a broadening in the diamond Raman peak is observed with increasing SiH_4/CH_4 ratios. Furthermore, a reduction of the G-band (compared to the sample without silane) could be due to the presence of less grain boundaries.

SiH_4/CH_4 (%)	**Raman peak** (cm^{-1})	**FWHM** (cm^{-1})
No silane	1332.11	11.23
0.16	1331.27	12.87
0.25	1331.63	9.83
0.33	1330.70	13.18
0.42	1331.26	14.00
0.50	1331.46	14.77

Table 6.2: First-order diamond Raman peak positions and FWHM values for diamond films with increasing silane-methane flow ratios.

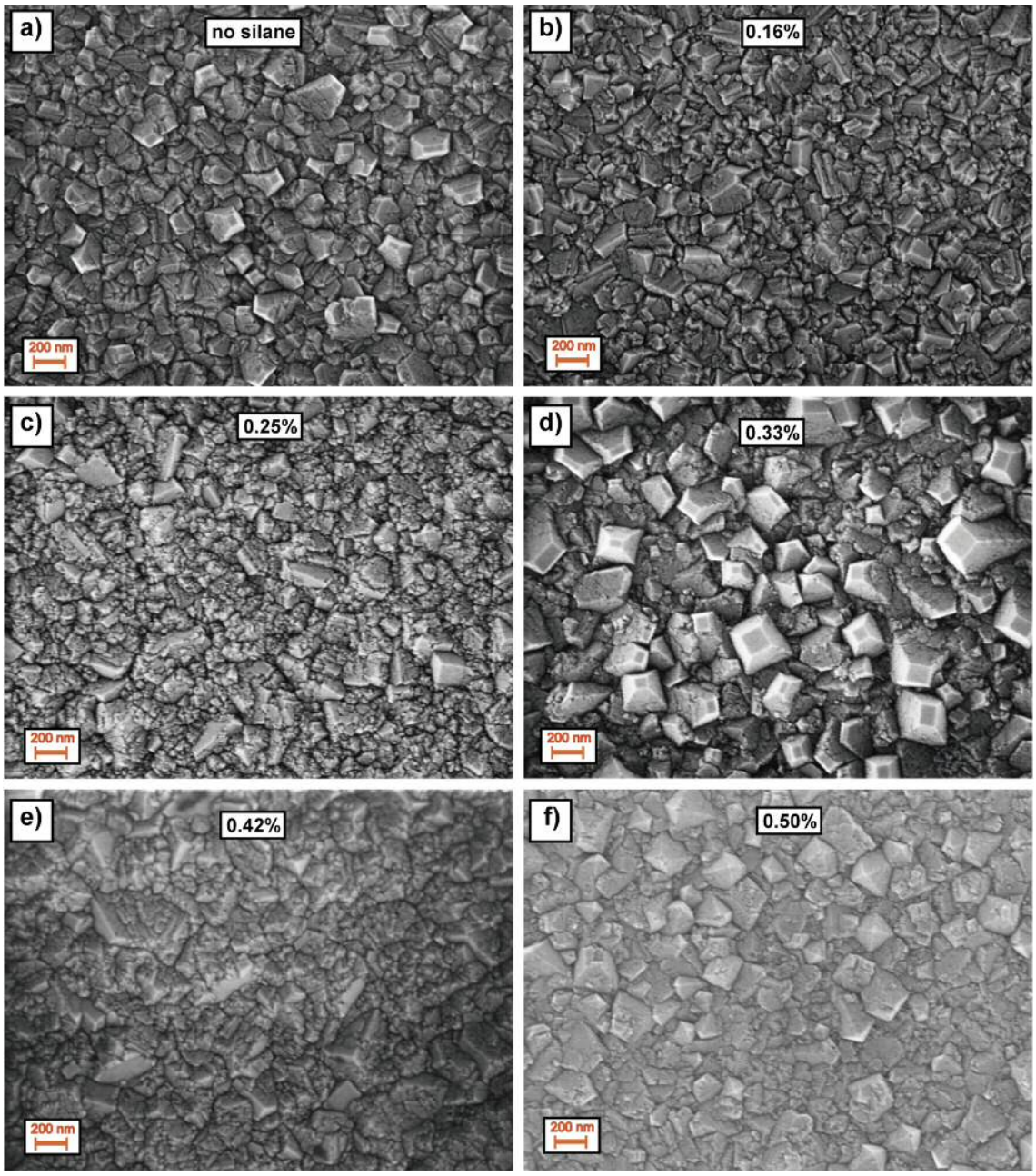

Figure 6.12: SEM images of the one-micron diamond films grown onto silicon substrates, with increasing silane-methane flow ratios. a) No silane addition, b) $SiH_4/CH_4 = 0.16\%$, c) $SiH_4/CH_4 = 0.25\%$, d) $SiH_4/CH_4 = 0.33\%$, e) $SiH_4/CH_4 = 0.42\%$ and f) $SiH_4/CH_4 = 0.50\%$.

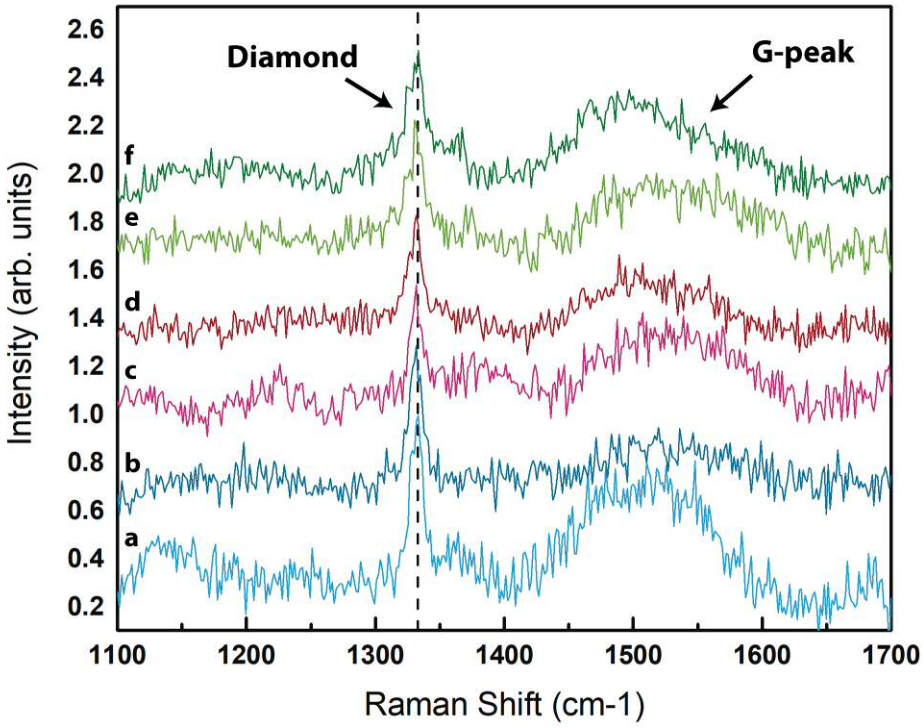

Figure 6.13: Raman spectra of the diamond films with increasing silane-methane ratios from bottom to top. a) Diamond film without silane incorporation, b) SiH_4/CH_4 = 0.16%, c) SiH_4/CH_4 = 0.25%, d) SiH_4/CH_4 = 0.33%, e) SiH_4/CH_4 = 0.42% and f) SiH_4/CH_4 = 0.50%.

6.4.3 PL measurements

In order to study how the silane flow variation influences the SiV emission, PL spectra were recorded in a *Renishaw in Via Reflex* spectrometer using a 633 nm He-Ne laser (figure 6.14). All the samples exhibit the characteristic SiV peak at 738.5 nm. Furthermore, the sample with no silane presents another peak at 758 nm. The SiV PL intensity shows a maximum for the sample in which there is no addition of silane, and this intensity decreases with further silane addition, as shown in figure 6.14c). The PL quenching observed as the SiH_4/CH_4 ratio is increased, highlight the necessity of using non-silicon substrates for silane incorporation. The amount of silicon present in the feed gas coming just from the plasma etching of the Si substrate produces an intense SiV peak, and the silane incorporation is completely masked. Furthermore, the SiV quenching can be related to the presence of more defects, as shown in the SEM images and in the broadening of the diamond Raman peak as shown in figure 6.13.

From the above SEM, Raman and PL results, it can be concluded that high silane doping results in change in surface morphology and in general, reduction of the quality of diamond films. *Cui et al.* [278] observed an increase in the amount of defective structure in highly doped microcrystalline diamond film (MCD) onto a silicon substrate, grown with the addition of tetraethoxysilane (TEOS). They associated this more defective structure with the stress caused by the lattice distortion and dilatation due to the incorporation of a larger size atom (compared to carbon) into the diamond lattice.

In order to reduce the silane doping and the Si incorporated, two strategies will be followed. In the first one, the Si substrate will be replaced by non-silicon substrates. In the second one, the MFC will be change to a one that can control less silane flow (minimum between 0.05 and 0.1 sccm and maximum flow 5 sccm). These flow rates will be translated into Si/C ratios between 16.6 ppm and 833.3 ppm.

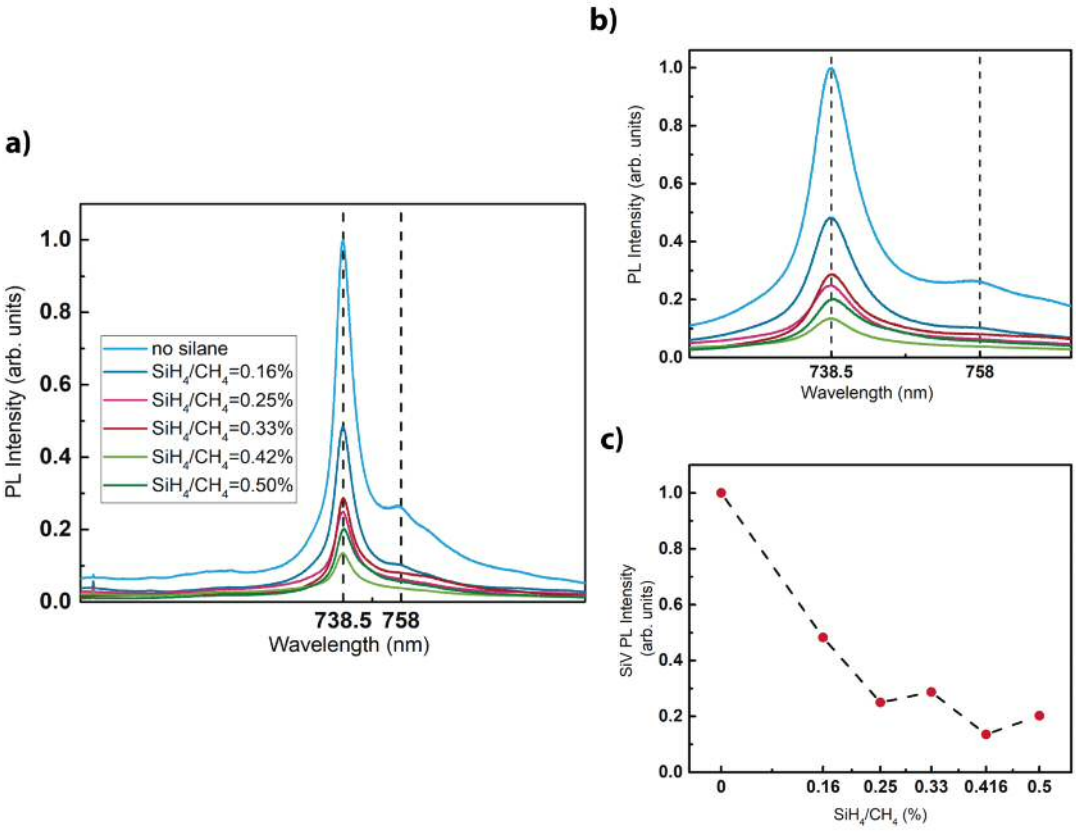

Figure 6.14: PL spectra of the diamond films with different silane content. a) SiV PL emission centred at 738.5 nm, b) detail of figure a), with a second peak centred at 758 nm and c) SiV maximum peak intensity for the different silane concentrations.

6.5 First attempts to grow onto different substrates

After diamond films growth onto Si substrates incorporating silane at different flow rates, several non-silicon substrates were used with the same purpose. Heteroepitaxial diamond growth on different substrates has been extensively studied and reported in the literature. [299, 300] The choice of the adequate substrate is influenced by the lattice mismatch between the substrate and the diamond film and the coefficient of thermal expansion, which will have an impact over the stability of the diamond film grown. [301] Diamond growth in this section, has been performed onto iridium-coated and W-coated Si substrates, but before the introduction of silane, the optimal conditions for CVD growth onto these substrates were established.

Due to the high surface energy of diamond relative to silicon ($6J/cm^2$ to $1.5J/cm^2$ for the (111) plane) [146] combined with low sticking coefficient of gaseous precursors and the competition of nondiamond phases, seeding the substrates with colloids containing 5 nm diamond nanoparticles, has been proved to facilitate the diamond growth upon an incubation step previous to the growth process. [145] Both chapter four and five explained the importance of seeding the substrate before the CVD growth to ensure high seeds density hence obtaining completely coalesced diamond films. The electrostatic interaction between the diamond seeds and the substrate, will determine this diamond nanoparticles density. As was also explained in these chapters, the charging behaviour between the different interfaces can be described with the zeta potential parameter, measured experimentally through electrokinetic effects. One of these electrokinetic effects, the electrophoretic mobility, was extensively described in chapter four as the main method to measure the zeta potential and stability of diamond nanoparticles with different surface groups dispersed in a colloid.

However, the seeding process is not as straightforward for substrates with unknown surface zeta potential (ζ), hence measurements to obtain this value need to be performed. Similar methods as the ones used to measured the zeta potential in a colloid, can be used to determine the surface zeta potential of a flat material. [129] The first one is based on a combination of the determination of the electrophoretic mobility and the electro-osmosis effects of tracer particles (already dispersed in a colloid) with respect to the surface of interest. [302] An optional tool for the *Zetasizer Nano* allows to determine the surface zeta potential. This accessory includes a special cell with electrodes, a holder to attach the flat surface sitting in between the electrodes and a cell cap with an adjustment screw.

After the sample is properly fixed to the holder and correctly aligned, the cell is introduced in a cuvette containing the tracer particles. The screw on top of the cell cap is used to move the sample so that the apparent tracer mobility is measured at different distances from the sample surface. Close to the surface, the tracer particles behaviour will be dominated by electro-osmotic effects. On the other hand, at further distances from the surface, the tracer particles behaviour will be dominated by their electrophoretic motion. The surface zeta potential will be determined by extrapolating values from the graph obtained with the values measured at the different distances and applying the following formula:

$$\zeta = -intercept + \zeta_{particles} \tag{6.1}$$

Although several attempts to determine the surface zeta potential on both iridium and tungsten substrates were performed, this was not the definitive method used to measure the surface zeta potential. The main drawback of this method is the necessity of using tracer particles. There are many available commercial tracer particles with different surface groups terminations (hence making the particle negatively charge, positively charge or neutral once in the solution), although any particle with known surface charges could be used (as nanodiamonds seeds for instance). As it is obvious, the tracer particles have to be chosen to carry the same surface charge as the substrate, as particles with the opposite sign of surface charge will provoke a electrostatic interaction between the flat surface and the particles, making impossible or masking the surface zeta potential measurements. Furthermore, if the aim is to measure the surface zeta potential of a substrate, this value will be unknown hence making the choice of the tracer particles impossible.

For this reason, a different method based on another electrokinetic effect, the streaming potential, was used to obtained the surface zeta potential value.

Streaming current/potential measurements

The streaming current and streaming potential are two related electrokinetic phenomena based on the production of an electric current/potential when a mechanical force is applied to a solution that moves along the surfaces of a stationary material. In this case, a pressure gradient makes an electrolyte go through a channel (formed between the solid sample and a reference solid material) with charged walls. The electrolyte flow produces a displacement of the ions of the electrochemical double layers of the flat samples that form the channel,

producing a charge difference between the Ag/AgCl electrodes (situated at both ends of the streaming channel) which gives raise to a measurable electrokinetic effect: the streaming current or the streaming potential. The streaming current is measured when the electrodes are connected through a low resistance, whereas the streaming potential is measured when a high resistance is placed between them (in an open circuit). [303,304] Both can be used to determine the surface zeta potential applying the following equations:

$$\zeta = \frac{dI}{dP} \times \frac{\eta}{\varepsilon \times \varepsilon_0} \times \frac{L}{A} \tag{6.2}$$

$$\zeta = \frac{dU}{dP} \times \frac{\eta}{\varepsilon \times \varepsilon_0} \times \kappa_B \tag{6.3}$$

with equation (6.2) been the equation for the streaming current and equation (6.3) for the streaming potential. In equation (6.2), dI/dP is the slope of the streaming current vs differential pressure, η is the electrolyte viscosity and ε and ε_0 are the dielectric coefficient and the permittivity of the electrolyte respectively. The last term corresponds to the streaming channel dimensions, L is the length of the channel and A its cross section. In equation (6.3), κ_B is the electrolyte conductivity. Although both equations are most of the time used indistinctly, it has been reported in the literature that lower surface zeta potential values have been obtained from streaming potential measurements. [305] Furthermore, the choice between both will depend on the sample properties.

Surface zeta potential measurements were carried out in an *Anton Paar* $SurPASS^{TM}3$ Electrokinetic Analyzer. The substrate was placed in a clamping cell, [306] facing a PMMA reference sample (provided by Anton Paar) forming the streaming channel with a distance between the plates set around $100\mu m$. A 10^{-3} M solution of potassium chloride was used as electrolyte, and the pressure was varied initially from 600 to 200 mbar. Surface zeta potential measurements were performed as a function of pH. The initial pH of the electrolyte, around pH 5.8, was varied to higher and lower pH values, using the in-built $SurPASS^{TM}3$ titrator with 0.1 M HCL and 0.1 M NaOH solutions. All the measurements performed are the average of 10 cycles.

Three different substrates were measured. The first one consists of a piece of a Si wafer, coated with 40 nm of Gold. In the second one, a two-inch wafer was coated with 40 nm of Ir and the third one consists of a two-inch Si wafer coated first with 20 nm of a Ti adhesion layer followed by 40 nm of W. The wafers were measured uncut.

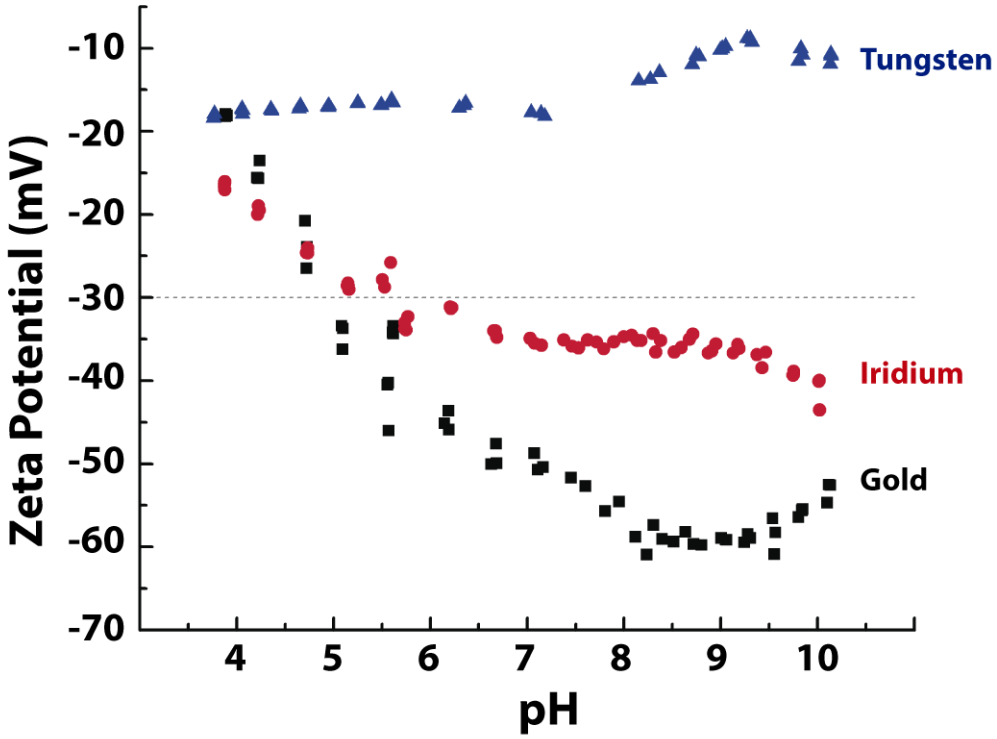

Figure 6.15: Surface zeta potential vs pH for Gold, Iridium and Tungsten coated Si substrates. Negative zeta potential values are measured in the whole pH range.

Figure6.15 shows the surface zeta potential as a function of pH for the three substrates. As can be observed, the three substrates present a negative zeta potential for the whole pH range, with gold having the most negative surface zeta potential. However, determining the surface zeta potential of metals (conductive materials) can sometimes be difficult as the sample conductivity can interfere with the electrokinetic channel conductivity, leading to unrealistic values of ζ. In these cases, it is better to obtain ζ measuring the streaming current instead of the streaming potential, as in theory the streaming current is not affected by the electronic conductance. [303, 304] All the samples were measured in the streaming current configuration. However, unreliable ζ values were obtained for the W-coated substrate (figure 6.15). Furthermore, the pressure range in which the measurements were performed, was adjusted such as the pressure ramp (streaming current vs differential pressure) shows a linear behaviour. [307]

As the results show a negative surface zeta potential, both the iridium coated substrates and the W coated substrates were seeded (as detailed before) in a mono-dispersed colloid containing hydrogen terminated diamond nanoparticles (to obtain high seeds density),

previous cleaning with Isopropanol and DI water. However, a piece of iridium was also seeded with a mono-dispersed colloid containing air-treated diamond nanoparticles for comparison. Both iridium seeded substrates were first introduced in a *Seki*, formerly *ASTEX*, *AX6500* series reactor. For the incubation period, 15 sccm of CH_4 were diluted in 285 sccm of H_2 ($CH_4/H_2 = 5\%$) for 5 min. The methane flow was then reduced for the CVD growth process to 3 sccm while increasing the hydrogen to 297 sccm ($CH_4/H_2 = 1\%$), ensuring a total flow of 300 sccm. The microwave power was set to 3.5 kW and the chamber pressure was set to 40 Torr, resulting in temperatures around 800°C, as determined by the dual wavelength pyrometer. The growth duration was 10 min. Optical microscope and SEM images are shown in figure 6.16. Figure 6.16a) and figure 6.16b) correspond to the Ir-coated substrates seeded with the air-annealed diamond seeds after the 10 min growth. As can be observed, the Ir layer has been partially etched with some patches of diamond growth. In figure 6.16b), a detail of the diamond growth on top of the etched substrate can be observed. On the other hand, the same substrate seeded with hydrogenated diamond seeds presents as well some etched areas, but the surface shows areas completely covered with diamond. These non-etched areas show some membrane-like bulged and wrinkled structures (figure 6.16c)).

The etching observed can be due to the reduced thickness of the Ir layer (40-50 nm) or due to the diamond growth conditions. However, diamond growth on top of Ir substrates has been reported in the literature, although a thicker Ir layer (150 nm) was deposited on top of Ir-coated $SrTiO_3$ buffer layers, [308] as well as on top of Ir/Yttria-stabilized zirconia buffer layers, [309] achieving completely-coalesced thick diamond films growth. Furthermore, the highly oriented diamond growth obtained as well as the capability of dissolve carbon at the beginning of the growth process and then expelling it to the surface resulting in efficient nucleation, [310] made Iridium an interesting substrate for SC diamond growth. [311]

As the main aim to try diamond growth in these kind of substrates is to study how the silicon incorporation (controlled changing the silane flow) affects the production and optical properties of the SiV centres, the Si incorporation from the substrate etching needs to be avoided. To avoid the etching, the CVD growth conditions were varied. The chamber pressure was reduced from 40 to 25 Torr and the microwave power was set to 2.5 kW. The methane and hydrogen flow rates were kept unchanged during the incubation and the growth processes and temperatures around 500 °C were measured. Figure 6.16e) and figure 6.16f) show the sample after 10 min growth at low temperature. No substrate etching was observed but there was not a complete coalescence of the diamond film, as

longer CVD growth durations are needed.

After the standard conditions for diamond growth onto Ir-coated substrates were established, similar conditions were translated for CVD growth in the NIRIM-type reactor. A piece of a seeded Ir-coated Si wafer was placed on top of the aluminium nitride holder and introduced in the NIRIM-type reactor. The incubation and growth processes were conducted for 5 and 10 min respectively at 40 Torr and 52 Torr chamber pressures. The microwave power was first set to 0.35 kW for the incubation process and was increased to 0.52 kW for the growth process. The methane and hydrogen gas flows were the same as for the iridium growth on the ASTEX reactor for both the incubation and the growth processes. The diamond films resulting after the growth present same characteristics as the ones in figure 6.16e) and in figure 6.16f).

Once the adequate conditions for growth onto Ir-substrates (without substrate etching) were established, growth onto W substrates was performed in the NIRIM reactor. Studies of nucleation and growth of ultrananocrystalline diamond films on W-coated Si substrates have been reported, with W promoting a high density seeding. [312, 313] A piece of a W-coated Si wafer was cleaved and cleaned with isopropanol and DI water, and seeded in the colloid containing hydrogen-treated diamond nanoparticles. Two runs of diamond growth were performed. In the first one, an incubation process was performed for 5 min at 40 Torr chamber pressure and 0.35 kW microwave power. The methane was set to 15 sccm diluted in 285 sccm of hydrogen $CH_4/H_2 = 5\%$. The methane flow was then reduced to 3 sccm while increasing the hydrogen flow up to 291 sccm during the diamond growth process ($CH_4/H_2 = 1\%$), performed for 10 min. The chamber pressure was 52 Torr, while keeping a microwave power of 0.55 kW. The sample was cooled down in a hydrogen flow, as performed after all the growth processes. As substrate etching was observed, the conditions were varied in the second round. A longer incubation process was performed (10 min) to allow the completely coalescence of the diamond film onto the Ir substrate, hence protecting it from plasma etching. After the incubation period, both the chamber pressure and the microwave power were increased to the values used during the first W growth, 52 Torr and 0.55 kW microwave power. Substrate etching was not observed and therefore, the conditions to growth onto W substrates were established.

However, due to plasma instability was observed (plasma flashing), it was not possible to continue with the silane incorporation as the magnetron was sent back to the reactor company.

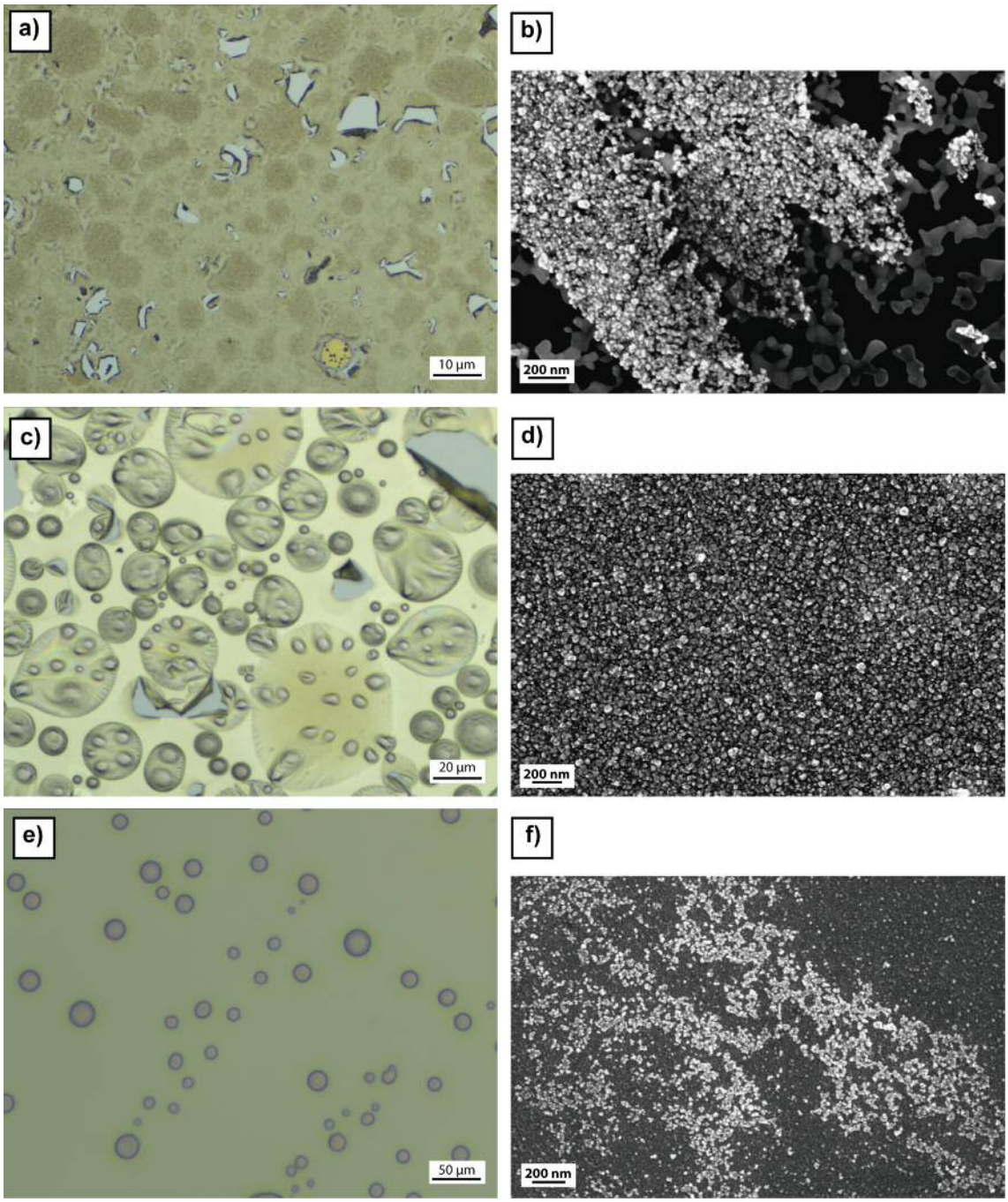

Figure 6.16: Optical microscope and SEM images of diamond growth onto Ir coated Si substrates. a) and b) Images of the sample seeded with the mono-dispersed colloid containing air-treated diamond seeds, after 10 min growth. c) and d) Images of the sample seeded with the mono-dispersed colloid containing hydrogen-treated diamond seeds after 10 min of growth. e) and f) Images of the sample seeded as c) and d) after the diamond CVD growth process at low temperature.

6.6 Conclusion

In this chapter, the design of a simple quartz tube CVD reactor has been proposed. The availability of files and details of the design, enable reactor replication at reduced cost as an alternative to commercial diamond plasma deposition systems. This reduced cost however, does not compromised the quality of the diamond films grown, as shown in the SEM images and Raman spectra. After establishing the most appropriate conditions for CVD growth in this reactor, silicon doping was controlled with the incorporation of silane, creating SiV centres in silicon substrates. Nevertheless, the use of non-silicon substrates is mandatory for the further creation of single SiV centres, as the solely silicon incorporation from the etching of the Si substrate produce SiV ensembles.

Chapter 7

Conclusions

The work performed in this thesis has been focused mainly on the study of diamond nanoparticles, customizing and controlling their surface charges and the defects intentionally introduced within the diamond lattice, creating colour centres.

Chapter 4 details different annealing procedures with the aim of manipulating these surface charges on both commercial detonation diamond particles (5 nm) and larger ones (50 nm). Controlling the surfaces charges has been crucial to avoid particle aggregation in a colloid (strongly observed for detonation diamond particles), [314] obtaining particles with high zeta potential (positive or negative) in a wide range of pH, in order to get good adhesion to substrates due to electrostatic interaction between them. This strong electrostatic interaction is crucial for subsequent diamond growth processes, as it ensures high nucleation densities and hence the coalescence of diamond films. For detonation diamond particles, low temperature hydrogenation (500°C), was proved to be a good method to prevent particles agglomeration obtaining particles with high positive zeta potential values once in solution (from low to high pH, 3 to 9). [96] However the mechanism behind the hydrogenation process was not understood until now. FTIR measurements as well as mass/charge spectrum performed on different samples, confirmed that the low hydrogenation process is possible due to the presence of sp^2 in the detonation diamond particles. The sp^2 is desorbed from the diamond particle surface as C_2 or C_3 and reacts with the molecular hydrogen, producing atomic hydrogen, which then interacts with carbon dangling bonds on the particles' surface producing the C-H bonds. [134] The same low temperature hydrogen annealing process was also performed on the 50 nm particles, but hydrogenation was not observed. However, after the intentionally introduction of sp^2 after subjecting the diamond particles to vacuum annealing processes, C-H features were

observed in FTIR, corroborating the surface hydrogenation. Furthermore, surface zeta potential and back titration measurements conducted on colloids containing different treated diamond nanoparticles have clarified the origin of the positive zeta potential, which has been controversial within the diamond community. This origin can only be explained due to the presence of some sp^2 on the particles surface and the absence (or low concentration) of oxygen groups. [147] The results obtained within this chapter have been published in. [134, 147]

Chapter 5 then seeks to improve and control the production of high quality customized diamond particles. With an increasingly demand of diamond nanoparticles for many different applications, it is fundamental to be able to produce them in consonance with their final application. Although there are many commercially available diamond nanoparticles, they usually present more than tolerable amounts of sp^2 or contaminants requiring further cleaning processes prior use. The first part of chapter 5 details the production of high quality diamond nanoparticles from commercial bulk diamond, following milling strategies. Commercial SC diamond samples are used as a starting material and milled down with two grinding bowls of different materials. Whilst milling with tempered steel produces small-rounded particles (confirmed by TEM), it however produces particles with iron-oxide in the diamond lattice, difficult to remove even with strong acid cleaning methods. The metal presence within the diamond nanoparticles is detrimental for magnetic-related applications. [233] On the other hand, this metal presence can be avoided using a silicon nitride grinding bowl, but produces more faceted diamond particles. Furthermore, XPS measurements confirmed the presence of non-sp^3 carbon and silicon nitride, negatively influencing their optical properties and hence limiting their use as single photon sources. A paper showing these results is in preparation. The second part of this chapter is then focused on the production of diamond nanoparticles containing colour centres, specially the SiV centre. Although this colour centre has better and more promising properties than the NV centre, [210] it is still not the most used, probably because its production methods, that requires the surface-damaging ion implantation technique for fully control over the amount of Si incorporated. [219] It is also advantageous to be able to produce particles ready to spin cast onto different optical cavities, necessary to improve the spectral overlap between emitters that complex quantum systems require. [229] CVD growth of diamond nanoparticles with SiV centres was successfully performed onto different substrates, incorporating Si during the CVD process either from the etching of the Si substrate or incorporating a solid Si source inside the reactor chamber. However, this method does not allow to easily control the nanodiamonds size or to remove/pick the particles from the

surface to be placed in a cavity. Thus, a better and more controlled method for particles production was performed, first growing a diamond film and then milling it down with the materials previously described. For diamond film growth, first a sacrificial Si substrate for a diamond film growth with subsequent substrate etching was used. In the second approach, the diamond film was directly grown onto a Molybdenum holder, in order to delaminate the film from the Mo holder easily and to avoid the substrate etching process. After milling, cleaning and centrifuge processes, colloids containing diamond particles with SiV centres were obtained, with stable and bright SiV emitters observed in all the particles analysed. However, the impossibility of controlling the amount of Si incorporated, produced, in general, SiV ensembles instead of single emitters.

Si doping control has been achieved by introducing Si in a gas phase, using silane. A reactor was built with this purpose and its design is fully detailed in chapter 6. The reactor consists of a quartz tube placed in a 2.45 GHz waveguide, in which conditions for CVD diamond growth are met. As most of the reactor components are based on commercially available KF fittings, these components are easy to replace and modify. This easily interchangeability or replacement of even the quartz tube allows the study and incorporation of different dopants, ensuring no cross-contamination, and opening new possibilities towards the discovery of new colour centres with. Furthermore, the reactor also incorporates a novel and simple mechanism to load and unload samples. With the CAD files freely available to download, [281] reactor replication is possible, considerably reducing the complexity and cost of other commercially available reactors, without compromising the quality of the samples grown. A paper detailing this reactor design and diamond film growth has just been submitted. [315]After the optimization of growing parameters, different diamond films with different silane content in the gas phase were studied. Changes in surface morphology, surface quality and SiV PL emission were observed, leading to the deterioration of the diamond films for high Si doping levels. It was also observed that the Si incorporation solely from a Si substrate is enough and even too much to ensure the presence of SiV single emitters instead of ensembles and hence the use of non-silicon substrates is mandatory.

It is hoped that the work presented in this thesis can contribute to a better understanding of some of the diamond properties as well as laying the foundations of particle creation improving their emission properties, and hence approaching the production of a practical single photon source, so important in the quantum information processing field. There is still much work to do but results on both chapter 5 and chapter 6 indicate that the pro-

duction of customized particles containing (the majority of them) single photon emitters is close and can be performed within the near future.

Bibliography

[1] Y.Y. Hui, C.-L. Cheng, and H.C. Chang. Nanodiamonds for optical bioimaging. *Journal of Physics D: Applied Physics*, 43(37):374021, 2010.

[2] V.N. Mochalin, O.A. Shenderova, D. Ho, and Y. Gogotsi. The properties and applications of nanodiamonds. *Nature nanotechnology*, 7(1):11–23, 2012.

[3] S. Prawer and I. Aharonovich. *Quantum information processing with diamond*. Woodhead Publishing. Elsevier, 2014.

[4] R.P. Feynman. Simulating physics with computers. *International Journal of Theoretical Physics*, 21(6-7):467–488, 1982.

[5] D.P. DiVincenzo and IBM. The Physical Implementation of Quantum Computation, 2000.

[6] M.F. Gonzalez-zalba. Solid-state qubits. *arXiv:1801.06722*, pages 1–5, 2018.

[7] E. Togan, Y. Chu, A. S. Trifonov, L. Jiang, J. Maze, L. Childress, M. V G Dutt, A. S. Sørensen, P. R. Hemmer, A. S. Zibrov, and M. D. Lukin. Quantum entanglement between an optical photon and a solid-state spin qubit. *Nature*, 466(7307):730–734, 2010.

[8] S. Prawer and A.D. Greentree. Diamond for quantum computing. *Science*, 320(5883):1601–1602, 2008.

[9] T. Schröder, M.E. Trusheim, M. Walsh, L. Li, J. Zheng, M. Schukraft, A. Sipahigil, R.E. Evans, D.D. Sukachev, C.T. Nguyen, J.L. Pacheco, R.M. Camacho, E.S. Bielejec, M.D. Lukin, and D. Englund. Scalable focused ion beam creation of nearly lifetime-limited single quantum emitters in diamond nanostructures. *Nature Communications*, 8(May):1–7, 2017.

[10] European Commission. Quantum Manifesto, 2016.

[11] M.A. Quiroz and E.R. Bandala. Types of Conducting Diamond Materials and their Properties. In *Synthetic Diamond Films: Preparation, Electrochemistry, Characterization, and Applications*, chapter 3, pages 57–75. 2011.

[12] H.O. Pierson. The Element Carbon. In *Handbook of Carbon, Graphite, Diamonds and Fullerenes*, pages 11–42. 1993.

[13] J.C. Angus, A. Argoitia, R. Gat, Z. Li, M. Sunkara, L. Wang, and Y. Wang. Chemical Vapour Deposition of Diamond. *Philosophical Transactions of the Royal Society of London A*, 342:195–208, 1993.

[14] P.W. May. Diamond thin films: a 21st-century material. *Philosophical Transactions of the Royal Society of London Series a-Mathematical Physical and Engineering Sciences*, 358(1766):473–495, 2000.

[15] F. Silva, K. Hassouni, X. Bonnin, and A. Gicquel. Microwave engineering of plasma-assisted CVD reactors for diamond deposition. *Journal of physics. Condensed matter : an Institute of Physics journal*, 21(36):364202, 2009.

[16] M.N.R. Ashfold, P.W. May, C.A. Rego, and N.M. Everitt. Thin film diamond by chemical vapour deposition methods. *Chemical Society Reviews*, 23(1):21, 1994.

[17] P.K. Bachmann. Diamond Deposition. *Advanced Materials*, 2(4):195–199, 1990.

[18] M.M. Besen, E. Sevillano, and D.K. Smith. Microwave Plasma Reactor. U.S. Patent No. 5,501,740, 1996.

[19] E. Sevillano and B. Williams. Reactor Development for Microwave Plasma Deposition of Diamond. *Diamond Films and Technology*, 8(2):73–91, 1998.

[20] A.R. Krauss, O. Auciello, D.M. Gruen, A. Jayatissa, and A. Sumant. Ultrananocrystalline diamond thin films for MEMS and moving mechanical assembly devices. *Diamond and Related Materials*, 10:1952–1961, 2001.

[21] B. Lux and R. Haubner. CVD Diamond for Cutting Tools. In Bernhard Dischler and Christoph Wild, editors, *Low-pressure synthetic diamond. Manufacturing and applications*, chapter 12, pages 224–242. Springer series in materials processing, 1998.

[22] O.A. Williams, A Kriele, J Hees, M Wolfer, and C E Nebel. High Young ' s modulus in ultra thin nanocrystalline diamond. *Chemical Physics Letters*, 495(1-3):84–89, 2010.

[23] M. Burek, D. Ramos, P. Patel, I.W. Frank, and M. Lončar. Nanomechanical resonant structures in single-crystal diamond. *Applied Physics Letters*, 103(13):6–9, 2013.

[24] H. D. Espinosa, B. C. Prorok, B. Peng, K. H. Kim, N. Moldovan, O. Auciello, J. A. Carlisle, D. M. Gruen, and D. C. Mancini. Mechanical properties of ultrananocrystalline diamond thin films relevant to MEMS/NEMS devices. *Experimental Mechanics*, 43(3):256–268, 2003.

[25] G. Davies. Basic Properties of Diamond : Phonon Spectra , Thermal Properties , Band Structure. In Ricardo S. Sussmann, editor, *CVD Diamond for Electronics Devices and Sensors*, chapter 1, pages 1–28. John Wiley & Sons, Ltd, 2009.

[26] S.V. Kidalov and F.M. Shakhov. Thermal conductivity of diamond composites. *Materials*, 2(4):2467–2495, 2009.

[27] A.M. Schrand, S.A.C. Hens, and O.A. Shenderova. Nanodiamond Particles: Properties and Perspectives for Bioapplications. *Critical Reviews in Solid State and Materials Sciences*, 34(1-2):18–74, 2009.

[28] C. Wild. CVD Diamond for Optical Windows. In *Low-pressure synthetic diamond. Manufacturing and applications*, chapter 10, pages 189–206. Springer series in materials processing, 1998.

[29] A Gicquel, K Hassouni, F Silva, and J Achard. CVD diamond films: From growth to applications. *Current Appl. Phys.*, 1:479–496, 2001.

[30] C.J.H. Wort and R.S. Balmer. Diamond as an electronic material. *Materials Today*, 11(1):22–28, 2008.

[31] E.A. Ekimov, V .A. Sidorov, E.D. Bauer, N.N. Mel'nik, N.J. Curro, J.D. Thompson, and S.M. Stishov. Superconductivity in diamond. *Nature*, 428(6982):542–5, 2004.

[32] T. Mulvey. Origins and Historical Development of the Electron Microscope. *Brittish Journal of Applied Physics*, 13:197, 1962.

[33] P.J. Goodhew, J. Humphreys, and R. Beanland. The scanning electron microscope. In *Electron Microscopy and Analysis*, chapter 5, pages 122–167. Taylor & Francis, third edition, 2001.

[34] R.C. Brundle. Scanning Electron Microscopy. In *Encyclopedia of Materials Characterization*, chapter 2, pages 70–85. Butxetworch-Heinemann, a division of Reed Publishing (USA) Inc, 1992.

[35] JEOL. Scanning Electron Microscope A To Z. *Serving Advanced Technology*, page 32, 2006.

[36] JEOL. Low Vacuum SEM. Technical report.

[37] JEOL application note. High resolution low vacuum SEM. Technical report.

[38] A. Bogner, P.H. Jouneau, G. Thollet, D. Basset, and C. Gauthier. A history of scanning electron microscopy developments: Towards "wet-STEM" imaging. *Micron*, 38(4):390–401, 2007.

[39] R.A. Ristau. Transmission Electron Microscope Primary Training.

[40] R. Howland and L. Benatar. *A Practical Guide To Scanning Probe Microscopy*. 1996.

[41] Y. Seo and W. Jhe. Atomic force microscopy and spectroscopy. *Reports on Progress in Physics*, 71(1):016101, 2008.

[42] R. García and R. Pérez. Dynamic atomic force microscopy methods. *Surface Science Reports*, 47(6-8):197–301, 2002.

[43] J.B. Bindell. Scanning Tunneling Microscopy and Scanning Force Microscopy. In *Encyclopedia of Materials Characterization*, chapter 2, pages 85–99. Butxetworch-Heinemann, a division of Reed Publishing (USA) Inc, 1992.

[44] F. Gołek, P. Mazur, Z. Ryszka, and S. Zuber. AFM image artifacts. *Applied Surface Science*, 304:11–19, 2014.

[45] B.J. Berne and R. Pecora. *Dynamic Light Scattering. With Applications to Chemistry, Biology and Physics*. Dover Publications, Inc., 2000.

[46] Malvern Instruments. Dynamic Light Scattering : An Introduction in 30 Minutes. Technical report, Malvern Instruments, 2014.

[47] B.J. Frisken. Revisiting the Method of Cumulants for the Analysis of Dynamic Light-Scattering Data. *Applied Optics*, 40(24):4087, 2001.

[48] A. Scotti, W. Liu, J.S. Hyatt, E.S. Herman, H.S. Choi, J. W. Kim, L.A. Lyon, U. Gasser, and A. Fernandez-Nieves. The CONTIN algorithm and its application to determine the size distribution of microgel suspensions. *The Journal of chemical physics*, 142(23):234905, 2015.

[49] R.D. Boyd, S.K. Pichaimuthu, and A. Cuenat. New approach to inter-technique comparisons for nanoparticle size measurements; using atomic force microscopy, nanoparticle tracking analysis and dynamic light scattering. *Colloids and Surfaces A: Physicochemical and Engineering Aspects*, 387(1-3):35–42, 2011.

[50] V. Filipe, A. Hawe, and W. Jiskoot. Critical evaluation of nanoparticle tracking analysis (NTA) by NanoSight for the measurement of nanoparticles and protein aggregates. *Pharmaceutical Research*, 27(5):796–810, 2010.

[51] H. Saveyn, B. De Baets, O. Thas, P. Hole, J. Smith, and P. Van der Meeren. Accurate particle size distribution determination by nanoparticle tracking analysis based on 2-D Brownian dynamics simulation. *Journal of Colloid and Interface Science*, 352(2):593–600, 2010.

[52] M.M. Mariani and V. Deckert. Part III Interfaces: Raman Spectroscopy Principles , Benefits , and Applications. In Rolf Schäfer and Peter C. Schmidt, editors, *Methods in Physical Chemistry*, chapter 13, pages 419–444. Wiley-VCH Verlag GmbH & Co. KGaA, 2012.

[53] J.X. Cheng and X.S. Xie. Coherent Anti-Stokes Raman Scattering Microscopy: Instrumentation, Theory, and Applications. *Journal of physics Chemical B*, 108(1):827–840, 2004.

[54] S. A. Solin and A. K. Ramdas. Raman spectrum of diamond. *Physical Review B*, 1(4):1687–1698, 1970.

[55] H.W. Siesler. Introduction. In *Near-Infrared Spectroscopy: Principles, Instruments, Applications*, chapter 1, pages 1–10. Wiley-Vch Verlag GmbH, 2002.

[56] B. Stuart. Introduction. In *Infrared Spectroscopy: Fundamentals and Applications*, chapter 1, pages 1–13. John Wiley & Sons, Ltd, 2004.

[57] P.R. Griffiths and J.A. de Haseth. Theoretical Background. In *Fourier Transform Infrared Spectroscopy*, chapter 2, pages 19–55. John Wiley Sons, Inc., second edition, 2006.

[58] P.R. Griffiths and J. A. de Haseth. Other Components of Ft-Ir Spectrometers. In *Fourier Transform Infrared Spectroscopy*, chapter 6, pages 143–160. John Wiley & Sons, Inc., second edition, 2007.

[59] R. Lobinski and Z. Marczenko. Recent Advances in Ultraviolet-Visible Spectrophotometry. *Critical Reviews in Analytical Chemistry*, 23(1):55–111, 1992.

[60] O.A. Williams, M. Nesladek, M. Daenen, S. Michaelson, and A. Hoffman. Growth , electronic properties and applications of nanodiamond. *Diamond and Related Materials*, 17:1080–1088, 2008.

[61] K. Meykens and L.M. Stals. Origin of characteristic subgap optical absorption in CVD diamond films. *Physical Review B*, 54(8):5552–5561, 1996.

[62] J.M. Smith. Characterization of single defects in diamond in the development of quantum devices. In *Quantum Information Processing with Diamond*, chapter 4, pages 68–98. Woodhead Publishing, Elsevier, 2014.

[63] E.K. Neu. *Silicon vacancy color centers in chemical vapor deposition diamond : new insights into promising solid state single photon sources*. PhD thesis, 2012.

[64] J Walker. Optical absorption and luminescence in diamond. *Reports on Progress in Physics*, 42(10):1605–1659, 1979.

[65] J.D. Andrade. X-ray Photoelectron Spectroscopy (XPS). In *Surface and Interfacial Aspects of Biomedical Polymers*, pages 105–195. Tsinghua University Press Limited, 1985.

[66] D.J. Morgan. X-Ray Photoelectron Spectroscopy (XPS): An Introduction. pages 1–7.

[67] R.C. Brundle. Dynamic Secondary Ion Mass Spectroscopy. In *Encyclopedia of Materials Characterization*, chapter 10, pages 532–579. Butxetworch-Heinemann, a division of Reed Publishing (USA) Inc, 1992.

[68] L. Tang, C. Tsai, W. W. Gerberich, L. Kruckeberg, and D. R. Kania. Biocompatibility of chemical-vapour-deposited diamond. *Biomaterials*, 16(6):483–488, 1995.

[69] L.A. Thomson, F.C. Law, N. Rushton, and J. Franks. Biocompatibility of diamond-like carbon coating. *Biomaterials*, 12(1):37–40, 1991.

[70] A.M. Schrand, H. Huang, C. Carlson, J.J. Schlager, E. Ōsawa, S.M. Hussain, and Li. Dai. Are Diamond Nanoparticles Cytotoxic? *The Journal of Physical Chemistry B*, 111(1):2–7, 2006.

[71] O.A. Williams, O. Douhéret, M. Daenen, K. Haenen, E. Osawa, and M. Takahashi. Enhanced diamond nucleation on monodispersed nanocrystalline diamond. *Chemical Physics Letters*, 445(4-6):255–258, 2007.

[72] T. Bautze, S. Mandal, O.A. Williams, P. Rodière, T. Meunier, and C. Bäuerle. Superconducting nano-mechanical diamond resonators. *Carbon*, 72:100–105, 2014.

[73] M. Imboden, O.A. Williams, and P. Mohanty. Nonlinear dissipation in diamond nanoelectromechanical resonators. *Applied Physics Letters*, 102(10), 2013.

[74] F. Jelezko and J. Wrachtrup. Single defect centres in diamond: A review. *Physica Status Solidi (A) Applications and Materials Science*, 203(13):3207–3225, 2006.

[75] B. Lounis and M. Orrit. Single-photon sources. *Reports on Progress in Physics*, 68:1129–1179, 2005.

[76] G. Balasubramanian, I.Y. Chan, R. Kolesov, M. Al-Hmoud, J. Tisler, C. Shin, C. Kim, A. Wojcik, P.R. Hemmer, A. Krueger, T. Hanke, A. Leitenstorfer, R. Bratschitsch, F. Jelezko, and J. Wrachtrup. Nanoscale imaging magnetometry with diamond spins under ambient conditions. *Nature*, 455(7213):648–51, 2008.

[77] F. P. Bundy. Pressure-temperature phase diagram of elemental carbon. *Physica A: Statistical Mechanics and its Applications*, 156(1):169–178, 1989.

[78] G. Galli. Structure, Stability and Electronic Properties of Nanodiamonds. In *Computer-Based Modeling of Novel Carbon Systems and Their Properties*, volume 3, chapter 2, pages 37–57. Springer Science, 2010.

[79] S. Landa and V. Machácek. Sur l' adamantane, nouvel hydrocarbure extrait du naphte. pages 1–6, 1932.

[80] L.D. Rollmann, L.A. Green, R. A. Bradway, and H.K.C. Timken. Adamantanes from petroleum with zeolites. *Catalysis Today*, 31(1-2):163–169, 1996.

[81] R.S. Lewis, T. Ming, J.F. Wacker, E. Anders, and E. Steel. Interstellar diamonds in meteorites. *Nature*, 326(6109):160–162, 1987.

[82] P.R. Heck. The Enigmatic Origin of Meteoritic Nanodiamonds - An Approach with Atom-Probe Tomography. *Microscopy and Microanalysis*, 23(S1):2276–2277, 2017.

[83] J.-P. Boudou, P.A. Curmi, F. Jelezko, J. Wrachtrup, P. Aubert, M. Sennour, G. Balasubramanian, R. Reuter, A. Thorel, and E. Gaffet. High yield fabrication of fluorescent nanodiamonds. *Nanotechnology*, 20(23):235602, 2009.

[84] V.V. Danilenko. On the History of the Discovery of Nanodiamond Synthesis. *Physics of the Solid State*, 46(4):595–599, 2004.

[85] A. Krueger. The structure and reactivity of nanoscale diamond. *Journal of Materials Chemistry*, 18(13):1485, 2008.

[86] V. Yu. Dolmatov. Detonation synthesis ultradispersed diamonds: properties and applications. *Russ. Chem. Rev.*, 70(7):607–626, 2001.

[87] V.V. Danilenko. *Nanocarbon Phase Diagram and Conditions for Detonation Nanodiamond Formation*, pages 181–198. Springer Netherlands, Dordrecht, 2005.

[88] N.R. Greiner, D.S. Phillips, J.D. Johnson, and F. Volk. Diamonds in detonation soot. *Nature*, 333(6172):440–442, 1988.

[89] O.A. Shenderova, A. Koscheev, N. Zaripov, I. Petrov, Y. Skryabin, P. Detkov, S. Turner, and G. Van Tendeloo. Surface chemistry and properties of ozone-purified detonation nanodiamonds. *Journal of Physical Chemistry C*, 115(20):9827–9837, 2011.

[90] O.A. Shenderova, I Petrov, J Walsh, and V Grichko. Modification of detonation nanodiamonds by heat treatment in air. *Diamond and Related Materials*, 15:1799–1803, 2006.

[91] M. Ozawa, M. Inaguma, M. Takahashi, F. Kataoka, A. Krueger, and E. Osawa. Preparation and behavior of brownish, clear nanodiamond colloids. *Advanced Materials*, 19(9):1201–1206, 2007.

[92] A. Krueger, F. Kataoka, M. Ozawa, T. Fujino, Y. Suzuki, A. E. Aleksenskii, A. Ya Vul', and E. Osawa. Unusually tight aggregation in detonation nanodiamond: Identification and disintegration. *Carbon*, 43(8):1722–1730, 2005.

[93] E. Osawa. Recent progress and perspectives in single-digit nanodiamond. *Diamond and Related Materials*, 16(12):2018–2022, 2007.

[94] A. E. Aleksenskiy, E. D. Eydelman, and A. Ya. Vul'. Deagglomeration of Detonation Nanodiamond. *Nanoscience and Nanotechnology Letters*, 3:68–74, 2011.

[95] A. Krueger, J. Stegk, L. Lu, and G. Jarre. Biotinylated Nanodiamond : Simple and Efficient Functionalisation of Detonation Diamond Supporting information. *Langmuir*, 24:4200–4204, 2008.

[96] O.A. Williams, J. Hees, C. Dieker, W. Jäger, L. Kirste, and C.E. Nebel. Size-dependent reactivity of diamond nanoparticles. *ACS Nano*, 4(8):4824–4830, 2010.

[97] F. P. Bundy, H.T. Hall, H.M. Strong, and R.H. Wentorf. Man-Made Diamonds. *Nature*, 175:642–643, 1955.

[98] H. Sumiya and S. Satoh. High-pressure synthesis of high-purity diamond crystal. *Diamond and Related Materials*, 5(11):1359–1365, 1996.

[99] A. YA. Vul', A. T. Dideikin, A. E. Aleksenskii, and M. V. Badaikova. Detonation Nanodiamonds: Synthesis, Properties and Applications. In *Nanodiamond*, chapter 2. 2014.

[100] A. Krueger. Current issues and challenges in surface chemistry of nanodiamonds. In *Nanodiamonds*, chapter 8, pages 183–242. Elsevier Inc., 6 edition, 2017.

[101] A. Krueger. The Chemistry of Nanodiamond. In *Nanodiamond*, chapter 3, pages 49–82. Royal Society of Chemistry, 2014.

[102] S. Osswald, G. Yushin, V. Mochalin, S.O. Kucheyev, and Y. Gogotsi. Control of sp2/sp3 Carbon Ratio and Surface Chemistry of Nanodiamond Powders by Selective Oxidation in Air. *Journal of the American Chemical Society*, 128(35):11635–11642, sep 2006.

[103] V. Pichot, M. Comet, E. Fousson, C. Baras, A. Senger, F. Le Normand, and D. Spitzer. An efficient purification method for detonation nanodiamonds. *Diamond and Related Materials*, 17(1):13–22, 2008.

[104] T. Gaebel, C. Bradac, J. Chen, J. M. Say, L. Brown, P. Hemmer, and J. R. Rabeau. Size-reduction of nanodiamonds via air oxidation. *Diamond and Related Materials*, 21:28–32, 2012.

[105] B.R. Smith, D. Gruber, and T. Plakhotnik. The effects of surface oxidation on luminescence of nano diamonds. *Diamond and Related Materials*, 19(4):314–318, 2010.

[106] A. Krueger and D. Lang. Functionality is key: Recent progress in the surface modification of nanodiamond. *Advanced Functional Materials*, 22(5):890–906, 2012.

[107] W.S. Yeap, S. Chen, and K.P. Loh. Detonation nanodiamond: An organic platform for the suzuki coupling of organic molecules. *Langmuir*, 25(1):185–191, 2009.

[108] M. Yeganeh, P. R. Coxon, A. C. Brieva, V. R. Dhanak, L. Šiller, and Yu V. Butenko. Atomic hydrogen treatment of nanodiamond powder studied with photoemission spectroscopy. *Physical Review B - Condensed Matter and Materials Physics*, 75(15):1–8, 2007.

[109] H. A. Girard, J.C. Arnault, S. Perruchas, S. Saada, T. Gacoin, J. P. Boilot, and P. Bergonzo. Hydrogenation of nanodiamonds using MPCVD: A new route toward organic functionalization. *Diamond and Related Materials*, 19(7-9):1117–1123, 2010.

[110] S. Ida, T. Tsubota, O. Hirabayashi, M. Nagata, Y. Matsumoto, and A. Fujishima. Chemical reaction of hydrogenated diamond surface with peroxide radical initiators. *Diamond and Related Materials*, 12(3-7):601–605, 2003.

[111] J.A. Viecelli, S. Bastea, J.N. Glosli, and F.H. Ree. Phase transformations of nanometer size carbon particles in shocked hydrocarbons and explosives. *Journal of Chemical Physics*, 115(6):2730–2736, 2001.

[112] V.L. Kuznetsov and Y.V. Butenko. Diamond phase transitions at nanoscale. In *Ultrananocrystalline Diamond*, chapter 7, pages 181–244. Elsevier Inc., second edition, 2012.

[113] S. Tomita, A. Burian, J.C. Dore, D. LeBolloch, M. Fujii, and S. Hayashi. Diamond nanoparticles to carbon onions transformation: X-ray diffraction studies. *Carbon*, 40(9):1469–1474, 2002.

[114] T. Petit, J.C. Arnault, H.A. Girard, M. Sennour, and P. Bergonzo. Early stages of surface graphitization on nanodiamond probed by x-ray photoelectron spectroscopy. *Physical Review B - Condensed Matter and Materials Physics*, 84(23):1–5, 2011.

[115] J. Sarquis. Colloidal systems. *Journal of Chemical Education*, 57(8):602, 1980.

[116] D.H Everett. What are colloids? In *Basic principles of colloid science*, chapter 1, pages 1–13. Royal Society of Chemistry, 1988.

[117] D.H Everett. Why are colloidal dispersions stable? I Basic Principles. In *Basic principles of colloid science*, chapter 2, pages 16–28. Royal Society of Chemistry, 1988.

[118] B. Derjaguin and L. Landau. Theory of the stability of strongly charged lyophobic sols and of the adhesion of strongly charged particles in solutions of electrolytes. *Progress in Surface Science*, 43(1):30–59, 1993.

[119] E.J.W. Verwey and J.Th.G. Overbeek. Theory of the stability of lyophobic colloids. *Journal of Colloid Science*, 10(2):224–225, 1955.

[120] Y. Liang, N. Hilal, P. Langston, and V. Starov. Interaction forces between colloidal particles in liquid: Theory and experiment. *Advances in Colloid and Interface Science*, 134-135:151–166, 2007.

[121] A.E. Larsen and D.G. Grier. Like-charge attractions in metastable colloidal crystallites. *Nature*, 385(6613):230–233, jan 1997.

[122] D. Grasso, K. Subramaniam, M. Butkus, K. Strevett, and J. Bergendahl. A review of non-DLVO interactions in environmental colloidal systems. *Reviews in Environmental Science and Biotechnology*, 1(1):17–38, 2002.

[123] D.H Everett. Why are colloidal dispersions stable? II Interparticle forces. In *Basic principles of colloid science*, chapter 3, pages 30–52. Royal Society of Chemistry, 1988.

[124] M. Namazian, S. Halvani, and M.R. Noorbala. Density functional theory response to the calculations of pKa values of some carboxylic acids in aqueous solution. *Journal of Molecular Structure: Theochem*, 711(1-3):13–18, 2004.

[125] J. Reijenga, A. van Hoof, A. van Loon, and B. Teunissen. Development of methods for the determination of pKa values. *Analytical Chemistry Insights*, 8(1):53–71, 2013.

[126] M. Namazian and S. Halvani. Calculations of pKa values of carboxylic acids in aqueous solution using density functional theory. *The Journal of Chemical Thermodynamics*, 38(12):1495–1502, 2006.

[127] L.L. Zhang and X.S. Zhao. Carbon-based materials as supercapacitor electrodes. *Chemical Society Reviews*, 38(9):2520, 2009.

[128] N. Kallay, T. Preocanin, D. Kovacevic, J. Lutzenkirchen, and E. Chibowski. Electrostatic Potentials at Solid/Liquid Interfaces. *Croatica Chemica Acta*, 83(3):357–370, 2010.

[129] A.V. Delgado, F. González-Caballero, R.J. Hunter, L.K. Koopal, and J. Lyklema. Measurement and interpretation of electrokinetic phenomena. *Journal of Colloid and Interface Science*, 309(2):194–224, 2007.

[130] R.W. O'Brien and L.R. White. Electrophoretic mobility of a spherical colloidal particle. *Journal of the Chemical Society, Faraday Transactions 2*, 74:1607, 1978.

[131] Malvern Instruments. Measuring Zeta Potential – Laser Doppler Electrophoresis. *Malvern Guides*, pages 1–2, 2015.

[132] C. Su, K.J. Song, Y. Wang, H.-L. Lu, T.J. Chuang, and J.-C. Lin. Hydrogen chemisorption and thermal desorption on the diamond C(111) surface. *The Journal of Chemical Physics*, 107(18):7543–7558, 1997.

[133] B.N. Jariwala, C.V. Ciobanu, and S. Agarwal. Atomic hydrogen interactions with amorphous carbon thin films. *Journal of Applied Physics*, 106(7), 2009.

[134] A.-I. Ahmed, S. Mandal, L. Ginés, O.A. Williams, and C.-L. Cheng. Low temperature catalytic reactivity of nanodiamond in molecular hydrogen. *Carbon*, 110:438–442, 2016.

[135] C.-L. Cheng, H.-C. Chang, J.-C. Lin, K.-J. Song, and J.-K. Wang. Direct Observation of Hydrogen Etching Anisotropy on Diamond Single Crystal Surfaces. *Physical Review Letters*, 78(19):3713–3716, 1997.

[136] C.-L. Cheng, C. F. Chen, W. C. Shaio, D. S. Tsai, and K. H. Chen. The CH stretching features on diamonds of different origins. *Diamond and Related Materials*, 14(9):1455–1462, 2005.

[137] C.-L. Cheng, J.C. Lin, H.C. Chang, and J.K. Wang. Characterization of CH stretches on diamond C(111) single- and nanocrystal surfaces by infrared absorption spectroscopy. *J.Chem.Phys*, 105(19):8888–8977, 1897.

[138] S. Tong Lee and G. Apai. Surface phonons and CH vibrational modes of diamond (100) and (111) surfaces. *Physical Review B*, 48(4):2684–2693, 1993.

[139] E. Neyts, M. Tacq, and A. Bogaerts. Reaction mechanisms of low-kinetic energy hydrocarbon radicals on typical hydrogenated amorphous carbon (a-C : H) sites : A molecular dynamics study. 15:1663–1676, 2006.

[140] D. Mahl, J. Diendorf, W. Meyer-Zaika, and M. Epple. Possibilities and limitations of different analytical methods for the size determination of a bimodal dispersion of metallic nanoparticles. *Colloids and Surfaces A: Physicochemical and Engineering Aspects*, 377(1-3):386–392, 2011.

[141] G. Bryant and J.C. Thomas. Improved Particle Size Distribution Measurements Using Multiangle Dynamic Light Scattering. *Langmuir*, 11(7):2480–2485, 1995.

[142] C.M. Hoo, N. Starostin, P. West, and M.L. Mecartney. A comparison of atomic force microscopy (AFM) and dynamic light scattering (DLS) methods to characterize nanoparticle size distributions. *Journal of Nanoparticle Research*, 10:89–96, 2008.

[143] S. Turner, O.I. Lebedev, O.A. Shenderova, I.I. Vlasov, J. Verbeeck, and G. Van Tendeloo. Determination of size, morphology, and nitrogen impurity location in treated detonation nanodiamond by transmission electron microscopy. *Advanced Functional Materials*, 19(13):2116–2124, 2009.

[144] C. Finder, M. Wohlgemuth, and C. Mayer. Analysis of particle size distribution by particle tracking. *Particle and Particle Systems Characterization*, 21(5):372–378, 2004.

[145] O.A. Williams. Nanocrystalline diamond. *Diamond and Related Materials*, 20(5-6):621–640, 2011.

[146] X. Jiang, K. Schiffmann, and C.-P. Klages. Nucleation and initial growth phase of diamond thin films on (100) silicon. *Physical Review B*, 50(12):8402–8410, 1994.

[147] L. Ginés, S. Mandal, A.-I. Ahmed, C.-L. Cheng, Maabur Sow, and O.A. Williams. Positive Zeta Potential of Nanodiamonds. *Nanoscale*, 9(34):12549–12555, 2017.

[148] M. Ozawa, H. Goto, Mi. Kusunoki, and E. Osawa. Continuously growing spiral carbon nanoparticles as the intermediates in the formation of fullerenes and nanoonions. *Journal of Physical Chemistry B*, 106(29):7135–7138, 2002.

[149] K. Iakoubovskii, K. Mitsuishi, and K. Furuya. High-resolution electron microscopy of detonation nanodiamond. *Nanotechnology*, 19(15):155705, 2008.

[150] O.A. Williams and R.B. Jackman. Surface conductivity on hydrogen terminated diamond. *Semiconductor Science and Technology*, 18(3):S34–S40, 2003.

[151] I.P. Chang, K.C. Hwang, J.A.A. Ho, C.C. Lin, R.J.R. Hwu, and J.C. Horng. Facile surface functionalization of nanodiamonds. *Langmuir*, 26(5):3685–3689, 2010.

[152] Z. Qiao, J. Li, N. Zhao, C. Shi, and P. Nash. Graphitization and microstructure transformation of nanodiamond to onion-like carbon. *Scripta Materialia*, 54(2):225–229, 2006.

[153] J. Qian, C. Pantea, J. Huang, T. W. Zerda, and Y. Zhao. Graphitization of diamond powders of different sizes at high pressure-high temperature. *Carbon*, 42(12-13):2691–2697, 2004.

[154] A. C. Ferrari and J. Robertson. Interpretation of Raman spectra of disordered and amorphous carbon. *Physical Review B*, 61(20):14095–14107, 2000.

[155] A. C. Ferrari and J. Robertson. Resonant Raman spectroscopy of disordered, amorphous, and diamondlike carbon. *Physical Review B*, 64(7):075414, 2001.

[156] J. Hees, A. Kriele, and O.A. Williams. Electrostatic self-assembly of diamond nanoparticles. *Chemical Physics Letters*, 509(1-3):12–15, 2011.

[157] J. Chen, S.Z. Deng, Z. X. Yu, and N. S. Xu. Graphitization of nanodiamond powder annealed in argon ambient. *Applied Physics Letters*, 74(24):3651–3653, 1999.

[158] A. C. Ferrari and J. Robertson. Origin of the 1150 cm-1 Raman mode in nanocrystralline diamond. *Physical Review B*, 63(12):121405, 2001.

[159] A.C. Ferrari and J. Robertson. Raman spectroscopy of amorphous, nanostructured, diamond-like carbon, and nanodiamond. *Philosophical transactions. Series A, Mathematical, physical, and engineering sciences*, 362(1824):2477–2512, 2004.

[160] Y. Hirohata. Hydrogen desorption behavior of aluminium materials used for extremely high vacuum chamber. *Journal of Vacuum Science & Technology A: Vacuum, Surfaces, and Films*, 11(5):2637, 1993.

[161] S. Reich and C. Thomsen. Raman spectroscopy of graphite. *Philosophical transactions. Series A, Mathematical, physical, and engineering sciences*, 362(1824):2271–2288, 2004.

[162] T. Jiang and S. Jib. FTIR studies on the spectral changes of the surface functional groups of ultradispersed diamond powder synthesized by explosive detonation after treatment in hydrogen, nitrogen, methane and air at different temperatures. *J. Chem. Soc.,Faraday Trans.*, 92(18):3401–3406, 1996.

[163] T. Ando, M. Ishii, M. Kamo, and Y. Sato. Thermal Hydrogenation of Diamond Surfaces studied by Diffuse Reflectance Fourier-transform Infrared, Temperature-programmed Desorption and Laser Raman Spectroscopy. *Journal of the Chemical Society, Faraday Transactions*, 89(11):1783–1789, 1993.

[164] J.L Figueiredo, M.F.R Pereira, M.M.A Freitas, and J.J.M Órfão. Modification of the surface chemistry of activated carbons. *Carbon*, 37(9):1379–1389, 1999.

[165] C.M. Chen, Q. Zhang, M.G. Yang, C.H. Huang, Y.G. Yang, and M.Z. Wang. Structural evolution during annealing of thermally reduced graphene nanosheets for application in supercapacitors. *Carbon*, 50(10):3572–3584, 2012.

[166] A. Dandekar, R.T.K. Baker, and M.A. Vannice. Characterization of activated carbon, graphitized carbon fibers and synthetic diamond powder using TPD and DRIFTS. *Carbon*, 36(12):1821–1831, 1998.

[167] K.M. McNamara, B.E. Williams, K.K. Gleason, and B.E. Scruggs. Identification of defects and impurities in chemical-vapor-deposited diamond through infrared spectroscopy. *Journal of Applied Physics*, 76(4):2466–2472, 1994.

[168] J. Ristein, R.T. Stief, L. Ley, and W. Beyer. A comparative analysis of a-C:H by infrared spectroscopy and mass selected thermal effusion. *Journal of Applied Physics*, 84(7):3836–3847, 1998.

[169] T. Petit, H.A. Girard, A. Trouvé, I. Batonneau-Gener, P. Bergonzo, and J.C. Arnault. Surface transfer doping can mediate both colloidal stability and self-assembly of nanodiamonds. *Nanoscale*, 5(19):8958–62, 2013.

[170] V. Chakrapani, J.C. Angus, A.B. Anderson, S.D. Wolter, B.R. Stoner, and G.U. Sumanasekera. Charge transfer equilibria between diamond and an aqueous oxygen electrochemical redox couple. *Science*, 318(5855):1424–1430, 2007.

[171] A. Härtl, J.A. Garrido, S. Nowy, R. Zimmermann, C. Werner, D. Horinek, R. Netz, and M. Stutzmann. The ion sensitivity of surface conductive single crystalline diamond. *Journal of the American Chemical Society*, 129(5):1287–1292, 2007.

[172] N. Gibson, O.A. Shenderova, T.J.M. Luo, S. Moseenkov, V. Bondar, A. Puzyr, K. Purtov, Z. Fitzgerald, and D.W. Brenner. Colloidal stability of modified nanodiamond particles. *Diamond and Related Materials*, 18(4):620–626, 2009.

[173] M.A. Montes-Morán, D. Suárez, J.A. Menéndez, and E. Fuente. On the nature of basic sites on carbon surfaces: An overview. *Carbon*, 42(7):1219–1224, 2004.

[174] H.P. Boehm. Some aspects of the surface chemistry of carbon blacks and other carbons. *Carbon*, 32(5):759–769, 1994.

[175] H.P. Boehm. Surface oxides on carbon and their analysis: A critical assessment. *Carbon*, 40(2):145–149, 2002.

[176] H.B. Man, B. Saha, D. Ho, and G.C. Schatz. Understanding the Surfaces of Nanodiamonds. *J. Phys. Chem. C*, 117:17256–17267, 2013.

[177] D. Suárez, J.A. Menéndez, E. Fuente, and M.A. Montes-Morán. Contribution of pyrone-type structures to carbon basicity: An ab initio study. *Langmuir*, 15(11):3897–3904, 1999.

[178] A. Contescu, M. Vass, C. Contescu, K. Putyera, and J.A. Schwarz. Acid buffering capacity of basic carbons revealed by their continuous pK distribution. *Carbon*, 36(3):247–258, 1998.

[179] X. Xu, Z. Yu, Y. Zhu, and B. Wang. Effect of sodium oleate adsorption on the colloidal stability and zeta potential of detonation synthesized diamond particles in aqueous solutions. *Diamond and Related Materials*, 14(2):206–212, 2005.

[180] C.A. Leon y Leon, J.M. Solar, V. Calemma, and L.R. Radovic. Evidence for the protonation of basal plane sites on carbon. *Carbon*, 30(5):797–811, 1992.

[181] M.A. Montes-morán, J.A. Menéndez, E. Fuente, and D. Suárez. Contribution of the Basal Planes to Carbon Basicity : An Ab Initio Study of the H3O+ - pi Interaction in Cluster Models. *J. Phys. Chem.*, 102(JULY):5595–5601, 1998.

[182] J.A. Menéndez, J. Phillips, B. Xia, and L.R. Radovic. On the Modification and Characterization of Chemical Surface Properties of Activated Carbon: In the Search of Carbons With Stable Basic Properties. *Langmuir*, 12(18):4404–4410, 1996.

[183] J. Robertson and E. O'Reilly. Electronic and atomic structure of amorphous carbon. *Physical Review B*, 35(6):2946–2957, 1987.

[184] P. Achatz, J.A. Garrido, M. Stutzmann, O.A. Williams, D.M. Gruen, A. Kromka, and D. Steinmüller. Optical properties of nanocrystalline diamond thin films. *Applied Physics Letters*, 88(10):10–13, 2006.

[185] O.A. Shenderova, V. Grichko, S. Hens, and J. Walch. Detonation nanodiamonds as UV radiation filter. *Diamond and Related Materials*, 16(2007):2003–2008, 2008.

[186] C. Jäger, Th. Henning, R. Schlögl, and O. Spillecke. Spectral properties of carbon black. *Journal of Non-Crystalline Solids*, 258(1):161–179, 1999.

[187] A.T. Collins. Intrinsic and extrinsic absorption and luminescence in diamond. *Physica B: Physics of Condensed Matter*, 185(1-4):284–296, 1993.

[188] R.P. Mildren and J.R. Rabeau. Intrinsic Optical Properties of Diamond. In *Optical Engineering of Diamond*, chapter 1, pages 1–34. Wiley-VCH Verlag GmbH & Co. KGaA, first edition, 2013.

[189] S. Dannefaer. Defects in diamond. *Physica Status Solidi (C) Current Topics in Solid State Physics*, 4(10):3605–3613, 2007.

[190] M.D. Eisaman, J. Fan, A. Migdall, and S.V. Polyakov. Single-photon sources and detectors. *Review of Scientific Instruments*, 82, 2011.

[191] C. Santorini, D. Fattal, and Y. Yamamoto. Introduction. In *Single-photon Devices and Applications*, chapter 1, pages 1–15. WILEY-VCH Verlag GmgH & Co. KGaA, Weinheim, 2010.

[192] H.J. Kimble, M. Dagenais, and L. Mandel. Photon antibunching in resonance fluorescence. *Physical Review Letters*, 39(11):691–695, 1977.

[193] M. Hennrich, T. Legero, A. Kuhn, and G. Rempe. Photon statistics of a non-stationary periodically driven single-photon source. *New Journal of Physics*, 6:1–9, 2004.

[194] B. Lounis and W.E. Moerner. Single photons on demand from a single molecule at room temperature. *Nature*, 407(6803):491–493, 2000.

[195] A. Kiraz, M. Atatüre, and A. Imamoğlu. Quantum-dot single-photon sources: Prospects for applications in linear optics quantum-information processing. *Physical Review A - Atomic, Molecular, and Optical Physics*, 69(3):1–10, 2004.

[196] A.D. Greentree, B.A. Fairchild, F.M. Hossain, and S. Prawer. Diamond integrated quantum photonics. *Materials Today*, 11(9):22–31, 2008.

[197] A.M. Zaitsev. Vibronic spectra of impurity-related optical centers in diamond. *Physical Review B*, 61(19):12909–12922, 2000.

[198] Y.N. Palyanov, I.N. Kupriyanov, Y.M. Borzdov, and N.V. Surovtsev. Germanium: a new catalyst for diamond synthesis and a new optically active impurity in diamond. *Scientific Reports*, 5:14789, 2015.

[199] A. Gruber, A. Dräbenstedt, C. Tietz, L. Fleury, J. Wrachtrup, and C. von Borczyskowski. Scanning Confocal Optical Microscopy and Scanning Confocal Optical Microscopy and Magnetic Resonance on Single Defect Centers. *Science*, 2012(1997):2012–2014, 2009.

[200] T. Gaebel, M. Domhan, C. Wittmann, I. Popa, F. Jelezko, J. Rabeau, A. Greentree, S. Prawer, E. Trajkov, P. R. Hemmer, and J. Wrachtrup. Photochromism in single nitrogen-vacancy defect in diamond. *Applied Physics B: Lasers and Optics*, 82:243–246, 2006.

[201] J.P. Goss, R. Jones, P.R. Briddon, A. Mainwood, A.T. Collins, G. Davies, J.A. van Wyk, M.E. Newton, J.M. Baker, A.M. Stoneham, and S.C. Lawson. Comment on "Electronic structure of the N-V center in diamond: Theory". *Physical Review B*, 56(24):16031–16032, 1997.

[202] M.W. Doherty, N.B. Manson, P. Delaney, F. Jelezko, J. Wrachtrup, and L.C.L. Hollenberg. The nitrogen-vacancy colour centre in diamond. *Physics Reports*, 528(1):1–45, 2013.

[203] J.R. Maze, P.L. Stanwix, J.S. Hodges, S. Hong, J.M. Taylor, P. Cappellaro, L. Jiang, M.V. Gurudev Dutt, E. Togan, A.S. Zibrov, A. Yacoby, R.L. Walsworth, and M.D. Lukin. Nanoscale magnetic sensing with an individual electronic spin in diamond. *Nature*, 455(7213):644–647, 2008.

[204] V.M. Acosta, E. Bauch, M.P. Ledbetter, C. Santori, K.M.C. Fu, P.E. Barclay, R.G. Beausoleil, H. Linget, J.F. Roch, F. Treussart, S. Chemerisov, W. Gawlik, and D. Budker. Diamonds with a high density of nitrogen-vacancy centers for magnetometry applications. *Physical Review B - Condensed Matter and Materials Physics*, 80(11):1–15, 2009.

[205] M.V. Gurudev Dutt, L. Childress, L. Jiang, E. Togan, J. Maze, F. Jelezko, A.S. Zibrov, P.R. Hemmer, and M.D. Lukin. Quantum register based on individual electronic and nuclear spin qubits in diamond. *Science*, 316(5829):1312–1316, 2007.

[206] L.C. Bassett, F.J Heremans, D.J. Christle, C.G. Yale, G. Burkard, B.B. Buckley, and D.D. Awschalom. Ultrafast optical control of orbital and spin dynamics in a solid-state defect. *Science*, 345(6202):1333–1337, 2014.

[207] J.P. Goss, R. Jones, S.J. Breuer, P.R. Briddon, and S. Öberg. The twelve-line 1.682 eV luminescence center in diamond and the vacancy-silicon complex. *Physical Review Letters*, 77(14):3041–3044, 1996.

[208] L.J. Rogers, K.D. Jahnke, M.W. Doherty, A. Dietrich, L.P. McGuinness, C. Müller, T. Teraji, H. Sumiya, J. Isoya, N.B. Manson, and F. Jelezko. Electronic structure of the negatively charged silicon-vacancy center in diamond. *Physical Review B - Condensed Matter and Materials Physics*, 89(23):1–8, 2014.

[209] C. Hepp, T. Müller, V. Waselowski, J.N. Becker, B. Pingault, H. Sternschulte, D. Steinmüller-Nethl, A. Gali, J.R. Maze, M. Atatüre, and C. Becher. Electronic structure of the silicon vacancy color center in diamond. *Physical Review Letters*, 112(3):1–5, 2014.

[210] E.K. Neu, D. Steinmetz, J. Riedrich-Möller, S. Gsell, M. Fischer, M. Schreck, and C. Becher. Single photon emission from silicon-vacancy colour centres in chemical vapour deposition nano-diamonds on iridium. *New Journal of Physics*, 13, 2011.

[211] E.K. Neu, M. Agio, and C. Becher. Photophysics of single silicon vacancy centers in diamond: implications for single photon emission. *Optics Express*, 20(18):19956–19971, 2012.

[212] J.N. Becker, J. Görlitz, C. Arend, M. Markham, and C. Becher. Ultrafast all-optical coherent control of single silicon vacancy colour centres in diamond. *Nature Communications*, 7:13512, 2016.

[213] G. Burkard. Diamond Spins Shining Bright. *Physics*, 7:131, 2014.

[214] S.L. Chang, A.S. Barnard, C. Dwyer, C. Boothroyd, R.K. Hocking, E. Osawa, and R.J. Nicholls. Counting vacancies and nitrogen-vacancy centers in detonation nanodiamond. *Nanoscale*, 1:10548–10552, 2016.

[215] J.O. Orwa, A.D. Greentree, I. Aharonovich, A.D.C. Alves, J. Van Donkelaar, A. Stacey, and S. Prawer. Fabrication of single optical centres in diamonda review. *Journal of Luminescence*, 130(9):1646–1654, 2010.

[216] J.R. Rabeau, P. Reichart, G. Tamanyan, D.N. Jamieson, S. Prawer, F. Jelezko, T. Gaebel, I. Popa, M. Domhan, and J. Wrachtrup. Implantation of labelled single nitrogen vacancy centers in diamond using15N. *Applied Physics Letters*, 88(2):1–3, 2006.

[217] S. Pezzagna, B. Naydenov, F. Jelezko, J. Wrachtrup, and J. Meijer. Creation efficiency of nitrogen-vacancy centres in diamond. *New Journal of Physics*, 12, 2010.

[218] S. Pezzagna, D. Rogalla, D. Wildanger, J. Meijer, and A. Zaitsev. Creation and nature of optical centres in diamond for single-photon emission-overview and critical remarks. *New Journal of Physics*, 13, 2011.

[219] C. Wang, C. Kurtsiefer, H. Weinfurter, and B. Burchard. Single photon emission from SiV centres in diamond produced by ion implantation. *Journal of Physics B: Atomic, Molecular and Optical Physics*, 39(1):37–41, 2006.

[220] J. Barjon, E. Rzepka, F. Jomard, J.M. Laroche, D. Ballutaud, T. Kociniewski, and J. Chevallier. Silicon incorporation in CVD diamond layers. *Physica Status Solidi (A) Applications and Materials Science*, 202(11):2177–2181, 2005.

[221] E.L.H. Thomas, S. Mandal, A.-I. Ahmed, J.E. Macdonald, T.G. Dane, J. Rawle, C.-L. Cheng, and O.A. Williams. Spectroscopic Ellipsometry of Nanocrystalline Diamond Film Growth. *ACS Omega*, 2(10):6715–6727, 2017.

[222] I. Horcas, R. Fernández, J.M. Gómez-Rodríguez, J. Colchero, J. Gómez-Herrero, and A.M. Baro. WSXM: A software for scanning probe microscopy and a tool for nanotechnology. *Review of Scientific Instruments*, 78(1), 2007.

[223] W. Kern. The Evolution of Silicon Wafer Cleaning Technology. *Journal of the Electrochemical Society*, 137(6):1887–1892, 1990.

[224] A. Beveratos, R. Brouri, T. Gacoin, J.-P. Poizat, and P. Grangier. Nonclassical radiation from diamond nanocrystals. *Physical Review A*, 64:61802, 2001.

[225] M. Daenen, O.A. Williams, J. D'Haen, K. Haenen, and M. Nesládek. Seeding, growth and characterization of nanocrystalline diamond films on various substrates. *Physica Status Solidi (a)*, 203(12):3005–3010, 2006.

[226] A. Stacey, I. Aharonovich, S. Prawer, and J.E. Butler. Controlled synthesis of high quality micro/nano-diamonds by microwave plasma chemical vapor deposition. *Diamond and Related Materials*, 18(1):51–55, 2009.

[227] I. Aharonovich, S. Castelletto, D.A. Simpson, C.-H. Su, A.D. Greentree, and S. Prawer. Diamond-based single-photon emitters. *Reports on Progress in Physics*, 74(7):076501, 2011.

[228] V.S. Sedov, I.I. Vlasov, V.G. Ralchenko, A.A. Khomich, V.I. Konov, A.G. Fabbri, and G. Conte. Gas-phase growth of silicon-doped luminescent diamond films and isolated nanocrystals. *Bulletin of the Lebedev Physics Institute*, 38(10):291–296, 2011.

[229] L.J. Rogers, K.D. Jahnke, T. Teraji, L. Marseglia, C. Müller, B. Naydenov, H. Schauffert, C. Kranz, J. Isoya, L.P. McGuinness, and F. Jelezko. Multiple intrinsically identical single-photon emitters in the solid state. *Nature communications*, 5:4739, 2014.

[230] E.K. Neu, M. Fischer, S. Gsell, M. Schreck, and C. Becher. Fluorescence and polarization spectroscopy of single silicon vacancy centers in heteroepitaxial nanodiamonds on iridium. *Physical Review B - Condensed Matter and Materials Physics*, 84(20):1–8, 2011.

[231] R.J. Kershner, J.W. Bullard, and M.J. Cima. Zeta potential orientation dependence of sapphire substrates. *Langmuir*, 20(10):4101–4108, 2004.

[232] G.V. Franks and L. Meagher. The isoelectric points of sapphire crystals and alpha-alumina powder. *Colloids and Surfaces A: Physicochemical and Engineering Aspects*, 214(1-3):99–110, 2003.

[233] S. Hong, M.S Grinolds, L.M. Pham, D. Sage, L. Luan, R.L. Walsworth, A. Yacoby, D. Le Sage, L. Luan, R.L. Walsworth, and A. Yacoby. Nanoscale magnetometry with NV centers in diamond. *MRS Bulletin*, 38(02):155–161, 2013.

[234] O. Romero-Isart, L. Clemente, C. Navau, A. Sanchez, and J.I. Cirac. Quantum magnetomechanics with levitating superconducting microspheres. *Physical Review Letters*, 109(14):1–5, 2012.

[235] Z.Q. Yin, T. Li, X. Zhang, and L.M. Duan. Large quantum superpositions of a levitated nanodiamond through spin-optomechanical coupling. *Physical Review A - Atomic, Molecular, and Optical Physics*, 88(3):1–6, 2013.

[236] A. Albrecht, A. Retzker, and M.B. Plenio. Testing quantum gravity by nanodiamond interferometry with nitrogen-vacancy centers. *Physical Review A - Atomic, Molecular, and Optical Physics*, 90(3):1–19, 2014.

[237] A.W. Schell, G. Kewes, T. Schröder, J. Wolters, T. Aichele, and O. Benson. A scanning probe-based pick-and-place procedure for assembly of integrated quantum optical hybrid devices. *Review of Scientific Instruments*, 82(7):1–5, 2011.

[238] A.T.M.A. Rahman, A.C. Frangeskou, M.S. Kim, S. Bose, G.W. Morley, and P.F. Barker. Burning and graphitization of optically levitated nanodiamonds in vacuum. *Scientific Reports*, 6:21633, 2016.

[239] D.S. Volkov, M.A. Proskurnin, and M.V. Korobov. Elemental analysis of nanodiamonds by inductively-coupled plasma atomic emission spectroscopy. *Carbon*, 74:1–13, 2014.

[240] D.P. Mitev, A.T. Townsend, B. Paull, and P.N. Nesterenko. Direct sector field ICP-MS determination of metal impurities in detonation nanodiamond. *Carbon*, 60:326–334, 2013.

[241] S. Heyer, W. Janssen, S. Turner, Y.G. Lu, W.S. Yeap, J. Verbeeck, K. Haenen, and A. Krueger. Toward deep blue nano hope diamonds: Heavily boron-doped diamond nanoparticles. *ACS Nano*, 8(6):5757–5764, 2014.

[242] M.J. Remy, M.J. Genet, G. Poncelet, P.F. Lardinois, and P.P. Notté. Investigation of dealuminated mordenites by X-ray photoelectron spectroscopy. *Journal of Physical Chemistry*, 96(6):2614–2617, 1992.

[243] S Ghodbane, D Ballutaud, F Omnès, and C Agnès. Comparison of the XPS spectra from homoepitaxial { 111 }, { 100 } and polycrystalline boron-doped diamond fi lms. *Diamond & Related Materials*, 19(5-6):630–636, 2010.

[244] F. Klauser, S. Ghodbane, R. Boukherroub, S. Szunerits, D. Steinmüller-Nethl, E. Bertel, and N. Memmel. Comparison of different oxidation techniques on single-crystal and nanocrystalline diamond surfaces. *Diamond and Related Materials*, 19(5-6):474–478, 2010.

[245] S. Ferro, M. Dal Colle, and A. De Battisti. Chemical surface characterization of electrochemically and thermally oxidized boron-doped diamond film electrodes. *Carbon*, 43(6):1191–1203, 2005.

[246] S.D. Gardner, C.S.K. Singamsetty, G.L. Booth, G.-R. He, and C.U. Pittman. Surface characterization of carbon fibers using angle-resolved XPS and ISS. *Carbon*, 33(5):587–595, 1995.

[247] H. Notsu. Introduction of Oxygen-Containing Functional Groups onto Diamond Electrode Surfaces by Oxygen Plasma and Anodic Polarization. *Electrochemical and Solid-State Letters*, 2(10):522, 1999.

[248] C. Goeting. Electrochemically induced surface modifications of boron-doped diamond electrodes: an X-ray photoelectron spectroscopy study. *Diamond and Related Materials*, 9(3-6):390–396, 2000.

[249] P. Mérel, M. Tabbal, M. Chaker, S. Moisa, and J. Margot. Direct evaluation of the sp3 content in diamond-like-carbon films by XPS. *Applied Surface Science*, 136(1-2):105–110, 1998.

[250] S.T. Jackson and R.G. Nuzzo. Determining hybridization differences for amorphous carbon from the XPS C1s envelope. 90:195–203, 1995.

[251] H. Estrade-Szwarckopf. XPS photoemission in carbonaceous materials: A "defect" peak beside the graphitic asymmetric peak. *Carbon*, 42(8-9):1713–1721, 2004.

[252] L. Feng, L. Yang, Z. Huang, J. Luo, M. Li, D. Wang, and Y. Chen. Enhancing electrocatalytic oxygen reduction on nitrogen-doped graphene by active sites implantation. *Scientific Reports*, 3:1–8, 2013.

[253] Y.J. Xu, G. Weinberg, X. Liu, O. Timpe, R. Schlögl, and D.S. Su. Nanoarchitecturing of activated carbon: Facile strategy for chemical functionalization of the surface of activated carbon. *Advanced Functional Materials*, 18(22):3613–3619, 2008.

[254] K. Yamamoto, Y. Koga, and S. Fujiwara. XPS studies of amorphous SiCN thin films prepared by nitrogen ion-assisted pulsed-laser deposition of SiC target. *Diamond and Related Materials*, 10(9-10):1921–1926, 2001.

[255] S. Zeppilli, J.C. Arnault, C. Gesset, P. Bergonzo, and R. Polini. Thermal stability and surface modifications of detonation diamond nanoparticles studied with X-ray photoelectron spectroscopy. *Diamond and Related Materials*, 19(7-9):846–853, 2010.

[256] B. Agius, S. Rigo, F. Rochet, M. Froment, C. Maillot, H. Roulet, and G. Dufour. Structural evolution of very thin silicon oxide films during thermal growth in dry oxygen. *Applied Physics Letters*, 44(1):48–50, 1984.

[257] G Hollinger and F.J. Himpsel. Multiple-bonding configurations for oxygen on silicon surfaces. *Physical Review B*, 28(6):3651–3653, 1983.

[258] A. Thøgersen, J.H. Selj, and E.S. Marstein. Oxidation effects on graded porous silicon anti-reflection coatings. *Journal of The Electrochemical Society*, 159(5):276–281, 2012.

[259] J.-W. He, X. Xu, J.S. Corneille, and D.W. Goodman. X-ray photoelectron spectroscopic characterization of ultra-thin silicon oxide films on a Mo(100) surface. *Surface Science*, 279(1-2):119–126, 1992.

[260] C.D. Wagner, L.E. Davis, M.V. Zeller, J.A. Taylor, R.H. Raymond, and L.H. Gale. Empirical atomic sensitivity factors for quantitative analysis by electron spectroscopy for chemical analysis. *Surface and Interface Analysis*, 3(5):211–225, 1981.

[261] B. Schwartz and H. Robbins. Chemical Etching of Silicon IV. *J. Electrochem. Soc.*, 123(12):1903–1909, 1976.

[262] P. Walker and W.H. Tarn. *Handbook of Metal Etchants*. 1991.

[263] M. Aslam. Bulk etching of silicon wafer and development of a polyimide membrane. *Journal of Physics: Conference Series*, 439(1), 2013.

[264] E.K. Neu, F. Guldner, C. Arend, Y. Liang, S. Ghodbane, H. Sternschulte, D. Steinmüller-Nethl, A. Krueger, and C. Becher. Low temperature investigations and surface treatments of colloidal narrowband fluorescent nanodiamonds. *Journal of Applied Physics*, 113(20), 2013.

[265] R. Hanbury Brown and R. Q. Twiss. A test of a new type of stellar interferometer on Sirius. *Nature*, 178(4541):1046–1048, 1956.

[266] A.T. Collins. A spectroscopic study of optical centers in diamond grown by microwave-assisted chemical vapor deposition. *Journal of Materials Research*, 5(11):2507–2514, 1990.

[267] H. Zhang, I. Aharonovich, D.R. Glenn, R. Schalek, A.P. Magyar, J.W. Lichtman, E.L. Hu, and R.L. Walsworth. Silicon-Vacancy Color Centers in Nanodiamonds : Cathodoluminescence Imaging Markers in the Near Infrared. *Small*, pages 1908–1913, 2014.

[268] R. Samlenski, C. Haug, R. Brenn, C. Wild, R. Locher, and P. Koidl. Incorporation of nitrogen in chemical vapor deposition diamond. *Applied Physics Letters*, 67(1995):2798, 1995.

[269] S. Dunst, H. Sternschulte, and M. Schreck. Growth rate enhancement by nitrogen in diamond chemical vapor deposition — a catalytic effect. *Applied Physics Letters*, 94(22):1–4, 2009.

[270] W. Müllersebert, E. Wörner, F. Fuchs, C. Wild, P. Koidl, and E. Wo. Nitrogen induced increase of growth rate in chemical vapor deposition of diamond. *Applied Physics Letters*, 759(68):1995–1997, 2009.

[271] I.I. Vlasov, V.G. Ralchenko, E. Goovaerts, A.V. Saveliev, and M.V. Kanzyuba. Bulk and surface-enhanced Raman spectroscopy of nitrogen-doped ultrananocrystalline diamond films. *Physica Status Solidi (a)*, 203(12):3028–3035, 2006.

[272] S. Singh and S.A. Catledge. Silicon vacancy color center photoluminescence enhancement in nanodiamond particles by isolated substitutional nitrogen on {100} surfaces. *Journal of Applied Physics*, 113(4), 2013.

[273] K.D. Jahnke, A. Sipahigil, J.M. Binder, M.W. Doherty, M. Metsch, L.J. Rogers, N.B. Manson, M.D. Lukin, and F. Jelezko. Electron-phonon processes of the silicon-vacancy centre in diamond. *New Journal of Physics*, 17(4):43011, 2015.

[274] B. Yang, J. Li, L. Guo, N. Huang, L. Liu, Z. Zhai, W. Long, and X. Jiang. Fabrication of silicon-vacancy color centers in diamond films: tetramethylsilane as a new dopant source. *CrystEngComm*, 20(8):1158–1167, 2018.

[275] D. Steinmetz, E.K. Neu, J. Meijer, W. Bolse, and C. Becher. Single photon emitters based on Ni/Si related defects in single crystalline diamond. *Applied Physics B: Lasers and Optics*, 102(3):451–458, 2011.

[276] V. Sedov, V. Ralchenko, A.A. Khomich, I. Vlasov, A. Vul, S. Savin, A. Goryachev, and V. Konov. Si-doped nano- and microcrystalline diamond films with controlled bright photoluminescence of silicon-vacancy color centers. *Diamond and Related Materials*, 56:23–28, 2015.

[277] V.A. Davydov, A.V. Rakhmanina, S.G. Lyapin, I.D. Ilichev, K.N. Boldyrev, A.A. Shiryaev, and V.N. Agafonov. Production of nano- and microdiamonds with Si-V and N-V luminescent centers at high pressures in systems based on mixtures of hydrocarbon and fluorocarbon compounds. *JETP Letters*, 99(10):585–589, 2014.

[278] Y.-X. Cui, J.-G. Zhang, F.-H. Sun, and Z.-M. Zhang. Si-doped diamond films prepared by chemical vapour deposition. *Transactions of Nonferrous Metals Society of China*, 23(10):2962–2970, 2013.

[279] S.A. Grudinkin, N.A. Feoktistov, A.V. Medvedev, K.V. Bogdanov, A.V. Baranov, A.Y. Vul', and V.G. Golubev. Luminescent isolated diamond particles with controllably embedded silicon-vacancy colour centres. *Journal Of Physics D-applied Physics*, 45:1–4, 2012.

[280] A. Bolshakov, V. Ralchenko, V. Sedov, A. Khomich, I. Vlasov, A. Khomich, N. Trofimov, V. Krivobok, S. Nikolaev, R. Khmelnitskii, and V. Saraykin. Photoluminescence of SiV centers in single crystal CVD diamond in situ doped with Si from silane. *Physica Status Solidi (A) Applications and Materials Science*, 212(11):2525–2532, 2015.

[281] E.L.H. Thomas and S. Mandal. Quartz tube chemical vapor deposition reactor. Retrieved March 7, 2018 from: https://en.m.wikiversity.org/wiki/Quartz tube chemical vapor deposition reactor, 2016.

[282] R.S. Balmer, J.R. Brandon, SL Clewes, H K Dhillon, J M Dodson, I Friel, P N Inglis, T D Madgwick, M L Markham, T P Mollart, N Perkins, G a Scarsbrook, D J Twitchen, a J Whitehead, J J Wilman, and S M Woollard. Chemical vapour deposition synthetic diamond: materials, technology and applications. *Journal of Physics: Condensed Matter*, 21(36):364221, 2009.

[283] W.G. Eversole. Synthesis of Diamond. U.S. Patent No. 3,030,188, 1962.

[284] B.V. Derjaguin, D.V. Fedoseev, V.M. Lukyanovich, B.V. Spitzin, V.A. Ryabov, and A.V. Lavrentyev. Filamentary diamond crystals. *Journal of Crystal Growth*, 2(6):380–384, 1968.

[285] W.G. Eversole. Synthesis of Diamond. U.S. Patent No. 3,030,187, 1962.

[286] J.J. Lander and J. Morrison. Low energy electron diffraction study of the (111) diamond surface. *Surface Science*, 4:241–246, 1966.

[287] D.V. Fedoseev, K.S. Uspenskaya, V.P. Varnin, and S.P. Vnukov. Effect of hydrogen on diamond growth from a gaseous phase. *Bulletin of the Academy of Sciences of the USSR Division of Chemical Science*, 27(6):1088–1091, 1978.

[288] S. Matsumoto, Y. Sato, M. Tsutsumi, and N. Setaka. Growth of diamond particles from methane-hydrogen gas. *Journal of Materials Science*, 17(11):3106–3112, 1982.

[289] M. Kamo, Y. Sato, S. Matsumoto, and N. Setaka. Diamond synthesis from gas phase in microwave plasma. *Journal of Crystal Growth*, 62(3):642–644, 1983.

[290] K. Mutsukazu, M. Seiichiro, S. Yoichiro, and N. Setaka. Method for Synthesizing Diamond. U.S. Patent No. 4,434,188, 1984.

[291] Y. Hirose, S. Amanuma, and K. Komaki. The synthesis of high-quality diamond in combustion flames. *Journal of Applied Physics*, 68(12):6401–6405, 1990.

[292] K. Kurihara, K. Sasaki, M. Kawarada, and N. Koshino. Method and apparatus for Vapor Deposition of Diamond. U.S. Patent 5,403,399, 1995.

[293] D.M. Pozar. *Microwave Engineering*. John Wiley & Sons, Inc, fourth edition, 2011.

[294] F. Silva, K. Hassouni, X. Bonnin, and A. Gicquel. Microwave engineering of plasma-assisted CVD reactors for diamond deposition. *Journal of Physics Condensed Matter*, 21(36), 2009.

[295] CST Computer Simulation Technology GmbH. Waveguides: rectangular waveguide. Retrieved March 7, 2018, from: https://www.cst.com/academia/examples/hollow-rectangular-waveguide.

[296] V. Mortet, M. Daenen, T. Teraji, A. Lazea, V. Vorlicek, J. D'Haen, K. Haenen, and M. D'Olieslaeger. Characterization of boron doped diamond epilayers grown in a NIRIM type reactor. *Diamond and Related Materials*, 17(7-10):1330–1334, 2008.

[297] M K S Instruments. MKS Type pi-MFC TM Digital Mass Flow Controller.

[298] J. Filik, J.N. Harvey, N.L. Allan, P.W. May, J.E.P. Dahl, S. Liu, and R.M.K. Carlson. Raman spectroscopy of nanocrystalline diamond: An ab initio approach. *Physical Review B - Condensed Matter and Materials Physics*, 74(3):1–10, 2006.

[299] C. Bednarski, Z. Dai, A. P. Li, and B. Golding. Studies of heteroepitaxial growth of diamond. *Diamond and Related Materials*, 12(3-7):241–245, 2003.

[300] D. Das and R.N. Singh. A review of nucleation, growth and low temperature synthesis of diamond thin films. *International Materials Reviews*, 52(1):29–64, 2007.

[301] J.C. Arnault. Highly Oriented Diamond Films on Heterosubstrates: Current State of the Art and Remaining Challenges. *Surface Review and Letters*, 10(01):127–146, 2003.

[302] Measure Surface Zeta Potential. Retrieved March 3, 2018, from http://www.materials-talks.com/blog/2015/01/06/surface-zeta-potential-what-it-is-and-how-to-measure-it/.

[303] T. Luxbacher. *The Zeta Potential for Solid Surface Analysis*. Anton Paar GmbH, Austria, first edition, 2014.

[304] A.M. Gallardo-Moreno, V. Vadillo-Rodríguez, J. Perera-Núñez, J.M. Bruque, and M.L. González-Martín. The zeta potential of extended dielectrics and conductors in terms of streaming potential and streaming current measurements. *Physical Chemistry Chemical Physics*, 14(27):9758, 2012.

[305] R. Schweiss, P.B. Welzel, C. Werner, and W. Knoll. Interfacial charge of organic thin films characterized by streaming potential and streaming current measurements. *Colloids and Surfaces A: Physicochemical and Engineering Aspects*, 195(1-3):97–102, 2001.

[306] S.L. Walker, S. Bhattacharjee, E.M.V. Hoek, and M. Elimelech. A novel asymmetric clamping cell for measuring streaming potential of flat surfaces. *Langmuir*, 18(6):2193–2198, 2002.

[307] Short Instruction: Conductive Material. Technical report, Anton Paar High-precision Instruments.

[308] T. Bauer, S. Gsell, M. Schreck, J. Goldfuß, J. Lettieri, D.G. Schlom, and B. Stritzker. Growth of epitaxial diamond on silicon via iridium/SrTiO3buffer layers. *Diamond and Related Materials*, 14(3-7):314–317, 2005.

[309] S. Gsell, T. Bauer, J. Goldfuß, M. Schreck, and B. Stritzker. A route to diamond wafers by epitaxial deposition on silicon via iridium/yttria-stabilized zirconia buffer layers. *Applied Physics Letters*, 84(22):4541–4543, 2004.

[310] M.J. Verstraete and J.C. Charlier. Why is iridium the best substrate for single crystal diamond growth? *Applied Physics Letters*, 86(19):1–3, 2005.

[311] M. Schreck, F. Hörmann, H. Roll, J.K.N. Lindner, and B. Stritzker. Diamond nucleation on iridium buffer layers and subsequent textured growth: A route for the realization of single-crystal diamond films. *Applied Physics Letters*, 78(2):192–194, 2001.

[312] Y.-C. Chu, C.-H. Tu, G. Jiang, C. Chang, C.-P. Liu, J.-M. Ting, H.-L. Lee, Y. Tzeng, and O. Auciello. Systematic studies of the nucleation and growth of ultrananocrystalline diamond films on silicon substrates coated with a tungsten layer. *Journal of Applied Physics*, 111(12):124328, 2012.

[313] L.J. Chen, C.C. Liu, N.H. Tai, C.Y. Lee, W. Fang, and I.N. Lin. Effects of tungsten metal coatings on enhancing the characteristics of ultrananocrystalline diamond films. *Journal of Physical Chemistry C*, 112(10):3759–3765, 2008.

[314] A. Krueger, Masaki Ozawa, Gerald Jarre, Yuejiang Liang, Jochen Stegk, and Li Lu. Deagglomeration and functionalisation of detonation diamond. *Physica Status Solidi (A) Applications and Materials Science*, 204(9):2881–2887, 2007.

[315] E.L.H. Thomas, L. Ginés, S. Mandal, G.M. Klemencic, and O.A. Williams. A simple, space constrained NIRIM type reactor for chemical vapour deposition of diamond. *AIP advances, In press*, 2018.